New approaches to the study of hydrophobicity and wetting of soils: methods and theories

Helen Mair Balshaw

A thesis submitted in fulfilment of the requirements for the degree of Doctor of Philosophy in Swansea University

College of Engineering
Swansea University
2019

Summary

New approaches to the study of hydrophobicity and wetting of soils were investigated with the following research objectives: 1) to evaluate the use of fluorescence probes, nile red and pyrene, as tools to assess the polarity and viscosity of organics adsorbed to soils; 2) to assess, using a variety of kinetic methods, what steps are involved in wetting soils; and 3) to assess the validity of current theories for the anomalously high contact angles often measured for water on soils, and investigate an alternative explanation based on the geometry of a water drop sitting on hydrophobic particles.

Whilst it was possible to image nile red emission after adsorption to soils, issues of emission intensity and soil auto-luminescence suggest that nile red is not a useful probe for soil studies.

Fluorescence measurements were made using pyrene as an *in-situ* polarity and viscosity/mobility probe. Using pyrene co-deposited with organics on acid-washed sand, excimer kinetics showed a decrease in environment mobility as the organic layer was changed from a liquid to a hard wax. Spectra from natural soils indicated varying environmental polarity and heterogeneity within the soil samples studied.

A theoretical model for soil wetting, involving adhesional-immersional wetting followed by branching capillary wetting, is proposed, and a series of experiments to assess the validity of this model described. Methods used include: water drop penetration time (WDPT) test, mass of soil grains wetted over time; time taken for penetration of a water drop into different soil thicknesses; optical microscopy; WDPT measurements with salt solutions of different densities.

An alternative interpretation of the anomalously high contact angles measured on soils is proposed based on a correction factor for water on particles. To assess this, measurements were made using regularly arranged ballpoint needles and metal spheres, and acid-washed sand and natural soil, coated in paraffin wax.

.

Declarations

This work has not previously been accepted in substance for any degree and is not being concurrently submitted in candidature for any degree.

Signed ..... (candidate)

Date .....

STATEMENT 1

This thesis is the result of my own investigations, except where otherwise stated.

Other sources are acknowledged by footnotes giving explicit references. A bibliography is appended.

Signed ..... (candidate)

Date .....

STATEMENT 2

I hereby give consent for my thesis, if accepted, to be available for photocopying and for inter-library loan, and for the title and summary to be made available to outside organisations.

Signed ..... (candidate)

Date .....

Contents

Acknowledgements

Thank you to the College of Engineering for providing a DTA funded bursary to allow me to follow my dream of completing a PhD in soil water repellency. Thank you to the RSC and BSSS for funding attendance at workshops and conferences.

To Stefan, who started this whole process many moons ago when I was an undergraduate and completed my dissertation in soil water repellency. The love of the phenomenon never faded and the opportunity of completing a PhD about it has been all I had hoped and more. Thank you for your help securing the funding for the PhD and of course your endless knowledge and support.

To my office buddy Rhys, who has been a great source of entertainment and support over the last few years. Thank you for your friendship, I've very much enjoyed sharing an office and attending conferences with you.

Thanks to Matthew for your enthusiasm, help and assistance with the photochemistry work. Very much appreciate you letting me take over your lab for weeks on end and trusting me with some very expensive pieces of equipment!

Thank you to Grahame and Rhodri in the Geography department for your assistance carrying out various experimental analysis and for letting me set up home in the constant temperature/humidity room with all my samples for months on end! And to Emilia for your help getting the goniometer functioning and suggesting suitable soil sampling sites around the Gower.

Thanks to Mike, Ian, Rod, Stan 'the man' and all the other regulars at lunchtime noshes! Your company over the last few years has been wonderful, I've felt welcome right from the start and I'll very much miss our Bouchon outings!

Thanks to Bill for the regular football chats and to John T. for letting me steal all your valuable tools at a moment's notice!

To Peter, thank you for your friendship, patience, guidance and support over the last few years, I've enjoyed travelling with you and learning from you very much, both academically and from the immense amount of knowledge you have about the world in general. Thank you for making my time doing a PhD the absolute best it could be. I'll miss you, and the fig rolls and Battenburg! Thank you for the laughter.

Finally, to my family. To my parents for their endless support and belief in me. So many things over the last few years would not have been possible if it wasn't for you. Thank you for helping my dream become a reality. Thanks to Ruth, Dean and Pots, who have been unwavering in their support. Thanks to Baz, who has made the last few years absolutely wonderful, your support has meant the world, Caru ti. I've thoroughly enjoyed my time returning to the city where 'Ambition is critical' and it will forever hold a fond place in my heart. Thank you all for the memories.

Abbreviations and Symbols

General soil and water repellency

AU2 – Australian water repellent soil
AU3 – Australian water repellent soil
AWS – acid-washed sand
CL – confidence limit
DSA –drop shape analysis software
HEX – hexadecane
LLAN1 – Llanmadoc water repellent soil (top 10 cm)
LLAN2 – Llanmadoc water repellent soil (10-20 cm)
NIC1 – Nicholaston water repellent soil (more repellent)
NIC2 – Nicholaston water repellent soil (less repellent)
NL1 – Netherlands water repellent soil
OCT – octadecane
PSD – particle size distribution
RH – relative humidity
SA – stearic acid
SQ – squalane
TC – total carbon
TOC – total organic carbon
UKC – a UK sourced wettable soil
WDPT – water drop penetration time

Photochemistry

A / Abs – absorbance
bw – bandwidth
F – fluorescence
HOMO – highest occupied molecular orbital
I – intensity
I_{abs} – absorbed intensity
I_{em} – emitted intensity
LUMO – lowest unoccupied molecular orbital
P - phosphorescence
$S_{0, 1, 2, \ldots}$ – singlet state
S/N – signal-to-noise ratio
$T_{1, 2, \ldots}$ – triplet state
TCSPC – time correlated single photon counting
UV – ultraviolet
UV/Vis – ultraviolet/visible
UV_{ex}/Vis_{em} – UV excitation/visual wavelength emission
$Green_{ex}/Red_{em}$ – green light excitation/red light emission
v – vibrational level
λ – wavelength
λ_{abs} – absorption wavelength, wavelength of maximum absorption
λ_{em} – emission wavelength, wavelength of maximum emission
$\lambda_{lonpass}$ – longpass wavelength
λ_{max} – wavelength where the property under discussion is a maximum

ε – molar absorption coefficient
$h\upsilon$ – photon
IC – internal conversion
ISC – intersystem crossing
k – Boltzmann constant
m_s – spin quantum number
Φ_F – quantum yield of fluorescence
Ψ – wavefunction
* – excited-state, or antibonding orbital
τ – lifetime
$\tau_{S,T}$ – lifetime of singlet state, triplet state

Kinetics and wetting

a – pre-exponential factor
BN - ballpoint needle
G_s – Gibbs surface energy
$G_s^{initial}$ – initial state Gibbs surface energy
G_s^{final} – final state Gibbs surface energy.
$Initial_{exp}$ – experimental initial mass
$Initial_{theo}$ – calculated theoretical initial mass
k – reaction rate constant
L_{CL} – length of contact line
MS – metal sphere
R – universal gas constant
t_{pen} – penetration time
t_{inf} – time taken for infiltration to start
t_t – time taken for drop to penetrate thickness of soil
γ – surface tension
γ^{SL} – surface tension of solid-liquid interface
γ^{SV} – surface tension of solid-vapour interface
γ^{LV} – surface tension liquid-vapour interface
$\theta_{critical}$ – critical contact angle required to contact second layer of grains
θ_A – advancing contact angle measured
d – depth
$d_{critical}$ – critical penetration depth to contact second layer of grains

Contact angle

E – energy
E_D – net energy
f_1 – total area of the solid-liquid interface
f_2 – total area of the liquid-vapour interface
κ – calculated correction factor
θ – contact angle
θ_A – advancing angle
$\theta_{corrected}$ – contact angle after geometric correction
θ_{flat} – measured contact angle on a planar flat surface (no correction)
$\theta_{measured}$ – measured contact angle (no correction)
r – radius (mm)
R – roughness factor (Wenzel)

Symbols

Δ – delta
π – mathematical constant 3.14159265359

General

t – time
T – temperature
V – volume
ε – dielectric constant
η – viscosity
r.t. – room temperature
m.pt – melting point
M – molar

Units

A – Angstrom (10^{-10} m)
^{o}C – degree centigrade
g – gram
h – hour
J – Joule
K – degree Kelvin
l – litre
m – metre
s – second
ns – nanosecond
ps – picosecond

Prefixes

Symbol	Name	Factor
p	pico	10^{-12}
n	nano	10^{-9}
μ	micro	10^{-6}
m	milli	10^{-3}
c	centi	10^{-2}
k	kilo	10^{3}

Common equations

Area of sphere = $4\pi r^2$

Volume of sphere = $\frac{4}{3}\pi r^3$

Volume of hemisphere = $\frac{2\pi r^3}{3}$

Volume of cylinder= $\pi r^2 h$

Publications and conference contributions

Aspects of the work reported in this thesis have been presented previously in the following formats.

Peer-reviewed papers:

Balshaw H.M., Douglas, P., Davies, M.L. & Doerr, S.H. On the use of pyrene and nile red fluorescence probes for in-situ study of polarity and viscosity of soil organic coatings implicated in soil water repellency. *European Journal of Soil Science* (Accepted subject to revision, October 2019, ID EJSS-061-19).

Conference proceedings:

Balshaw, H.M., Douglas, P., Ahn, S. & Doerr, S.H. Soil water repellency a global problem: impact, measurement and mechanisms. The fifth annual Asian conference on sustainability, energy and the environment. *Official conference proceedings*. 2015. (ISSN: 2186-2311).

Oral presentations:

1. Fluorescent probes for understanding soil water repellency: the novel application of a chemist's tool to soil science. European Geosciences Union (EGU) conference, Vienna, Austria. April 2015.
2. Soil water repellency – a global phenomenon: impact, measurement and mechanisms. 5th Asian conference on Sustainability, Energy and Environment. Kobe, Japan. June 2015.
3. Pyrene as a probe for understanding soil water repellency. RSC, Environmental Chemistry of Water, Sediment and Soil Early Career Researchers Meeting. Burlington House, London. November 2016.

Poster presentations:

1. The influence of chemical and physical factors in determining soil water repellency. 5th EuCheMS Chemistry Congress. WOW convention centre, Istanbul, Turkey. Bridging the Gap project. August 2014.
2. Measuring and understanding soil wetting, the first step in nutrient/agrochemical retention. International Fertiliser Society (IFS) Agronomic Conference, Robinson College, Cambridge. Brian Chambers International Award for early career researchers in crop nutrition finalist. December 2016.

3. Measuring and understanding soil wetting, the first step in nutrient/agrochemical retention. British Society of Soil Science. Early Career Researchers Conference, Lancaster University, Lancaster. April 2017.
4. Measuring and understanding soil water repellency through novel interdisciplinary approaches. European Geosciences Union (EGU) conference. April 2017.
5. Pyrene fluorescence probe: the application of a chemist's tool to characterizing the organic matter on soil grains of model and sandy soils. 6th International Symposium on Soil Organic Matter, Rothamsted Research, Harpenden. September 2017.

To my parents

Chapter 1 Introduction

This chapter gives an overview of the phenomenon of soil water repellency. The key factors that cause and enhance soil water repellency are considered, together with the environmental implications it causes. The key measurement methods for assessing the severity and the persistence of soil water repellency are also included. Experimental research objectives are outlined in line with current research gaps in the field of soil water repellency research.

1.1. Introduction

Soil water repellency has been studied by researchers for many decades (DeBano, 2000; Mao *et al.*, 2019). It is defined as the reduced ability of some soils to be wetted and absorb water, in some instances for prolonged periods of time. Before addressing the physical and chemical mechanisms behind soil water repellency it is first important to consider the components that give rise to its occurrence, namely, soil and water, and how their interaction leads to a complicated, yet common, global phenomenon.

1.1.1. Soil

Soil is a heterogeneous mix of inorganic, organic and mineral particles that exist within a three-phase system (solid, liquid and gas), which is responsible for supporting life by regulating nutrient and water supplies to promote the growth of vegetation and macro and micro flora and fauna; and is constantly evolving in response to natural climatic factors and human and animal influences (Sumner and Wilding, 1999). Every soil has a profile made up of one or more horizons of varying depths, and soil textural classes can range from sandy, loamy, silty, clay and peat. Over time, physical and chemical formation processes will influence the size and shape of soil aggregates and particles, many of which are often coated by other materials such as organic matter, clay, and precipitated salts (Sumner and Wilding, 1999).

1.1.2. Water

A water molecule comprises two hydrogen atoms covalently bonded to an oxygen atom in a bent arrangement, with an inter-bond angle of 104.5^{o} (Figure 1.1). Whilst a water molecule as a whole is electrically neutral the positive and negative charges within are not distributed evenly. There is a negative charge surrounding the oxygen atom, arising from non-bonding electron pairs and the high nuclear charge of the oxygen atom itself giving a stronger attraction between itself and the bonding electrons, which results in a positive charge on the hydrogen atoms.

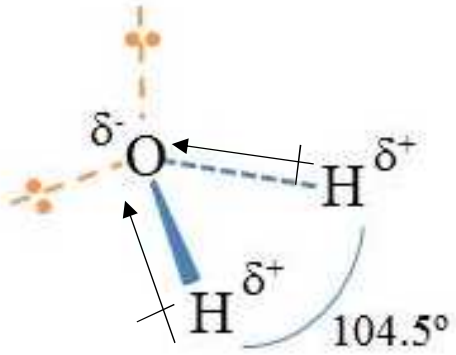

Figure 1.1 Geometric structure of a water molecule, with O-H bond length of 0.096 nm (adapted from Petrucci, 1989).

This charge distribution leads to strong intermolecular forces, which in turn leads to the many unusual properties of liquid water, notably a higher boiling point and higher surface tension compared to other small molecular species (Brini *et al*., 2017).

1.1.3. Intermolecular forces

Intermolecular forces are due to electrostatic interactions between molecules.

Dispersion forces exist between all molecules and are due to attractive electrostatic interactions between instantaneous dipoles, formed from the continual movement of electrons in atoms or molecules (Rigby *et al.*, 1986). Although individually weaker than polar forces, dispersion forces increase with molecular size such that they dominate even for moderately sized polar molecules. Apart from highly polar molecules such as water, dispersion forces are the dominant intermolecular forces (Rigby *et al.*, 1986).

Polar intermolecular forces exist between molecules, such as water, which have an uneven charge distribution leading to permanent electric dipoles; polar forces can be dipole-dipole, or dipole-induced dipole, in nature. Hydrogen bonding is a particular type of polar intermolecular force which arises from, in the example of water, an electropositive hydrogen atom covalently bonded to an electronegative oxygen atom, oriented towards an electronegative oxygen atom on another molecule (Rigby *et al.*, 1986). Hydrogen bonds are considerably weaker than covalent bonds, in water hydrogen bond energies have been estimated to be around 18.86 kJ mol^{-1}, compared with 460.9 kJ mol^{-1} for the H-O electron pair bonds (Hillel, 1998). There is currently

much debate amongst researchers regarding the structure of liquid water, particularly whether the water molecules are in tetrahedral or 'ring-and-chain' like structures (Liu *et al.*, 2017). The tetrahedral arrangement of four hydrogen atoms, two covalently bonded and two hydrogen bonded, around a central oxygen atom (Rigby *et al.*, 1986) is shown in Figure 1.2.

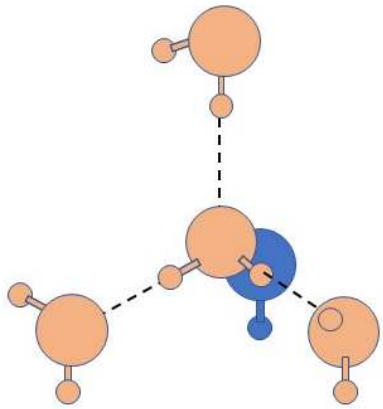

Figure 1.2 Tetrahedral structure of a water molecule (based on Petrucci, 1989).

1.1.4. Polar molecules (hydrophilic)

Polar molecules such as water exist as a result of an imbalance between positive and negative charges across the molecule from polar bonds causing an electric dipole, in this instance, the negative charge of the oxygen atom and the positive charge of the hydrogen atoms. Examples of polar molecules include water (H_2O), ammonia (NH_3) and ethanol (C_2H_5OH).

1.1.5. Non-polar molecules (hydrophobic)

A non-polar molecule occurs as a result of equal sharing of electrons between two atoms or due to the symmetrical arrangement of polar bonds in some complex molecules (Ratcliff *et al.*, 2000). Examples of non-polar molecules include methane (CH_4) carbon dioxide (CO_2) and hydrocarbons such as hexadecane ($C_{16}H_{34}$) and octadecane ($C_{18}H_{38}$).

1.1.6. Amphiphilic molecules

Amphiphilic molecules consist of a polar head group attached to a non-polar chain/group. A typical example of a common fatty acid naturally found to occur in

soils is stearic acid (Deng and Dixon, 2002). Stearic acid ($C_{18}H_{36}O_2$) consists of a hydrophilic polar carboxyl head group and a hydrophobic, non-polar hydrocarbon chain (Figure 1.3). Amphiphilic molecules make good surfactants.

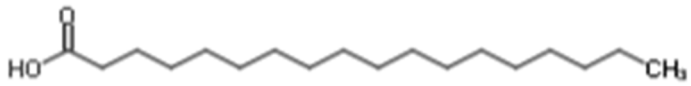

Figure 1.3 Structure of stearic acid showing the polar carboxyl head group (COOH) and non-polar hydrocarbon chain.

1.1.7. Surface tension

Surface tension can be defined as the force required to expand a surface, the force per unit length. It is generally given the symbol, γ, with SI units of N m^{-1}.

1.1.8. Surface energy

A surface has excess Gibbs energy (G) relative to the interior of the material, this is termed the surface Gibbs energy and referred to hereafter as G_s.

The relationship between surface tension and surface energy is where energy is force multiplied by the distance over which the force is opposed; therefore, the increase in Gibbs energy as a surface expands is given by (Equation 1.1):

$$\Delta G = \gamma \Delta_{area} \tag{1.1}$$

The surface Gibbs energy (G_s) of an object, such as a water droplet, is given by Equation 1.2:

$$G_s = \gamma area_{surface} \tag{1.2}$$

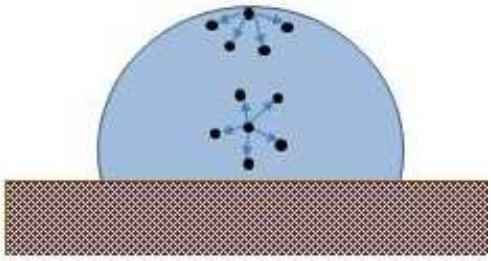

Figure 1.4 Attractive forces between surface molecules in a water drop. Molecules at the surface experience a net downward force compared to those in the interior of the droplet.

The SI units of G_s are J m^{-2}. Considering a water droplet on a hydrophobic soil surface (Figure 1.4), the water molecules at the liquid-vapour interface will be exposed to different attractive forces than the molecules within the liquid. The molecules at the liquid-vapour interface will be attracted back down towards the bulk of the liquid due to cohesive forces, resulting in a net downward force. Whereas an interior water molecule will be attracted equally in all directions and can move freely.

When considering the situation at the contact line of the liquid-solid-vapour junction it is most convenient to work with surface tensions, forces and contact angles. When considering the energetics of a liquid wetting a solid it is most convenient to work in terms of changes in surface energies.

1.1.9. Wetting and water repellency

The theory behind the phenomenon of wetting of a solid surface is based upon Young's equation (Young, 1805), which considers the balance of interfacial forces between the three phases of solid, liquid (water) and vapour (air) (Equation 1.3, Figure 1.5). At equilibrium the liquid at the intersection between the three interfaces is stationary and the contact angle adopted is determined by the need for a resultant zero force acting along the liquid-solid-vapour contact line. In terms of the energetics of the arrangement, at equilibrium, the water drop adopts a shape which gives the lowest Gibbs energy; which, ignoring gravity, is equivalent to an arrangement in which the sum of the three surface energies ($\gamma^{SL}A^{SL}$ + $\gamma^{SV}A^{SV}$ + $\gamma^{LV}A^{LV}$) is at a minimum, where γ is surface tension, A is area, SL is solid-liquid interface, SV is solid-vapour interface and LV is liquid-vapour interface.

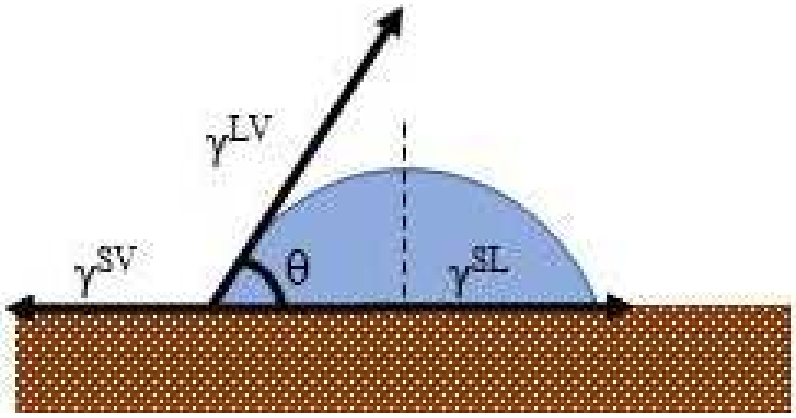

Figure 1.5 Water drop on a soil surface showing application of Young's equation and the balance of interfacial forces between a solid (S), liquid (L) and vapour/air (V).

$$\gamma^{SV} = \gamma^{SL} + \gamma^{LV} \cos\theta \qquad (1.3)$$

In the terminology used to described a liquid wetting a solid, if the contact angle of $\theta > 90^o$ it is said that the liquid does not wet the solid and if $\theta \leq 90^o$ it is said that the liquid does wet the solid. However, for all angles $\theta > 0^o$ the water drop remains as a drop but one with an increasing solid-liquid interfacial area as θ is reduced; at $\theta = 90^o$, ignoring the effects of gravity, the drop adopts a hemispherical shape, while at $\theta = 0^o$ the water spreads completely across the surface (Jaycock and Parfitt, 1981). Figure 1.6 presents a range of contact angles (θ) between 0 and 180°, along with the energies involved in the formation and destruction of the interfaces involved based on the balance between interfaces as given by Young's equation (Equation 1.3).

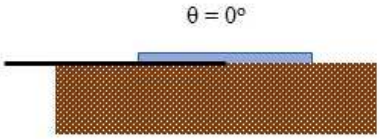

θ / degrees	cos θ	$\gamma^{LV}\cos\theta$	$\gamma^{SV}-\gamma^{SL}$
0	1	72.75	72.75
Energy is released in forming solid-liquid interface, it compensates exactly for increase in liquid-vapour interface and therefore water spreads freely over the surface until it is completely wetted.			

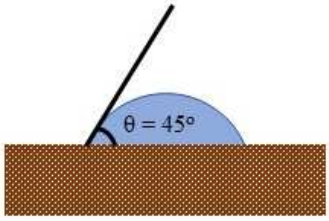

θ / degrees	cos θ	$\gamma^{LV}\cos\theta$	$\gamma^{SV}-\gamma^{SL}$
45	0.707	51.44	51.44
Enough energy is released to allow for the formation of solid-liquid interface from destruction of liquid-vapour interface, however energy from $\gamma^{SV}-\gamma^{SL}$ is not enough to compensate for the increase in liquid-vapour surface and therefore the droplet only undergoes partial spreading.			

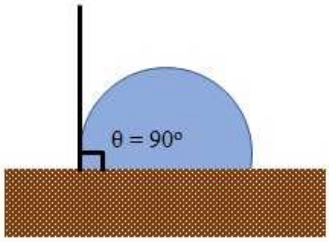

θ / degrees	cos θ	$\gamma^{LV}\cos\theta$	$\gamma^{SV}-\gamma^{SL}$
90	0	0	0
There is zero energy change for γ of a solid-vapour interface into a solid-liquid interface. The droplet is hemispherical in shape.			

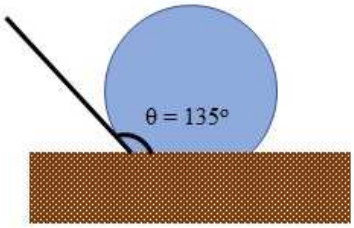

θ / degrees	cos θ	$\gamma^{LV}\cos\theta$	$\gamma^{SV}-\gamma^{SL}$
135	-0.707	-51.44	-51.44
Energy is required for formation of the solid-liquid interface but this is less than the energy required for formation of the liquid-vapour interface. Therefore, the droplet sits on the soil surface.			

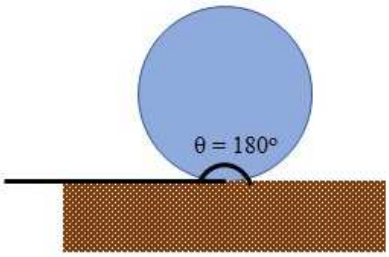

θ / degrees	cos θ	$\gamma^{LV}\cos\theta$	$\gamma^{SV}-\gamma^{SL}$
180	-1	-72.75	-72.75
Energy required to form solid-liquid interface is exactly same as energy required to destroy a liquid-vapour interface, therefore droplet does not change shape and sits on surface without any solid-liquid interaction.			

Figure 1.6 Contact angle and required energies in the formation and destruction of the interfaces involved and corresponding schematics, for contact angles between 0 and 180 ^{o} of a water drop on a soil surface.

For wetting of a smooth, homogenous surface there are three different types of wetting: adhesional, spreading and immersional (Jaycock and Parfitt, 1981). The issue of wetting of particles (i.e. a soil surface) is discussed in detail in chapter 6 and in this case it is useful to think of processes involved as adhesional-immersional wetting and branching capillary wetting. Adhesional-immersional wetting is the first stage of the wetting process where a particle becomes adhered to the outside of the droplet and this process is energetically favourable for any contact angle where $\theta < 180^{o}$. The penetration of the water drop through the soil is best considered as a form of branching capillary wetting, the rate of wetting during this stage will depend upon the length of the three-phase contact line and the free energy of activation for the wetting process.

1.1.10. Soil wettability and water repellency

When working with soils, if upon contact a water drop immediately infiltrates the soil surface (< 5 s) the soil is considered to be wettable (hydrophilic) (Bisdom *et al.*, 1993). However, in water repellent soils the water drop will not immediately infiltrate (> 5 s) and instead will form a bead on the soil surface (hydrophobic) (Bisdom *et al.*, 1993). The severity and persistence of the water repellency present is dependent on a number of factors, the most significant of which are covered in the next section.

1.2. Causes and occurrences

1.2.1. Vegetation and soil organic matter

Soil organic matter has long been thought of as the predominant cause of soil water repellency (Ma'Shum *et al.*, 1988; Bisdom *et al.*, 1993; Mainwaring *et al.*, 2013). A wide range of vegetation types have been linked with the presence of soil water repellency including: forests, particularly Pinus and Eucalyptus species (Scott, 1991; Doerr *et al.,* 2000; Alanis *et al*., 2017), shrubs (Mallik and Rahman 1985; DeBano, 1991; Cesarano *et al.*, 2016), grassland (Dekker and Ritsema, 1994; Scott, 2000; Mao *et al.*, 2016), pasture (Crockford *et al*., 1991; Horne and McIntosh, 2000; Hermansen *et al.*, 2019), and dune grass (Horne and McIntosh, 2000). The deposition of hydrophobic compounds from these vegetation types has been identified as a key cause of water repellency in soils (Doerr *et al.*, 2005; Mainwaring *et al.*, 2013).

Possible sources of hydrophobic, organic compounds that lead to reductions in surface tension include: plant roots (Dekker and Ritsema, 1996; Doerr *et al.*, 1998) which can provide lipid-rich organic matter; decomposing eucalyptus tree litter (McGhie and Posner, 1980, 1981); leaf surface waxes (McIntosh and Horne, 1994) that can be mechanically eroded from plant leaves; and fungal hyphae (Savage *et al.*, 1969, 1972; Jex *et al.*, 1985; Chan, 1992; Hallett *et al.*, 2001). Wildfires can lead to vaporization of organic matter which once cooled and condensed can return hydrophobic compounds back to the soil (DeBano, 2000). Mao *et al.* (2014) suggested that the contribution of root waxes (suberins) were more likely to cause soil water repellency than leaf waxes.

Due to the way in which hydrophobic compounds come to be deposited on soil it is unsurprising that the most severe repellency levels are usually found in the uppermost layer of the topsoil (0-30 cm) due to higher accumulation of organic matter here, and subsequently repellency levels decrease or even disappear with depth (McGhie and Posner, 1981; Jaramillo *et al.*, 2000; Woche *et al.*, 2005; Rye and Smettem, 2017). Jimenez-Morillo *et al.* (2016) noted it is the outermost interfacial layer of the organic matter that will be most influential in the level of repellency induced rather than the overall bulk organic matter.

The relationship between soil organic matter and the level of water repellency present in a soil remains a key area of research. Some studies reported that total organic carbon (TOC) shows a positive linear correlation with the degree of water repellency (Wallis *et al.*, 1990a, 1990b; Mao *et al.*, 2014, 2016). However, other studies (Doerr *et al.*, 2005; de Blas *et al.*, 2010) have found no correlation between TOC and repellency level of the soils assessed. Therefore, TOC cannot be identified as the key parameter influencing soil water repellency levels (Mao *et al.*, 2019).

The surface Gibbs energy of organic compounds present in soils is generally lower than that of the mineral (i.e. silica) surfaces (Leelamanie and Karube, 2009). There is also a notable difference between organic compounds, with hydrophilic organic compounds having a higher surface free energy compared with those of hydrophobic organic compounds (Leelamanie and Karube, 2009).

1.2.2. Soil texture

Physical factors such as soil texture can influence the occurrence and severity of soil water repellency. The phenomenon was originally thought to only occur in sandy soils, however studies have confirmed its occurrence in many different soil types around the world (Wallis and Horne, 1992; Ritsema *et al.*, 1997a, 1997b; Jamarillo *et al.*, 2000) for example in: loamy soils (Dekker and Ritsema, 1995; Hansel *et al.*, 2008; de Blas *et al.*, 2010; Vogelmann *et al.*, 2015); clay soils (Doerr *et al.*, 2000); peat soils (Michel *et al.*, 2001; Moore *et al.*, 2017) and most frequently, sandy soils (Roberts and Carbon, 1971; DeBano *et al.*, 1970, 1976; McGhie and Posner, 1980; Franco *et al.*, 2000; Doerr *et al.*, 2005; Morley *et al.,* 2005).

Researchers suggest that the ratio between hydrophobic material and surface area will be considerably higher in a sandy soil compared to that of a loamy or clay soil (Ma'Shum *et al.*, 1989; Blackwell, 1993; Scott, 2000; Woche *et al.*, 2005), due to the lower surface area per unit volume associated with sandy soils compared to other soil textures. This might also explain why coarser textured soils are more prone to developing water repellency (Scott, 2000), as less hydrophobic material would be required to bind to fewer adsorption sites to induce repellency. However, by way of contrast, Doerr *et al*. (1996) and Rodriguez-Alleres *et al.* (2007) reported that the finer sieve fraction induced the most severe levels of water repellency in studies under grass and forest areas.

Mataix-Solera and Doerr (2004) assessed a range of soil particle fractions on several medium textured soils, all of which confirmed the presence of water repellency, albeit to different degrees. The study highlights the importance of recognizing the source of hydrophobic components attributed to causing the repellency and that it could be as a result of finer hydrophobic particles within the interstitial matter of the soil or present as a hydrophobic coating on individual grains, or indeed a combination of the two. This demonstrates that when assessing soils all soil particle fractions should be considered as a potential source of water repellency. McHale *et al.* (2005) discuss how surface roughness can give rise to increased levels of water repellency in soils and describe the current theoretical models of Wenzel (1936) and Cassie and Baxter (1944) that are currently often used to explain the phenomenon. These theories are explored in greater detail in chapter 7.

1.2.3. Soil moisture

Soil moisture content plays a key role in the initial occurrence and any subsequent return of soil water repellency post soil wetting (Dekker and Ritsema, 1994; 2000). The transient nature of water repellency is often a result of seasonal variations in soil moisture content (Lemmnitz *et al.*, 2008). Generally, studies have found that repellency tends to occur most commonly in soils which have low soil moisture content over prolonged lengths of time (Dekker and Ritsema, 1994; Doerr and Thomas, 2000; Michel *et al.*, 2001). However, some studies (King, 1981; de Jonge *et al.*, 1999) have reported repellency in soils with higher moisture contents, although the severity and persistence overall may be lower than in corresponding 'dry' soils. Dekker and Ritsema (1994) addressed the issue of soil moisture content by identifying a difference between potential and actual water repellency, where the former could be obtained from air-dried soils studied in the laboratory and the latter would be from field-moist measurements taken in the field. The relationship between repellency levels and soil moisture content is complicated, which led to Dekker and Ritsema (1994) proposing a critical moisture threshold for water repellent soils, whereby above a certain moisture content soils would become wettable and below it they would be repellent. However, once a soil has been wetted it does not always return to the same level of repellency when dry. The complex relationship between water repellency and soil moisture is still yet to be unravelled.

1.2.4. Soil microorganisms and fungi

Soil microorganisms and fungi have been found to play a role in inducing soil water repellency. Lozano *et al.* (2014) noted that microbial decomposition of soil organic matter can lead to an accumulation of hydrophobic compounds over time as hydrophilic compounds are more readily broken down by soil microorganisms, although this is dependent on the compound and microorganism species type. Lozano *et al.* (2014) suggested that actinobacteria were particularly predominant in soils classified as water repellent. Basidiomycetes have been recognised as capable of producing amphiphilic proteins which can also give rise to water repellent conditions in soils (Spohn and Rillig, 2012). A study by York and Canaway (2000) considered the possibility for basidiomycete-type fungi to induce water repellency in soils and found that *M. oreades* ('fairy ring' mushroom) rings could render a soil

water repellent and the occurrence of 'fairy rings' are often considered an issue on golf courses. Hallett *et al.* (2001) identified fungi as the most dominant microbial group that lead to water repellency in soils.

1.2.5. Wildfires

One of the impacts of wildfires on natural environments is the creation of water repellency in soils. Elevated temperatures during the burning process can cause volatilization of hydrophobic compounds, which will eventually condense post-burning resulting in the deposition of a hydrophobic layer on the soil surface, potentially rendering soils repellent (DeBano, 2000; McHale *et al.*, 2005). Hydrophobic waxes in the soils may also melt under high temperatures and coat soil particles (DeBano, 2000). Water repellency levels already present in some soils may also become more severe as a result of wildfires, but this will be dependent on the duration and severity of the wildfire along with the soil type and surface vegetation (Doerr *et al.*, 1996; Doerr *et al.,* 2009).

1.2.6. Organics

Organic compounds with hydrophobic properties can be present as a full or partial coating adsorbed onto soil mineral and aggregate surfaces (Van't Woudt, 1959; DeBano *et al.*, 1970; Roberts and Carbon, 1971, 1972; Bisdom *et al.*, 1993; Doerr *et al.*, 2000; Poulenard *et al., 2004;* Mainwaring *et al.*, 2013) and also within the interstitial matter (Franco *et al.*, 2000). The relationship between organic compounds and water repellency is complex and hydrophobicity is not necessarily induced just by the presence of hydrophobic compounds in the soil (Doerr *et al*., 2005; Leelamanie and Karube, 2007) nor does it correlate with the quantity of organics present although combinations of particular organics can lead to hydrophobicity (Contreras *et al.*, 2008; de Blas *et al.*, 2013; Mainwaring *et al.*, 2013). The main groups of organic compounds thought to induce water repellency are long chain acids, alkanes, amides, aldehydes/ketones and sterols (Ma'Shum, 1988; Mainwaring *et al.*, 2004; Morley *et al.*, 2005). McIntosh and Horne (1994) identified aliphatic hydrocarbons and amphiphilic compounds as being most important in inducing soil hydrophobicity.

Leelamanie and Karube (2009) suggested that it is specifically the hydrophobic organic matter content of soils that is the dominant factor in influencing soil water

repellency, rather than the total organic matter content. Mainwaring *et al.* (2013) found that the extent of water repellency induced on acid-washed sand varied considerably with compound type and laydown, with a combination of long chain acids and alkanes to be most effective at inducing water repellency.

Amphiphilic compounds play a key role in soil water repellency due to their polar and non-polar components which influence their orientation on a soil surface and as a result the degree of water repellency. A typical example of a fatty acid naturally found to occur in soils is stearic acid (Deng and Dixon, 2002). Stearic acid consists of a hydrophilic polar carboxyl head group and a hydrophobic, non-polar hydrocarbon chain. Stearic acid has been extensively used in many water repellency studies on model soils (Leelamanie *et al.,* 2008; Leelamanie and Karube; 2007, 2009; Leelamanie *et al.*, 2010; Leelamanie *et al.,* 2012; Mainwaring *et al.*, 2013; Whelan *et al.*, 2015). Yiannos (1962) noted that upon contact with water it was possible for the stearic acid molecule to reorientate itself and therefore alter the water repellency level of the soil, this has been confirmed by other researchers since, Leelamanie and Karube (2009) and Whelan *et al.* (2015).

For amphiphilic molecules it is suggested that in severely water repellent soils, under a dry environment, the polar head is attracted towards the charged silica surface, resulting in molecules becoming packed polar head down with non-polar hydrocarbon chains extending upwards and therefore promoting a hydrophobic environment (Swift, 1989; Horne and McIntosh, 2000). However, upon contact with water, the hydrophilic polar head groups become attracted to the polar water molecules and orient in their direction leading to soil becoming less repellent.

1.3. Methods for studying soil water repellency

There are many methods available for assessing the persistence and severity of soil water repellency in bulk soil samples, many of which are discussed by Doerr *et al.* (2000); Letey *et al.* (2000) and Bachmann *et al.* (2003). The most popular and frequently used methods are outlined in the following section.

1.3.1. Water Drop Penetration Time (WDPT) test

The Water Drop Penetration Time (WDPT) test, first designed and used by Van't Woudt (1959) and later by Letey (1969) and Doerr (1998), is used to measure the persistence of hydrophobicity of soils. It has been widely used over the last few decades by researchers in both the laboratory and the field.

The WDPT test involves dispensing water drops on to a flattened soil surface and recording the time taken for complete penetration (Letey, 1969). WDPT can vary from instant penetration (< 5 s), where the soil is classed as hydrophilic; to droplets remaining on the surface for many hours. Dekker *et al.* (2009) suggested that if a WDPT measurement exceeded 5 seconds that the soil should be considered as water repellent. Watson and Letey (1970) suggested it was only suitable as a method for coarsely differentiating between soils that are classified as wettable and those that are water repellent. However, the WDPT test remains a popular and convenient method for measuring water repellency due to its simplicity (Letey *et al.*, 2000) and it is cheap and easily replicated without the requirement for specialist equipment.

Due to the persistence of repellency in some soils, some studies have previously opted for a cut off time, typically after 1 hour (Leelamanie and Karube, 2009; Leelamanie *et al.*, 2010) whereby WDPT times exceeding this point automatically classified a soil as extremely repellent. This reduces the time-consuming nature of the test and eradicates the issue of evaporation which becomes a significant factor with increased WDPT times. Doerr (1998) used lids to cover soil samples with water drops persisting over 1 hour to prevent droplet evaporation and this then allowed the tests to continue to the > 5 hour category. However, the application of a lid will alter the localised environmental conditions of the test i.e. increasing relative humidity levels and therefore will influence the results obtained. However, it could be argued if this was done to all samples being tested, the results would remain comparable.

Hallin *et al.* (2013) noted that a lot of published studies that utilise the WDPT test fail to indicate the drop volume and number of drops used. Having assessed drop volume, Hallin *et al.* (2013) suggested that large drop volumes will give a better indication of overall repellency levels in soil, whereas smaller drop volumes will give a reflection of the microtopography of the surface and level of heterogeneity due to the smaller surface area covered by each drop. To obtain a 95 % confidence in

assignment of water repellency class, a recommendation of six drops per sample was given (Hallin *et al.*, 2013).

1.3.2. Molarity of ethanol droplet (MED) test

The molarity of ethanol droplet (MED) test developed by King (1981) and later by Roy and McGill (2000, 2002) uses a series of aqueous ethanol solutions with known surface tensions to assess the level of repellency in soils. The method is adapted from a previous experiment by Watson and Letey (1970) called the 90^{o} surface tension test or percentage alcohol test. The MED test is an indirect measurement of surface tension (Doerr, 1998). Drops are applied to the soil surface with increasing surface tensions (decreasing ethanol concentrations) until a point is reached where the drop resists infiltration for longer than a set time period; King (1981) used 5 s, Crockford *et al.* (1991) 3 s whereas Harper and Gilkes (1994) used 10 s. Water repellency classification is made between the last class where infiltration occurred and the first class where it existed for longer than the allocated time. How precise the classification of repellency is, is dependent upon the variation in concentrations between the aqueous ethanol solutions. A significant advantage of the MED test over the WDPT test is its speed; it removes the requirement for laborious monitoring times in extremely repellent soils and removes the issues of evaporation due to the speed with which the test is conducted. The MED test, like the WDPT is cheap and easily replicated in both the field and laboratory and therefore it remains a popular test amongst researchers.

1.3.3. Repellency index method

The Repellency Index (RI) method by Tillman *et al.* (1989) is a measurement of the intrinsic sorptivity of soils, which gives an indication of water transport rates. An infiltrometer probe assesses wetting rates in soil columns where the sorptivity is responsible for water flow (as opposed to gravity). Comparison is made between sorption of ethanol and water and the index is given by the ratio of the two (Hallett *et al.*, 2001). Whilst this is quite a sensitive method, it does have limitations as it can be time consuming and fails to provide information regarding the persistence of water repellency that exceeds the 5 minute measurement period (Doerr, 1998). A repellency index value (*RI*) can range between 1 (wettable) and 100 (highly repellent), a *RI* value of >1.95 indicates the presence of water repellency (Urbanek *et*

al., 2007). Clothier *et al.* (2000) suggested that RI between 20-40 were typical for moderately repellent soil, and RIs nearer to 80 indicate a severely repellent soil.

1.3.4. Contact angle: Capillary rise method (CRM)

The capillary rise method (CRM), was originally designed by Letey *et al.* (1962) and developed further by Siebold *et al. (*1997) and Michel *et al.* (2001). The indirect method measures the height of water achieved in a soil column (packed powder) via capillary rise in order to assess soil-water contact angle. In comparison to the MED and WDPT tests this is much more time consuming, and due to the nature and set up of the test best suited for laboratory measurements only. The CRM is applicable to soils with a contact angle of < 90^o (Bachmann *et al.*, 2003; Leelamanie *et al.*, 2008), therefore making it less suitable as a method for studying severely repellent soils. However, a Modified Capillary Rise Method (MCRM) using a range of molarity methanol-water solutions instead of water allows for soils with contact angles > 90^o to be measured using the same methodology as the CRM (Bachmann *et al.*, 2003).

1.3.5. Contact angle: Wilhelmy plate method

Another laboratory-based measurement of soil-water contact angle, the Wilhelmy plate method is described by Adamson (1990) and later by Bachmann *et al.* (2003). Soil is applied and fixed to a glass slide which is attached to a balance and the weight recorded. The slide is then slowly immersed into the test liquid before lifting the slide again in the opposite direction, the force on the plate during the wetting process can be used to calculate the surface tension. The Wilhelmy plate method allows for the measurement of both advancing and receding contact angles and theoretically can determine contact angles ranging from 0 to 180^o (Bachmann *et al.*, 2003).

1.3.6. Contact angle: Sessile drop method

The initial degree of soil water repellency can be assessed by measurement of the soil-water contact angle and this is often done using the sessile drop method (Bachmann *et al.*, 2000a, 2000b). The contact angle between a liquid and a solid surface is determined by the balance of interfacial tensions of the three phases present (solid, liquid and vapour) (Jaycock and Parfitt, 1981). A liquid drop with high surface tension resting on a low surface energy, solid, flat surface gives a high contact angle. As the solid surface energy increases, the drop gives a lower contact

angle (Llewellyn, 2005). Hence, a large contact angle indicates high water repellency, and a low contact angle indicates a low water repellency. The sessile drop method involves preparation of a monolayer of soil grains adhered to a glass slide using double-sided adhesive tape (Bachmann *et al.*, 2003). The soil-water contact angle is measured by dispensing a drop of water onto the soil surface using a goniometer. Analysis software determines the contact angle of the droplet from static images of the drop and can, potentially, be used to determine contact angles ranging from 0 to 180^{o}. The method can be time consuming, although it can be easily reproduced once the equipment is set-up. There is also the difficulty of dealing with a non-uniform non-flat surface, something which will be examined further in chapter 7.

1.4. Environmental impacts of soil water repellency

Soil water repellency can have serious environmental implications and further investigation into the chemical and physical mechanisms behind its occurrence is needed to inform how we might manage and mitigate it against it.

1.4.1. Preferential flow, groundwater pollution and food security

The hydrological functions of soils can be greatly affected by soil water repellency (Wallis and Horne, 1992; Leelamanie and Karube, 2009). Uneven wetting caused by varying water repellency levels within soils can lead to the formation of preferential flow pathways (Dekker and Ritsema, 1995; Scott, 2000; Dekker and Ritsema, 2000; de Jonge *et al.*, 2009). Not only does this result in depletion of plant available water (Dekker and Ritsema, 1996), but valuable nutrients, fertilizers and agrochemicals can be rapidly leached though the soil profile via these pathways resulting in groundwater pollution. Pollution of water sources will negatively affect aquatic habitats and water quality. Areas of crop and pasture land that do not receive sufficient levels of water and nutrients will result in crop and soil nutrient deficiencies which will impact upon food production. Decreased soil fertility, patchy crops and increased disease levels, leading to reduced overall yields and production are all potential consequences of uneven wetting in soils (Roy and McGill, 2002; Müller *et al.*, 2014, Fishkis *et al.*, 2016; Rye and Smettem, 2017). With the increasing global population this is a significant issue for regions responsible for food production.

1.4.2. Wind erosion

Water repellency also indirectly contributes to soil erosion by wind as soils can become more susceptible to erosion when left bare and dry, which is more likely to occur in soils that are water repellent (Carter, 1990). Wind erosion is likely to occur in both wettable and water repellent soils when they are dry and left exposed. However, reduced water holding capacity and formation of preferential flow pathways in water repellent soils can lead to delays in germination of crop and pasture land which results in decreased crop yields and increases soil susceptibility to wind erosion from reduced surface coverage (McKissock *et al.*, 2000; York and Canaway, 2000; Müller *et al.*, 2014; Papierowska *et al.*, 2018). Wind erosion of topsoil causes a loss of the nutrient rich topsoil which will lead to further reduction in vegetation cover and exacerbate the problem of wind erosion further.

1.4.3. Overland flow and erosion

Reduction of soil-water holding capacity due to water repellency can lead to an increased risk of overland flow which can result in both erosion (Burch *et al.*, 1989; Leighton-Boyce *et al.*, 2007) and flooding. Hallett *et al.* (2001) noted that the risk of flooding is particularly high following extended dry periods in soils prone to water repellency. Soil water repellency has been a cause of overland flow in studies of forests (Butzen *et al.*, 2015); and areas which experience wildfires (DeBano, 2000). A notable example in the last few years was the Californian wildfires in late 2017 which resulted in extensive flooding and mudslides as a result of the hydrophobic layer caused from melted waxes and resins within the soils along with deposition of hydrophobic compounds after volatilization (AGCS, 2018).

1.4.4. Impact of climate change

Soil water repellency is knowingly affected by soil water content and temperature (Doerr *et al.*, 2000). It is generally considered that a water repellent soil subjected to prolonged dry periods at high temperatures is likely to resist wetting for longer (Goebel *et al.*, 2011).

The latest IPCC special report in 2018 studied the impacts a global increase in temperature of 1.5 ^{o}C above pre-industrial levels (1850-1900) would have. The IPCC report (2018) noted that most land regions are already experiencing elevated

warming levels above the global average and reports of increase in intensity and frequency of climate and weather extremes. The report to policymakers notes the importance of limiting global warming by 1.5 ^{o}C and the environmental impacts of exceeding this level. The risk of exceeding this level is predicated (with medium confidence) to lead to increases in heavy precipitation events and probability of extreme droughts in other regions. The IPCC report (2018) predicts a 2^{o}C rise in global temperatures would lead to an increased risk in frequency and magnitude of droughts, along with significant increases in runoff in areas affected by heavy precipitation events which in turn could lead to the occurrence of floods.

Based on proposed climate model and scenarios, Goebel *et al.* (2011) studied the potential for soil water repellency to be affected by extreme climate events and found that whilst water repellent soils have the potential to reduce the process of carbon mineralization, that extreme events could lead to a reduction in nitrogen and water availability within the soils and therefore compromise plant growth and therefore reduce the potential positive effect of the phenomenon on carbon sequestration.

Goebel *et al.* (2011) noted that wildfires were likely to occur more frequently due to climate change and increased occurrence of extreme events which would lead to exacerbation of soil water repellency. An increase in global temperatures and fluctuating precipitation patterns due to climate change will have an effect on the extent and duration of soil water repellency occurrence (Goebel *et al.,* 2011).

1.4.5. Beneficial uses of soil water repellency

Whilst many of the environmental implications of soil water repellency are detrimental, there are also some beneficial applications. In drought-prone areas water repellent soils have been utilized to help direct water flow and collect any runoff so it can be reused (Blackwell, 2000). Similarly, in drought-prone environments, an upper water repellent layer of soil has proven to act as an effective mulch, as it helps to reduce the capillary rise of water and subsequently lowers losses via evaporation (Wallis and Horne, 1992; Rye and Smettem, 2017). Wijewardana *et al.* (2015) discusses the successful use of water repellent grains in Capillary Barrier Cover Systems (CBCSs), which are used to prevent water infiltration and limit seepage at waste landfill sites. Jordan *et al.* (2017) also suggested the use of silanised soils to help provide a water repellent barrier for uses in geoenvironmental

engineering, similar to those described by Wijewardana *et al.* (2015). Mainwaring (2004) noted that some plants in areas prone to water repellency have adapted over time to the extreme conditions.

1.5. Amendments

Whilst amendments are not the subject of this thesis it is important to note their place in tackling the issue of soil water repellency. To date biochar and clay additions, along with surfactant applications, have been identified as potential amendments for water repellent soils.

1.5.1. Biochar

Biochar, a porous, carbon-rich product formed from the pyrolysis of biomass under oxygen-limited conditions and used as a soil amendment, has become extensively studied over the last couple of decades, and has been successfully applied to agricultural and contaminated soils to help improve features such as water holding capacity (Lehmann and Joseph, 2009), although the extent of the success depends upon the physical and chemical characteristics of the biochar, which is dependent on the pyrolysis process and feedstock (Lehmann and Joseph, 2009).

Research using biochar as an amendment for water repellent soils is currently still relatively limited. Hallin *et al.* (2015) suggested that wettable biochar had the potential to be used as an amendment for water repellent soils. In a review by Blanco-Canqui (2017), the small number of studies available reported little or no effect of biochar additions to soil water repellency levels. However, biochar did significantly increase saturated hydraulic conductivity in fine-textured soils and reduce it in coarse-textured soils (Blanco-Canqui, 2017). More studies are required to fully assess its impact on water repellency in soils.

1.5.2. Clay

Clay additions to soils have been shown to reduce soil water repellency. Clay helps to create hydrophilic surfaces by attaching to soil grains and hydrophobic compounds (Diamantis *et al.*, 2017). McKissock *et al.* (2000, 2002) found clays applied to water repellent soils were effective at reducing repellency levels, although the degree of effectiveness varied with clay type. Similarly, Leelamanie and Karube (2007) and Leelamanie *et al.* (2010) suggested that higher clay contents in soils (around 5 %)

could lead to reductions in water repellency due to the creation of flow pathways of surface water through the soil profile via an increase in surface area available for wetting.

A recent study by Diamantis *et al.* (2017) used kaolinite-rich clay soil dispersed in water for repellency mitigation. Results yielded a 74 % reduction in soil water repellency levels by using a wet clay method compared to additions of dry clay which required subsequent wetting/drying cycles to become as effective. This result builds upon a study by Ward and Oades (1993) which found that clay additions were not effective unless they had undergone a wetting and drying cycle.

1.5.3. Surfactants

Soil surfactants are amphiphilic molecules that can be applied to soils to lower the surface tension of water and therefore reduce the contact angle between the water and soil surface, thus allowing the soil to wet more readily (Müller and Deurer, 2011; Dekker *et al.*, 2019). Surfactants are particularly popular as treatments on turf grass and golf courses to eradicate issues linked to water repellency such as preferential flow pathways, and localized dry spots which cause patchy grass cover. Dekker *et al.* (2019) found that surfactants help to restore the wettability of soils in root zones and that regular treatments throughout the growing season could lead to the eradication of water repellency issues. The use of surfactants as an amendment to water repellent soils need to be considered against any possible ecological impacts of their application and also against the financial considerations as they can be quite expensive.

1.6. Research gaps addressed in this thesis

The research described in this thesis aims to address the following research gaps.

1.6.1. In-situ measurements of the polarity and viscosity within the organic coating on soil grains

Given the important role of surface polarity in determining soil water repellency, the opportunity to explore and apply cross-disciplinary techniques to study polarity of organics adsorbed to soils was taken. Fluorescent probes have been successfully used for decades to study biological and chemical environments (Evans *et al.*, 2013). The research described in chapters 4 and 5 explores the use of fluorescent probes as a

method for both the direct *in-situ* determination of the polarity of organics on soil surfaces, and the molecular mobility within the organic layer.

1.6.2. Wetting process of water repellent soils

The process of wetting is well researched and the different types of wetting that can occur with a water drop on a flat surface, or particles with bulk water, can be found in Jaycock and Parfitt (1981), but the wetting process of a water droplet on a water repellent soil is more complex. Many practitioners will have observed a water droplet sitting on a water repellent soil surface, in chapter 6 research is described in which a two-stage model of the kinetic processes involved in the wetting of a water repellent soil from initial dispensation to complete infiltration is discussed. The model is then tested experimentally via a variety of measurements.

1.6.3. Contact angle measurements on non-planar (soil) surfaces

In general, the contact angles of irregular surfaces measured using a goniometer are higher than those of a flat surface of the same material using the same technique. Understanding the amplification of contact angle by surface structure has for many years been based on the thermodynamic theoretical models of Cassie and Baxter (1944), for bridge-like wetting over the top of protrusions, and Wenzel (1936) for complete wetting of an irregular surface. Even though still widely used, there is currently much ongoing debate in the literature about the validity of these models and their applicability to soil science and soil water repellency (Gao and McCarthy, 2007; 2009; Marmur and Bittoun, 2009; Kwon *et al.*, 2010; Cheng and McCarthy, 2011; Li and Shan, 2012; Milne and Amirfazli, 2012). The research described in chapter 7 examined this problem via the study of precisely controlled model soil surfaces.

1.6.4. Research objectives

The experimental chapters aim to address current research gaps via the following key research objectives.

1) To evaluate the use of fluorescence probes, namely nile red and pyrene, as tools to assess the polarity and viscosity of the environment of organics adsorbed to soils.

2) To assess if water infiltration is a single step process and if not, what steps are involved in the wetting process of water repellent soils, using a variety of kinetic methods.

3) To assess the validity of current soil contact angle measurements and the theories used to explain the anomalously high contact angles often measured for water on a surface of hydrophobic particles, and to investigate an alternative explanation based on the geometry of a water drop sitting on hydrophobic particles.

Due to the heterogeneity of natural soils it is often difficult to assess new methodologies and techniques because of the degree of variability present. Therefore, model soils in the form of acid-washed sand (AWS) co-deposited with organics naturally found in water repellent soils; and man-made materials such as metal spheres and ballpoint needles have been used as homogenous substrates to represent water repellent soils and surfaces. The choice of natural soils used focuses specifically on oven-dried, water repellent, sandy soils, which have been extracted from the top 0-20 cm of the soil profile.

1.7. Thesis outline

The thesis is divided into a further seven chapters.

Chapter 2: the materials, general instrumentation and methods used in the experimental work are described.

Chapter 3: here an introduction to photochemistry is given for readers unfamiliar with the subject. Key terms, and experimental and theoretical fundamentals related to the use of fluorescent probes (chapters 4 and 5), are described.

Chapter 4: in this chapter the application of the fluorescent probe nile red to assess soil environmental polarity via optical and fluorescence microscopy techniques is described.

Chapter 5: experimental work is described which explores the use of the fluorescent probe pyrene as a potential tool to identify soil environment polarity and viscosity, using steady-state fluorimetry and time correlated single photon counting techniques.

Chapter 6: experimental work exploring the different stages of wetting in water repellent soils is described and a model of the wetting process is proposed.

Chapter 7: here the current experimental and theoretical approaches to soil contact angle measurements using dynamic sessile drops measurements on a goniometer are discussed. Research described in this chapter challenges the current approach and suggests an alternative interpretation of the anomalously high contact angles measured on soils in terms of a geometric correction factor for a water drop sitting on hydrophobic particles, modelled here using regularly arranged metal spheres and ballpoint needles coated in wax.

Chapter 8: summarises the key findings and suggests future opportunities for the development of techniques, and experimental work that could be carried out to build on the advances made here.

Chapter 2 Materials and methods

This chapter describes the materials, sample preparation, and key instrumentation and experimental methods used in this work.

2.1. Materials

A list of chemicals and materials used is presented in Table 2.1. Chemicals were used as received.

Table 2.1 Chemicals and materials.

Chemicals			
Product	**Description**	**Supplier**	**Relevant thesis chapter(s)**
Acetone	Analytical reagent grade	Sigma Aldrich	4,5
Acetonitrile	HPLC grade	Fisher Scientific	4,5
Acid-washed sand	Silicon dioxide, low iron, 40-100 mesh	Fisher Scientific	4,5,7
Caesium chloride	99.5 % Reagent grade	Fisher Scientific	6
Humonitor® Humidity indicator cards	Cobalt chloride water sensitive discs	Sigma Aldrich	6
Diethyl ether		Sigma Aldrich	4,5
Distilled water			4,5,6,7
Ethanol	Analytical reagent grade	Fisher Scientific	4,5,6,7
Ethyl acetate	Analytical reagent grade	Fisher Scientific	4,5
Hexadecane	98 %	BDH	5
Hexane		Sigma Aldrich	4,5
Hydrochloric acid	Analytical reagent grade	Fisher Scientific	4
Liquid nitrogen		BOC	6
Lithium chloride	99.0 %	Sigma Aldrich	6
Methanol	HPLC grade	Fisher Scientific	4,5
Nile red	Bioreagent 98.0 %	Sigma Aldrich	4
Nitric acid	Analytical reagent grade	Fisher Scientific	5
n-Heptane	Analytical reagent grade	Pronalys*ar	7
Octadecane	99 %	BDH	5
Petroleum ether		BDH	7
Potassium chloride	99.5 % AnalaR	BDH	6
Pyrene	99 %	Sigma Aldrich	5
Sodium chloride	Laboratory reagent grade	Fisher Scientific	6
Sodium hydroxide	GPR	BDH	4
Squalane (2,6,10,15,19,23-Hexamethyltetracosane)		BDH	5
Stearic acid	99 %	BDH	5

Paraffin wax	C.P. 58-62 D	Sigma Aldrich	7
Other Materials			
Product	**Description**	**Supplier**	**Relevant thesis chapter(s)**
Ballpoint needle	Size 10, 0.53 mm	John James Needles	7
Chrome steel ball	Grade 100 hardened, 52100, 1.00 mm	Simple Bearings Ltd	7
Magnetic squares	Self-adhesive 25 x 25 x 0.76 mm	**www.first4magnets.com**	**7**

2.2. Natural soils and bulk soil sampling and preparation

Eight natural sandy soils of similar textural class were used in this work (Table 2.2). Methods for collection of AU2, AU3, NL1 and UKC have been described previously by Doerr *et al.* (2005) and since collection they have been stored in sealed glass jars at room temperature. NIC1, NIC2, LLAN1 and LLAN2 were collected by the author from Gower, South Wales. NIC1 and NIC2 were sampled from the top 10 cm of the soil profile under vegetated sand dunes, LLAN1 and LLAN2 soils were obtained from under pine forest at different depths in the soil profile, LLAN1 from 0-10 cm and LLAN2 from 10-20 cm (Table 2.2). For all soils the litter layer was removed, the soils sieved using a 2 mm sieve to remove any large pieces of organic debris but allowing the inclusion of all primary soil particles for mineral soils, and the new soils i.e. NIC1, NIC2, LLAN1 and LLAN2, were oven dried at 30 ^{o}C for 48 hours post-collection and prior to sieving.

Table 2.2 Source locations and characteristics of soils.

Sample	Country	Site location	Latitude/ longitude	Vegetation	Depth/ Cm	Mean diameter/ mm	Total organic carbon content/ g kg^{-1}	Water repellency class*	Relevant thesis chapter(s)
AU2†	Australia	Pine Views, Naracoorte	36°26'S 140°40'E	Cropland	0-10	0.29	[a] 5.1 (±1.1)	Strongly	4,5
AU3†	Australia	Pine Views, Naracoorte	36°26'S 140°41'E	Cropland	0-10	0.23	[a] 2.5 (±0.5)	Extremely	4,5
LLAN1‡	Wales	Llanmadoc, Gower	51°37'N 04°15'W	Pine forest	0-10	0.27	[b] 4.5 (±0.3)	Strongly	5,6
LLAN2‡	Wales	Llanmadoc, Gower	51°37'N 04°15'W	Pine forest	10-20	0.29	[b] 6.7 (±0.7)	Strongly	5,6
NIC1‡	Wales	Nicholaston, Gower	51°34'N 04°07'W	Dune grass	0-10	0.32	[c] 21.9 (±4.4)	Severely	5,6
NIC2‡	Wales	Nicholaston, Gower	51°34'N 04°07'W	Dune grass	0-10	0.33	[c] 19.7 (±5.3)	Strongly	5,6
NL1†	Netherlands	Zuid Holland, Ouddorp	51°48'N 03°54'W	Grass/moss	0-10	0.27	[a] 5.1 (±1.1)	Extremely	6
UKC†	Wales	Nicholaston, Gower	51°35'N 04°06'W	Dune	0-5	0.39	[a] 2.5 (±0.5)	Wettable	6,7

† = soils sampled during "Water Repellent Soils Project" EU grant FAIR-CT98-4027 (1999); ‡ = soils sampled during this work

[a]Previous work with AU2 and AU3 have shown the inorganic carbon content to be negligible and total carbon content to be organic in origin (Doerr *et al.*, 2005).

[b] Previous work using soils obtained from a similar Nicholaston location recorded 27 % inorganic carbon as part of the total carbon present (Personal communication, Hallin, 2019). In this work the shape of the peak detection curves for total carbon analysis indicates an inorganic carbon contribution of ≤ ~20 %.

[c] In this work an assessment of the detection curves for Llanmadoc soils indicates a contribution of ≤ ~10 %.

*****Determined from WDPT test and classification of Bisdom *et al.,* 1993.

2.2.1. Cone and quartering

The collected soil was cone and quartered (Jackson, 1958) to obtain representative sub-samples for experimental work. In brief, the process involves creating a cone shape of the bulk soil sample with a slightly flattened top, which is subsequently divided into four equal segments. Opposite quarters are then recombined, with the 2nd and 4th quarters being removed from the process each time. The process is then repeated for the bulk sample now made up of the 1st and 3rd quarters and continues until the sub-sample size reaches an appropriate size required for experimental use. The removed segments are all recombined at the end to create a bulk sample again. A schematic representation of the cone and quartering methodology is shown in Figure 2.1.

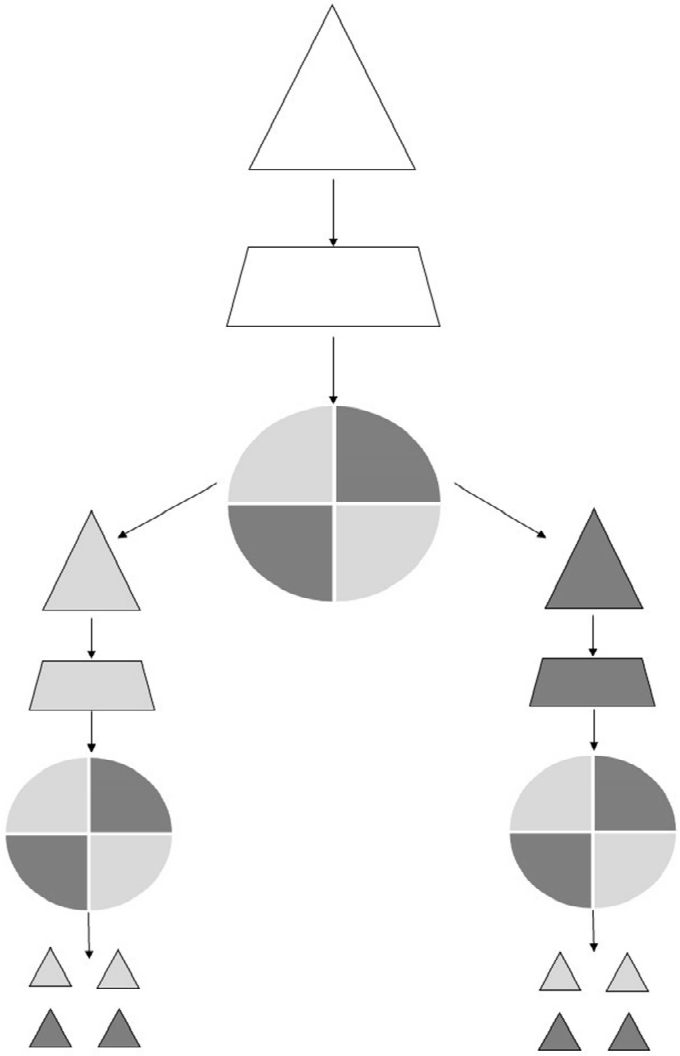

Figure 2.1 Schematic of cone and quartering method as described by Jackson (1958).

2.2.2. Bulk density

Loose and close packed bulk density measurements were made as follows. An empty, stoppered, 10 ml glass volumetric flask was weighed. Soil was then added to the flask until the sample reached the 10 ml line; the flask was then stoppered and the weight recorded. Next the stopper was removed and flask gently tapped, causing the soil to fill the voids within the sample and pack more tightly; additional soil was added to the flask until it reached the 10 ml calibration line and no further tapping would create any extra space. The sample was then re-weighed and the close-packed density calculated.

2.3. General laboratory equipment

2.3.1. Balance

Unless otherwise stated, all masses were determined using a Sartorius 4-figure analytical balance, which allowed weights to be measured to within 0.1 mg.

2.3.2. Pipettes

A calibrated Eppendorf Multipette plus pipette was used for all water repellency assessment measurements, with volume settings between 20 – 100 µl respectively. Calibrated fixed volume air-displacement Eppendorf pipettes were used to make up chemical solutions as appropriate.

2.3.3. Rotory evaporator

Rotory evaporators permit the removal of solvents from samples through evaporation at temperatures below their boiling point whilst under a vacuum (Skoog *et al.*, 1998). A round bottomed sample flask with vacuum applied is lowered into a pre-heated water bath and rotated to commence evaporation. Solvent is extracted via a condenser. Rotory speed and water bath temperatures can be adjusted as required.

A Büchi Rotovap-R rotory evaporator (Figure 2.2) was used for sample preparation described in chapters 5 and 7, specifically for the co-deposition of fluorescent probes and organic compounds on to model and natural soils for fluorescence work, and the deposition of paraffin wax onto model soils for contact angle work.

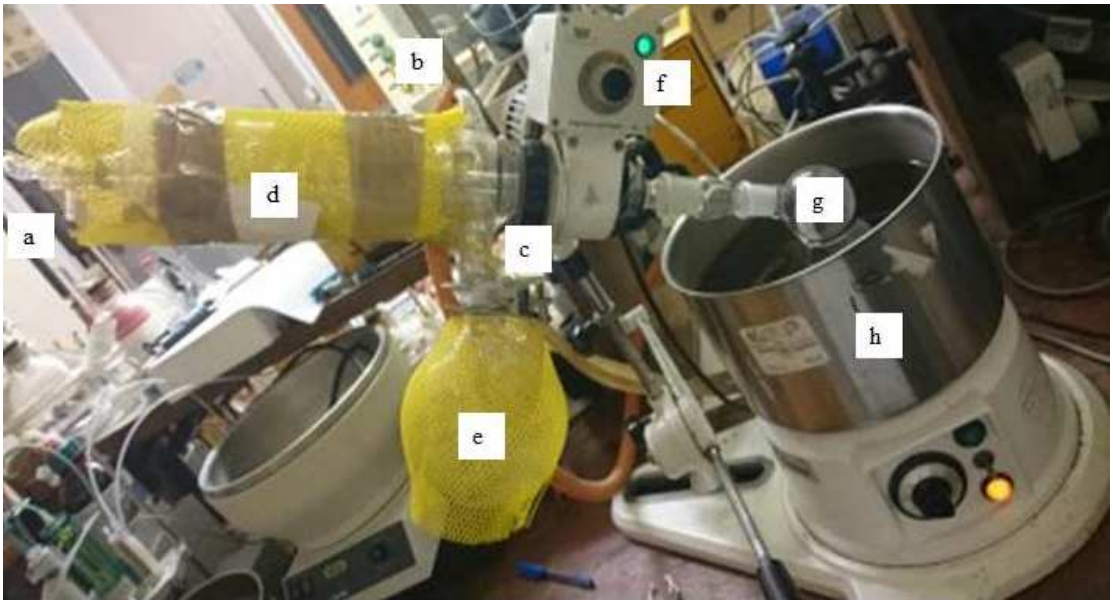

Figure 2.2 Rotory evaporator set-up with components as follows: (a) vacuum release valve, (b) water outlet point, (c) water inlet point, (d) condenser, (e) waste solvent collection flask, (f) speed control, (g) sample flask and (h) water bath.

2.4. Instrumental methods

2.4.1. Particle size distribution

Particle size distributions were measured using a Beckman Coulter LS Series Laser Diffraction Particle Size Analyser. The instrument can measure particle fraction sizes between 0.04 and 2000 µm. Calgon solution was added to each soil sample slowly, followed by gentle rotation and inversion several times to ensure good mixing, complete wetting, and no air bubbles, and then left for 48 hours to settle before analysis. The Calgon solution helps to separate the individual soil particles so that they can be accurately analysed by the laser. Triplicate runs were used to measure both mean particle diameter (µm) by volume and specific surface area.

2.4.2. Total organic carbon

Total carbon content of samples was measured using a SKALAR Primacs Solid Sample TOC Analyzer. Bulk samples were ground to < 250 µm using a mortar and pestle and three replicates each weighing approximately 1000 mg were measured for total carbon by combustion at 1050 ^{o}C. Previous work with AU2, AU3, NL and UKC soils has shown the inorganic carbon content to be negligible and total carbon content to be organic in origin (Doerr *et al.*, 2005). However, previous work using

soils obtained from a similar Nicholaston location to that of NIC1 and NIC2 soils, recorded 27 % inorganic carbon as part of the total carbon present (Personal communication, Hallin, 2019). For the soils in this work, the shape of the peak detection curves for total carbon analysis indicated an inorganic carbon contribution of ≤ ~30 % for NIC1 and NIC2 soils, and ≤ ~10 % for LLAN1 and LLAN2 soils.

2.5. Statistical analysis

2.5.1. General analysis

Microsoft Excel statistics package was used for all statistical analysis, unless otherwise stated. The mean and standard deviation were calculated based on the normal distribution (Miller and Miller, 1993).

2.5.2. Standard deviation (s)

$$s = \sqrt{\left(\sum_{i=1}^{n} \frac{(x_i - \bar{x})}{n-1}\right)^2}$$

where $\bar{x}$ is the mean value and *n* is sample size.

2.5.3. Standard error of the mean (s.e.m)

$$s.e.m. = \sigma/\sqrt{n}$$

where σ is the standard deviation of the original distribution and *n* is the sample size.

2.5.4. Confidence limits are reported to 95%

$$\mu = \bar{x} \pm t\left(s/\sqrt{n}\right)$$

where $\bar{x}$ is the mean value, *t* value is dependent on sample size-1 (*n-1*) and the degree of confidence required, *s* is the standard deviation and *n* is sample size.

2.5.5. Curve-fitting analysis

TableCurve 2D software (Jandell Scientific) was used for curve fitting analysis.

2.5.6. Error bars

Unless otherwise stated, error estimates are given as ± one standard error of the mean.

2.5.7. Outliers

Very rarely, a single data point was found far from the average for that experiment, and inclusion of the data point when averaging would shift the average significantly. In such cases, if a data point had a residual that was more than four times the standard deviation of the data with that datum removed, it was considered an outlier based on the approach used by Chatfield (1983) and removed from the dataset.

Whilst this value is arbitrary it was necessary to have a standard approach to the datasets. The probability of a value being greater than four standard deviations away from the mean is less than 0.1 % (i.e. 1 in 1000) and therefore it is highly unlikely a datum beyond this level will be found in the number of data collected in these experiments.

Chapter 3 Introduction to photochemistry, fluorescence probes and photochemical instrumentation

This chapter provides an introduction to photochemistry for readers unfamiliar with the subject. Key terms, and experimental and theoretical fundamentals related to the use of the fluorescent probes nile red and pyrene (used in work described in chapters 4 and 5) are discussed.

3.1. Molecular probes

Molecular probes are widely used in chemistry and biochemistry due to their sensitive response to their physical and chemical environment (Evans *et al.*, 2013). Fluorescent probes are useful because they can absorb light of a specific wavelength and emit at a different wavelength, and the separation of the excitation and emission wavelengths allows them to be studied effectively (Johnson and Spence, 2010). Fluorescent probes are commonly used to measure environment polarity, and viscosity (Mazur and Blanchard, 2005; Evans *et al.*, 2013); and there are many spectroscopic techniques that can be used to measure their photophysical properties such as fluorimetry, fluorescence microscopy and time-correlated single photon counting.

Before considering the individual probes used in the research reported here, namely, nile red (chapter 4) and pyrene (chapter 5), it is useful to consider the photochemistry principles and processes that allow them to be used as effective tools. To date, fluorescent probes have not been used to study *in situ* soil water repellency. Work by Borisover *et al.* (2006) studied the use of probes for dissolved organic matter effluent, and Ganaye *et al.* (1997) used pyrene to examine the polarity soil organics after extraction, but neither address the nature of the organic 'environment' *in situ* in solid-state soils. Bayer (2009) briefly used nile red to study fluorescence on single grains and identified that nile red was capable of binding to chemical groups typically present in soil organic matter however had minimal success due to the high intensity emissions which prevented subtle differences in surface polarity being established.

3.2. Principles of photochemistry

3.2.1. Jablonski diagram

The molecular processes involved in the absorption and emission of light are best represented using a Jablonski diagram (Figure 3.1) where the 'radiative' transitions, i.e. those between states involving absorption or emission of a photon, are depicted via vertical lines, and other, 'non-radiative', processes are shown as wavy lines.

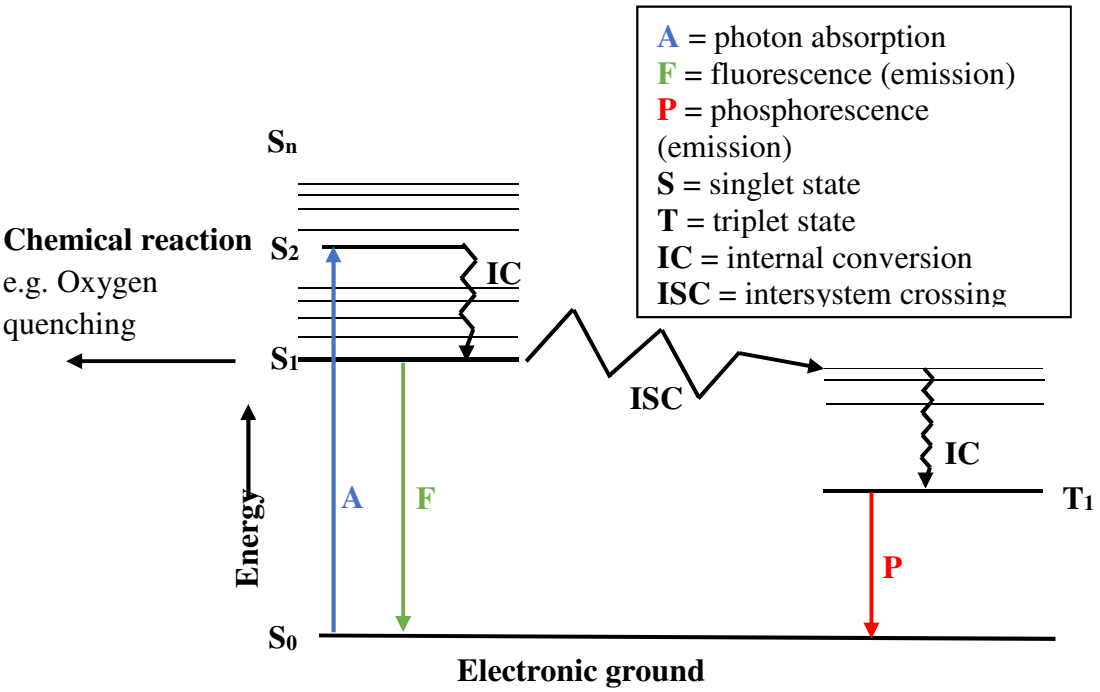

Figure 3.1 Jablonski diagram showing the processes involved in the absorption of light by a molecule and subsequent degradation of the excitation energy by internal conversion, intersystem crossing, fluorescence, and phosphorescence (adapted from Evans *et al.*, 2013).

3.2.2. Absorption

Absorption (A) is the process by which a molecule is taken from one state (e.g. ground state) to a higher state (e.g. excited state), whereby an electron is moved from one orbital to another by absorption of a photon. How efficient, probable, or 'allowed', this process is, is reflected by the molar extinction coefficient (ε). The greater the extinction coefficient, the higher the probability of a transition between states occurring.

3.2.3. Electron spin and the spin selection rule

Electrons have 'spin', a quantum mechanical property which has a rough macroscopic analogy in a spinning particle which can spin in one of two ways, clockwise or anticlockwise. This is described using the spin quantum number, m_s, which can take values of +½ and -½ only. These arrangements are often referred to as 'spin up' and 'spin down', represented diagrammatically by ↑, and ↓. The photon also has spin, with spin quantum number 1 or -1.

In a molecule, electrons occupy molecular orbitals of specific energy. Two orbitals are of particular importance in chemistry and photochemistry, the highest occupied molecular orbital (HOMO) and the lowest unoccupied molecular orbital (LUMO). As a consequence of the Pauli Exclusion Principle only two electrons can occupy any molecular orbital because there cannot be more than one electron of the same spin in an orbital, and if there are two electrons in one orbital then they must be spin paired, i.e. ↑↓. For almost all organic molecules (i.e. those predominantly made up of carbon and hydrogen atoms, and sometimes including oxygen, nitrogen, and halogens and a few other elements) there is an even number of electrons in the molecule, and in the lowest energy 'ground' state these are arranged spin paired in molecular orbitals. For these molecules the ground state is a 'singlet' state, the term singlet arising from quantum mechanics which shows there is only one state of that energy possible.

Within quantum mechanics there are selection rules that indicate the allowedness of transitions. As a result of these rules certain transitions are more likely to occur than others. Those with a high probability of occurring are called allowed transitions whilst those that are very much less likely to occur are called forbidden transitions. There are different ways these rules can be relaxed, and so some selection rules are more definitive than others. The most definitive rule is the 'spin selection rule' which forbids a change in electron spin during absorption, and, as a consequence, absorption of a photon by a singlet ground state results in a singlet excited state, i.e. the electron in the excited orbital is still spin-paired with the electron in the ground state orbital (Figure 3.2).

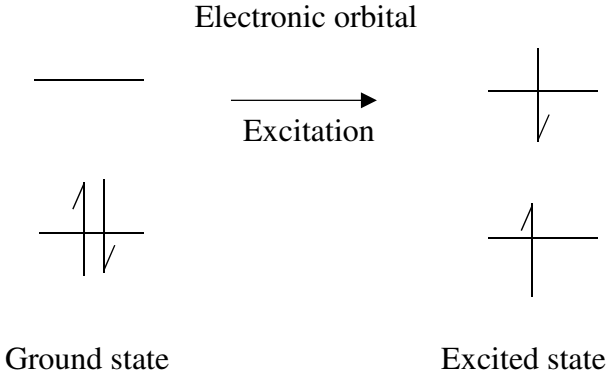

Figure 3.2 Spin paired electrons in electronic orbitals in ground state and excited state.

3.2.4. Allowed/forbidden transitions – orbital, or symmetry, selection rule

There is another selection rule which is of particular importance to molecules which are highly symmetrical, such a pyrene. The origin of this orbital, or symmetry, selection rule is the need for conservation of 'spin' during the transition. The symmetry of the two orbitals involved in a transition must be different to accommodate the 'absorption' of the photon spin in the molecular transition. This rule is less definitive than the spin selection rule. Table 3.1 outlines the relative intensity ranges for allowed and forbidden electronic transitions.

Table 3.1 Relative intensities of electronic transition.

Transition	Relative intensity
Spin and orbitally allowed	10^{3} to 10^{5}
Spin allowed but orbitally forbidden	10^{0} to 10^{3}
Spin forbidden but orbitally allowed	10^{-5} to 10^{0}

3.2.5. Radiative and non-radiative decay pathways (from excited state)

Once a molecule is in the excited state S_1 it will return to ground state S_0 through one of the following competitive processes which include both radiative and non-radiative pathways, the latter being isoenergetic transitions.

3.2.6. Intersystem crossing (ISC)

Intersystem crossing (ISC) is the radiationless process that occurs when there is a transition between two electronic states of different spin multiplicity, e.g. from a singlet excited state to a triplet excited state. In the triplet excited state, the two electrons are still in different orbitals but now both have the same spin quantum state, i.e. spins parallel, ↑↑.

3.2.7. Internal conversion (IC)

Internal conversion (IC) is a non-radiative transition from a higher to a lower electronic state of the same spin multiplicity which leads to the de-excitation of the molecule. The process usually leads to the release of heat from the excitation energy. IC is usually fast between high excited states of the same spin, e.g. $S_2 \rightarrow S_1$ but usually much slower for $S_1 \rightarrow S_0$, which gives rise to 'Kasha's rule' which states

that fluorescence will usually occur from the lowest excited state, S_1 (Lakowicz, 2006).

3.2.8. Vibrational relaxation (VR)

In solution, or the solid state, molecules with high vibrational energy, produced by absorption, IC or ISC, rapidly lose energy by collisions with neighbouring molecules leading to vibrational relaxation; therefore, emission usually occurs from the lowest vibrational state of an excited-state.

3.3. Fluorescence

Fluorescence is the process where a molecule in an excited state emits a photon of light in a transition between states of the same spin multiplicity, this is almost always from S_1 to S_0. In terms of a population of excited states, the lifetime (τ) of a fluorophore is the time taken for $1/e$ (where e is the mathematical constant, the Euler number, 2.718…) of the initial population to transition from the excited state back to ground state. In terms of a single excited molecule it is the time for which there is a $1/e$ probability of transition from the excited state back to ground state. Typical emission rates for fluorescence are in the range of 10^8 s^{-1} and therefore a typical fluorescence lifetime is around 10 ns (10×10^{-9} s) for a highly fluorescent molecule decaying by a fully allowed transition; for a symmetry forbidden transition it is closer to 1000 ns (Lakowicz, 2006).

3.3.1. Quenching

Quenching is the reduction of fluorescence intensity because of interaction with other molecules, quenchers. If quenching is by molecules already adjacent to the excited-state it is termed ‘static’ quenching, but if the process requires molecular mobility and collision between the excited state and quencher it is known as ‘collisional’ or ‘dynamic’, quenching. Molecular oxygen (which has a triplet ground state) is a well-known quencher (Lakowicz, 2006). It is also possible for a fluorophore to be self-quenched, and pyrene excimer formation which is discussed later is an example of self-quenching.

3.3.2. Franck-Condon principle

The Franck-Condon principle states that the rate of vibronic transitions between states depends on the overlap of the vibrational wavefunctions (Ψ); the transitions are fast if the overlap between the two wavefunctions is large (Figure 3.3). Vibronic transitions can occur in both the absorption and emission of a photon and the Franck-Condon principle is equally applicable to both absorption and fluorescence.

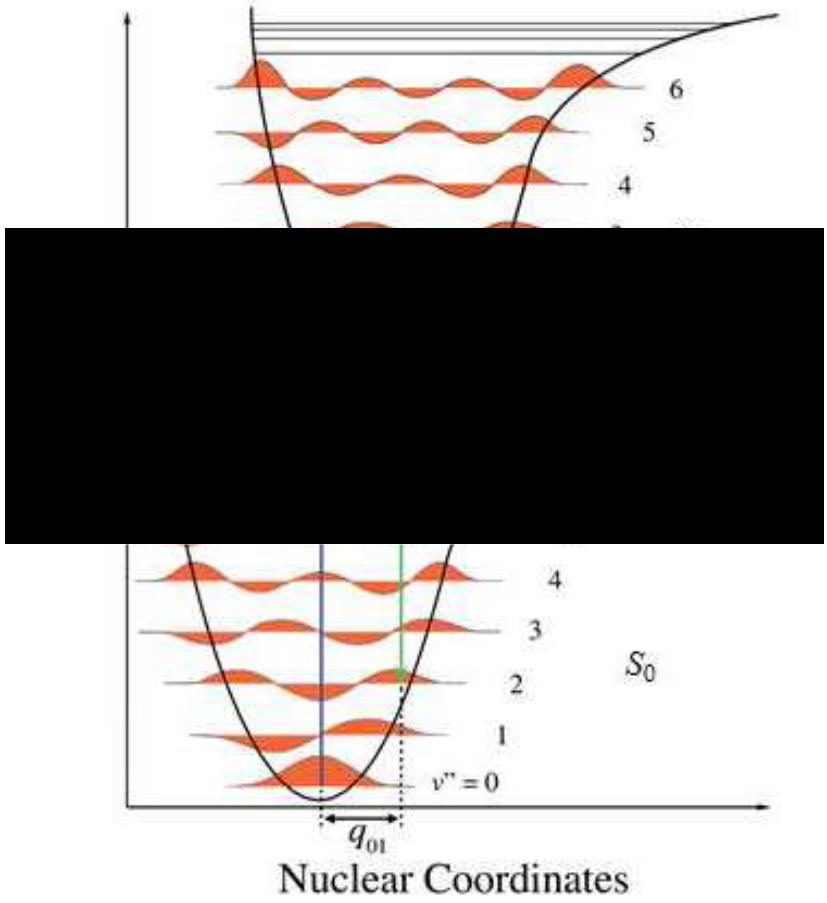

Figure 3.3 Franck-Condon principle for vibronic transitions in a molecule (Chmyrov, 2010), whereby transitions take place so rapidly that the transition is vertical.

3.3.3. Quantum Yield Φ_F

The fluorescence quantum yield, Φ_F is ratio of the number of photons emitted to the number of photons absorbed by a molecule (Equation 3.1). A reference molecule with a known quantum yield is usually used for comparison against the sample molecule to assess fluorescence quantum yield (Albani, 2007).

$$Quantum\ yield\ \Phi_F = \frac{number\ of\ photons\ emitted}{number\ of\ photons\ absorbed} \quad (3.1)$$

3.3.4. Stokes shift

The 'Stokes shift' refers to the difference in energy/wavelength between the absorption maximum and emission maximum (Albani, 2007).

3.3.5. Mirror image rule

The vibrational levels of the electronically excited state of a fluorophore are given by its absorption spectrum, whilst an emission spectrum depicts the vibrational levels of the electronic ground state. The mirror image rule is found where ground and excited state have very similar molecular structure and thus similar vibrational energy levels. In these cases, the fluorescence spectrum is an approximate mirror image of the absorption spectrum.

3.4. Phosphorescence

Phosphorescence is a radiative transition between states of different spin multiplicity, e.g. $T_1 \rightarrow S_0$. Because of the need for an electron spin change, phosphorescence lifetimes are usually much longer than fluorescence lifetimes, typically milliseconds to seconds. Phosphorescence is mentioned here for completeness but is not discussed further in this thesis.

3.5. Instrumentation: fluorimeter

Specialist equipment is required to measure the photophysical properties of fluorescent probes. For the research described in this thesis (chapters 4 and 5) a fluorimeter, and a Time Correlated Single Photon Counting (TCSPC) lifetime spectrometer were used. These instruments have specific instrumental parameters that influence the measurements obtained.

3.5.1. Fluorimeter: fluorescence measurements

The following settings on the fluorimeter need to be chosen: excitation wavelength (λ_{exc}), excitation slit width (nm), emission wavelength (λ_{em}), emission slit widths (nm), step increments (nm) and integration time (seconds).

Two types of spectra can be produced on a fluorimeter: emission and excitation. An emission spectrum is produced by constant excitation at a single wavelength and shows the wavelength distribution of emission obtained, experimentally the excitation monochromator is fixed and the emission monochomator is scanned. By contrast, an excitation spectrum shows the wavelength distribution of excitation for a single emission wavelength, experimentally the emission monochromator is fixed and the excitation monochomator is scanned (Lakowicz, 2006).

3.5.2. Monochromator slit widths

Monochromators typically have both entrance and exit slits which have variable widths and the light intensity that passes through is approximately proportional to the square of the slit width (Lakowicz, 2006). Large slit widths give increased signal-to-noise (S/N) but decreased spectral resolution. Small slit widths give higher spectral resolution but decreased light intensity and S/N ratio (Lakowicz, 2006).

3.5.3. Integration time

Integration time is the length of time allowed for photons to be collected by the detector before moving on for processing. A long integration time will give higher S/N, i.e. a much 'smoother' spectrum compared to that obtained using a short integration time.

3.5.4. Increment

For a digitally 'stepped' monochromator, the increment setting is the step size in nm between each measurement over the course of the wavelengths being measured. A smaller step size will give a more detailed spectrum but collecting the spectrum will take longer.

3.5.5. Cuvette, path lengths and front face attachment

Optical quartz transmits UV whereas glass does not, so quartz cells were used throughout. Standard fluorimeter cells are 1 cm square and all four faces of the cuvette are polished, unlike absorption cells where only two faces are polished (Evans *et al.*, 2013), and the emitted light is collected at 90^{o} from the sample (Figure 3.4), thus minimising interference from scatter of the excitation beam. However, for work with solids, such as soils, a front face attachment is used. The front face

attachment is useful for measurements on solid samples as it allows the excitation light to be focused directly on the front surface of the sample and any emitted light is collected at a relatively small angle to the sample, rather than 90°.

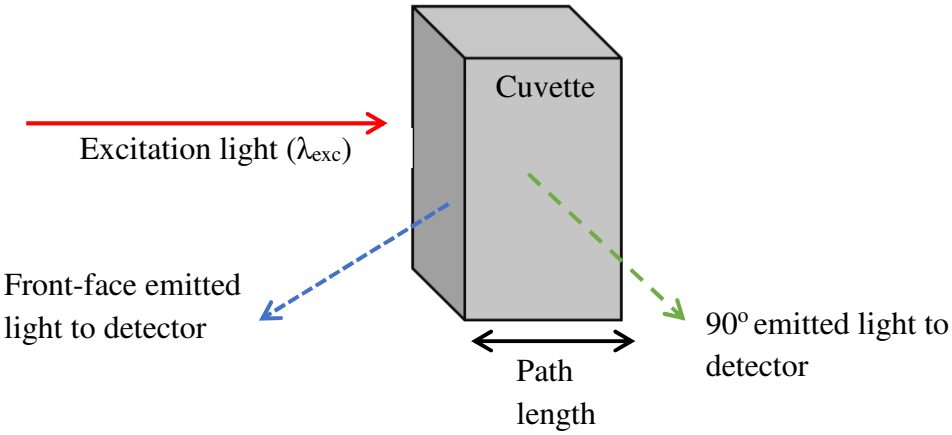

Figure 3.4 Schematic of a sample cuvette showing path of fluorescence excitation source and direction of light emitted to detector for 90° and front facing.

Background signals in fluorescence need to be carefully considered. For studies with soils there are two factors: the natural luminescence of the soil, soil 'auto–luminescence', and scatter because of the irregular nature/surface of the sample being studied. In this work, emission spectra were corrected for background by running a blank control sample and then subtracting this from the sample spectra. Samples and blanks need to be prepared and run under the same conditions in order for this method to be viable.

3.5.7. Filters

Fluorescence measurements can be significantly affected by interference from scattered or straylight, so it is important to take steps to try and reduce this source of error. Optical filters can be used to reduce scattered light and eliminate any unwanted wavelengths from the excitation/emission beam (Albani, 2007).

An optical bandpass filter transmits only a certain section of the spectrum and rejects all other wavelengths. Lakowicz (2006) noted that filters should be chosen not only for their effectiveness at transmitting chosen wavelengths but also for their ability to reject those that are unwanted from possible sources of interference.

3.6. Instrumentation: time correlated single photon counting (TCSPC) lifetime spectrometer

Time correlated single photon counting (TCSPC) is a technique in which a relatively weak laser pulse is used as an excitation source and a very fast response photomultiplier, capable of detecting a single photon is used a detector, with source and detector arranged so that only a maximum of one photon is detected per laser pulse. The instrument is set-up to measure the time delay between excitation and photon emission (i.e. detection), and to count the number of photons detected within regular specific time intervals (channels) after excitation. The fluorescence photons are emitted over a range of time after excitation, and for a single fluorophore more photons are emitted earlier, and fewer later, as the excited-states decay. The 'decay curve' is then a histogram of photons counted in each detection 'channel', with the number of photons counted usually plotted on a logarithmic scale.

Chapter 4 The use of nile red probe as a tool for studying soil surface polarity

In this chapter, experimental work is described which assesses the natural auto-luminescence of model and natural soils and the suitability of the fluorescent probe nile red for in-situ soil grain surface measurements, via optical and fluorescence microscopy. Overall, the results show that, whilst it is possible to image nile red emission after adsorption to soils, several issues regarding emission intensity and the interference of auto-luminescence suggest that nile red may not be suitable for the study of soil surface polarity. However, the general methodology is promising and further exploration with alternative probes may prove to be more successful.

4.1. Background

Fluorescent probes have been successfully used for many decades to study biological and chemical environments (Evans *et al.*, 2013). Nile red (Figure 4.1) is an environment polarity probe which shows an increase in both absorption and emission wavelength maxima with environment polarity, from non-polar e.g. hexane (λ_{abs} *ca.* 484 nm, λ_{em} *ca.* 526 nm), to polar e.g. methanol, (λ_{abs} *ca.* 549 nm, λ_{em} *ca.* 633 nm) environments, and a marked decrease in fluorescence emission intensity in very polar environments, e.g. water (Deye *et al.*, 1990; Zhang *et al.*, 2011). Jee *et al.* (2009) measured a quantum yield of 0.76 for nile red in dioxane compared to 0.02 in water. Nile red can be used in the pH range 4.5-8.5 (Sackett and Wolff, 1987).

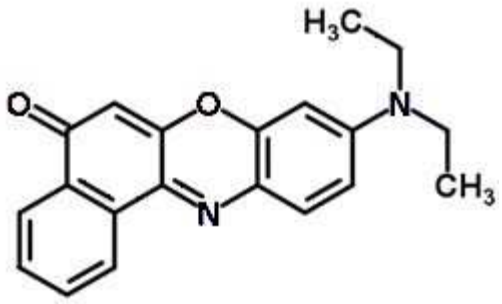

Figure 4.1 Structural formula of nile red.

In terms of application to soil studies, it was anticipated that emission from absorption of nile red into organics on the soil grains would give an indication of the distribution of organics on the grains, and the emission wavelength might give an indication of the polarity of these organics. In addition, since nile red fluorescence is quenched by water, in a soil undergoing wetting the fluorescence intensity of the nile red would be expected to decrease due to the presence of water. Nile red is also easy to handle and apply to soil grain surfaces in much the same way biochemists use it for staining cells. Bayer (2009) briefly used nile red to study fluorescence on single soil grains, however had minimal success due to high intensity emission which prevented subtle differences in surface polarity being established. Further work was therefore not continued.

However, prior to any fluorescent probe studies an assessment of model and natural soil auto-luminescence was required. There are numerous sources of auto-luminescence within soils, defects and impurities in minerals, and organic substances

(Altemuller and Van Vliet-Lanoe, 1990; Tippkotter, 1990 and FitzPatrick, 1993). Whilst the origin of any auto-luminescence observed was outside the scope of this study, it was necessary to consider if large background signals, which would influence fluorescence measurements, were present from soil auto-luminescence.

4.1.1. Research objectives

In the work described here, following an assessment of the auto-luminescence of the model and natural soils used, nile red was applied to model and natural soils and examined as an *in-situ* fluorescent probe to address the following research questions:

1) Can nile red identify localised areas of organics by visualisation of localised absorption of the probe?
2) Can nile red give an indication of the general polarity of the nile red environment, and hence, by extension, the polarity of the organics at the soil grain surface?

4.2. Materials and methods

The following study uses acid-washed sand as a model soil, along with two natural sandy soils AU2 and AU3. Sample origins and characteristics for these soils are detailed in Table 2.2.

4.2.1. Addition of nile red to soils

The adsorption method used is based on that described by Greenspan *et al.* (1985) for addition of nile red to cells. 1 g of soil was added to 5 ml of distilled water and 10, 20, 50, or 100 µl aliquots of either a 2.17×10^{-4} M nile red in ethanol solution or 2.17×10^{-3} M nile red in acetone solution was added. The sample was inverted back and forth for *ca.* 1 min, water decanted off and the sample rinsed with 1 ml of water and then placed onto a filter paper in a Petri dish and allowed to dry. 100 µl of acetone without nile red was similarly used for the preparation of blank/control samples.

4.2.2. Laydown of nile red probe

Finding an optimum level of probe application was necessary. At too high a concentration everything becomes saturated with probe, and no differentiation of probe response across the soil grains is possible. By contrast, at too low a concentration not enough probe is present to provide a useful signal/image. In order to obtain an optimum concentration for selective adsorption, a series of concentrations were made up and tested for each soil type as given in Table 4.1.

Table 4.1 Nile red probe concentration, application rates and laydowns on model (AWS) and natural soils (AU2 and AU3).

Soils	Nile Red Concentration M	Application µl	Laydown $Mol_{dye}\ g^{-1}_{sand}$	Laydown $g_{dye}\ g^{-1}_{sand}$
AWS AU2 AU3	Blank Control	N/A	N/A	N/A
	2.17×10^{-4}	10	2.17×10^{-9}	6.91×10^{-7}
		50	1.09×10^{-8}	3.45×10^{-6}
		100	2.17×10^{-8}	6.91×10^{-6}
	2.17×10^{-3}	20	4.34×10^{-8}	1.38×10^{-5}
		50	1.09×10^{-7}	3.45×10^{-5}
		100	2.17×10^{-7}	6.91×10^{-5}

Assuming complete adsorption of nile red, the highest concentration solution gives a laydown of: 2.17×10^{-7} Mol_{dye} g^{-1}_{sand}; 6.91×10^{-5} g_{dye} g^{-1}_{sand}, with the other concentrations *pro-rata*.

4.2.3. Stripping of organics from natural soils

For visualisation experiments with nile red, natural soils were stripped of their organics using the following procedures based on Mainwaring (2004), to create basic and acidic soil surfaces to see if there was any differentiation between nile red emission from an acidic soil surface compared to a basic soil surface.

4.2.3.1. Basic soil surface

To strip organics and leave a basic soil surface, 100 ml of 1 M NaOH solution was added to 50 g of soil and stirred for 30 minutes using a magnetic stirrer. The solution was decanted off, 400 ml of water added, and the sample left overnight. Rinses of 100 ml of distilled water were used until a pH of ~7.0 – 8.0 was achieved, the soil collected by filtration under vacuum, and then oven dried at 100 ^{o}C for 24 hours.

4.2.3.2. Acidic soil surface

To create an acidic soil surface, 100 ml of 0.1 M HCl was added to approximately 25 g of the NaOH stripped soil and stirred for 5-10 minutes using a magnetic stirrer. The samples were rinsed three times with distilled water until the pH reached ~7.0 and the soils collected by filtration under vacuum. Samples were then oven dried at 100 ^{o}C for 24 hours.

Samples were prepared using 10, 50 or 100 µl of 2.17×10^{-4} M nile red solution added per gram of soil, 100 µl of acetone without nile red was added in place of nile red in blank control samples.

4.2.4. Fluorescence microscopy

Fluorescence microscopy with vertical (episcopic) illumination was carried out using an Olympus BX51 polarising microscope fitted with a medium pressure mercury arc lamp and Olympus Soft Imaging Solutions XC10 camera. The lamp gives strong atomic emission lines superimposed on a weaker continuum. All images were recorded with an exposure time of 115.5 ms and camera sensitivity (gain) of '0', so for 'raw' images collected using the same filter arrangements absolute intensities are directly comparable. Any subsequent image manipulation is described in the text.

A ×4 Olympus objective was used for most imaging, with ×20 for higher magnification for spectral analysis for soil auto-luminescence, along with two illumination/detection filter (Thorlab) arrangements, and a third room light illumination detailed as below:

1) *Green light excitation, red light emission* – Excitation filter maximum 559 nm with 34 nm bandwidth; a dichroic reflecting 533-580 nm and transmitting 595-800 nm; with a 665 nm longpass emission filter. The spectral information for this filter is shown in Figure 4.2a.
2) *Near UV excitation, visible wavelength emission* – Excitation filter maximum 390 nm with 18 nm band pass; a dichroic 360-407 nm, with a 435 nm longpass emission filter to allow imaging across the visible spectrum. The spectral information for this filter is shown in Figure 4.2b.
3) *Room light excitation, visible wavelength emission* – for room light (fluorescent) excitation no emission filters were used, to allow imaging across the visible spectrum.

The green light excitation source was used to image the presence of nile red, while the UV (blue) light excitation source was used for the auto-luminescence studies. No emission filters were used for room-light (visible wavelength) imaging. Two other filter arrangements expected to give images of nile red in very non-polar environments were also tried but gave no useful images and were therefore discounted from further imaging work (an excitation filter with maximum 475 nm and 35 nm bandwidth; and an excitation filter with maximum 497 nm and 16 nm bandwidth).

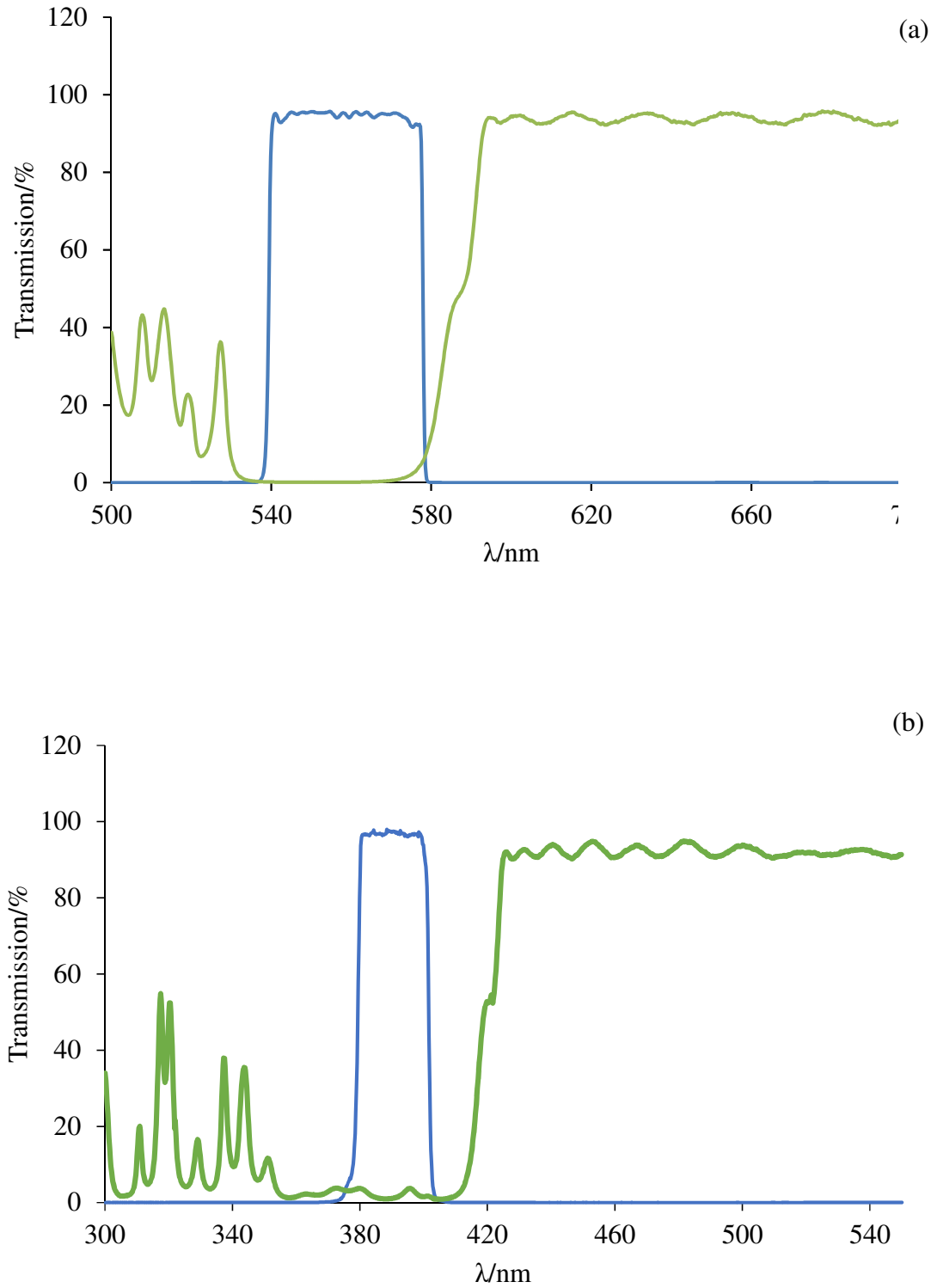

Figure 4.2 (a) Green light excitation, red light emission and (b) Near UV excitation, visible wavelength emission. Excitation filter in blue, and dichroic mirror in green.

4.2.5. Visible colour spectrum

To assist the reader a spectrum showing the relationship between colour and wavelength is given in Figure 4.3.

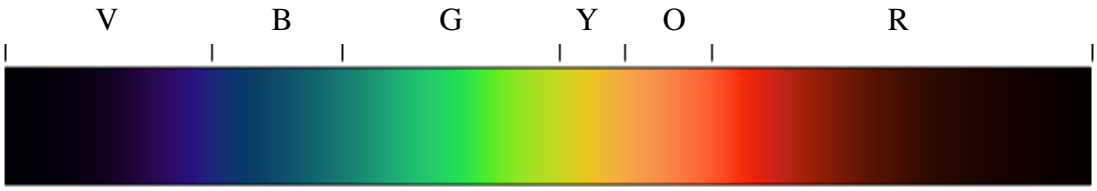

Figure 4.3 Visible colour spectrum showing the relationship between colour and wavelength (Tilley, 2000), from violet (V), blue (B), green (G), yellow (Y), orange (O), to red (R).

4.2.6. Soil auto-luminescence spectroscopy

Spectral analysis of auto-luminescence of specific soil grains was made using a HR2000+ Ocean Optics high-resolution fibre optic spectrometer imaged through the eyepiece of a BX51 Olympus microscope via a 1 mm fibre optic probe placed at the centre of the eyepiece. Where a particular grain, or part of grain, was identified of interest a ×20 objective was used to maximise the collection of emission specifically from that grain.

4.2.7. Transmission microscopy

An Olympus BH3 transmission microscope was used for transmission microscopy. Analysis through crossed-polarisers gave some advantage for viewing organics on soil grains since quartz grains are optically anisotropic and therefore coloured and bright through crossed-polarisers, whereas organics are isotropic and therefore dark through crossed-polarisers.

4.3. Results and discussion

4.3.1. Distribution of organics on natural soils

Figures 4.4a and b show the typical heterogeneous distribution of organics adhered to soil grain surfaces and loose organics between the grains. Ma'shum *et al*. (1988) suggested that organics present in soils may not adsorb to the grain surfaces in uniform monolayers but rather as smaller globules of material.

Figure 4.5 shows natural AU2 soil grains under ×20 objective in transmission microscopy, with and without crossed-polarisers. Similarly to Figures 4.4a and b localised collections of organics can be clearly seen, however it is also possible that what appears to be the bare mineral surface of the grains is actually covered in an optically undetectable coating of organics which makes the grains hydrophobic. Further investigation with other instrumentation, such as infrared microscopy, may be able to detect this layer.

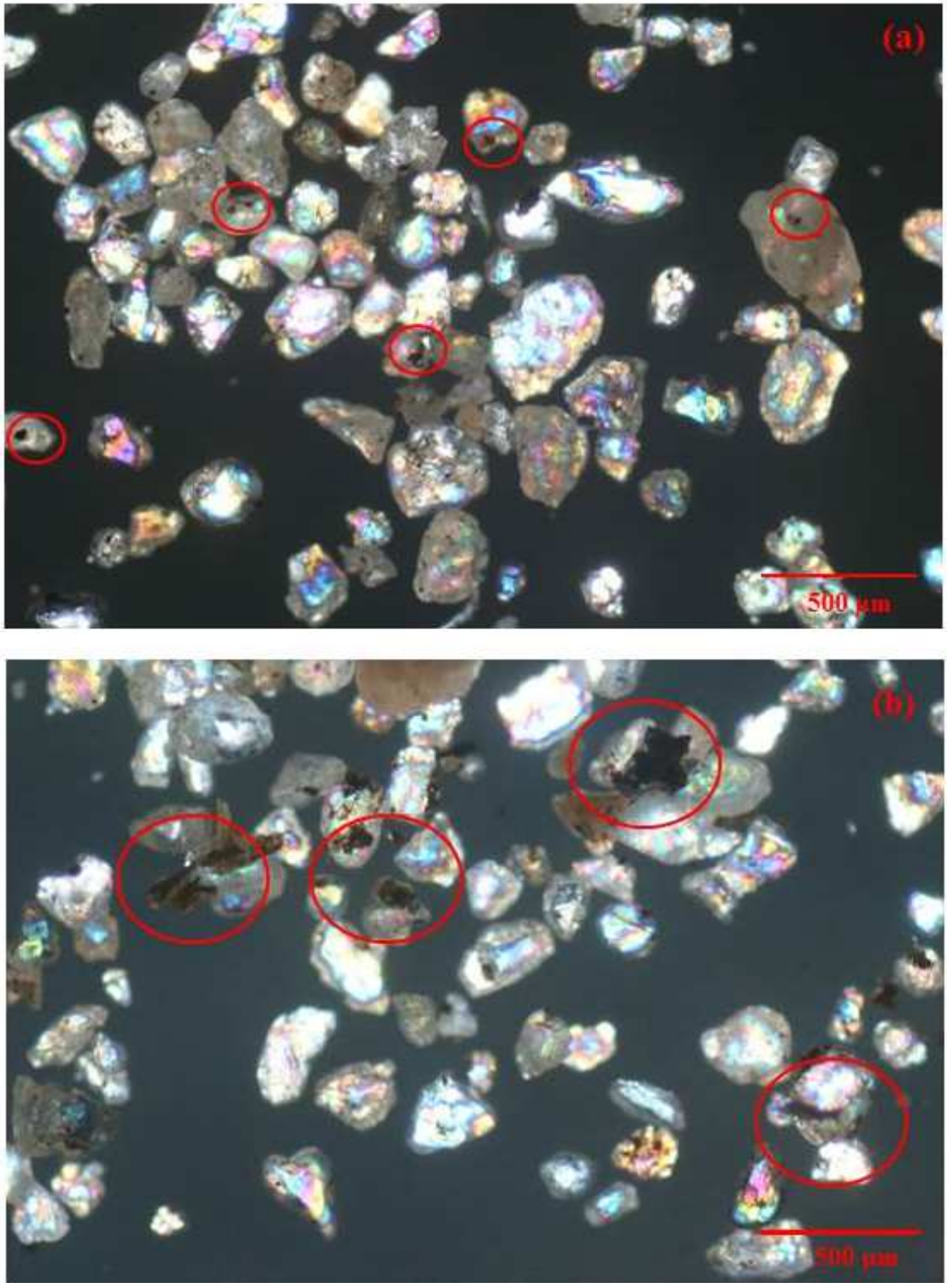

Figure 4.4a and b Transmission microscope images of natural soil (AU2) under cross-polarised light showing the distribution of organics within the sample. Examples of small globules of organics present on the soil grain surfaces have been circled. (See section 4.3.1 for discussion).

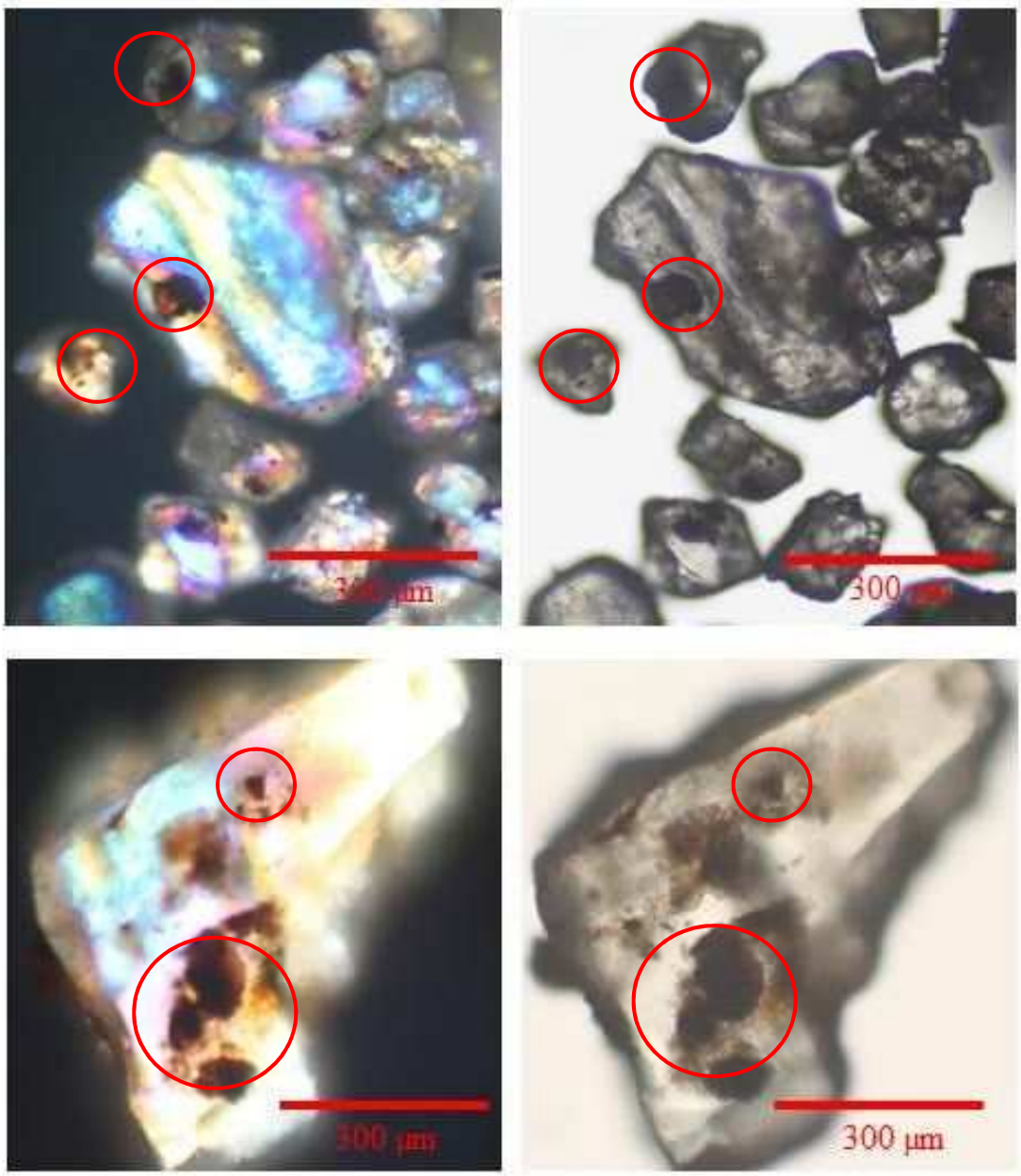

Figure 4.5 Transmission microscope images of organics on AU2 soil grains under crossed-polarisers (left) and parallel-polarisers (right). The top images show multiple soil grains whilst the bottom images focus on a single grain. Examples of small globules of organics present on the grains have been circled. (See section 4.3.1 for discussion).

4.3.2. Auto-luminescence

A typical emission image from a natural soil (AU3), with UV_{ex}/vis_{em} detection is shown in Figure 4.6a. Throughout the soil, individual grains, and sometimes parts of grains, give intense emission with colours varying from blue to red. Two examples of this intense emission and confirming the occurrence of auto-luminescence from the natural soil AU3 are presented in the spectra in Figure 4.6b (orange/yellow) and 4.6c (blue). The emission spectra are very broad, and, significantly for this work, extend across the visible spectrum into the red i.e. the same region in which nile red emits. It should be noted that the apparent structure in the emission is due to scatter of intense atomic emission lines from the mercury lamp (Figure 4.7). For example, the sharp emission lines found in both spectra in Figures 4.6b and c. at approximately 540 nm are attributed to emission lines from the medium pressure mercury lamp excitation source (Figure 4.7). The dashed line on the blue spectrum marks the longpass short wavelength cut off, so for this spectrum λ_{max} may not be visible due to the filter cut off.

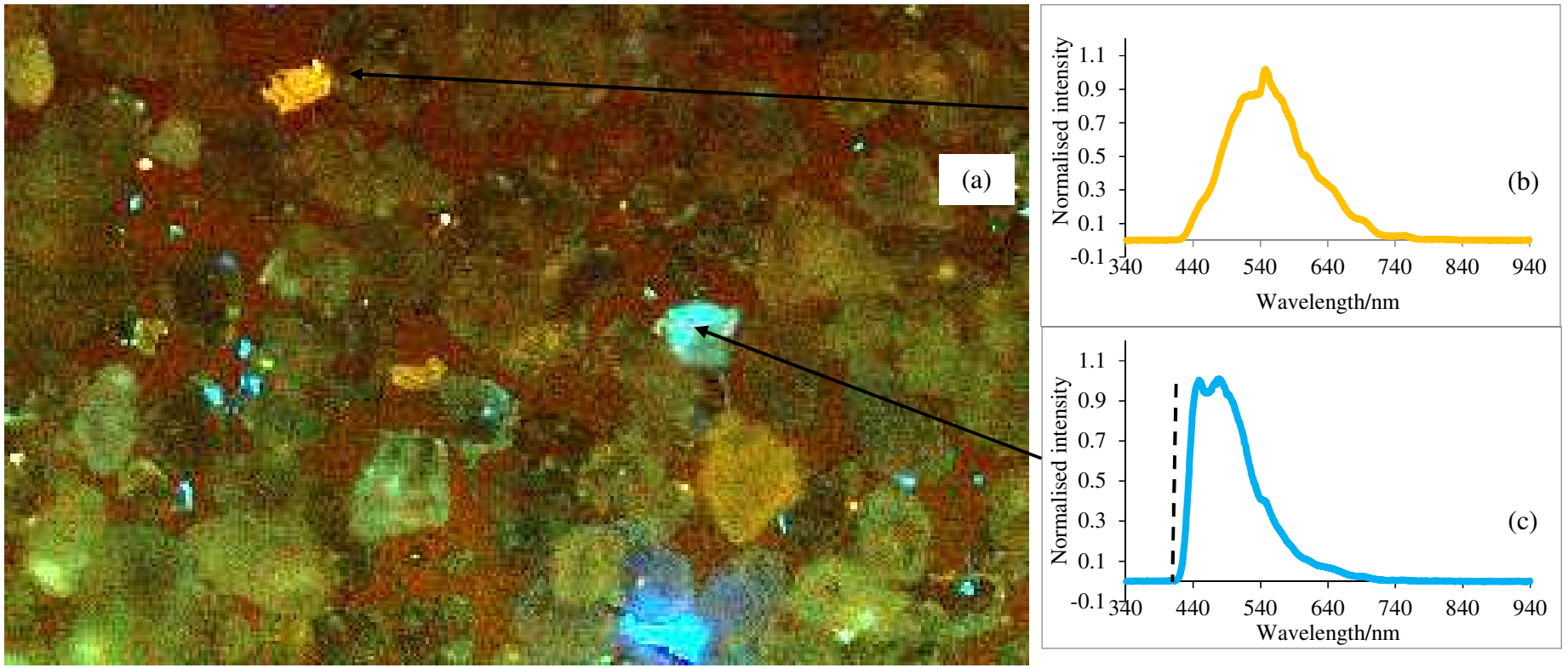

Figure 4.6 (a) Auto-luminescence microscopy image of AU3 soil grains under UV_{ex}/vis_{em} detection (image contrast digitally enhanced); (b) spectra of the yellow-orange and (c) of blue auto-luminescence. Dashed line on (c) marks the longpass cut off point for the filter used. (See section 4.3.2. for discussion). Individual grains and sometimes parts of grains, give intense emission with colours varying from blue to red. , This is natural auto-luminesce of the soil and typical examples of auto-luminescence are imaged here (b, c) using a BX51 microscope collecting the light from the centre of the microscope eyepiece using a 1 mm fibre optic connected to a high-resolution HR2000+ Ocean Optics spectrometer.

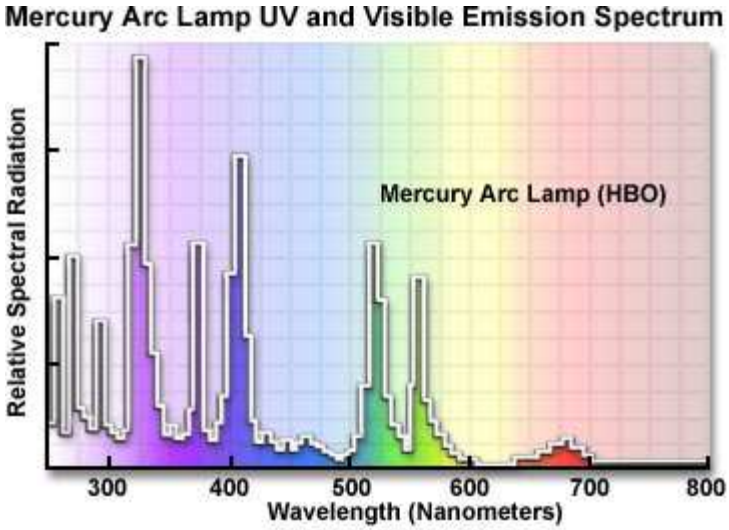

Figure 4.7 Olympus medium pressure mercury lamp spectrum showing intense atomic emission lines (Olympus-lifescience, 2019). The sharp emission lines at approximately 540 nm can be seen in emission spectra obtained using a fibre optic connected to an Ocean Optics spectrometer. (See section 4.3.2. for discussion).

Acid-washed sand (AWS) has a lower level of auto-luminescence under UV_{ex}/vis_{em} than natural soils AU2 and AU3 (Figure 4.8). Figure 4.8 shows AWS, AU2 and AU3 soil under $green_{ex}/red_{em}$ and UV_{ex}/vis_{em} respectively. Examples of auto-luminescence have been highlighted in each instance. It is not possible to make any direct comparisons of emission intensities between samples excited under the UV (blue) light and the green light because of the differences in excitation intensities at different wavelengths.

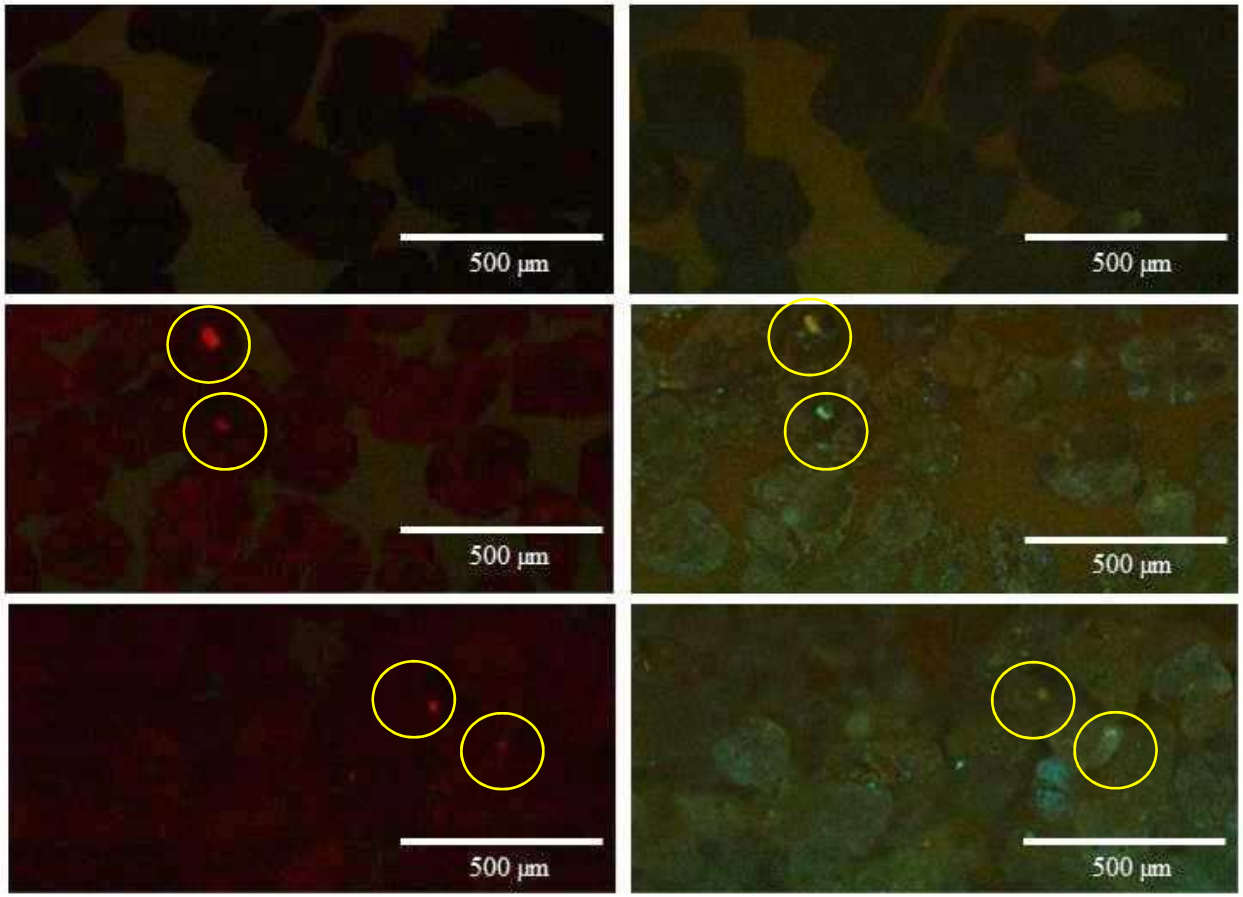

Figure 4.8 Auto-luminescence of AWS (top), AU2 (middle) and AU3 (bottom) under $green_{ex}/red_{em}$ (left) and UV_{ex}/vis_{em} (right). Image contrast has had saturation, gamma and brightness digitally enhanced. Examples of auto-luminescence have been highlighted for soils AU2 and AU3, acid-washed sand has a lower level of auto-luminescence than natural soils. (See section 4.3.2 for discussion).

4.3.3. Solvatochromism and nile red

There are many empirical solvent scales, which give a more comprehensive measure of solvent polarity than dielectric constant or any other single physical characteristic.

Researchers have long established that the absorption spectra of chemical compounds can be affected by their surrounding environments and that solvents can cause a change in position, intensity and shape of desorption bands, referred to as solvatochromism (Reichardt, 1994). A study by Reichardt (1994) provides molar electronic transition energies (ET) in kcal/mol using the negatively solvatochromic pyridinium *N*-phenolate betaine dye 36 as the probe in a range of solvents. This probe was chosen due to its unusually high solvatochromic band shift of 357 nm from water at 453 nm to diphenyl ether at 810 nm. The scale provided by this study is referred to as the ET(30) scale, where a high value corresponds to high solvent polarity and a low value to a low solvent polarity. For a discussion of the interrelation of this solvent polarity scale and others see for example Reichardt (1988). Nile red can be used as a probe to identify different polarity environments from its shift in both absorption and emission wavelength maxima. Data taken from Deye *et al.* (1990) of nile red in different polarity solvents is presented in Figure 4.9. In more polar environments the λ_{max} shifts to longer wavelengths.

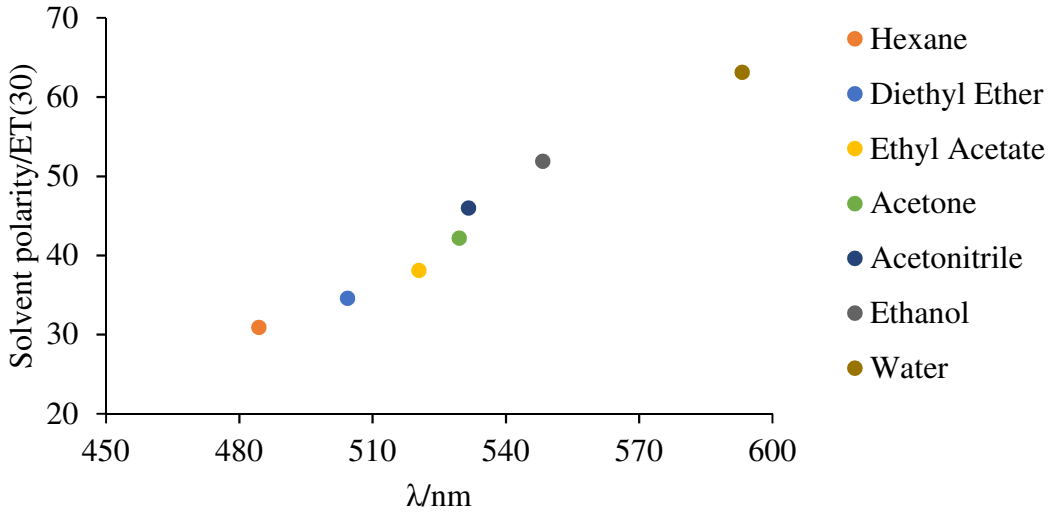

Figure 4.9 Solvatochromism of nile red transition energies (from adsorption max) against Reichardt's ET(30) – data from Deye *et al.* (1990). For Reichardt's ET(30) scale, a high value corresponds to high solvent polarity and a low value to a low solvent polarity, here λ_{max} shifts to longer wavelength with increasing polarity.

Figures 4.10 and 4.11, show nile red in solvents of increasing polarity from left to right, under room light and under a 366 nm blacklight. These show the possible colour range that may be observed when the probe is applied to different polarity environments.

Figure 4.10 Colour under room light of nile red in solvents of increasing polarity from left to right: hexane, hexadecane, diethyl ether, ethyl acetate, octanoic acid, acetone, acetonitrile, octanol, ethanol and water. (See section 4.3.3. for discussion).

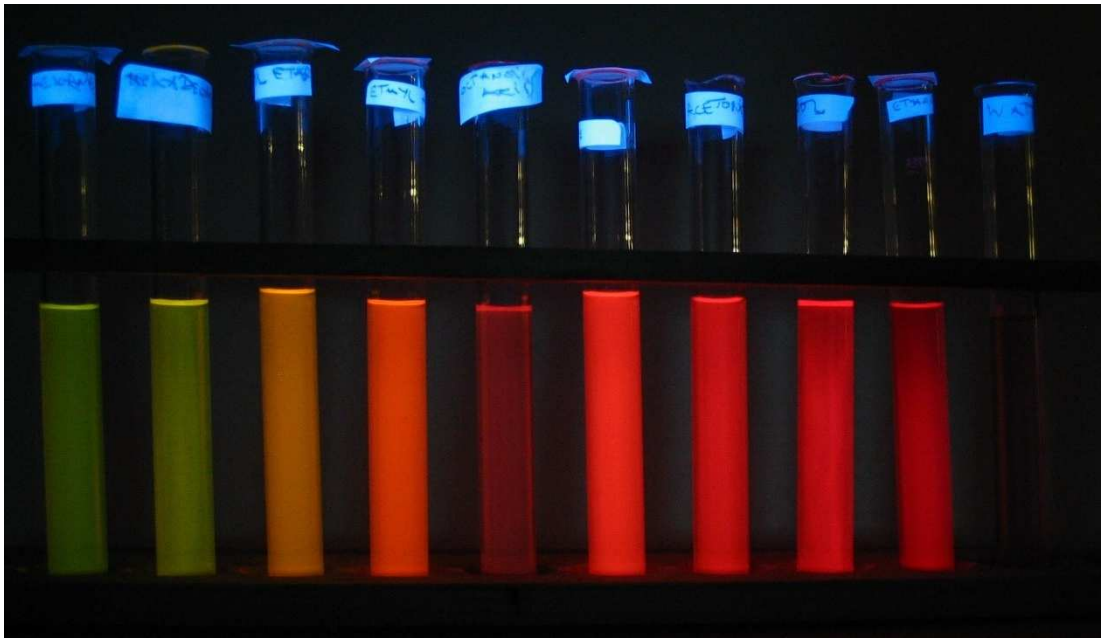

Figure 4.11 Emission from nile red in solvents of increasing polarity from left to right: hexane, hexadecane, diethyl ether, ethyl acetate, octanoic acid, acetone, acetonitrile, octanol, ethanol and water, using a 366 nm light – black lamp light source. Note the very low emission intensity from nile red to water. (See section 4.3.3. for discussion).

4.3.4. Optimum application levels of nile red probe

In order to establish an optimum level of nile red probe application a series of solutions of varying concentration were applied to samples and imaged to assess what level offered a measurable signal but did not saturate the sample. Results from this experiment are displayed in Figure 4.12a-g. Emission intensity of microscopy images increased with increased nile red application. Following this preliminary study, it was decided that 3.45×10^{-6} g_{dye} g^{-1}_{sand} was a suitable application for imaging without saturation, and with probe laydown kept to the minimum for useful imaging.

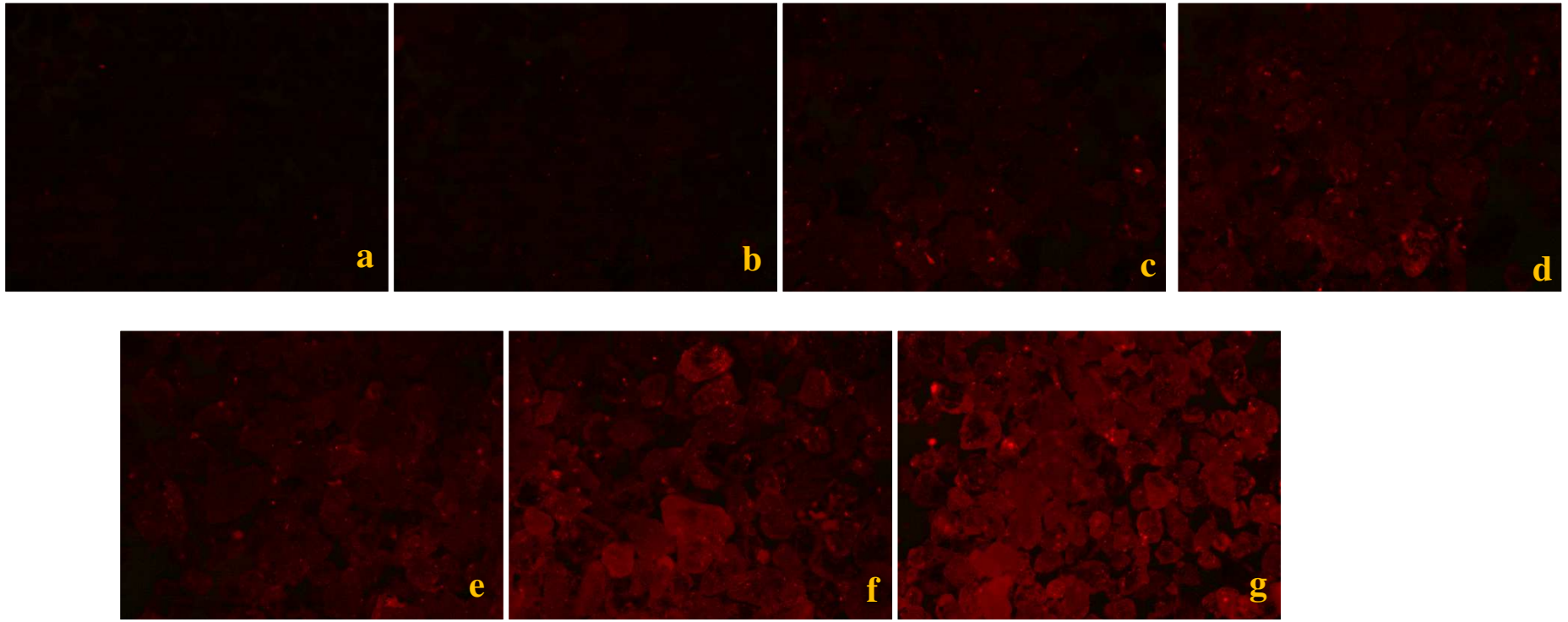

Figure 4.12 Fluorescent microscopy images under $green_{ex}/red_{em}$ light on AU3 soil with nile red at the following laydowns ($g_{dye}\ g^{-1}{}_{sand}$): (a) 0, (b) 6.91×10^{-7}, (c) 3.45×10^{-6} , (d) 6.91×10^{-6} , I 1.38×10^{-5} , (f) 3.45×10^{-5} , (g) 6.91×10^{-5}. To establish an optimum level of nile red probe application a series of solutions of varying concentrations were applied to samples to identify a suitable application for imaging without saturation and with probe laydown kept to a minimum. (See section 4.3.4 for discussion).

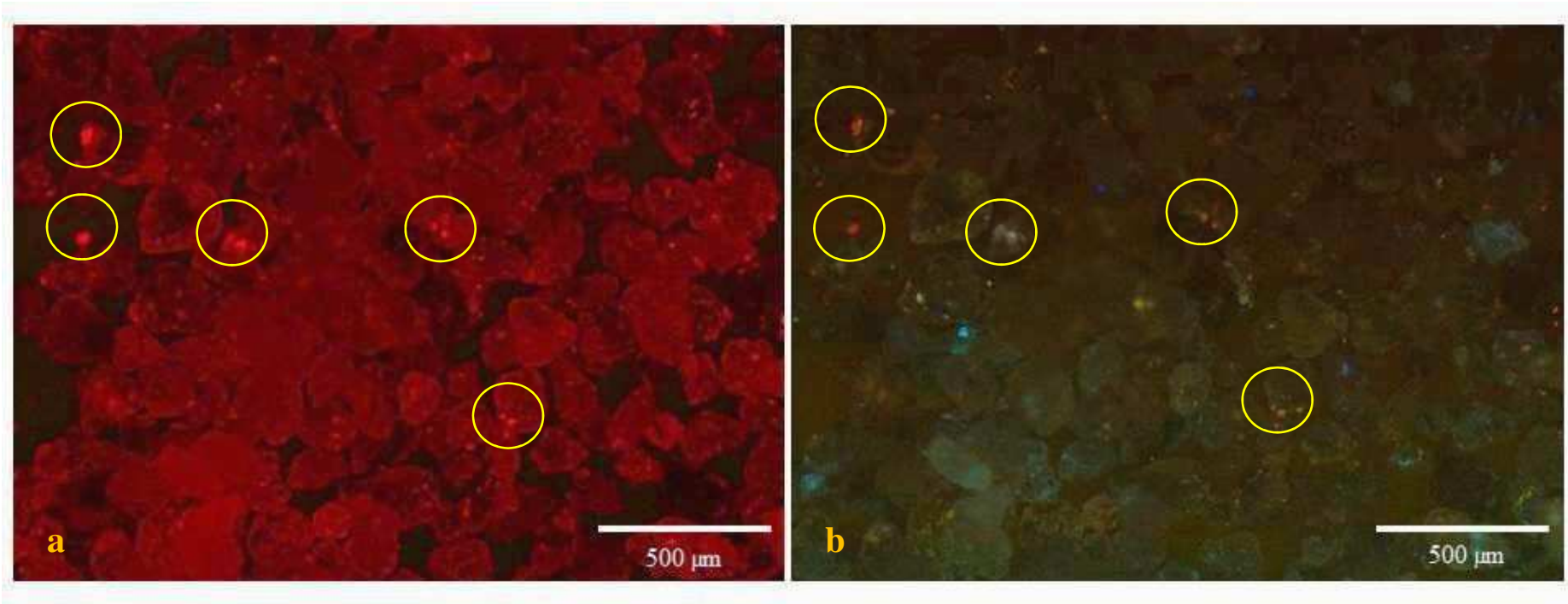

Figure 4.13 Fluorescence microscopy images of AU3 soil grains treated with nile red, under green (a) and UV light (b) excitation with 6.91×10^{-5} g_{dye} g^{-1}_{sand}. Image contrast has had saturation, gamma and brightness digitally enhanced. Examples of regions of high intensity emission under green and UV light respectively are highlighted to illustrate regions of auto-luminescence. (See section 4.3.4 for discussion).

The images in Figures 4.13 show regions of high relative emission intensity; however, these are predominantly due to auto-luminescence rather than emission from nile red. This is confirmed by images from both UV_{ex}/vis_{em} and $green_{ex}/red_{em}$ of the same collection of AU3 soil grains with nile red deposited, as shown in Figure 4.13a and b. Even with the microscope filters set for $green_{ex}/red_{em}$ soil auto-luminescence generates regions of bright red emission, spatially well correlated with regions of intense coloured auto-luminescence when examined under UV_{ex}/vis_{em}.

4.3.5. Nile red probe applications to natural soils

Images of AU2 and AU3 with 3.45×10^{-6} g_{dye} g^{-1}_{sand} nile red laydowns under $green_{ex}/red_{em}$, room $light_{ex}/vis_{em}$, and UV_{ex}/vis_{em} are given in Figure 4.14 and Figure 4.15. Localised adsorption of nile red can be seen when viewed under room light but these regions do not give high red emission intensity. Although room light shows adsorption in regions considered to be localised organics it is difficult to correlate local areas of organics with increasing levels of emission intensity. There are some brighter areas under $green_{ex}/red_{em}$ but these correlate with yellow/orange/red auto-luminescence. It is possible to identify regions on individual grains that are dark and evidently have organic material adhered to the grain surface, however this does not necessarily correlate with fluorescence emission under $green_{ex}/red_{em}$ light.

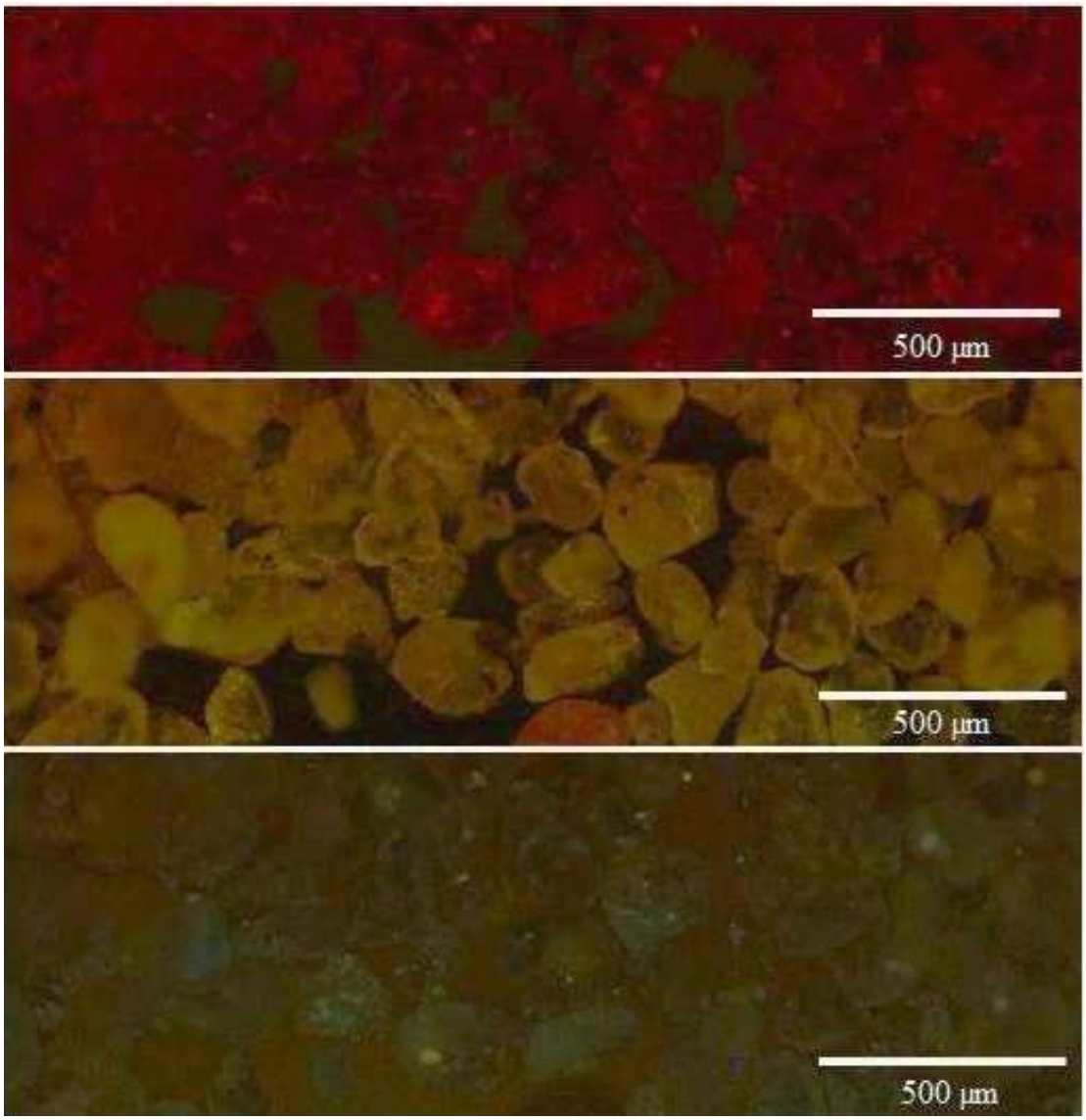

Figure 4.14 Fluorescence microscopy images of AU2 soil grains prepared by adsorption using 3.45×10^{-6} g_{dye} g^{-1}_{sand} nile red under $green_{ex}/red_{em}$, (top) room $light_{ex}/vis_{em}$ (middle) and UV_{ex}/vis_{em} (bottom). Image saturation, gamma and brightness have been digitally enhanced to the same degree for each image. (See section 4.3.5 for discussion).

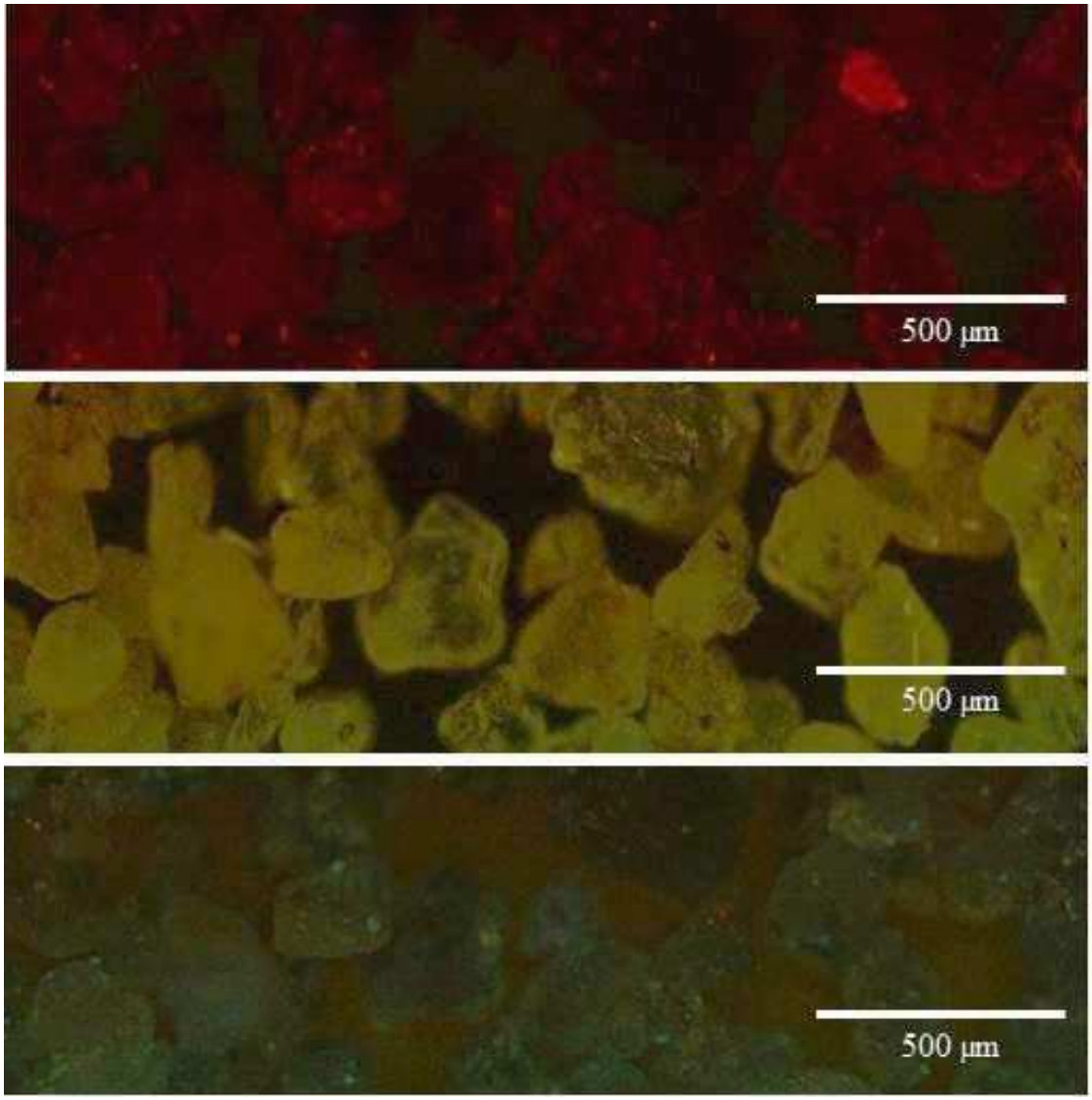

Figure 4.15 Fluorescence microscopy images of AU3 soil grains prepared by adsorption using 3.45×10^{-6} g_{dye} g^{-1}_{sand} nile red under $green_{ex}/red_{em}$, (top) room $light_{ex}/vis_{em}$ (middle) and UV_{ex}/vis_{em} (bottom). Image saturation, gamma and brightness have been digitally enhanced to the same degree for each image. (See section 4.3.5 for discussion).

4.3.6. Nile red probe applications to AWS

With nile red on acid-washed sand (Figure 4.16) the emission intensity is relatively high and uniform across the grains, there is no obvious regions of colouration due to nile red when viewed under room light, and there is much less auto-luminescence than observed with natural soils.

4.3.7. Natural soils with basic and acidic surfaces under room light

Acid-washed sand (AWS) appears to readily adsorb nile red onto the sand grain surface. It is possible, for the natural soils, that solid waxes coating the soil grains prevent the adsorption of nile red. To explore this idea AU2 and AU3 soils were stripped of their organics with sodium hydroxide (Mainwaring, 2004). In addition to removing organics this also creates a basic quartz surface. Washing a base stripped soil with hydrochloric acid creates an acidic quartz surface. Fluorescence microscopy images of AWS, and untreated, acid stripped, and base stripped AU3 soil, after deposition of nile red at the same laydown, are shown in Figure 4.17.

The images show that an acidic quartz surface adsorbs nile red to give a relatively highly emissive surface, whereas a basic quartz surface either does not adsorb nile red, or if it does the probe is in a non-fluorescent state, with the natural soil sitting somewhere between the two in terms of emission intensity.

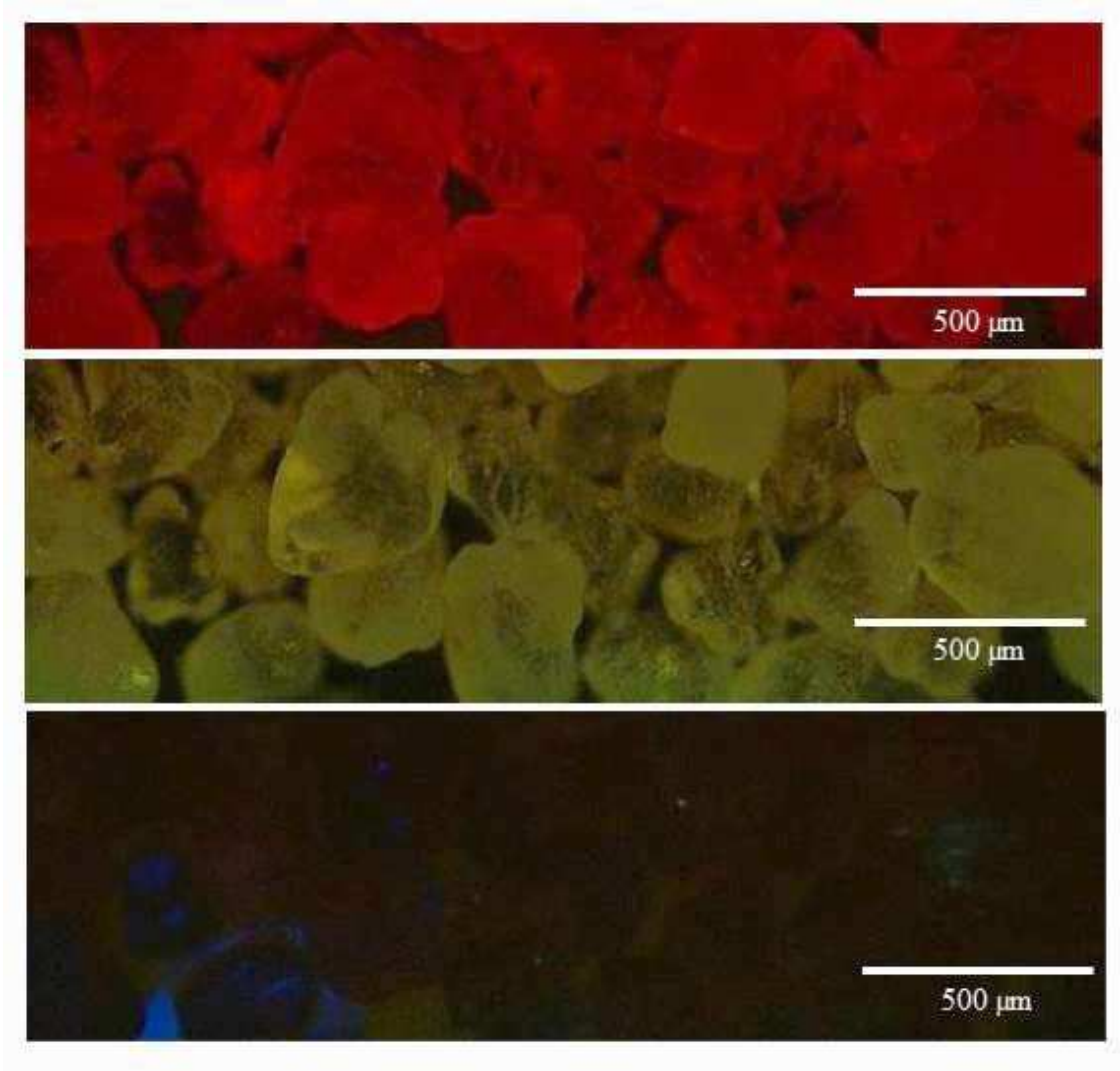

Figure 4.16 Fluorescence microscopy images of AWS soil grains prepared by adsorption using 3.45×10^{-6} g_{dye} $g^{-1}{}_{sand}$ nile red under $green_{ex}/red_{em}$, (top) room $light_{ex}/vis_{em}$ (middle) and UV_{ex}/vis_{em} (bottom). Image saturation, gamma and brightness have been digitally enhanced to the same degree for all images. (See section 4.3.6 for discussion).

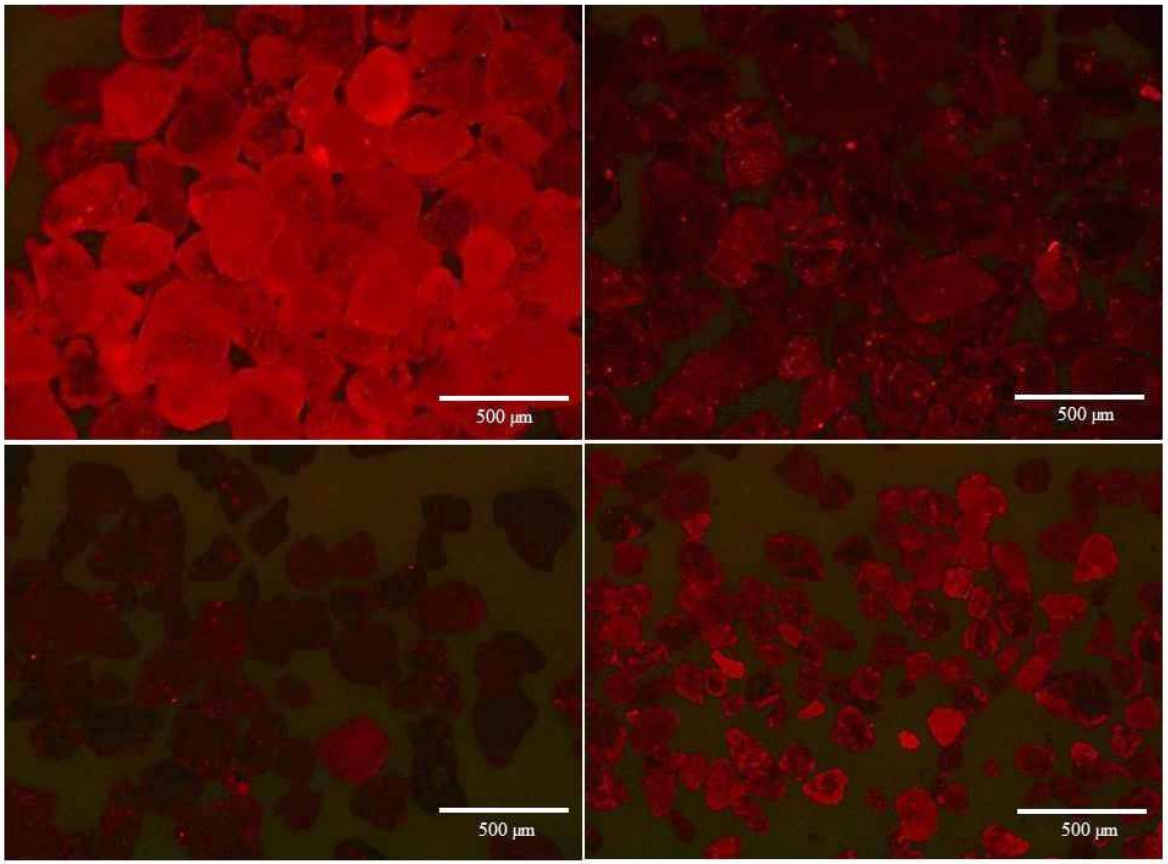

Figure 4.17 Fluorescence microscopy images of AWS (top left) and AU3 soil grains (top right) under green excitation light both prepared by adsorption using 3.45×10^{-6} g_{dye} g^{-1}_{sand}. Base stripped/basic surface (bottom left) and base stripped/acidic surface (bottom right) AU3 soil grains with same application of nile red. (Image saturation, gamma and brightness have been digitally enhanced to the same degree for all images). (See section 4.3.7 for discussion).

4.3.8. Nile red spectroscopy

The emission spectrum of nile red adsorbed on AU3 after correction for background (but without front face/90° correction) obtained using a Horiba Spectromax 4 fluorimeter is given in Figure 4.18. The spectrum is broad with a maximum at *ca.* 650 nm indicative of a highly polar environment and/or acidic sites, based on comparison with data from Zhang *et al.* (2011).

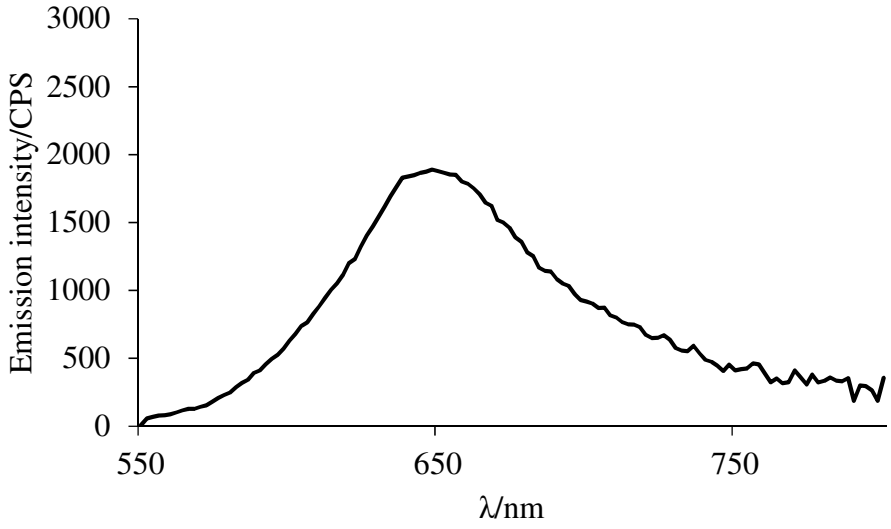

Figure 4.18 Emission spectrum of 6.91×10^{-6} g_{dye} g^{-1}_{sand} nile red on AU3 natural soil after background correction obtained using a Horiba Spectromax 4 fluorimeter.

4.4. Conclusions

Nile red fluorescent probe was applied to model and natural soils and examined as an *in-situ* fluorescent probe using fluorescence microscopy and fluorescence spectroscopy to establish if nile red can be used to identify localised areas of organics by visualisation of localised emission from the probe, and if it can give an indication of the general polarity of the nile red environment, and hence, by extension, the polarity of the organics at the soil grain surface.

The experiments described in this chapter show that it is possible to image emission of nile red after adsorption to soils. However, nile red gave results contrary to expectation in that areas of organics which could be seen to be dyed red by nile red under room light did not give intense emission. Instead, nile red adsorbed onto

uncoated AWS gave a more intense emission image than nile red adsorbed onto natural soils. Similarly, nile red on natural soil surfaces stripped of organics and made acidic gave a more intense emission than observed on basic surface, or natural unstripped soils. Furthermore soil auto-luminescence was identified as a serious interferent in imaging, with grains or parts of grain showing intense auto-luminescence, and this will probably be a problem for any luminescence imaging probe work.

Overall, the results show that, whilst it is possible to image nile red emission after adsorption to soils, several issues regarding emission intensity and the interference of auto-luminescence suggest that nile red may not be suitable for the study of soil surface polarity. However, the general methodology is promising and further exploration with alternative probes may prove to be more successful.

Chapter 5 Pyrene fluorescence probe as a tool for studying soil environmental polarity and viscosity

In this chapter experimental work is described which explores the use of the fluorescent probe pyrene as a potential in-situ tool to identify soil environment polarity and viscosity, using steady-state fluorimetry and time correlated single photon counting. Pyrene was applied, via either co-deposition or adsorption, to model soils deposited with amphiphilic and hydrocarbon organic compounds commonly found in natural soils. The results show that it is possible to obtain both steady-state and time resolved spectra in-situ from pyrene co-deposited with organics onto acid-washed sand or adsorbed directly onto soil. The spectra obtained showed variation in properties related to environment polarity and viscosity, although further work, with a wider range of natural soils, will be necessary to determine how well any of the spectral features correlate with soil hydrophobicity.

5.1. Background

Molecular probes, such as the polycyclic aromatic hydrocarbon, pyrene, are widely used in chemistry and biochemistry due to their sensitive response to their physical and chemical environment (Evans *et al.*, 2013). Fluorescent probes are useful because they can absorb light of a specific wavelength and will then emit at a different wavelength so they can be studied effectively (Johnson and Spence, 2010). Probes are commonly used to measure environment polarity and viscosity (Mazur and Blanchard, 2005; Evans *et al.*, 2013). Pyrene has a polarity dependent emission spectrum, and the kinetics and extent of formation of the excimer can be used to assess the viscosity of the environment in which it is present (Mazur and Blanchard, 2005).

Pyrene has been widely studied in many different environments (Birks *et al.*, 1963, 1964; Montalti *et al.*, 2006). Work by Borisover *et al.* (2006) considered the use of pyrene as a probe in effluent dissolved organic matter, and Ganaye *et al.* (1997) used pyrene to examine soil organics after extraction, but to date fluorescent probes have not been used to study soil environments *in-situ*. Investigating the nature of the organic layer present around soil grains via the application of fluorescent probes could help to improve understanding of the nature of the polarity and viscosity of the soil surface environment and if successful, may help to inform future soil management techniques.

Pyrene is a relatively long-lived polarity and viscosity probe. Pyrene monomer fluorescence shows a series of vibrational bands in the 370-410 nm range, the relative intensities of which vary with environment polarity (Kalyanasundaram and Thomas, 1977). The kinetics of pyrene excimer formation (420-600 nm) can be used to assess environment viscosity (Glushko *et al.*, 1981; Costa *et al.*, 2015). The unquenched pyrene monomer lifetime is *ca.* 650 ns, excimer formation occurs at the diffusion-controlled rate, and both monomer and excimer are quenched by oxygen (Birks *et al.*, 1963).

5.1.1. Organics

Organic compounds deposited on soil mineral or aggregate surfaces have long been recognised as a major factor in causing soil water repellency (Ma'Shum *et al*., 1988; Mainwaring *et al.*, 2004, 2013; Morley *et al.*, 2005). Water repellency does not correlate with the amount of organics present but with combinations of particular organics (Contreras *et al.*, 2008; de Blas *et al.*, 2013; Mainwaring *et al.*, 2013, Mao *et al.*, 2016). It is generally accepted that the main groups of compounds responsible are long-chain acids, alkanes and other organic compounds with hydrophobic properties (Ma'shum *et al*., 1988; Horne and McIntosh, 2000; Mainwaring *et al.*, 2013). In this work, stearic acid, octadecane and hexadecane were selected for application to model soils as representative of typical organics naturally found in soils (Deng and Dixon, 2002; Doerr *et al.*, 2005; Atanassova and Doerr, 2010; Mainwaring *et al.*, 2013). As well as their key properties such as bond type and melting points, consideration should be given to how organics pack on soil grain surfaces as this is likely to influence the environmental polarity and viscosity.

5.1.2. *Pyrene probe*

Pyrene is a polycyclic aromatic hydrocarbon, ($C_{16}H_{10}$, molecular weight 202.26 g/mol), consisting of four fused benzene rings (Figure 5.1) and has several key photophysical properties that make it an effective probe.

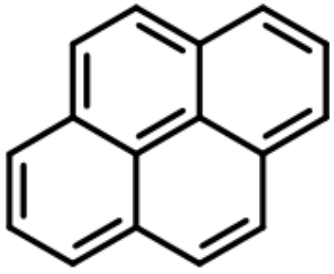

Figure 5.1 Structure of polycyclic aromatic hydrocarbon, pyrene.

The schematic diagram in Figure 5.2 explains the excitation and radiative and non-radiative decay pathways that can occur during the process of pyrene fluorescence. When a sample is excited by a light source the molecules become excited, forming excited monomer. Excimers (excited state dimers) form from one excited state

molecule and one ground state molecule. Excimers can decay radiatively, i.e. with emission of radiation, or non-radiatively.

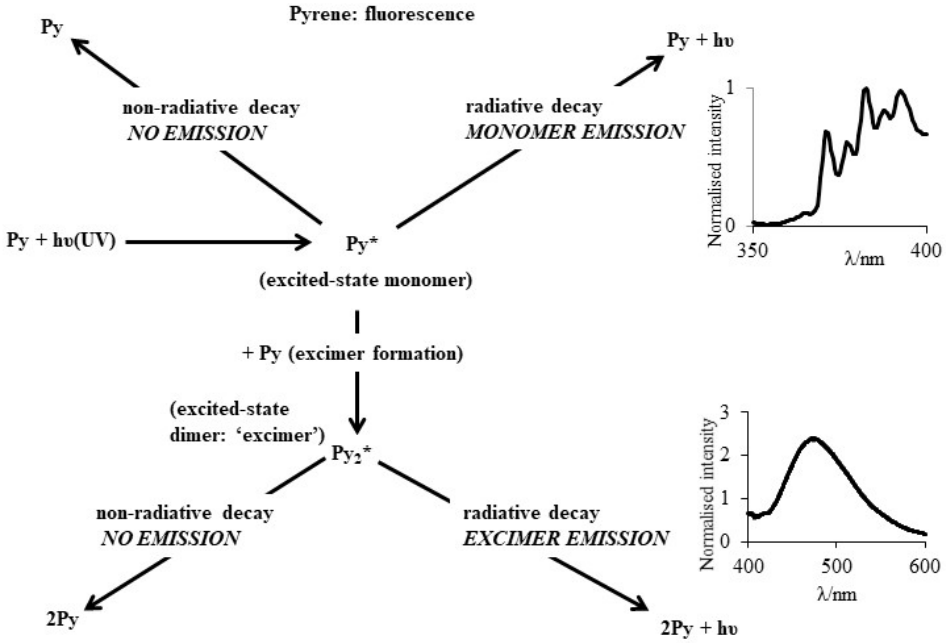

Figure 5.2 Schematic diagram showing processes of pyrene fluorescence.

A photon (hυ) of excitation light is absorbed, causing electrons to be raised to a higher energy and vibrational state (Py*). There are then several possible decay pathways:

(1) to emit a photon and return to ground state, giving monomer emission;

(2) to return to ground state without emitting a photon through non-radiative decay processes such as vibrational relaxation and internal conversion;

(3) to join with another pyrene molecule and form an excimer, (Py_2*), followed by excimer emission of a photon and return to ground state; or,

(4) for the excimer to return to ground state through non-radiative decay processes without emission of a photon.

While monomer emission shows vibrational structure, excimer emission is a broad band because the ground state product dissociates into two monomers.

As a general summary of the photophysics, in non-polar organics, due to the lowest energy absorption/emission being a symmetry forbidden transition, it is a long-lived probe, the unquenched pyrene monomer lifetime is *ca.* 650 ns, excimer formation occurs at the diffusion-controlled rate, and both monomer and excimer are quenched by oxygen (which is present in all studies in this chapter due to working under an air atmosphere) at the diffusion-controlled rate (Birks *et al.*, 1963).

5.1.3. Polarity

Pyrene monomer fluorescence produces a distinctive fine vibronic structure, the relative intensities of which are sensitive to environment polarity (Nakajima, 1971, 1974, 1976; Kalyanasundaram and Thomas, 1977). The five key peaks to consider occur at 372, 378, 383, 388 and 393 nm (Figure 5.3) and relate to different vibrational transitions within the molecule.

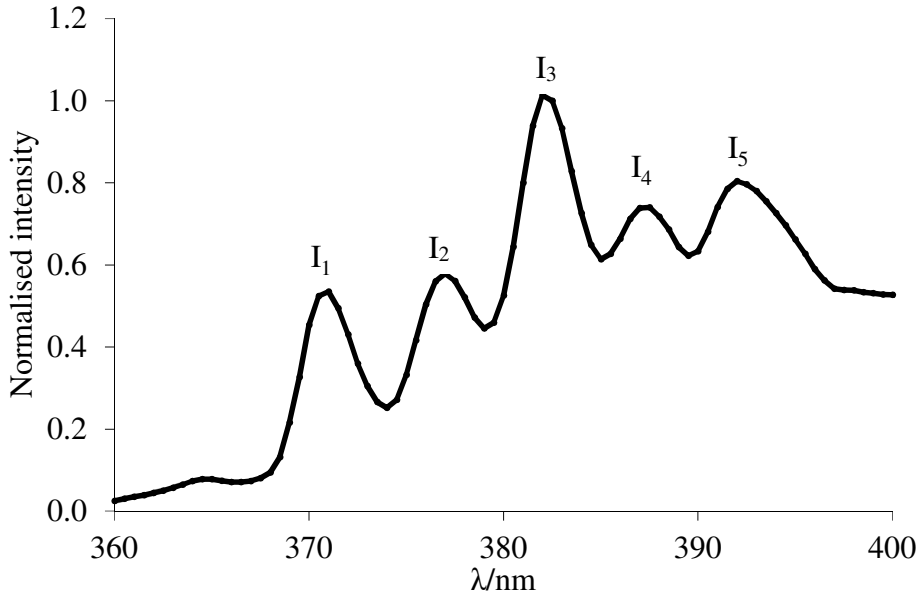

Figure 5.3 Example monomer emission from 1.01×10^{-3} M pyrene in ethanol solution showing the distinct five vibrational bands at approximately 372, 378, 383, 388 and 393 nm.

Due to the very high symmetry of pyrene, some of these bands are, for isolated molecules, quantum mechanically 'forbidden', notably band I_1 and I_4 and I_5, while

others are 'allowed', notably band I_3. The intensities of the allowed bands do not change much with environment but those of the forbidden bands change significantly. The presence of neighbouring molecules 'relaxes' the quantum mechanical rules so the formally forbidden bands become allowed and as the 'allowedness' increases with environment polarity so does the intensity of these bands. Therefore, the relative intensity of bands gives a measure of the polarity of the environment around the pyrene molecule. The key relationship to consider is the commonly used ratio between the first and third peaks (I_3/I_1), which is used as a measure of environment polarity (Kalyanasundarum and Thomas, 1977), where the smaller the value, the more polar the environment. For example, pyrene in hexane, which is a non-polar environment, has a I_3/I_1 ratio of 1.65, compared to the polar environment of pyrene in acetonitrile which has a I_3/I_1 ratio of 0.54 (Kalyanasundarum and Thomas, 1977).

5.1.4. Viscosity

Pyrene has also been used as a probe to study the viscosity of its surrounding environment (Glushko *et al.*, 1981; Gago *et al.*, 2008; Costa *et al.*, 2009; Costa *et al.*, 2015). Time correlated single photon counting (TCSPC) permits the study of static and dynamic excimer production, as pyrene molecules move together on the nanosecond timescale. The dynamic excimer production gives an indication of the ease of molecular mobility within the sample. In the following studies on model soils, TCSPC was used to assess the viscosity of the organic layer present around model soil grains by monitoring pyrene monomer and excimer formation. If pyrene can identify if organics are present in different forms e.g. liquid, soft solid, solid etc. then it could enhance understanding of how organics found on soils may be packed on the soil grain surface.

5.1.5. Research objectives

Model soils are useful tools for this work because they permit a controlled approach to the experimentation.

The studies described in this chapter aim to address the following two research questions:

1) Can pyrene be used as a tool to interrogate the polarity of the organic layers on both natural and model soils?

2) Can pyrene be utilised as a tool to interrogate the viscosity of the organic layers on both natural and model soils?

5.2. Materials and Methods

The following studies use acid-washed sand as a model soil and six natural sandy soils, AU2, AU3, NIC1, NIC2, LLAN1 and LLAN2 respectively. Sample origin and characteristics are given in Table 2.2.

5.2.1. Organics

Three of the four organics co-deposited on to model soils in this chapter are found to occur naturally in soils (Doerr *et al.*, 2000; Deng and Dixon, 2002; Atanassova and Doerr, 2010). Hexadecane and octadecane are two linear, highly non-polar, hydrocarbons of slightly different chain lengths, whilst stearic acid is an amphiphilic molecule with a long, non-polar hydrocarbon chain attached to a polar carboxylic acid 'head group'. Chemical characterisation and structures for these organics are shown in Table 5.1. Squalane, which is used in gas chromatography to provide a stationary surface liquid phase, is not found naturally on soils but was used, in preliminary work, to give a guaranteed liquid phase adsorbed onto soils.

Table 5.1 Chemical characterisation and structures for organics co-deposited onto model soils.

Organic	Chemical formula	Molecular weight/ g mol^{-1}	Melting point/ ^{o}C	Description	Structural formula
Hexadecane	$C_{16}H_{34}$	226.44	18.18[1]	Non-polar long chain hydrocarbon	
Octadecane	$C_{18}H_{38}$	254.49	28.17[1]	Non-polar long chain hydrocarbon	
Stearic acid	$C_{18}H_{36}O_2$	284.48	69.3[2]	Amphiphilic molecule - non-polar hydrocarbon chain with strongly polar carboxylic acid head group	
Squalane	$C_{30}H_{62}$	422.83	-38[3]	Long chain hydrocarbon with branching	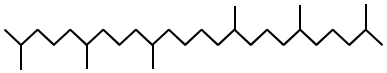

[1]Haynes (2015), [2]Lide (2005), [3]PubChem (2019)

5.2.2. Model soil studies: co-deposition of pyrene to acid-washed sand

The methodology for co-deposition was based on that previously used by Mainwaring *et al.* (2013). Pyrene was co-deposited on to acid-washed sand (AWS) with either: stearic acid, hexadecane, octadecane or squalane, from an ethanol solution, using a rotory evaporator to remove solvent. 5 g of AWS and 10 ml ethanol was placed in a round bottom flask, followed by 10 ml of *ca.* 10^{-3} M organic solution (concentrations used: 1.03×10^{-3} M stearic acid, 9.7×10^{-4} M octadecane, 9.1×10^{-4} M hexadecane and 1.03×10^{-3} M squalane) and 50 µl of 1.01×10^{-3} M pyrene in ethanol solution, which equates to a laydown of 1.01×10^{-7} $Mol_{pyrene}\ g^{-1}_{sand}$ and 2.04×10^{-5} $g_{pyrene}\ g^{-1}_{sand}$. Samples were placed on the rotary evaporator, lowered into a preheated water bath at 40 ºC with the rotary evaporator initially set to ~120 rpm. Once all visible liquid had evaporated the rotary speed was increased to 140 rpm for 15 minutes until the sand/soil was dry and flowing freely within the flask. Samples were stored in stoppered flasks.

Samples of AWS with organics deposited but without co-deposited pyrene were also prepared for use in the deposition method described in section 5.2.3.

5.2.3. Natural soil studies: adsorption of pyrene

5 g of soil was placed in a beaker with 25 ml distilled water and allowed to settle for 1 minute before adding 500 µl of 1.01×10^{-3} M pyrene in ethanol solution (1.01×10^{-7} $Mol_{pyrene}\ g^{-1}_{sand}$ and 2.04×10^{-5} $g_{pyrene}\ g^{-1}_{sand}$) (an amount chosen as a compromise between lowest possible probe concentration and adequate signal to background and/or noise ratio). The sample was covered to avoid evaporation and stirred for 3 hours, after this the sample was removed and filtered under vacuum. The sample was washed twice with deionised water and dried 'on the pump' for 15 minutes, then transferred to a Petri dish on the filter paper and allowed to dry overnight. A sample with pyrene added to AWS was also made, using the same method, as a blank.

5.2.4. Laydowns and 'monolayer equivalent' coverage

The quantity of pyrene deposited/adsorbed by the samples was considered. For model soils co-deposited with organics, the following maximum laydowns and concentrations were calculated assuming complete adsorption of organics (Table 5.2). It is important to note that throughout the text, laydowns are given assuming complete deposition of all the organic and probe added. While this is a very good

approximation for co-deposition with rotary evaporation to remove solvent (Mainwaring *et al.*, 2013; Hallin *et al.*, 2017) it might not be the case for adsorption onto soils from aqueous solution.

Table 5.2 Laydowns of organics and pyrene concentrations on model soils.

Co-deposited organic	Laydown/ $g_{org}\ g^{-1}_{sand}$	Pyrene concentration/ M
Stearic acid (SA)	5.86×10^{-4}	0.013
Hexadecane (HEX)	4.12×10^{-4}	0.019
Octadecane (OCT)	4.94×10^{-4}	0.016
Squalane (SQ)	8.71×10^{-4}	0.009

The stearic acid solution gives a laydown of 5.86 x 10^{-4} g_{SA} g^{-1}_{sand}. The specific surface area of AWS used is 292 ± 3 cm^2 g^{-1} (Hallin *et al.*, 2017). The specific surface area of stearic acid when adsorbed sticking vertically from the soil surface is 2.00×10^{-15} cm^2 $molecule^{-1}$ (Moore, 1972), with 5.86×10^{-4} g of stearic acid deposited per g of sand this gives a coverage *ca.* 21 nm thick which is *ca.* 8.5 monolayer equivalents (Hallin *et al.*, 2017). The ratio of pyrene to organics gives, assuming a bulk solution, pyrene concentrations of ~0.01- 0.02 M.

Table 5.3 Pyrene probe concentration, application rates and laydowns on model and natural soils.

Soils	Pyrene concentration/ M	Application/ µl	Soil/ g	Laydown/ $Mol_{pyrene}\ g^{-1}_{sand}$	Laydown/ $g_{pyrene}\ g^{-1}_{sand}$
AWS AU2 AU3 NIC1 NIC2 LLAN1 LLAN2	1.01×10^{-3}	50	1	1.01×10^{-7}	2.04×10^{-5}

Assuming complete adsorption of pyrene to the soil grain surface 50 µl of 1.01×10^{-3} M pyrene added to 1 g of soil gives a laydown of 1.01×10^{-7} $Mol_{pyrene}\ g^{-1}_{soil}$ and 2.04×10^{-5} $g_{pyrene}\ g^{-1}_{soil}$ (Table 5.3).

Stearic acid is an amphiphilic molecule with a long non-polar hydrocarbon chain and polar carboxyl acid head. Current thought (Chen and Frank, 1989; Shimoaka *et al.*,

2012) is that, when stearic acid is deposited onto a surface under ambient air conditions, the polar head is attracted to the surface causing the heads of the molecule to pack head down with long hydrocarbon chains extending upwards, as illustrated in Figure 5.4.

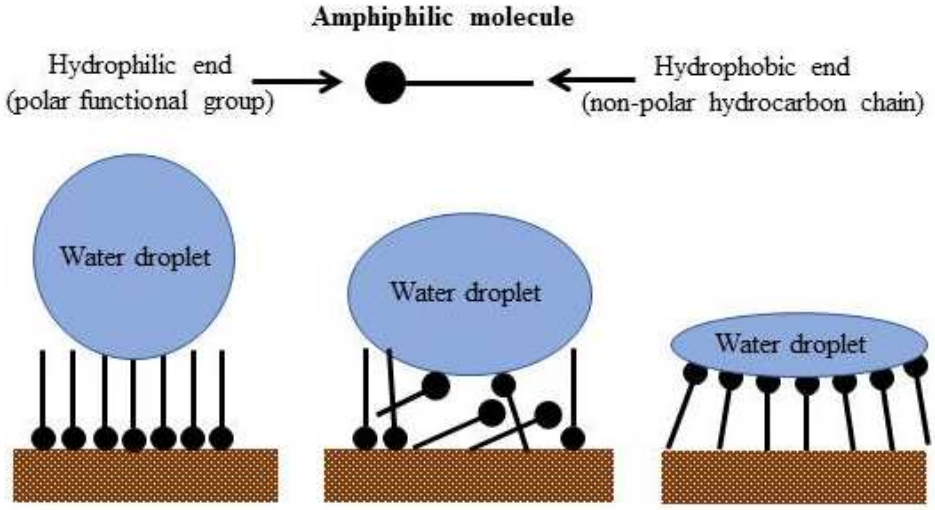

Figure 5.4 Simplified schematic of orientation of an amphiphilic molecule (such as stearic acid) before and during contact with a water droplet – redrawn from Doerr *et al.* (2000) (a) polar head attracted head down towards silica surface with hydrocarbon chains extending upwards, (b) commencement of reorientation of amphiphilic molecule due to interaction with water, (c) reorientation of amphiphilic molecules to water creating a wettable, polar environment.

5.2.5. Fluorescence spectroscopy

A Horiba Spectromax 4 fluorimeter with front face accessory was used, with samples held in 1 or 2 mm path length quartz cuvettes (Figure 5.5). A 337 nm CWL (10 nm FWHM) bandpass interference filter (Edmund Optics) was used to reduce scattered excitation light (without this filter, spectra showed too high a background signal to be useful) (Figure 5.6). Spectra were corrected for detector response using files provided by the manufacturer. For this particular instrument front face and 90° detection gave slightly different spectra for the same sample, for 90° detection compared to front face detection, with a general increase in relative intensity with wavelength observed in the front face measurement. The reason for this is not clear, but where spectra have been corrected for this, using data from samples recorded using both front face and 90° detection, this is stated in the text. After this correction

spectra are directly comparable to most corrected spectra in the literature where 90° detection and detector correction is usually used.

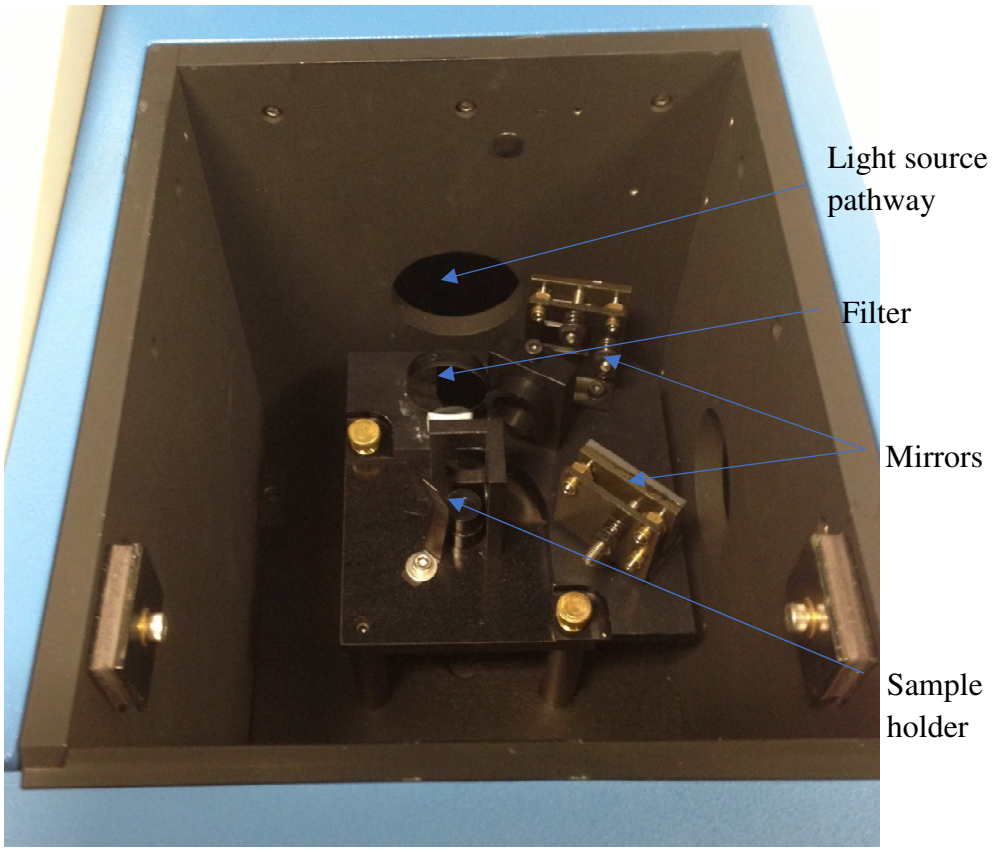

Figure 5.5 Horiba Spectromax 4 fluorimeter and filter set-up.

Several parameters will influence the measurements made using the fluorimeter, including: excitation wavelength, excitation and emission slit widths, increment size and integration time. The significance of each of these is discussed in greater detail in chapter 3.

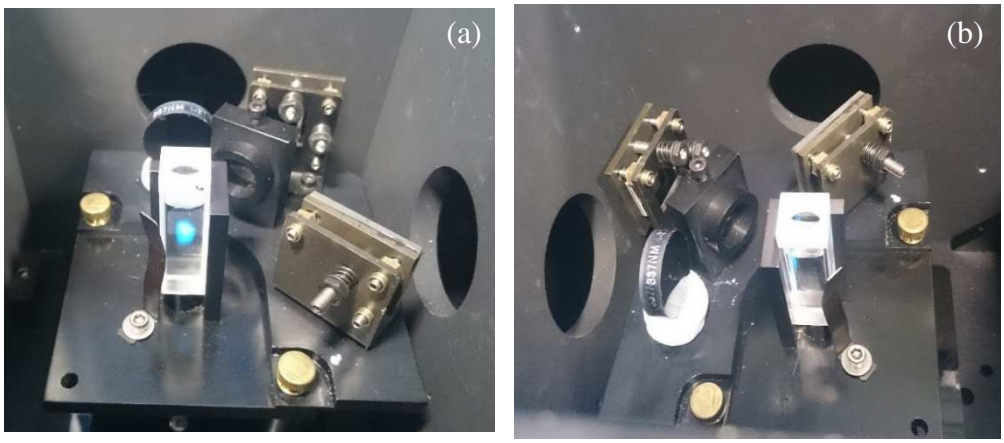

Figure 5.6 a) Placement of 337 nm pyrene bandpass interference filter b) shows pyrene excited by excitation source in front facing set-up.

5.2.6. Fluorescence lifetime studies: Time correlated single photon counting (TCSPC): University of Coimbra, Portugal

Following discussion with Dr. Peter Douglas, a series of samples were prepared by the author for emission lifetime studies to be carried out at University of Coimbra, by Dr. Douglas, (in collaboration with Dr. J. Pina and Prof. S. Seixas de Melo), on pyrene co-deposited with either hexadecane, octadecane or stearic acid, onto AWS, in order to evaluate pyrene as a probe for molecular mobility within the organic layer around the AWS grains. The following instrument set-up description was provided by Dr. J. Pina.

Fluorescence decays were measured using a home-built time correlated single photon counting (TCSPC) apparatus. The excitation source was a Horiba-Jobin-Yvon nanoled with l_{exc}= 337 nm with the 337 nm CWL (10 nm FWHM) bandpass interference filter used for fluorimetry above. Emission at 90° geometry was collected through a double subtractive Oriel Cornerstone 260 monochromator and detected by a Hamamatsu microchannel plate photomultiplier (R3809U-50). A longpass glass colour filter with transmittance onset at 375 nm was used in the emission optical path to discard scattered light from the sample. Signal acquisition and data processing was performed employing a Becker & Hickl SPC-630 TCSPC module. The fluorescence decays and the instrumental response function (IRF) were collected using a time scale of 1024 channels with 400 ps/channel. The soil samples were slightly pressed in a circular (10 mm) powdered sample holder well (used without quartz window) and were positioned at a 45º angle with respect to the TCSPC emission path to avoid interference from the excitation source. Experiments were carried out at 19-20 °C. Deconvolution of the fluorescence decay curves was performed using the modulating function method as implemented by Striker *et al.* (1999) in the SAND program.

5.3. Results and discussion

As mentioned in the introduction to this chapter (section 5.1.3), the emission spectrum of pyrene shows five distinctive bands corresponding to transitions to different ground state vibrational states, at 372, 378, 383, 388 and 393 nm respectively (Figure 5.3) (Kalyanasundarum and Thomas, 1977). In the following studies, the three vibronic bands of interest are I_1 and I_3. The ratios of these vibrational bands are used to assess environment polarity (Kalyanasundaram and Thomas, 1977). In non-polar environments such as hexane, Kalyanasundaram and Thomas (1977) found band I_3 to be stronger than I_1, by contrast, in strongly polar environments such as acetonitrile, they found band I_1 to be much stronger than band I_3.

5.3.1. Absorption spectrum of pyrene

The absorption spectrum of pyrene (Figure 5.7) shows the amount of light absorbed by the sample as a function of wavelength. The absorption spectrum was important to establish a suitable concentration of pyrene in ethanol solution that could be applied to samples so that the emission spectra produced would be measurable and within the detection parameters of the instrument. As previously mentioned, the key fingerprint region for pyrene emission occurs between ~ 370-395 nm. A useful feature of pyrene is the low intensity absorbance for S_0 to S_1 due to the symmetry forbidden transition, since this effectively allows a big spectral gap between the absorbance and excitation spectra. Furthermore, the symmetry forbidden nature of the transition results in a long fluorescence lifetime which allows efficient excimer formation.

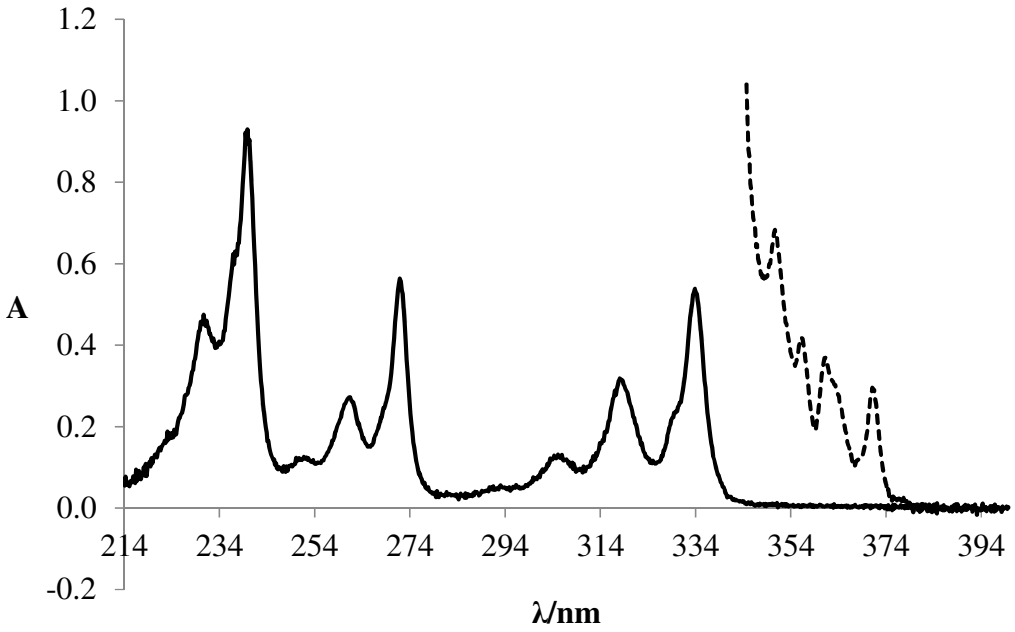

Figure 5.7 Pyrene absorption spectra showing difference between pyrene concentration of 1.01×10^{-5} M (solid line) and 1.01×10^{-2} M solutions (dashed line) in 10 mm path length cell.

5.3.2. Preliminary experiments for instrument set-up

Preliminary fluorimeter tests were carried out to inform decisions on the optimum settings for the following instrument parameters: excitation wavelength, excitation and emission slit widths, increment size, and integration time. Consideration was given to sample concentration so that it was within acceptable linearity parameters (counts per second) for the instrument (above 1.0×10^{-4} CPS and below 2.0×10^{6} counts per second).

5.3.2.1. Excitation wavelength

Excitation at 337 nm was chosen because it is on the edge of a strong absorption band (Figure 5.7) and because of the availability of a 337 nm bandpass interference filter which was very effective in reducing an otherwise high background due to excitation light scatter.

5.3.2.2. Excitation slit widths

Excitation slit widths control the signal-to-noise ratio. With a 337 nm filter it was possible to use very wide excitation slits of 16 nm to maximise excitation intensity and hence signal to noise ratio.

5.3.2.3. Emission slit widths

Large emission slit widths give increased signal-to-noise (S/N) but decreased spectral resolution, whereas small emission slit widths give higher spectral resolution but decreased light intensity and S/N ratio. Because of the narrowness of the emission bands in the pyrene spectrum, a narrow band width was necessary, with 0.5 nm chosen as the best compromise between resolution and signal to noise ratio.

5.3.2.4. Integration time

Integration time is the length of time allowed for photons to be collected by the detector before moving on for processing. A long integration time will give higher S/N, i.e. a much 'smoother' spectrum compared to a short integration time but will result in a very long time for collection of a spectrum. For natural soil spectra an integration time of 20 s was used.

5.3.2.5. Increment (step size)

The instrument used has a stepper motor-controlled monochromator and the increment dictates the monochromator step size, in nm, between each data point over the course of the wavelength range measured. A smaller step size will give better spectral resolution but collecting the spectrum will take longer. An increment of 0.75 nm was chosen for natural soil sample spectra.

5.3.3. Pyrene probe concentration and excimer formation

A series of different concentration pyrene in ethanol solutions were run from 10^{-5} M up to 10^{-2} M (see Figure 5.8). It was important that the sample concentration was within the detectable limit of the fluorimeter so that spectra results remained below 2.0×10^{6} counts per second (CPS) and above 1.0×10^{-4} CPS, as the latter would produce a weak signal. Figure 5.8 shows the increase in excimer emission as pyrene concentration is increased.

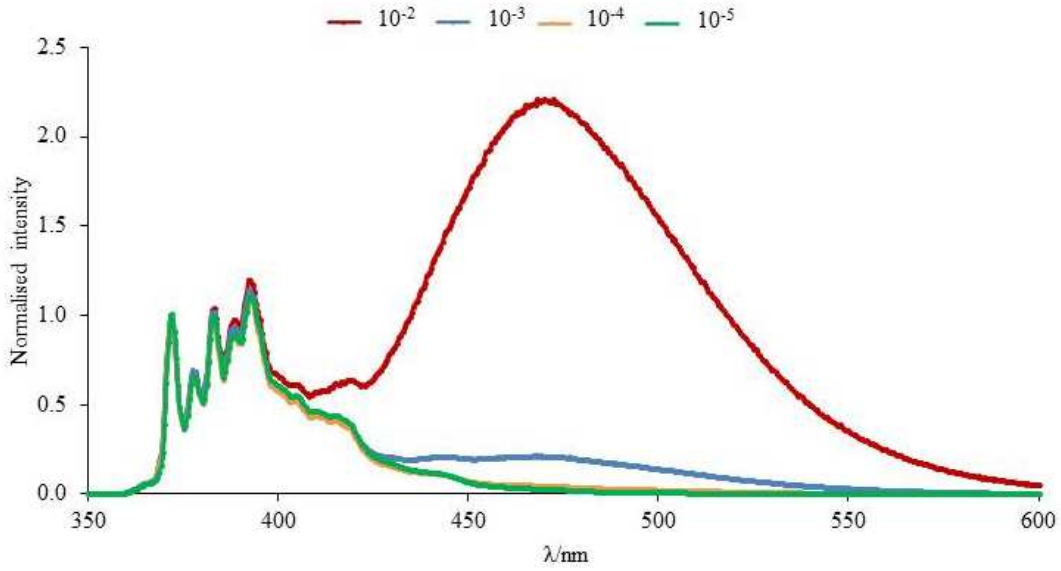

Figure 5.8 Variable concentrations from 10^{-2} to 10^{-5} M pyrene in ethanol solutions demonstrating the formation of excimer using front face attachment.

5.3.4. Model soils: steady state fluorescence

Figure 5.9 shows fluorescence from pyrene when co-deposited with squalane (m.pt -38 ºC), stearic acid (m.pt 69 ºC), hexadecane (m.pt 18 ºC), or octadecane (m.pt 28 ºC) onto AWS. Total emission intensities are comparable, differing only by a factor ~2; all spectra show the fine structure of monomer emission around 360-420 nm and broad excimer emission across ~420–600 nm, although the relative intensities of monomer (~360-420 nm) to excimer (420-600 nm) emission differ (Table 5.4). The ratio of bands I_3/I_1 in monomer emission increases in order of decreasing polarity from stearic acid > hexadecane ~ octadecane > squalane.

Table 5.4 I_3/I_1 peak height ratios for pyrene co-deposited with (a) stearic acid 5.86×10^{-4} g_{SA} g^{-1}_{sand}, [pyrene] = 0.013 M (b) hexadecane 4.12×10^{-4} g_{HEX} g^{-1}_{sand}, [pyrene] = 0.019 M (c) octadecane 4.94×10^{-4} g_{OCT} g^{-1}_{sand}, [pyrene] = 0.016 M (d) squalane 8.71×10^{-4} g_{SQ} $g^{-1}_{sand,}$ [pyrene] = 0.009 M.

Organic	I_3:I_1 ratio	Excimer: monomer ratio*
Stearic acid	1.33	1.00
Hexadecane	1.71	5.18
Octadecane	1.47	6.27
Squalane	1.89	1.26

*An estimation of the excimer to monomer ratio was obtained by integrating the area from 350-420 for the monomer and 420-600 nm for the excimer.

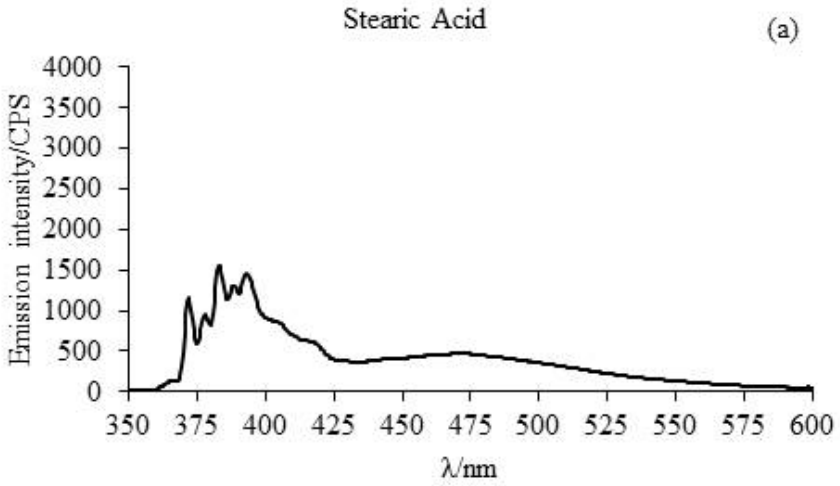
Stearic Acid
(a)
Emission intensity/CPS
λ/nm

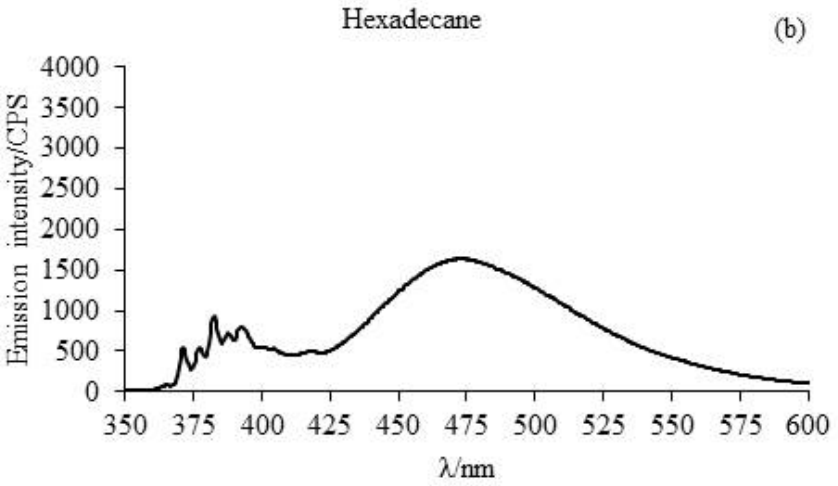
Hexadecane
(b)
Emission intensity/CPS
λ/nm

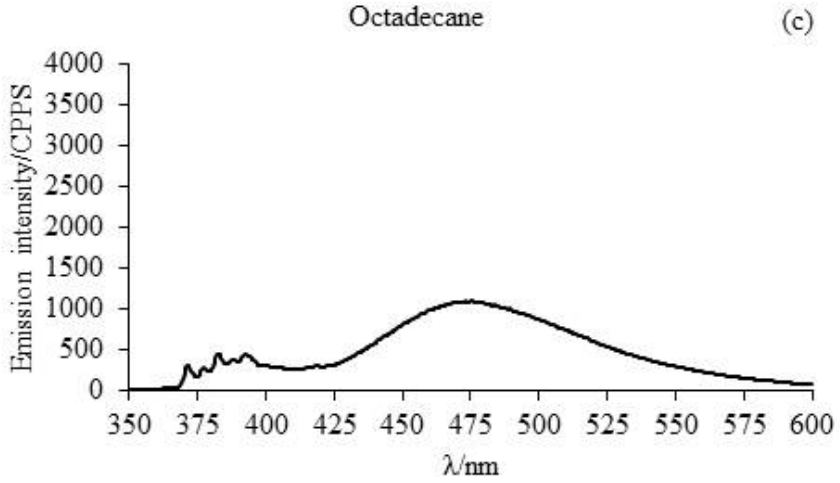
Octadecane
(c)
Emission intensity/CPPS
λ/nm

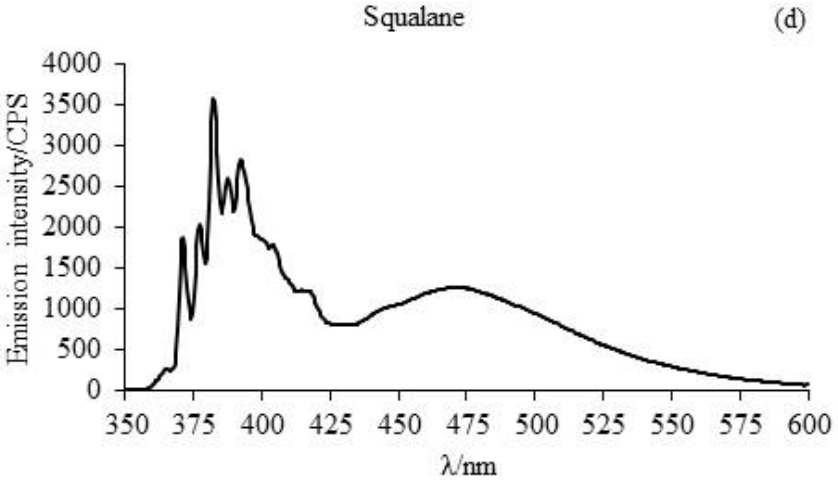
Squalane
(d)
Emission intensity/CPS
λ/nm

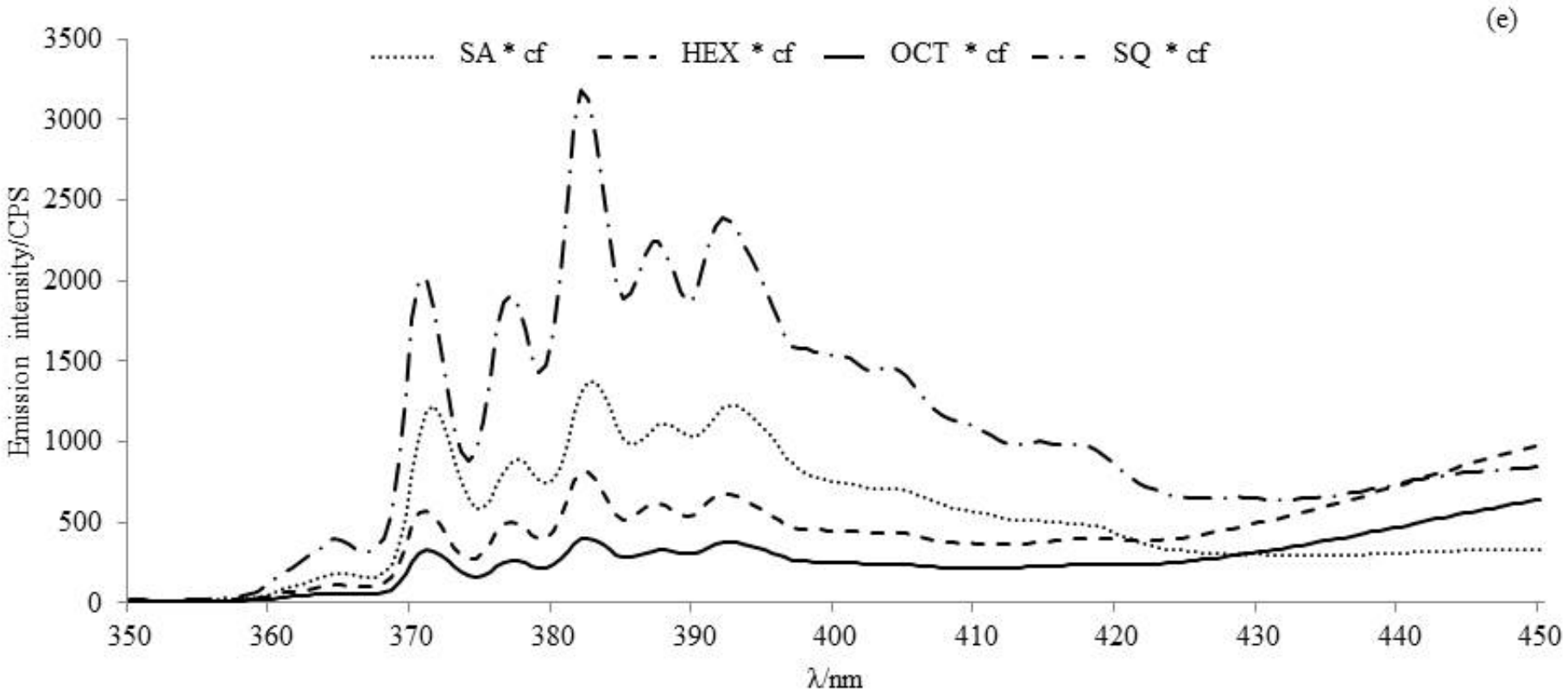

Figure 5.9 Emission spectra of pyrene co-deposited on AWS, with: (a) stearic acid 5.86×10^{-4} g_{SA} g^{-1}_{sand}, [pyrene] = 0.013 M (b) hexadecane 4.12×10^{-4} g_{HEX} g^{-1}_{sand}, [pyrene] = 0.019 M (c) octadecane 4.94×10^{-4} g_{OCT} g^{-1}_{sand}, [pyrene] = 0.016M (d) squalane 8.71×10^{-4} g_{SQ} $g^{-1}_{sand,}$ [pyrene] = 0.009 M (e). All corrected for front face (*cf).

5.3.5. Time-resolved studies of pyrene on model soils

Time resolved emission curves for pyrene co-deposited with hexadecane, octadecane and stearic acid, measured at wavelengths corresponding to primarily monomer emission (380 nm) and primarily excimer emission (500 nm) are presented in Figure 5.10a-c and Table 5.5 gives kinetic analysis using global best fits for both wavelengths.

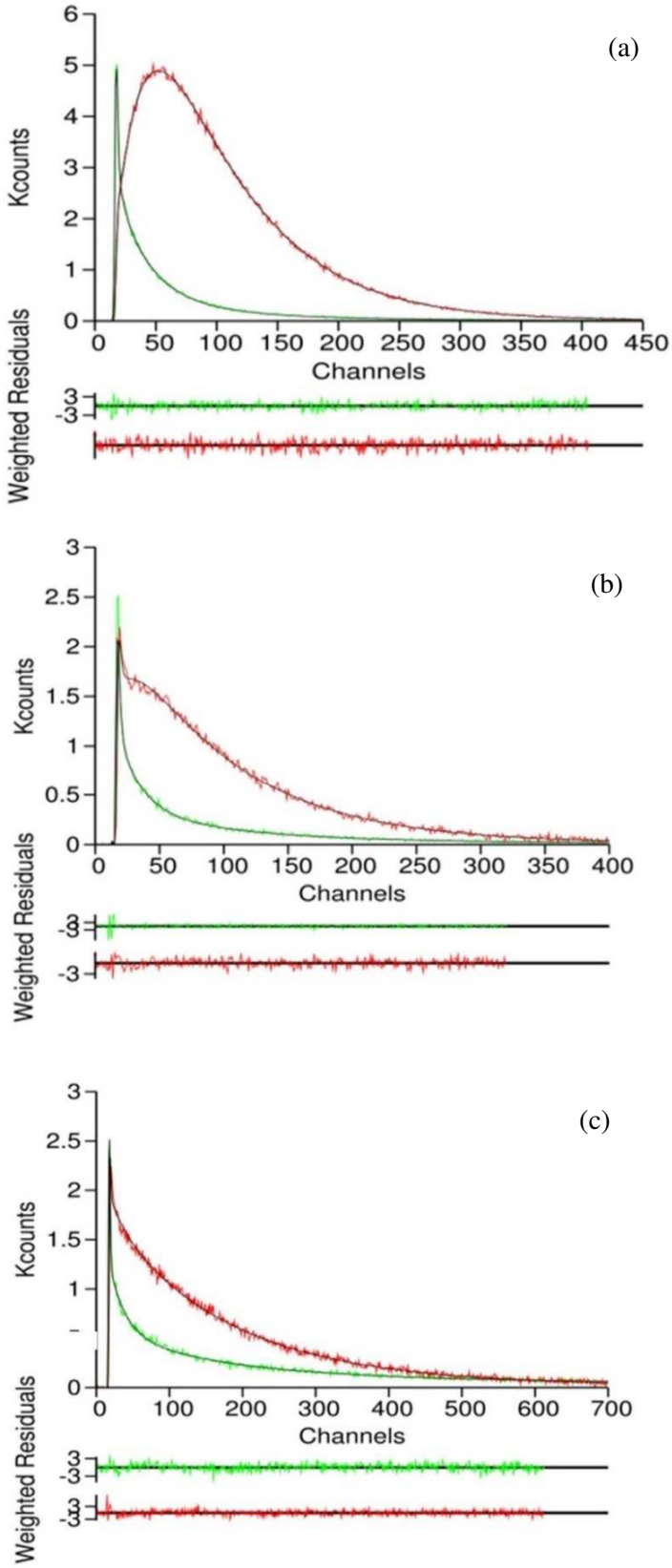

Figure 5.10 Emission decay curves of pyrene co-deposited on AWS with: (a) hexadecane 4.12×10^{-4} g_{HEX} g^{-1}_{sand}, [pyrene] = 0.019 M (b) octadecane 4.94×10^{-4} g_{OCT} g^{-1}_{sand}, [pyrene] = 0.016 M (c) stearic acid 5.86×10^{-4} g_{SA} g^{-1}_{sand}, [pyrene] = 0.013 M. Monomer emission (λ = 380 nm) is shown in green and excimer emission (λ = 500 nm) in red. Excitation wavelength was run at 337 nm and used a 337 nm bandpass interference filter.

Table 5.5 Fluorescence decay times (τ_i) and pre-exponential factors (a_i) obtained from the global analysis of the fluorescence decays of pyrene in ethanol co-deposited with organics on acid-washed sand.

Organic in ethanol on AWS	**λ_{em} /nm**	**τ_1 /ns**	**τ_2 /ns**	**τ_3/ns**	**τ_4 /ns**	**a_1**	**a_2**	**a_3**	**a_4**	**χ^2**
Stearic acid	380	8.68	-	66.48	607.80	0.565	-	0.367	0.068	1.20
	500					0.129	-	0.856	0.015	1.23
Hexadecane	380	1.56	10.20	27.72	55.72	0.222	0.619	0.116	0.043	1.17
	500					0.042	-0.851	0.958	-0.004	1.05
Octadecane	380	0.60	7.04	33.88	142.44	0.872	0.091	0.033	0.005	2.33
	500					0.660	-0.118	0.335	0.005	1.08

Data fitted to $\mathbf{I = a_1e^{-(t/\tau_1)} + a_2e^{-(t/\tau_2)} + a_3e^{-(t/\tau_3)} + a_4e^{-(t/\tau_4)}}$
where **I** is emission intensity; **τ**, lifetime; **a**, the pre-exponential factor i.e. the initial intensity for that decay component, and χ^2 is a measure of the quality of fit, the lower χ^2 the better the fit). Small **a** and **τ** values indicate that the process makes a small contribution to the total emission intensity, a positive **a** value indicates a kinetic decay while a negative **a** value indicates a 'grow-in'.

The difference in behaviour is striking: hexadecane, a liquid at the temperature of measurement, shows a very strong 'grow-in' at 500 nm (indicated by the negative value of $\mathbf{a}_3$) corresponding to kinetic formation of excimer, i.e. formation by molecular diffusion of pyrene; stearic acid, which is a solid at temperature of measurement shows only static excimer emission, i.e. there is no molecular diffusion of pyrene and excimer emission is only from those dimers already present in the sample; whereas octadecane which is a soft wax at the measurement temperature, gives both kinetic and static excimer formation. In terms of the aims of this chapter, the data clearly shows a difference in pyrene molecular mobility within the organics adsorbed at the soil surface consistent with a change from liquid through soft wax to rigid solid in going from hexadecane to octadecane to stearic acid. Overall, as the environments moves from liquid, to soft, to hard wax, a decrease in dynamic excimer formation and an increase in static excimer formation can be seen.

When considering the analysis given in Table 5.5 it is important to note: 1) some overlap of monomer and excimer emission bands at 380 and 500 nm can be expected, so at either wavelength there will be small contributions from emission from the other species; 2) the experiments were carried out in an air-equilibrated environment where an oxygen concentration of *ca.* 2×10^{-3} M in the organics (Montalti *et al.*, 2006) could be expected, and therefore oxygen quenching of both monomer and excimer emission (Birks *et al.*, 1963) is expected; 3) in non-polar organics, the unquenched pyrene monomer lifetime is *ca.* 650 ns, the unquenched excimer lifetime *ca.* 65 ns, and both excimer formation and oxygen quenching occur at approximately the diffusion controlled rate. Without a much more detailed kinetic study, working with different excitation/emission wavelengths, varying organic and pyrene laydowns, and studies in oxygen or nitrogen atmospheres, rather than air, (work beyond the scope of this preliminary assessment of the potential of pyrene as a probe in hydrophobicity studies), it is difficult to make a definite statement of the nature of these decay processes, however some tentative interpretations can be offered.

5.3.5.1. Hexadecane

Considering the hexadecane data first. Emission with $\boldsymbol{\tau}_1$, $\boldsymbol{\tau}_2$ and $\boldsymbol{\tau}_4$ are assigned to decay from three different monomer environments: one quenched very quickly, $\boldsymbol{\tau}_1$,

with no excimer production; τ_4 is relatively long lived and may involve excimer production (although the excimer grow-in is very weak and may just be a fitting artefact); and, τ_2 which accounts for 62 % of monomer decay and generates excimer. τ_3 was assigned to excimer decay because this is the major decay component at 500 nm.

The concentration of pyrene in hexadecane is 0.0189 M and taking the viscosity of hexadecane at 20 °C to be 3.474 mPa s this gives a diffusion controlled observed pseudo first order rate constant, of 3.5×10^7 s^{-1} for monomer decay by excimer formation ($k = 8kT/3\eta\times[py]$, where k is rate constant, k is Boltzmann constant, T is temperature, η is viscosity and [py] is concentration of pyrene, Birks *et al.*, 1964). The excimer lifetime in hexadecane is 27.72 ns, which if reduced from *ca.* 65 ns due to oxygen quenching, indicates a pseudo first order oxygen quenching rate constant of *ca.* 3.6×10^7 s^{-1}. Assuming the same value for monomer quenching gives an estimated monomer lifetime when quenched by both pyrene and oxygen of *ca.* 14 ns, rather longer than the 10.2 ns observed, possibly suggesting some other monomer quenching process.

The concentration of oxygen is of the order of 2×10^{-3} M, and because of the small molecular size, oxygen quenching is usually somewhat faster than other diffusional quenching, but even so, it is still expected oxygen quenching will not be much faster than 1×10^7 s^{-1}. This gives an estimated lifetime of *ca.* 20 ns, which is twice that observed, suggesting some other monomer quenching process. Similarly, the excimer lifetimes in hexadecane and octadecane are much shorter than the unquenched values of *ca.* 65 ns reported by others, suggesting some other excimer quenching process, although the nature of these processes is at present unknown.

5.3.5.2. Octadecane

In octadecane there is a mixed picture with excimer being formed both *statically* and *dynamically*. Analysis at 380 nm shows a rapid monomer decay τ_1 accounting for *ca.* 87 % of the monomer, with a smaller fraction, 9 %, of monomer ground state quenched to generate excimer, τ_3. There is also a very small fraction 0.5 % giving a long-lived emission, τ_4. Measuring at the predominantly excimer wavelength of 500 nm gives two excimer decays, one very short but accounting for *ca*. 2/3rds of excimer decay, τ_1, another with a lifetime of 34 ns, accounting for the other third.

At first sight it is surprising to see regions which are fluid enough in the octadecane layers for pyrene diffusion, but pyrene is present at quite a high concentration and it may act to reduce the melting point of the octadecane solvent enough for regions of octadecane/pyrene to remain liquid even at *ca.* 8 ^{o}C below the octadecane melting point (28 ^{o}C). Further studies with lower pyrene concentrations will be necessary to explore this.

5.3.5.3. Stearic acid

In stearic acid, which gives a much lower excimer emission than hexadecane, no *dynamic* excimer formation is seen, i.e. all excimer is produced by *static* quenching of monomer and is complete within a few hundred ps. The analysis gives two monomer decays; τ_1 which is very rapid; and τ_4 which is much longer, approaching that of unquenched monomer, which may be due to isolated monomer with neither oxygen nor pyrene quenching. Excimer decay shows two predominate processes, one fast, τ_1, the other, τ_3, is much longer and at 66.48 ns comparable to the unquenched excimer lifetime (Birks *et al.*, 1963, 1964). These results point to a highly viscous/solid environment.

These exploratory studies on model soils show that pyrene can be utilised as a tool to assess the viscosity of the organic layer surrounding sand grains. It should be possible to extend and apply the technique to natural soils.

5.3.6. Pyrene adsorbed to natural soils

Figure 5.11 shows spectra for pyrene adsorbed onto bare AWS and AWS with organics (stearic acid, hexadecane). Figures 5.12-14 show spectra for pyrene adsorbed onto natural soils. It is interesting to note that AWS itself, without any organic layer, either does not adsorb pyrene, or if it does the adsorbed pyrene is non-emissive. This is useful because it removes the need to worry about any emission contribution from pyrene adsorbed onto any uncoated sand surface, all emission is from pyrene either absorbed within the organic layer, on the organic/air interface, or at the organic/inorganic interface. This is a distinct advantage of using pyrene as a probe compared to nile red.

When pyrene is either co-deposited with, or adsorbed on, AWS with stearic acid, the I_3/I_1 band ratio are similar, all > 1 indicating a relatively non-polar environment. With hexadecane the I_3/I_1 band ratio for adsorbed pyrene is lower than co-deposited,

suggesting a more polar environment in the co-deposited samples compared to the adsorbed samples.

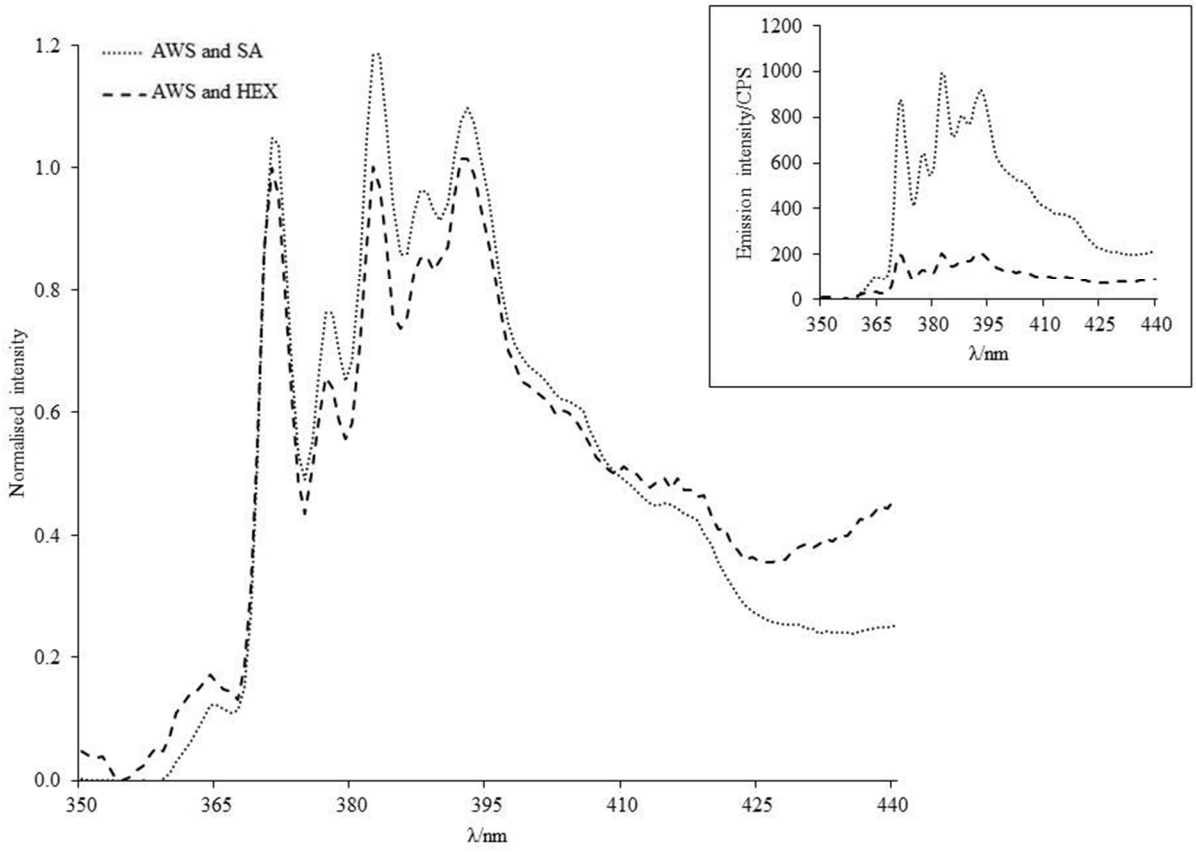

Figure 5.11 AWS and pyrene co-deposited with hexadecane (4.12×10^{-4} g_{HEX} g^{-1}_{sand}) and stearic acid (5.86×10^{-4} g_{SA} g^{-1}_{sand}) normalised fluorescence spectra and insert emission intensity spectra fluorescence spectra. Excitation 337 nm, filter 337 nm, excitation slits 15 nm, 360-410 emission, integration 20 seconds, increment 0.75 nm, emission slits 0.5 nm. Background and front face corrected. Pyrene at 1.01×10^{-7} mol_{py} g^{-1}_{sand}, 2.04×10^{-5} g_{py} g^{-1}_{sand}.

For the natural soils the intensities of emission vary. Emission intensity does not correlate with amount of organic, since AU2, which has a higher organic content than AU3, gives a lower emission intensity than AU3, and the AWS with SA sample gives a much higher signal than the natural soil even though it has much less organic present.

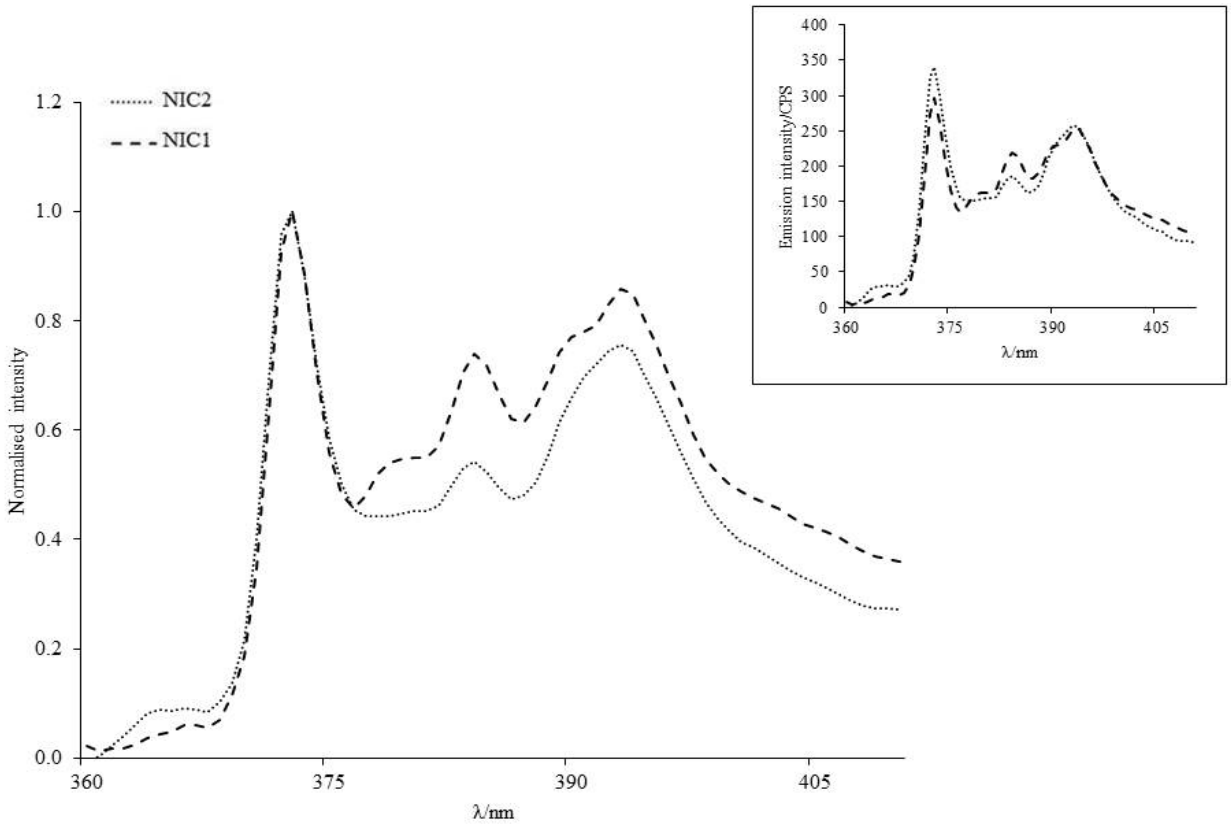

Figure 5.12 NIC1 and NIC2 normalised summed fluorescence spectra and insert NIC1 and NIC2 summed emission intensity fluorescence spectra. Excitation 337 nm, filter 337 nm, excitation slits 15 nm, 360-410 emission, integration 20 seconds, increment 0.75 nm, emission slits 0.5 nm. Background and front face corrected. Pyrene at 1.01×10^{-7} mol_{py} $g^{-1}{}_{sand}$, 2.04×10^{-5} g_{py} $g^{-1}{}_{sand}$.

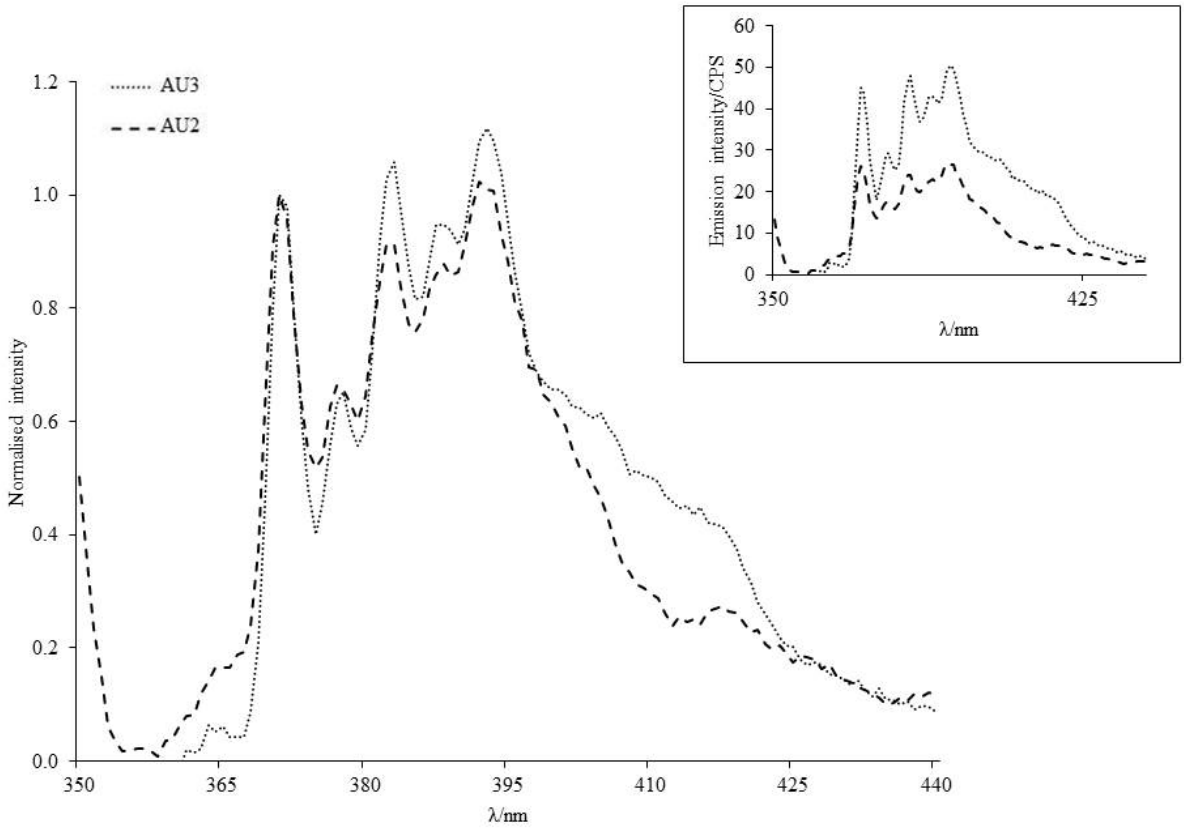

Figure 5.13 AU2 and AU3 normalised summed fluorescence spectra and insert AU2 and AU3 summed emission intensity fluorescence spectra. Excitation 337 nm, filter 337 nm, excitation slits 15 nm, 360-410 emission, integration 20 seconds, increment 0.75 nm, emission slits 0.5 nm. Background and front face corrected. Pyrene at 1.01×10^{-7} mol_{py} g^{-1}_{sand}, 2.04×10^{-5} g_{py} g^{-1}_{sand}.

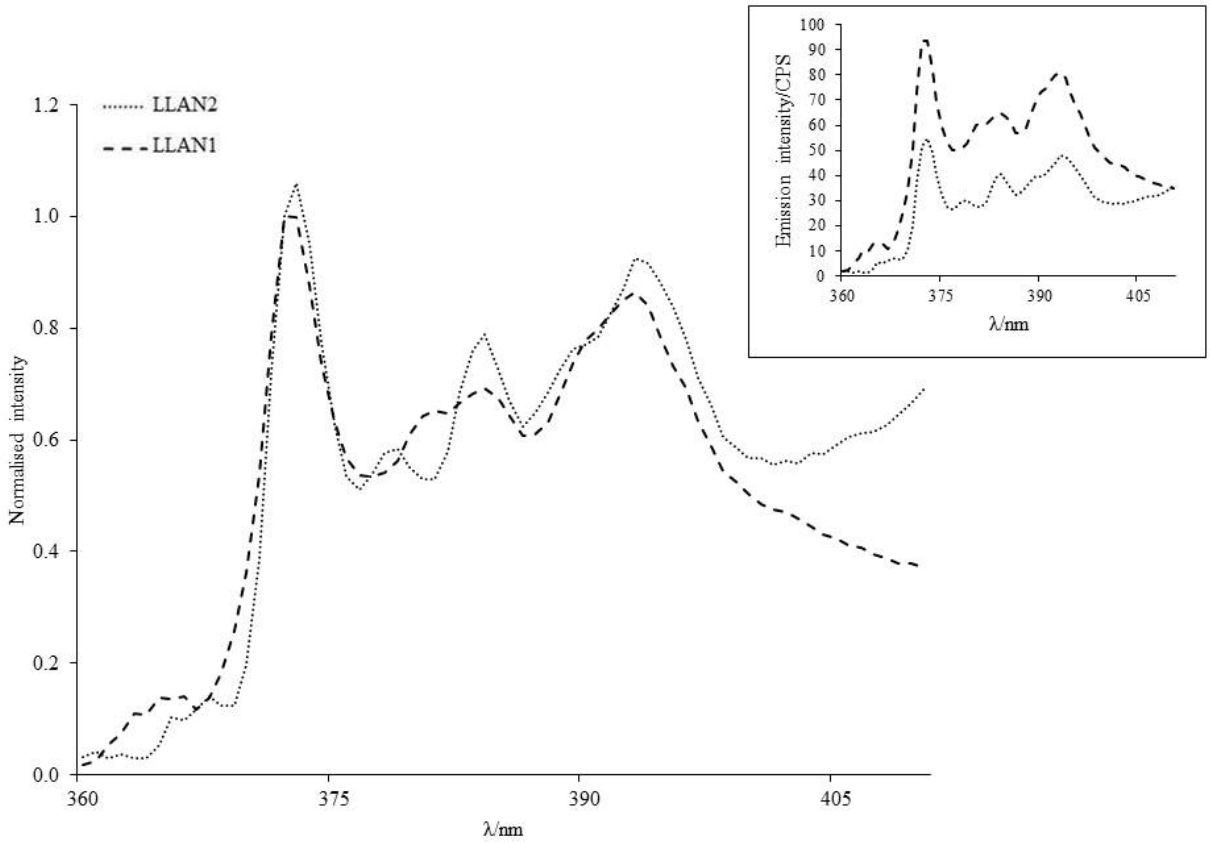

Figure 5.14 LLAN1and LLAN2 normalised summed fluorescence spectra and insert LLAN1 and LLAN2 summed emission intensity fluorescence spectra. Excitation 337 nm, filter 337 nm, excitation slits 15 nm, 360-410 emission, integration 20 seconds, increment 0.75 nm, emission slits 0.5 nm. Background and front face corrected. Pyrene at 1.01×10^{-7} mol_{py} $g^{-1}{}_{sand}$, 2.04×10^{-5} g_{py} $g^{-1}{}_{sand}$.

Table 5.5 I_3/I_1 peak height ratios for AU2, AU3, NIC1, NIC2, LLAN1 and LLAN2. The molar laydown of pyrene per gram of sand for each sample was 1.01×10^{-7} mol_{py} $g^{-1}{}_{sand}$ with a mass laydown of 2.04×10^{-5} g_{py} $g^{-1}{}_{sand}$.

Soil	$I_3:I_1$ ratio
AWS+HEX	1.00
AWS+SA	1.13
AU2	0.91
AU3	1.06
NIC1	0.74
NIC2	0.54
LLAN1	0.69
LLAN2	0.79

Figures 5.12-5.14 show spectra normalised to the first vibronic peak, 372 nm, to allow comparison of vibration band emission intensities. In such a heterogeneous

system as a soil, spectra can be expected to be weighted averages across all environments, and so some broadening of bands and loss of structure might be expected. The first thing to note is that the spectra for all soil samples are different, the overall band shape, vibrational intensity ratios, and structural resolution, do vary across the samples, indicating that pyrene is in different environments in these soils. With the natural soils, all except AU3 show a I_3/I_1 ratio < 1 indicating a relatively polar environment (Table 5.6). AU3 has I_3/I_1 ~1 indicating an environment of intermediate polarity. Of all the soils NIC2 shows a spectrum with least obvious fine structure, perhaps indicating a soil with a wider range of environments for pyrene adsorption – resulting in loss of fine structure in the averaged spectrum. A small but measurable difference in environment polarity was found between soil types; both soils show pyrene in a generally polar environment, but the less repellent soil, NIC2, shows the more polar environment as shown by the difference in the ratio of the peaks I_1 and I_3 in Figure 5.12.

In Figure 5.11 it can be noted that stearic acid coated acid-washed sand (AWS) absorbs around five times more pyrene than hexadecane coated acid-washed sand. By comparison to model soils, both natural repellent sandy soils AU2 and AU3 (Figure 5.13) adsorb significantly less pyrene than the AWS based samples, only a few percent of that absorbed by the stearic acid sample, and again there is a noticeable difference in adsorption efficiency between the two natural soils with AU3 adsorbing more than AU2.

5.4. Conclusions

Pyrene gives measurable steady-state and time-resolved emission spectra when absorbed into the organic layer around natural soils. On model soils, pyrene fluorescence response varies with polarity and viscosity of organics used. For natural soils there are small but measurable differences in polarity of the pyrene environment. Co-deposition with typical hydrophobic compounds found on soils, gives pyrene emission spectra and excimer formation kinetics which indicates environments of varying polarity and fluidity depending on the organic compounds present. When natural soils are used there are differences in both the efficiency of pyrene adsorption and polarity of the pyrene environment.

With model soils, high quality spectra could be obtained, and for these spectra vibration band ratios correlated well with the polarity of the organic under examination. Furthermore, lifetime studies show clearly different behaviour as the organic layer was changed from a liquid (hexadecane), through a relatively soft wax (octadecane) to a harder wax (stearic acid). This immediately suggests the possibility of using pyrene to examine the fluidity of the organic layer as say a hexadecane coated AWS is taken across its melting point (5-25 °C), to see if this correlates with changes in soil water drop penetration time.

For natural soils adsorption of pyrene from water gives samples which also give useable spectra, although these are much weaker than those found for pyrene co-deposited directly with organics, and soil auto-luminescence gives rise to large background signals for these spectra.

Overall, this work shows that it is possible to obtain both steady-state and time resolved spectra *in-situ* from pyrene co-deposited onto AWS or adsorbed directly onto soil. Work with AWS and model soils may allow studies of correlation of organic polarity and soil hydrophobicity for model soils made using different organics and combinations of organics (Mainwaring *et al.*, 2013), and may also allow time dependent studies of polarity as a soil is wetted. For natural soils, further work, with a wider range of soils and soil hydrophobicities, will be necessary to determine how well any of the spectral features correlate with the hydrophobicity of soils.

Chapter 6 Wetting process of water repellent soils

In this chapter experimental work is described which explores the wetting of soils. A theoretical model, involving an initial stage of adhesional-immersional wetting and a secondary stage of branching capillary wetting, is proposed, and a series of simple experiments aimed to assess the validity of this model are described. Experimental methods used include: WDPT, measurement of the mass of soil grains wetted over time; measurement of the time taken for penetration of a water drop into different soil thicknesses; optical microscopy; and WDPT measurements with salt solutions of different densities but very similar surface tensions.

6.1. Background

6.1.1. Wetting (Jaycock and Parfitt, 1981)

The process of wetting is key to understanding the phenomenon of soil water repellency. When a droplet of water is placed on a hydrophobic soil surface the water will bead up due to the difference in surface tension between the water and soil. The severity of this process is a result of the relative magnitudes of the molecular forces present where, for a hydrophobic surface, the cohesive forces between the water molecules are stronger than the adhesive forces between the soil and water interface.

The theory behind the phenomena of wetting is based upon Young's equation (1805) which considers the forces that exist at the three-phase contact line, namely between the solid-vapour (SV), solid-liquid (SL), and liquid-vapour (LV) interfaces (Figure 6.1 and Equation 6.1, below). Young's equation is directly applicable to ideal, smooth, homogenous surfaces, but may not be fully applicable to other scenarios such as those of soil surfaces. The interactions taking place at the three-phase contact line between solid, liquid and vapour (air) interfaces need to be considered to understand the different stages involved in the wetting process. As mentioned previously (chapter 1, section 1.3), if the contact angle, θ, is $> 90^{o}$ a surface is considered hydrophobic and will not wet, but if θ is $\leq 90^{o}$ the surface is considered hydrophilic and will wet, although some degree of contact i.e. 'wetting', occurs for all theta $\leq 180°$, and total wetting does not occur unless $\theta = 0$ (Jaycock and Parfitt, 1981).

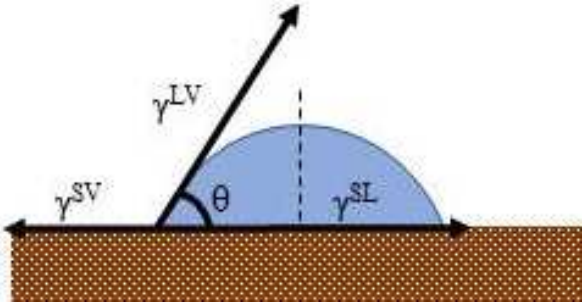

Figure 6.1 Water drop on a soil surface showing application of Young's equation and the balance of interfacial forces between a solid, liquid and vapour/air.

$$\gamma^{SV} = \gamma^{SL} + \gamma^{LV} \cos\theta \tag{6.1}$$

Jaycock and Parfitt (1981) identify three distinct types of wetting; adhesional (Figure 6.2), immersional (Figure 6.3) and spreading wetting (Figure 6.4). Most of the literature discusses spreading wetting for situations in which there is a large solid planar surface upon which a water droplet is placed; and immersional wetting where a large bulk of water wets a small cubic particle. The situation discussed later in this work, a small drop of water on a surface of moveable small grains of variable shape which can undergo adhesional, spreading and immersional wetting, is more complex. Here the stages of wetting of a cubic particle in an infinite volume of water are described as identified by Jaycock and Parfitt (1981).

For the purposes of this chapter the interfaces shall be hereafter referred to as solid-liquid (SL), solid-vapour (SV) and liquid-vapour (LV), where the term 'liquid' may be used interchangeably with water, and the term 'vapour' with humid air.

6.1.2. Adhesional wetting: cubic particle in infinite volume of water

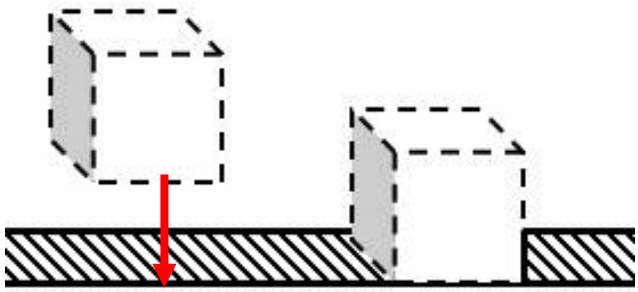

Figure 6.2 Adhesional wetting process of a cubic particle by an infinite volume of water (Redrawn from Jaycock and Parfitt, 1981).

Consider a cubic particle with six surface planes, each of area *a*, which makes adhesional contact with a volume of water across a single plane of area *a* (Figure 6.2).

Considering only the surfaces that change, the initial Gibbs energy state is:

$$G_s^{initial} = a\gamma^{SV} + a\gamma^{LV} \quad (6.2)$$

where: $G_s^{initial}$ = Gibbs energy of initial state
γ^{SV}= solid-vapour(air) interface
γ^{LV}= liquid(water)-vapour interface

Considering only the surfaces that change with a particle surface area, *a,* the Gibbs final energy state is given by Equations 6.3-6.5:

$$G_s^{final} = a\gamma^{SL} \quad (6.3)$$

$$\Delta G_s = G_s^{final} - G_s^{initial} = a\gamma^{SL} - (a\gamma^{SV} + a\gamma^{LV}) \quad (6.4)$$

$$\Delta G_s = a[(\gamma^{SL} - \gamma^{SV}) - \gamma^{LV}] \quad (6.5)$$

where: G_s^{final} = Gibbs energy of final state
γ^{SL}= solid-liquid (water) interface

6.1.3. Immersional wetting: cubic particle in infinite volume of water

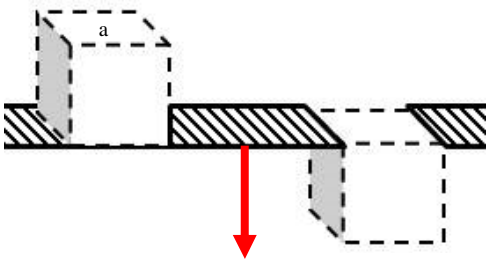

Figure 6.3 Immersional wetting of a cubic particle into an infinite volume of water (Redrawn from Jaycock and Parfitt, 1981).

For a cube immersed in an infinite volume of water, or immersed in a column of water, there is no change in the water-air interfacial area. The energy change for immersion wetting with a leading face can be given by Equations 6.6-6.8 and is depicted in Figure 6.3.

Considering the particle total area, the initial Gibbs energy state is:

$$G_s^{initial} = a\gamma^{SV} \tag{6.6}$$

Considering only the surfaces that change with a particle surface area, *a,* the final Gibbs energy state is:

$$G_s^{final} = a\gamma^{SL} \tag{6.7}$$

$$\Delta G_s = G_s^{final} - G_s^{initial} = a\gamma^{SL} - a\gamma^{SV} \tag{6.8}$$

For immersion into a finite droplet of water the water-air interface is increased as the volume of material within the droplet, i.e. water plus cube, increases as the cube penetrates. This is discussed for a spherical particle in section 6.3.1.

6.1.4. Spreading wetting: cubic particle in infinite volume of water

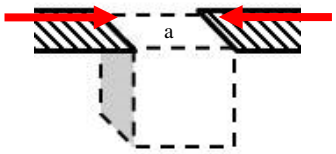

Figure 6.4 Spreading wetting of an infinite volume of water over a cubic particle (Redrawn from Jaycock and Parfitt, 1981).

The final stage for a cubic particle immersed with a leading plane is spreading wetting. If adhesional forces are greater than cohesive forces the liquid will spread over the surface. The change in energy states are identified in Figure. 6.4 and subsequent initial and final state equations (Equations 6.9-6.11).

Considering only the surfaces that change with a contact surface area, *a*, the initial and final Gibbs energy states are:

$$G_s^{initial} = a\gamma^{SV} \tag{6.9}$$

$$G_s^{final} = a\gamma^{SL} + a\gamma^{LV} \tag{6.10}$$

$$\Delta G_S = G_s^{final} - G_s^{initial} = (a\gamma^{SL} + a\gamma^{LV}) - a\gamma^{SV} \tag{6.11}$$

As Equation 6.11 shows, the only condition when spreading wetting is energetically favourable is when $\theta = 0^o$; for all other values of θ the Gibbs energy change for the process is positive.

6.1.5. Wetting of a spherical soil particle in a finite droplet of water

The wetting of a spherical particle (such as a model soil grain), by a finite volume of water (such as a water drop), is more complex, and it is the theory for this along with a proposed model for wetting, which forms the first part of the work presented in this chapter (section 6.3.1). The second part of the work given here deals with branching capillary action wetting which is important for soils as it plays a role in the process of water infiltrating into the voids between soil grains (section 6.3.2).

6.1.6. Research objectives

The research described in the following chapter aims to address the following research objectives:

1) Is wetting of water repellent soils a single step process? If not, what steps are involved?

2) What factors determine the rates of the different steps? (e.g. soil wettability, water droplet volume etc.)

3) Is there one wetting process model that fits all water repellent soils?

To address the research objectives a series of simple methods were conducted to study the process of wetting to identify any discrete stages involved and to validate the proposed model. Methods include the use of the WDPT test, optical microscopy, profilometry, goniometer time-lapse images, and the assessment of the role of droplet density and the effect of gravity.

6.2. Materials and methods

Five natural sandy soils were used in the experiments in the following chapter, NIC1, NIC2, LLAN1, NL1 and UKC respectively. Sample origins and characteristics are detailed in Table 2.2.

For all experiments, droplets were dispensed using a calibrated fixed Eppendorf Multipipette. Droplet volumes, radii, diameters and surface areas are given in Table 6.1.

Table 6.1 Droplet volume, dimensions and surface areas.

Drop volume/µl	Radius r/mm	Diameter d/mm	Surface area/mm^2
20	1.68	3.37	35.6
50	2.29	4.57	65.6
80	2.67	5.35	89.8
100	2.88	5.76	104.2

6.2.1. WDPTs and end masses

The water drop penetration time (WDPT) test, as described by Letey (1969) and later in depth by Doerr (1998), with water repellency classifications based on those by Bisdom *et al.* (1993) given in Table 6.2, was used to characterise the water repellency of the soils.

Table 6.2 WDPT classification used for identifying water repellency in soils as described by Bisdom *et al.* (1993).

Classification	Seconds
Wettable	< 5
Slightly water repellent	5-60
Strongly water repellent	60-600
Severely water repellent	600-3600
Extremely water repellent	> 3600

Soil samples were placed in plastic Petri dishes which were gently tapped to create a level surface, with enough soil to allow sufficient depth for full penetration of droplets. It is important to note that vigorous shaking should be avoided as this encourages particle separation by size and brings smaller particles and organics to the surface resulting in an unrepresentative surface. Six droplets of distilled water of

a given volume were dispensed on to the soil surface at timed intervals. Droplets were dispensed from a height no greater than 5 mm to avoid soil displacement upon contact, and the time from initial contact to full infiltration recorded using a stopwatch.

Once a droplet had fully infiltrated, the wet pellet was carefully extracted using a small spatula into an empty weighing boat. The side of the boat was gently tapped to remove any excess dry grains from the pellet and then the pellet was transferred into a pre-weighed weighing boat. The weight of the wet pellet was recorded immediately, with the dry pellet weight obtained after air drying for 24 hours.

6.2.2. Bulk density measurements

Loose and close packed bulk density measurements were calculated as described in section 2.2.2.

6.2.3. Particle size distribution

Particle size distributions were measured using a Beckman Coulter LS Series Laser Diffraction Particle Size Analyser (section 2.4.1). The instrument calculated the mean particle diameter (μm) and specific surface area (by volume), using triplicate runs.

6.2.4. Total organic carbon

Total carbon content of samples was measured using a SKALAR Primacs Solid Sample TOC Analyzer, as described in section 2.4.2.

6.2.5. Mass removal of soil grains over time methodology

The aim of the experiment was to measure the mass of soil grains wetted at different intervals of penetration over time. Soil samples of NIC1, NIC2, LLAN1 and NL1 were prepared as described in section 6.2.1. For each soil tested a series of intervals were sampled based on the overall Water Drop Penetration Time (WDPT) for that soil. For example, a soil with a 5 minute WDPT repellency result was sampled every 30 seconds, whereas a soil with a 15 minute WDPT repellency was sampled every 60 seconds.

Each soil sample was placed on a 4-figure balance and the balance tared. The weight of the soil sample prior to each droplet being dispensed on to the surface was

recorded, followed by the weight immediately after, 6 droplets were dispensed for each sample interval. After the appropriate time had elapsed, a pre-weighed cotton bud was brought into contact with the water droplet and the water and grains that had been wetted adhered to the cotton bud and were removed for weighing (Figure 6.5).

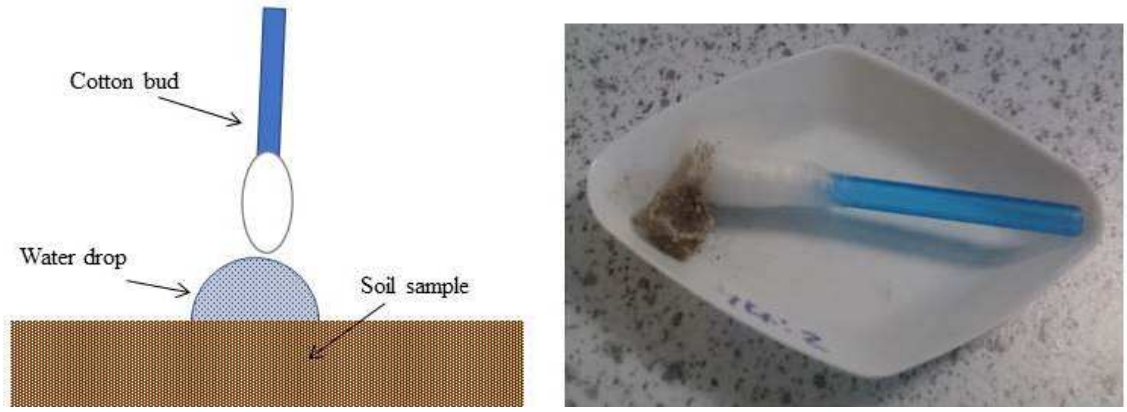

Figure 6.5 Schematic showing cotton bud being brought into contact with a water drop (left) and example of mass removed sample using the cotton bud method (right).

It was important to only remove the grains that had been wetted at that stage and so care was taken not to bring the bud into contact with the soil surface directly or to push down on the droplet so that more grains were picked up. The method was easily reproduced and the cotton bud was effective at removing the droplet and attached wetted soil grains for each extraction for the drop volumes used.

6.2.6. Sinter based water drop penetration time measurements

The following experiments carried out in a constant temperature and humidity room were designed to measure how long water droplets take to infiltrate different thicknesses of soil. Different depths of soil, as determined by soil mass over the measured surface area of the sinter, were placed in 18-20 mm diameter grade 3.0-4.0 (40-120 µm) glass sinter funnels (Figure 6.6) and the time taken for water droplets to infiltrate the soil recorded. In these experiments the sinter disc acts as a hydrophilic layer which presents a very low barrier to water penetration, and so the time measured gives the time for the water drop to penetrate the soil layer.

To confirm that the water droplet was reaching the sinter surface, cobalt chloride water sensitive discs (Humonitor®, Sigma Aldrich) were placed on top of a set of sinter discs and different depths of NIC1 soil was used to cover them. Droplets were

applied and left until they infiltrated the soil. Upon complete penetration the soil was gently removed to reveal the cobalt chloride test disc which had turned from blue to pink confirming that the droplet had reached this depth in the soil profile.

The soil samples were weighed into small glass vials and placed in the constant temperature-humidity room for 48 hours prior to testing. Droplets of 20, 30, 50 and 80 µl were used with a minimum of 3 droplets for each depth tested.

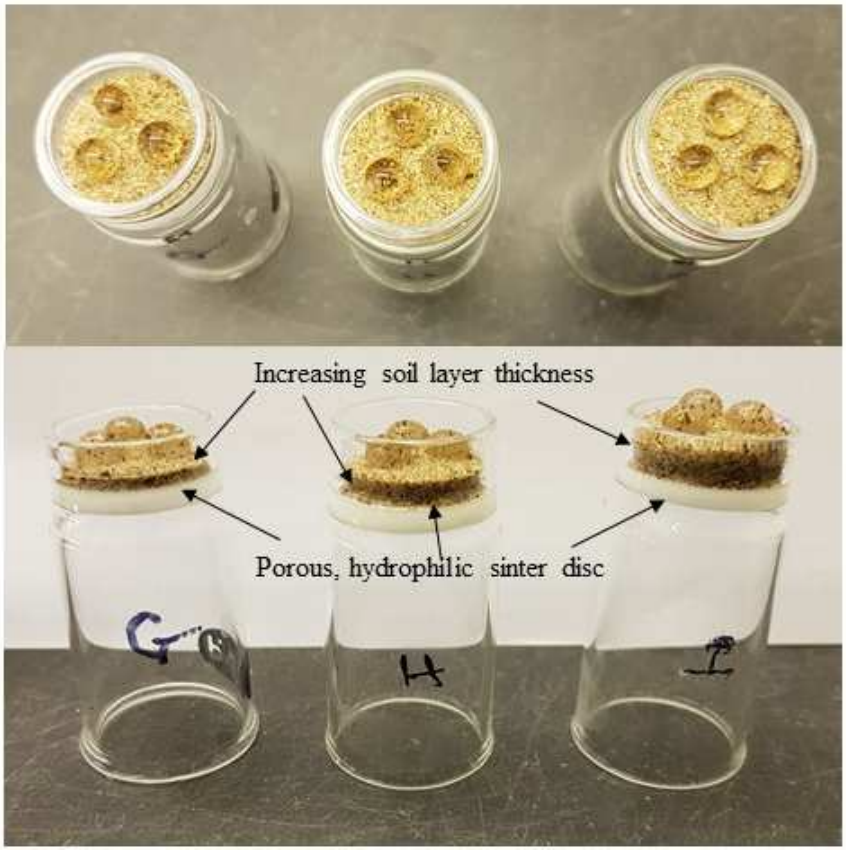

Figure 6.6 Sinter experiment sample set-up showing droplets dispensed on to sinters with increasing soil layer depths.

6.2.7. Density experiment

To assess if gravity was a significant factor in the wetting process, WDPT measurements were made using aqueous solutions of varying densities but very similar surface tensions prepared using caesium chloride, potassium chloride, sodium chloride and lithium chloride (Slavchov *et al.,* 2012; Ozdemir *et al.,* 2009 and Jarvis and Scheiman, 1967).

6.2.8. Time-lapse infiltration images: goniometer

Time-lapse images of the complete infiltration of a dispensed, detached water droplet over time (Figure 6.7) were obtained using a KRUSS Easydrop FM40 goniometer. A 1000 µl syringe was set up to dispense droplet volumes of 20, 50, 80 and 100 µl respectively at a rate of 200 µl / min for each sample. Images were collected every 3-6 seconds depending on the rate of penetration and repellency level of the soil being studied. Fifteen frames were selected at equal time intervals based on the WDPT. These were converted into negative images in IrfanView (www.irfanview.com) (Figure 6.7) and printed onto 1 mm graph paper for measurement, using the width of the goniometer syringe tip, measured using electronic callipers, as a 'scale bar' for calibration.

Drop volume was calculated by splitting the droplet printed image into 2 mm high segments and the lengths for each were recorded to the nearest mm. The volume for each of these segments was then calculated using the equation for the volume of a cylinder ($V = \pi r^2 h$). The individual segments were then summed to give an overall volume for that droplet. As soil grains cover the surface of the water drop, the drop will sit slightly lower than the initial soil surface in the small crater created from the movement of grains up and around the drop. A small correction was made to the data to correct for this hidden volume, discussed later in section 6.3.9.2.

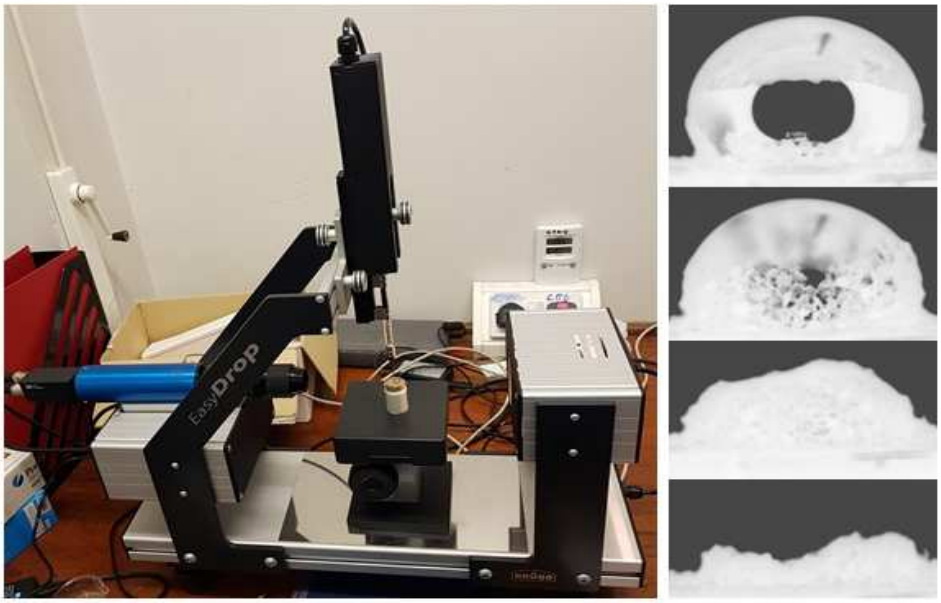

Figure. 6.7 Goniometer and sample set up for time-lapse imaging (left), examples of negative time-lapse imaging over the course of water drop infiltration (right).

6.2.9. Optical microscopy

A Wessex WSA1 optical microscope fitted with an Eyecam Plus (Brunel Microscopes Ltd) eyepiece was used to take time-lapse images of water drops penetrating into different soil types. The images were taken as a visual aid of the stages involved during the wetting process.

6.2.10. Profilometer

UKC soil was sprinkled onto a square of adhesive tape attached to a glass microscope slide. The slide was tapped to remove any loose grains and the process repeated until a close packed covering of soil grains was achieved. Profilometer measurements of this soil surface were made using a Dektak profilometer with a 12.5 µm stylus and a manual moving platform (Figure 6.8). Profile data was collected over 10,000 µm lengths and at 25 µm spaced intervals.

Figure 6.8 Sample set up of Dektak 150 profilometer.

6.2.11. Dimensions of wetted soil pellet: liquid nitrogen measurements

A set of preliminary tests to assess the dimensions of the soil pellets at different stages of penetration, used liquid nitrogen to freeze the water drops at different times of penetration, was carried out using AUC soil, with the height and depth of the frozen pellet measured using electronic callipers. The dried pellets were also weighed. Soil samples were placed into small glass vials and tapped gently to give a level surface. A water drop was then dispensed onto the soil surface. At a set time the glass vial with sample was carefully lowered into liquid nitrogen a left there for

approximately 60 s. The glass vial with the sample in was removed and tipped out with the pellet retrieved for measurement (Figure 6.9).

Figure 6.9 Example of a frozen pellet retrieved from liquid nitrogen experiments.

6.2.12. Activation energy

Activation energy is used to describe the minimum energy that is required in order for a chemical system to undergo a chemical reaction. To determine the activation energy, WDPT tests were carried out over a range of temperatures from 4 ^{o}C to 32 ^{o}C at 4 ^{o}C increments by cooling/heating samples in a Petri dish in a water bath.

6.2.13. Evaporation rate for WDPT tests

Evaporation rates were measured by monitoring the change in mass over time of 6 droplets dispensed on to a Petri dish of soil on a tared 4-figure analytical balance in a constant temperature/humidity room until they fully penetrated the soil. The weight after all six droplets were dispensed was recorded and then at timed intervals the total sample weight was recorded to monitor the evaporation rate until complete infiltration of all droplets.

6.2.14. Colour/symbol key for soil and droplet volume data points

The following key will be used throughout the results and discussion section for ease of differentiation between the data presented (Table 6.3). Where possible the data for each experiment will also be presented in increasing level of repellency i.e. from NIC2 soil which is the least repellent according to WDPT classification up to NL1 which is extremely repellent.

Table 6.3 Colour/symbol key for soil and droplet volume.

Soil	Repellency class	Droplet/µl			
		20	50	80	100
NIC2	Strongly	▲	◆	●	■
LLAN1	Strongly	▲	◆	●	■
NIC1	Strongly-severely	▲	◆	●	■
NL1	Severely-extremely	▲	◆	●	■

6.3. Results and discussion

6.3.1. The proposed model for two stage wetting of water repellent soils

The following sections 6.3.1-6.3.3 describe a two stage model of wetting of a spherical particle in a finite volume of water, considering firstly adhesional-immersional wetting and secondly branching capillary wetting.

6.3.1.1. Adhesional-immersional wetting: wetting of a particle in a finite volume of water

Unlike wetting of a cubic particle (previously described in section 6.1.2-6.1.4), adhesional wetting of a spherical particle cannot be considered distinct from, immersional and spreading wetting because the particle has no flat plane. Similarly, immersional wetting, where a particle is taken into a finite volume water droplet, is more complicated than the infinite water volume scenario.

For complete immersion wetting of a spherical particle into a finite volume of water the following process is suggested.

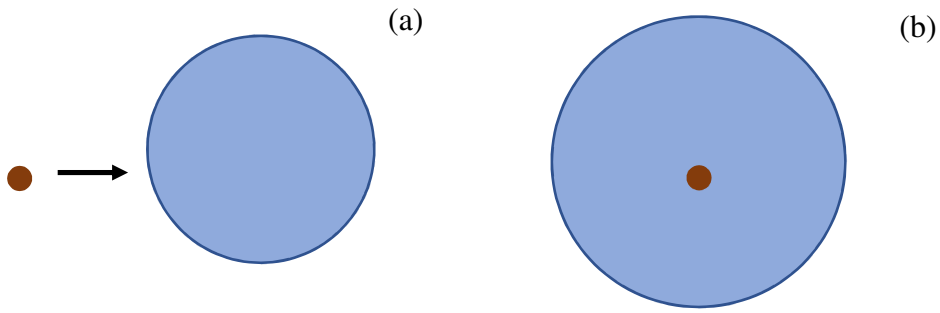

Figure 6.10 (a) Initial state of a spherical particle and finite water drop (b) Final state of spherical particle fully immersed into finite water drop.

Consider a spherical particle of total surface a and volume v (Figure 6.10a) totally immersed into a water droplet of volume V and radius $(3V/4\pi)^{1/3}$ and surface area $4\ \pi\ (3V/4\ \pi)^{2/3}$ (Figure 6.10b); the final volume of the water droplet with the particle inside is $V + v$, and it has a radius of $(3(V+v)/4\pi)^{1/3}$ and area of $4\ \pi\ (3(V+v)/4\ \pi)^{2/3}$.

For the initial Gibbs energy state, considering only the surfaces that change in the process, let these be area, *a*, and therefore:

$$G_s^{initial} = a\gamma^{SV} + 4\pi\left(\frac{3V}{4\pi}\right)^{2/3}\gamma^{LV} \quad (6.12)$$

where the first term on the right-hand side of Equation 6.12 is the solid-vapour surface area which becomes wetted in the final state, and the second term is the surface energy of the water drop that increases with volume upon immersion of the particle (Equation 6.13). Therefore, the final energy state may be given as:

$$G_S^{final} = a\gamma^{SL} + 4\pi\left(\frac{3(V+v)}{4\pi}\right)^{2/3}\gamma^{LV} \quad (6.13)$$

$$\Delta G_s = G_s^{final} - G_s^{initial} = (a\gamma^{SL} - a\gamma^{SV}) + 4\pi\left[\left(\frac{3(V+v)}{4\pi}\right)^{2/3} - \left(\frac{3V}{4\pi}\right)^{2/3}\right]\gamma^{LV} \quad (6.14)$$

The final energy state in Equation 6.14 gives the first term in brackets on the right-hand side as the change in energy as a solid-vapour surface is replaced by a solid-liquid surface of area *a*; and the second term is the energy change due to the increase in volume, and hence liquid-vapour surface area, of the droplet. From this (Equation 6.14), it appears that any particle with $\theta < 90^o$ might become completely immersed in a droplet of water of suitable size. However, in practice the wetting of a particle involves the process of moving through the surface of the water drop where it reaches a position of minimum Gibbs energy and will remain held at this point.

6.3.1.2. Adhesion and partial immersion wetting of a single spherical particle

When considering a spherical particle moving into a water surface as the particle is immersed, ignoring for the moment any change in water body volume:

The portion of the particle immersed in the water drop is a spherical cap (Figure 6.11). Where the area of the spherical cap is obtained by $2\pi rd$ (Wolfram Mathworld, 2019) and the change in energy in making the solid-liquid surface formed is given by (Equation 6.15):

$$\Delta G^{SL} = (\gamma^{SL} - \gamma^{SV})2\pi rd \quad (6.15)$$

The area of the circle across the interface plane of the spherical cap (Wolfram Mathworld, 2019) and resultant change in energy from the loss of liquid-vapour surface area is given by (Equation 6.16):

$$\Delta G_{LV} = \gamma^{LV}(2rd - d^2) \tag{6.16}$$

where *r* is the radius, and *d* is the depth of penetration of the soil particle.

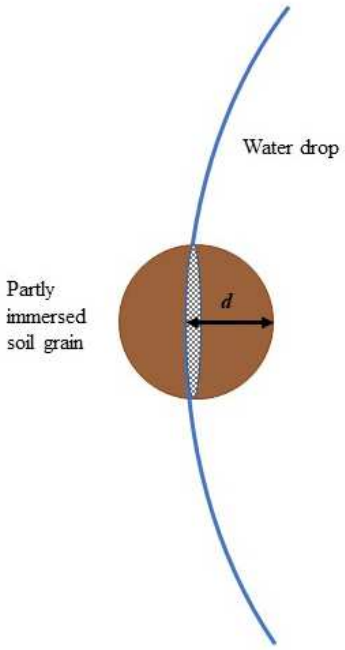

Figure 6.11 Adhesional-immersional wetting of a single grain of soil into a water drop, with depth of penetration of particle into the water drop given as *d*.

For this situation the Gibbs energy at any penetration depth, *d*, is given by the sum of two terms: the first term, *a*, which is the increase in solid-liquid interface from the formation of the spherical cap (Equation 6.15) and the second term, which is the decrease in liquid-vapour interface which is equal to the area of the circle of the particle at the depth of contact (Equation 6.16). Figures 6.12-6.14 show both energy terms and their summation for a particle of 0.15 mm radius, and θ of 45, 90 and 135° respectively. The depth (*d*) to which the particle penetrates the water is determined by the contact angle (θ), as demonstrated in Figures 6.12-6.14, where, the Gibbs energy gained from the loss of liquid-vapour interface is given in orange; the Gibbs

energy gained by the increase of solid-liquid interface is given in blue and the overall Gibbs energy (summation of previous two terms) is given in red.

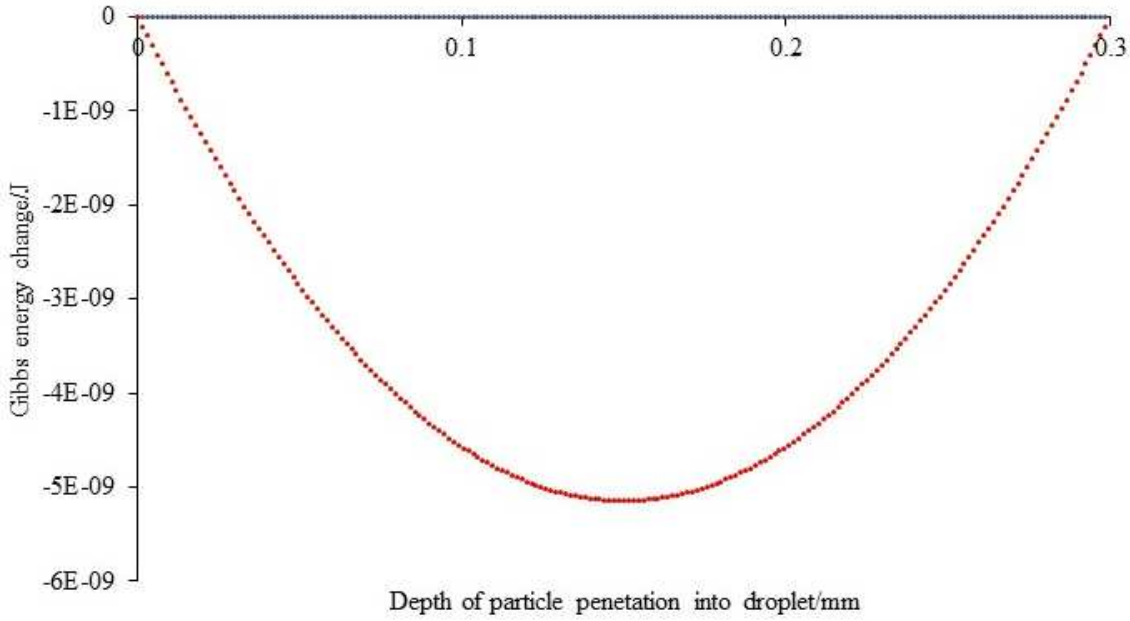

Figure 6.12 Gibbs energy change (J) with depth for a single particle penetration into a droplet (mm) during the wetting process, where $\theta = 90^o$ and particle radius is 0.15 mm. The surface area of the spherical drop wetted by the liquid is proportional to the depth of penetration. For a 90^o contact angle the Gibbs energy for increasing the surface is 0 and so this component is a straight horizontal line on the plot; this term is shown in blue. As the particle enters the drop, the water-air interface is decreased by an amount equal to the area of base of the spherical cap at the water-particle contact. This starts at 0, decreases to a minimum when the particle is half way into the water and increases again until the particle moves into the water drop, and when the particle is completely immersed, the liquid-vapour interface is the same as before the particle entered. Therefore, this component is the area of the circle of the particle at the depth of penetration in Figure 6.11. This term is given in orange in Figure 6.12, and since, for a 90^o contact angle, this is the only term to vary with penetration depth, the resultant curve given in red, overlies this curve.

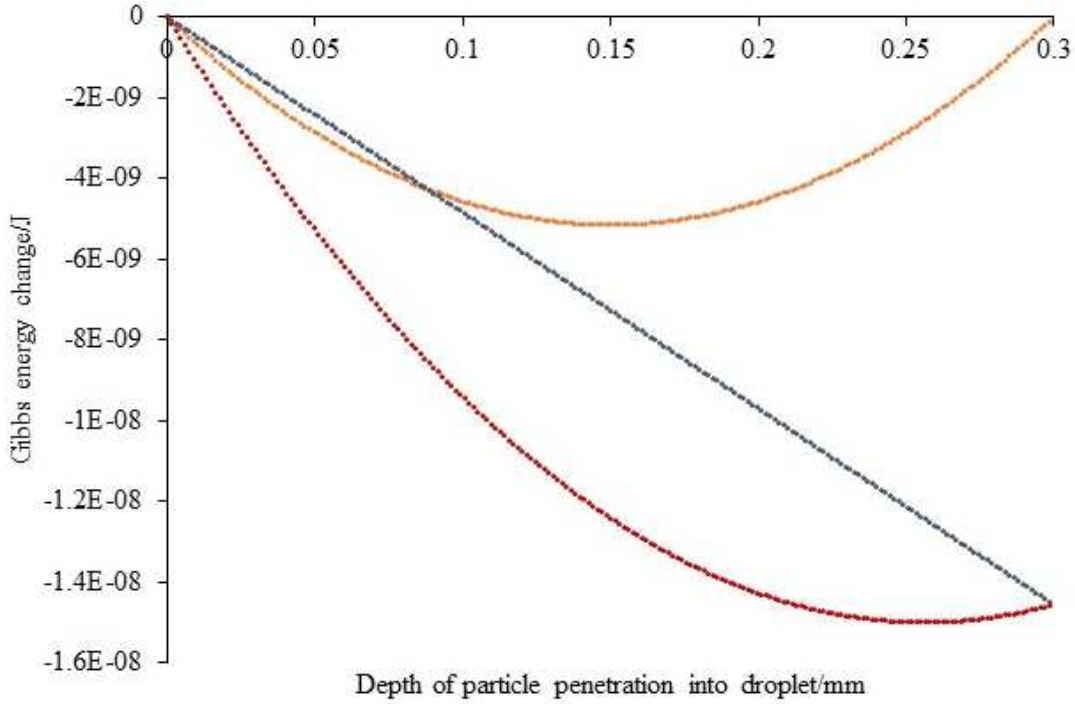

Figure 6.13 Gibbs energy change (J) with depth of a single particle penetration into a droplet (mm) during the wetting process, where $\theta = 45^{o}$ and particle radius is 0.15 mm. The surface area of the spherical drop wetted by the liquid is proportional to the depth of penetration. For a 45^{o} contact angle the Gibbs energy for increasing the surface is negative and so this component is a straight line, decreasing with penetration depth on the plot; starting at 0 when the particle is just in contact with the liquid and decreasing linearly as the particle moves through the liquid; this term is shown in blue. As the particle enters the drop, the water-air interface is decreased by an amount equal to the area of base of the spherical cap at the water-particle contact. This term is the same as that in Figure 6.12. This starts at 0, increases to a maximum until the particle is half way into the water and decreases again as the particle continues to move into the water drop until it is 0 again at complete immersion; this term is shown in orange. The summation of the two terms is given in red.

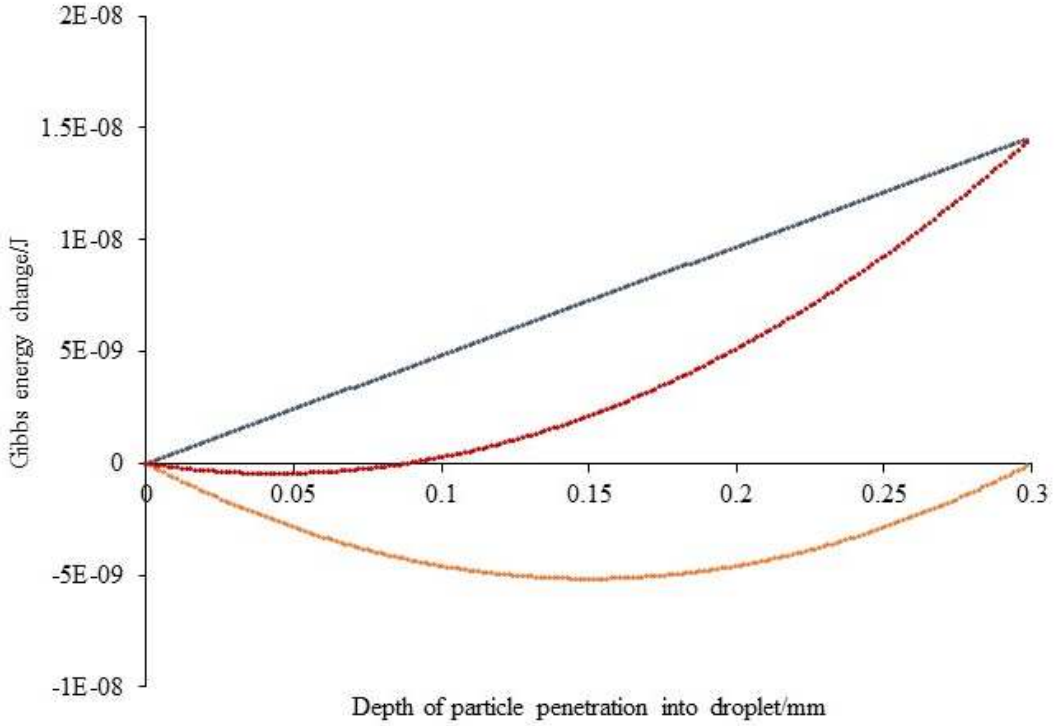

Figure 6.14 Gibbs energy change (J) with depth of single particle penetration into a droplet (mm) during the wetting process, where $\theta = 135^{o}$ and particle radius of 0.15 mm. The surface area of the spherical drop wetted by the liquid is proportional to the depth of penetration. For a 135^{o} contact angle the Gibbs energy change for increasing the solid-liquid surface is positive and so this component is a straight line increasing in energy on the plot; this term is shown in blue. Starting at 0 when the particle is just in contact with the liquid and increases linearly as the particle moves through and the solid-liquid surface area is increased. As the particle enters the drop, the water-air interface is decreased by an amount equal to the area of base of the spherical cap at the water-particle contact. As the particle enters the drop, the water-air interface is decreased by an amount equal to the area of base of the spherical cap at the water-particle contact. This term is the same as that in Figure 6.12. This starts at 0, increases to a maximum until the particle is half way into the water and decreases again as the particle continues to move into the water drop, until it is 0 again at complete immersion; this term is shown in orange. The summation of the two terms is given in red.

For a particle with $\theta = 90^o$ drawn into an infinitely large drop the particle is drawn in up to the halfway point (Figure 6.12) as this gives the greatest decrease in liquid-vapour surface area. For $\theta < 90^o$ the particle is drawn in further but never fully covered (Figure 6.13), while for $\theta > 90^o$ the particle is drawn in to a shallower depth (Figure 6.13) and for $\theta = 180^o$ not drawn in at all.

Adhesional-immersional wetting is energetically favourable where $\theta < 180^o$ and the depth to which the particle is drawn into the water is determined by the contact angle (θ). It is the energy of adhesional-immersional wetting that causes the droplet to pick up soil grains from underneath and to the side of drop (when in contact with soil) and to allow them to jostle and move such that the droplet is covered by as many accessible grains as is energetically possible.

Once the drop is on top of the soil it is now coated, to a variable degree depending on the soil hydrophobicity, with a single layer of soil grains. The next stage in the wetting process is infiltration through that layer into the soil beneath and this process is referred to here as branching capillary wetting.

6.3.2. Branching capillary wetting

Branching capillary wetting is proposed here as the process which occurs during the infiltration of a water drop into a soil resulting in an increased wetting front contact line between solid-vapour and solid-liquid interfaces.

Since water flows in between soil particles and wets them, and assuming close-packing, there is no change in the liquid-vapour area (Figure 6.15). Therefore, the overall Gibbs energy change for this process may be given as (Equation 6.17):

$$\Delta G_s = \Delta_{area}(\gamma^{SL} - \gamma^{SV}) \tag{6.17}$$

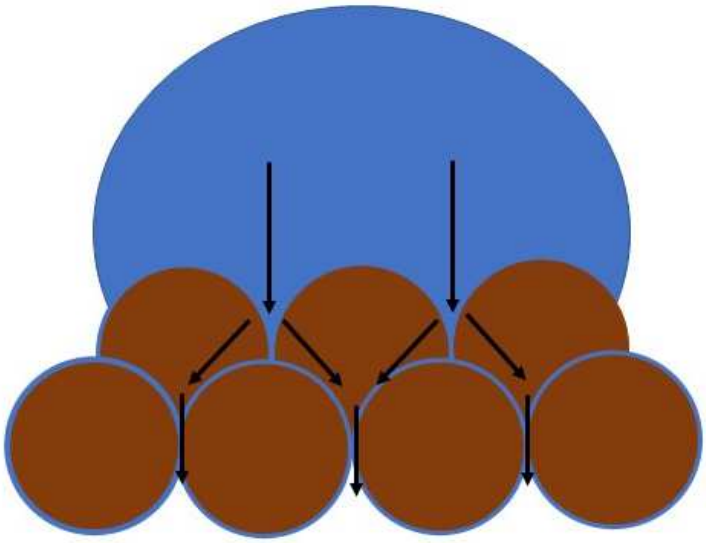

Figure 6.15 Branching capillary wetting schematic showing a water drop infiltrating through pores between soil grains. Arrows show direction of flow between soil particles.

Branching capillary wetting will occur for any contact angle where $\theta < 90^{o}$ and will not occur for any contact angle where $\theta > 90^{o}$. It is worth noting that the transition from the initial state of a water drop prior to contact with a soil, to the final state where it has fully infiltrated, results in an increase in solid-liquid surface which is hundreds of times greater than the initial liquid-vapour surface area of a drop.

6.3.2.1. Energy terms, total energy change, and depth of droplet penetrating into the surface for a hemisphere drop wetting a single layer of close-packed spheres

The Gibbs energy change involved in the wetting of a single layer of spherical particles depends on, θ, the volume of the particle and the volume of the drop. Using an approach developed in collaboration with Dr. Douglas, some idea of these energies can be calculated for a hemisphere of water sitting on homogenous, close-packed, spherical particles. The calculations are based on the following approximations.

1) The drop is a hemisphere and retains this shape throughout the wetting process. No allowance is made for the increased surface area of the drop due to curvature of the surface upon contact with the soil.

2) The soil is made up of uniform, smooth, spherical particles with a packing density of close-packed spheres, 0.9 (Chang and Wang, 2010).

3) The number of soil grains covered by the drop is given by the ratio of the area of the base of the water hemisphere to the maximum cross sectional area of a soil particle, multiplied by the packing density factor of 0.9.

4) As the drop infiltrates it does so with no lateral spread, and when accounting for gravitational energy (which is considered a small contributor to the overall energy) the centre of mass of the hemisphere moves by the depth of penetration even though the particles occupy some of the volume of the base of the hemisphere.

5) The increase in volume of the hemisphere as the particles penetrate into the hemisphere causes a corresponding increase in the liquid-vapour surface area. No consideration at this stage is made for adhesional wetted grains taking up this expansion in surface area, again because it is a refinement to a term which has a small energy contribution.

The change in energy as the sphere is drawn into the droplet for a 0.3 mm particle, 100 µl water drop and varying contact angles from θ = 0-180^{o} without initially considering the effect of gravity, are shown in Figures 6.16-6.21, where, the terms for blue and orange given in Figures 6.16 to 6.22 are exactly the same as those in Figures 6.13 and 6.14. The additional term given in purple is energy from the increase in the liquid-vapour surface which is calculated from the change in volume of the hemisphere as it is increased by the volume of particles penetrating into the hemisphere.

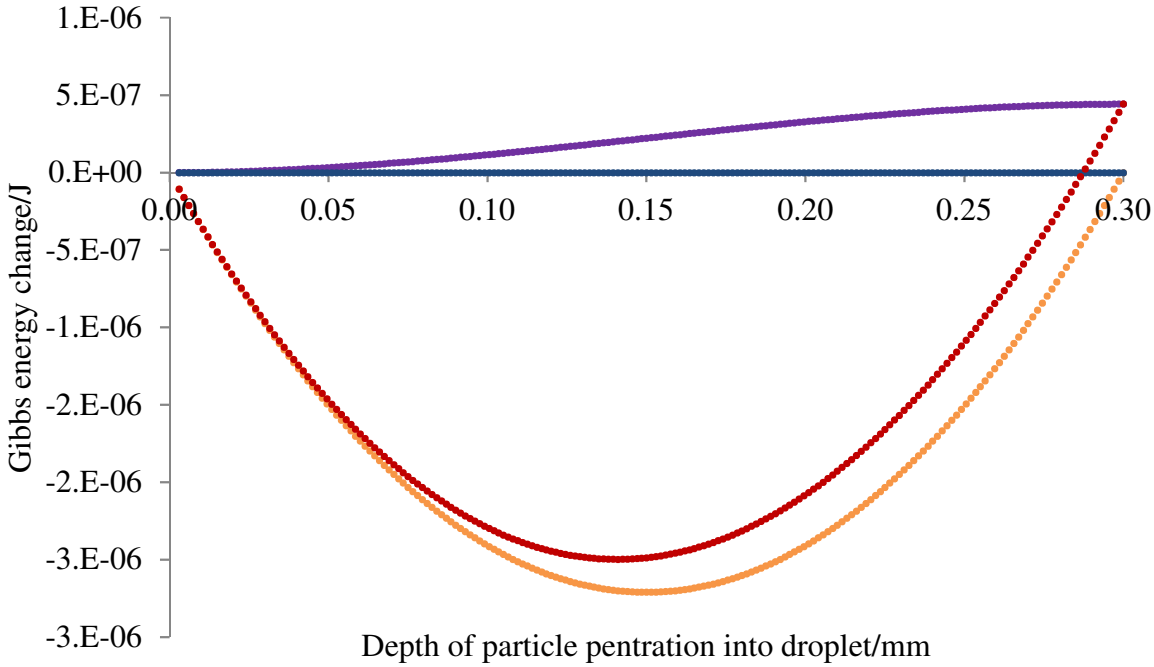

Figure 6.16 Gibbs energy change (J) with depth of particle penetration into a droplet (mm) during the wetting process, where θ = 90°, drop volume of 100 µl and particle radius of 0.15 mm, (i.e. as Figure 6.12) but with the addition of the energy change for the increasing liquid-vapour interface as the particles penetrate the droplet shown in purple. The blue and orange curves are as described for Figure 6.12. The additional term shown in purple is energy from the increase in the liquid-vapour surface which is calculated from the change in volume of the hemisphere as it is increased by the volume of particles penetrating into the hemisphere. The red line is the summation of all the energy terms i.e. the final energy term.

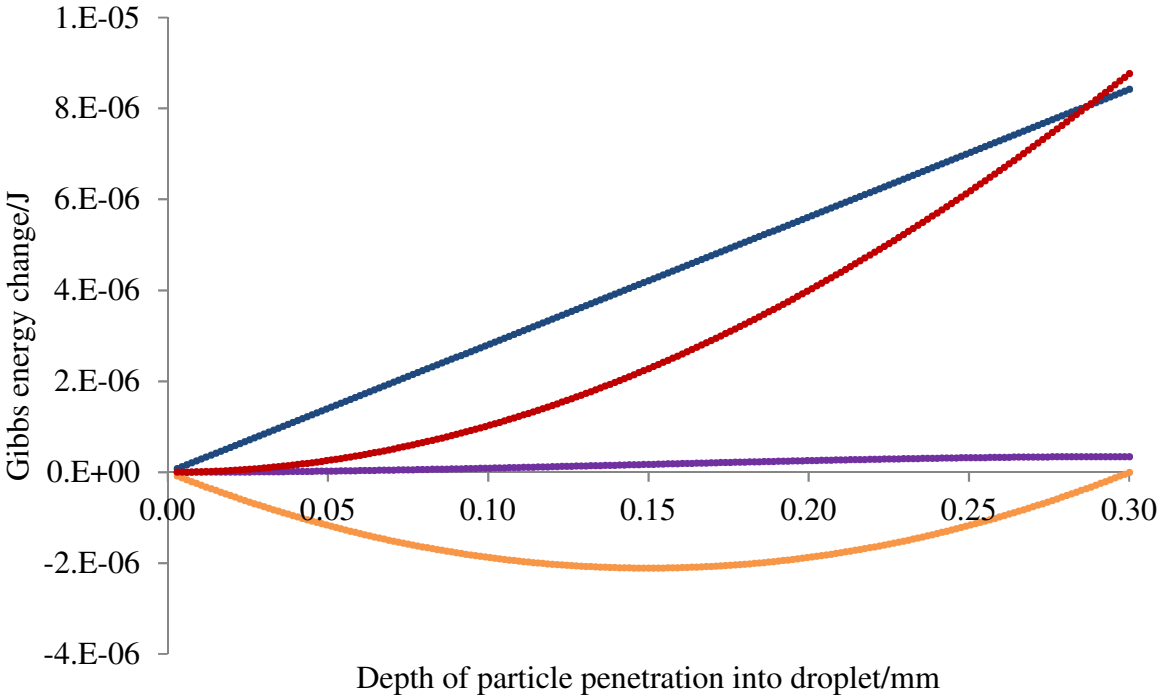

Figure 6.17 Gibbs energy change (J) with depth of particle penetration into a droplet (mm) during the wetting process, where θ = 180°, drop volume of 100 µl and particle radius of 0.15 mm, including the addition of the energy change for the increasing liquid-vapour interface as the particles penetrate the droplet, shown in purple. The surface area of the spherical particle wetted by the liquid is proportional to the depth of penetration. For a 180° contact angle the Gibbs energy for increasing the solid-liquid surface is positive and so this component is a straight line increasing in energy on the plot, shown in blue. As the particle enters the drop, the water-air interface is decreased by an amount equal to the area of base of the spherical cap at the water-particle contact. This starts at 0, increases to a maximum until the particle is half way into the water and decreases again as the particle moves into the water drop, until, when the particle is completely immersed, it is again 0, this is shown in orange. The additional term, given in purple is energy from the increase in the liquid-vapour surface which is calculated from a hemisphere of the initial volume plus the volume of particles to the penetration depth. The red curve is the summation of all the energy terms i.e. the overall energy change.

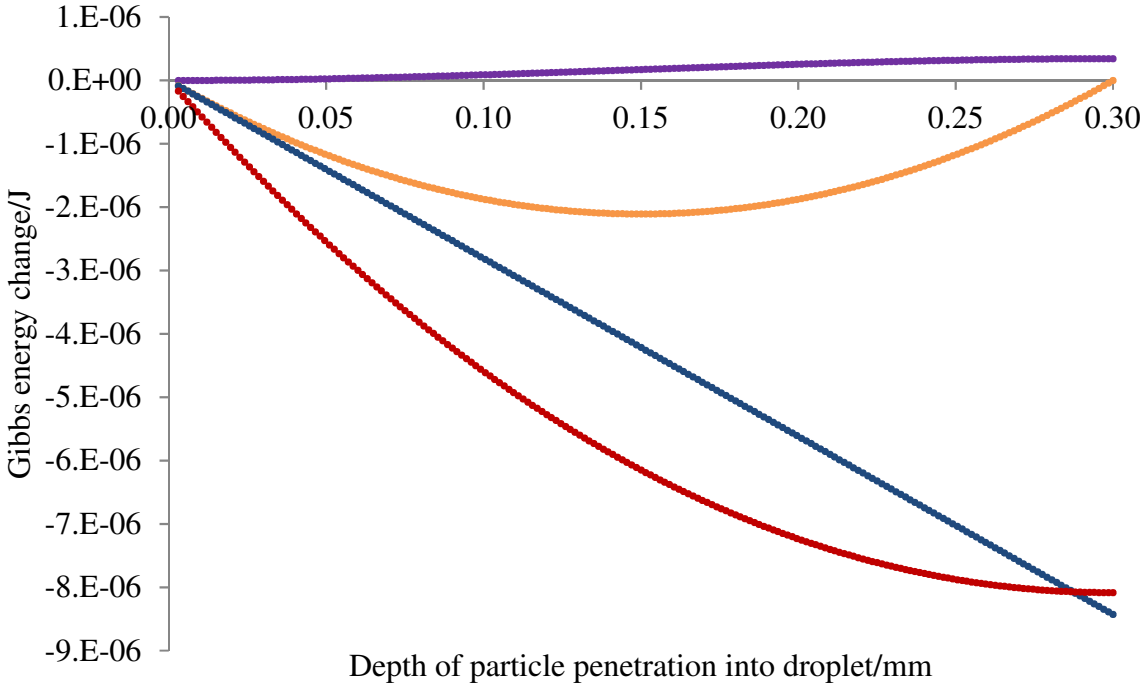

Figure 6.18 Gibbs energy change (J) with depth of particle penetration into a droplet (mm) during the wetting process, where θ = 0°, drop volume of 100 µl and particle radius of 0.15 mm, including the energy change for the increasing liquid-vapour interface as the particles penetrate the droplet, shown in purple. The surface area of the spherical particle wetted by the liquid is proportional to the depth of penetration. For a 0° contact angle the change in Gibbs energy for increasing the solid-liquid surface is negative and so this component is a straight line decreasing in energy on the plot; shown in blue. As the particle enters the drop, the water-air interface is decreased by an amount equal to the area of base of the spherical cap at the water-particle contact. This starts at 0, increases to a maximum until the particle is half way into the water and decreases again as the particle moves into the water drop, until, when the particle is completely immersed, it is again 0, this is shown in orange. The change in Gibbs energy from the increase in the liquid-vapour surface calculated as the volume increases from a hemisphere of the initial volume plus the volume of particles to the penetration depth is shown in purple. The red curve is the summation of all the energy terms i.e. the overall energy change.

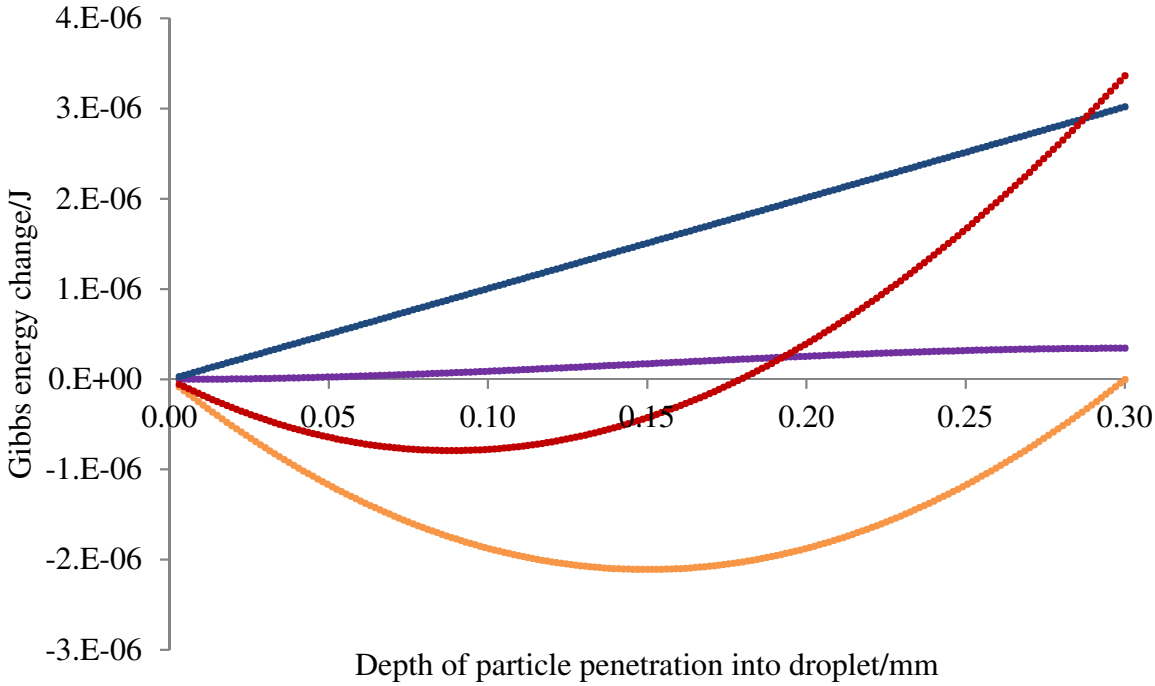

Figure 6.19 Gibbs energy change (J) with depth of particle penetration into a droplet (mm) during the wetting process, where θ = 111°, drop volume of 100 µl and particle radius of 0.15 mm, including the energy change for the increasing liquid-vapour interface as the particles penetrate the droplet, shown in purple. The surface area of the spherical particle wetted by the liquid is proportional to the depth of penetration. For a 111° contact angle the change in Gibbs energy for increasing the solid-liquid surface is positive and so this component is a straight line increasing in energy; shown in blue on the plot. As the particle enters the drop, the water-air interface is decreased by an amount equal to the area of base of the spherical cap at the water-particle contact. This starts at 0, increases to a maximum until the particle is half way into the water and decreases again as the particle moves into the water drop, until, when the particle is completely immersed, it is again 0, this is shown in orange. The change in Gibbs energy from the increase in the liquid-vapour surface calculated as the volume increases from a hemisphere of the initial volume plus the volume of particles to the penetration depth is shown in purple. The red curve is the summation of all the energy terms i.e. the overall energy change.

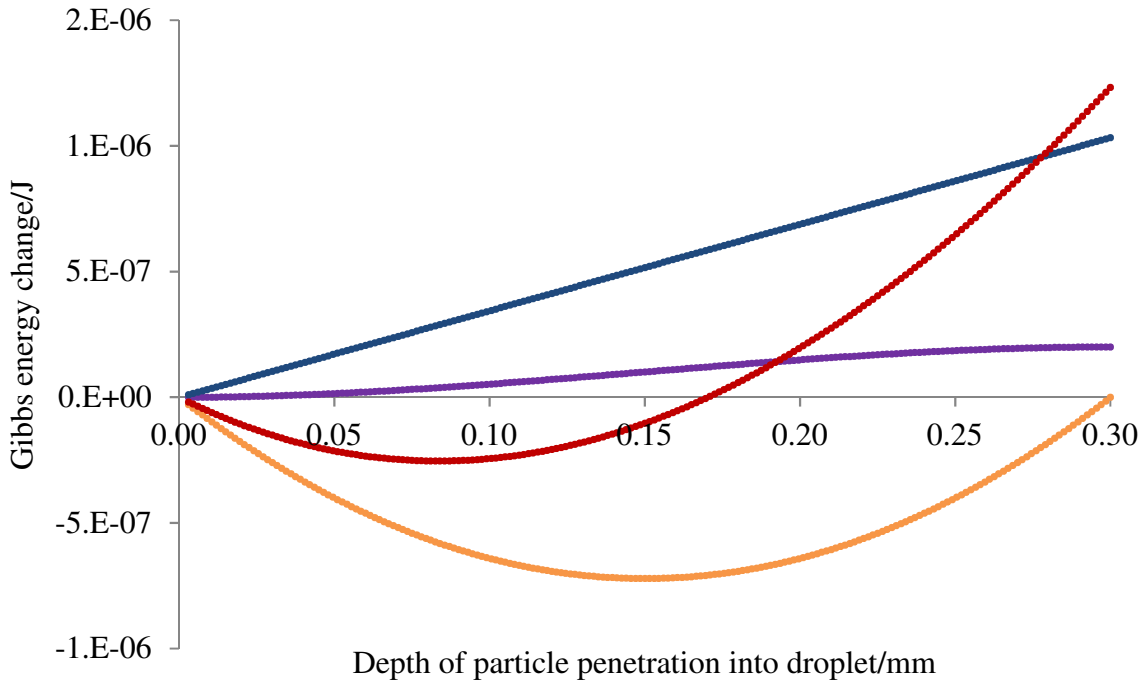

Figure 6.20 Gibbs energy change (J) with depth of particle penetration into a droplet (mm) during the wetting process, where θ = 111°, drop volume of 20 µl and particle radius of 0.15 mm, including the energy change for the increasing liquid-vapour interface as the particles penetrate the droplet, shown in purple. The surface area of the spherical particle wetted by the liquid is proportional to the depth of penetration. For a 111° contact angle the change in Gibbs energy for increasing the solid-liquid surface is positive and so this component is a straight line increasing in energy; shown in blue on the plot. As the particle enters the drop, the water-air interface is decreased by an amount equal to the area of base of the spherical cap at the water-particle contact. This starts at 0, increases to a maximum until the particle is half way into the water and decreases again as the particle moves into the water drop, until, when the particle is completely immersed, it is again 0, this is shown in orange. The change in Gibbs energy from the increase in the liquid-vapour surface calculated as the volume increases from a hemisphere of the initial volume plus the volume of particles to the penetration depth is shown in purple. The red curve is the summation of all the energy terms i.e. the overall energy change

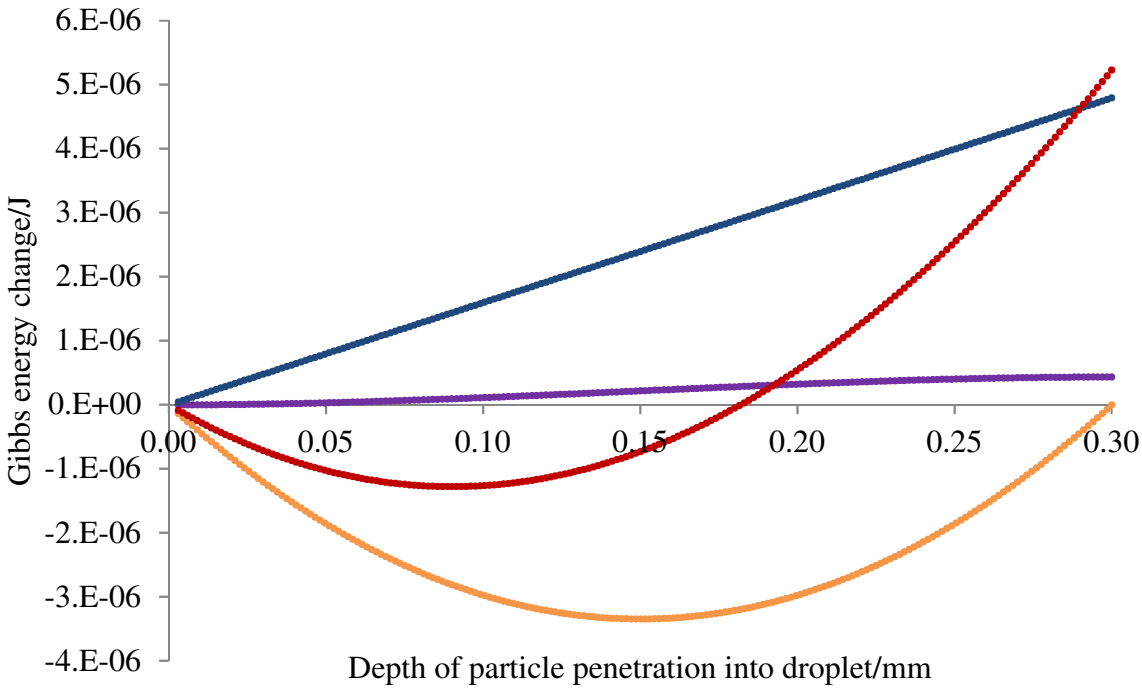

Figure 6.21 Gibbs energy change (J) with depth of particle penetration into a droplet (mm) during the wetting process, where θ = 111°, drop volume of 200 µl and particle radius of 0.15 mm, including the energy change for the increasing liquid-vapour interface as the particles penetrate the droplet, shown in purple. The surface area of the spherical particle wetted by the liquid is proportional to the depth of penetration. For a 111° contact angle the change in Gibbs energy for increasing the solid-liquid surface is positive and so this component is a straight line increasing in energy; shown in blue on the plot. As the particle enters the drop, the water-air interface is decreased by an amount equal to the area of base of the spherical cap at the water-particle contact. This starts at 0, increases to a maximum until the particle is half way into the water and decreases again as the particle moves into the water drop, until, when the particle is completely immersed, it is again 0, this is shown in orange. The change in Gibbs energy from the increase in the liquid-vapour surface calculated as the volume increases from a hemisphere of the initial volume plus the volume of particles to the penetration depth is shown in purple. The red curve is the summation of all the energy terms i.e. the overall energy change.

For particles with θ = 90° the drop penetrates to *ca.* a depth half way across the particles (Figure 6.16) as this gives the greatest decrease in liquid-vapour surface area. For θ < 90° the water penetrates further but the particles are never fully covered, while for θ > 90° the water penetrates to a shallower depth and for θ = 180° (Figure 6.17) not penetrate at all. The situation for θ = 111° is included here (Figures 6.19-6.21) as it is the measured contact angle of paraffin wax on a flat surface which is significant for the measurements made in the next chapter (7) on contact angles.

Figure 6.22 and accompanying Table 6.4 presents the change in Gibbs energy accounting for the influence of gravity (given in green) on a range of droplet sizes where θ = 111°.

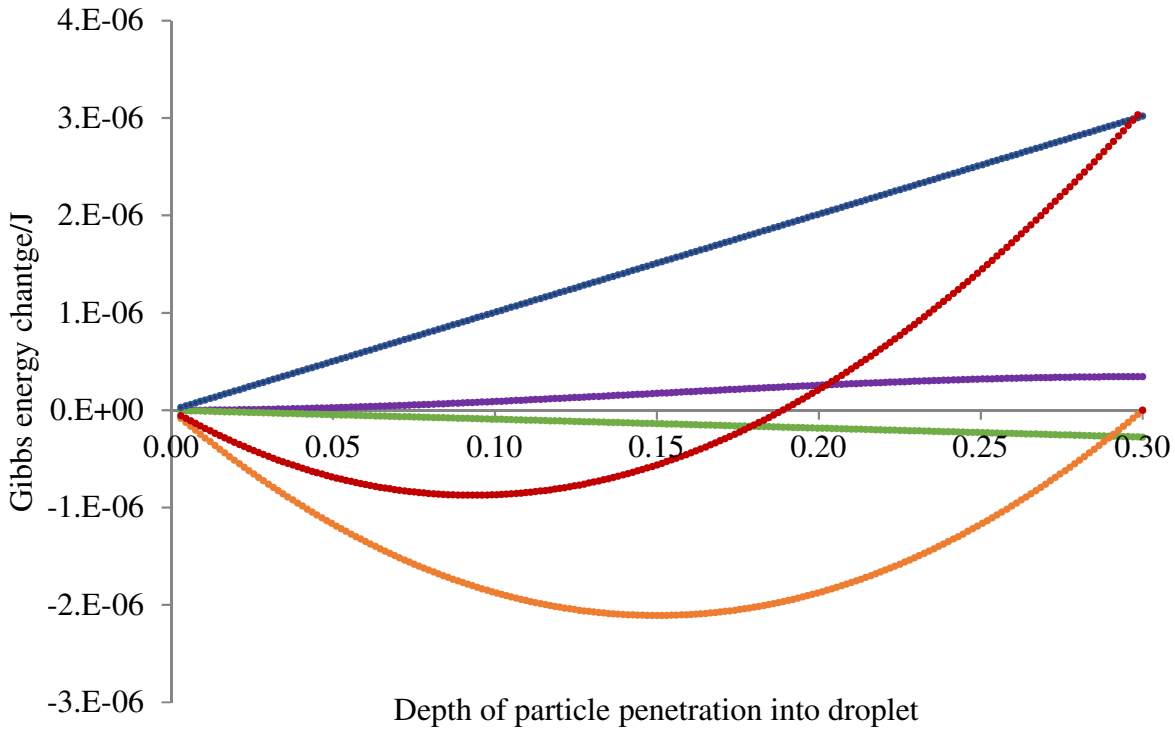

Figure 6.22 Gibbs energy change (J) with depth of particle penetration into a droplet (mm) during the wetting process, where θ = 111°, drop volume of 100 µl and particle radius of 0.15 mm, including the term for the effect of gravity, shown in green, as the drop settles on the particles. The three terms shown in blue, orange and purple are the same as those in Figure 6.19. The Gibbs energy change dues to gravity as the water drop settle is a negative energy term ,which is linear with depth of penetration, and therefore it is a straight line in the plot, decreasing uniformly as the drop settles over the soil grains. Again, the final, overall Gibbs energy change is shown in red.

Table 6.4 Resultant depth of particle penetration for contact angles of 111° by varying drop volume, taking gravity into account.

Drop volume/µl	Depth/mm
20	0.0855
100	0.0915
200	0.0945

Overall it can be concluded that for this work gravity is not a major energy term; however, it does have some influence on the depth to which a drop will sit on the soil grains.

6.3.3. Transition from adhesional-immersional wetting to branching capillary wetting

The transition from adhesional-immersional wetting to branching capillary wetting occurs as soon as the droplet has reached a depth over the first contact layer of particles to allow access to a surface of subsequent particles.

For the transition from adhesional-immersional to branching capillary wetting to occur the water must penetrate enough to come into contact with the soil layer below the surface layer. For close-packed spheres the separation between successive close-packed layers is equal to 1.633 × radius of the spheres (Krishna and Pandey, 1981). The critical contact angle to allow this to happen can be obtained graphically from plots of penetration depth against contact angle for the conditions under consideration. As an example, Figure 6.23 shows depth of penetration for various contact angles for a 100 µl drop, and from this diagram the critical contact angle which allows penetration to the critical depth, (in this case 0.244 mm), is 51°.

The depth of immersion of the particle into the water surface against the contact angle (θ) for 100 µl droplet is given in Figure 6.23 and Figure 6.24 shows the depth of immersion of the particle for different droplet volumes.

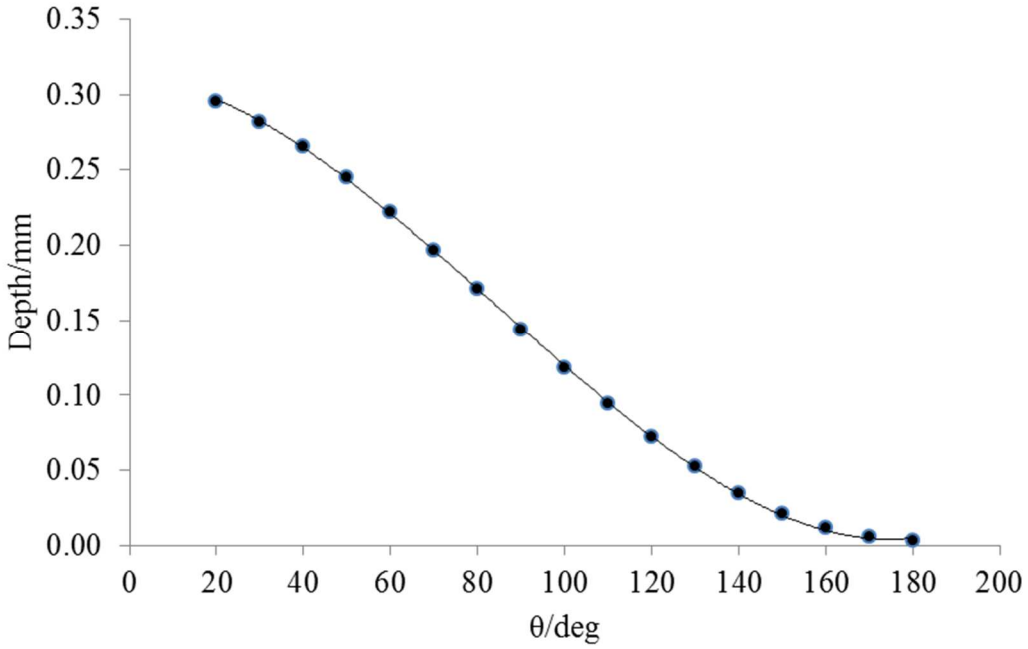

Figure 6.23 Depth of penetration of the particle into a water drop against the contact angle (θ) for 100 µl drop assuming random close packing of 0.9 (Chang and Wang, 2010) and 0.15 mm radius particle. Data is obtained from Figure 6.22 by varying the contact angle (θ).

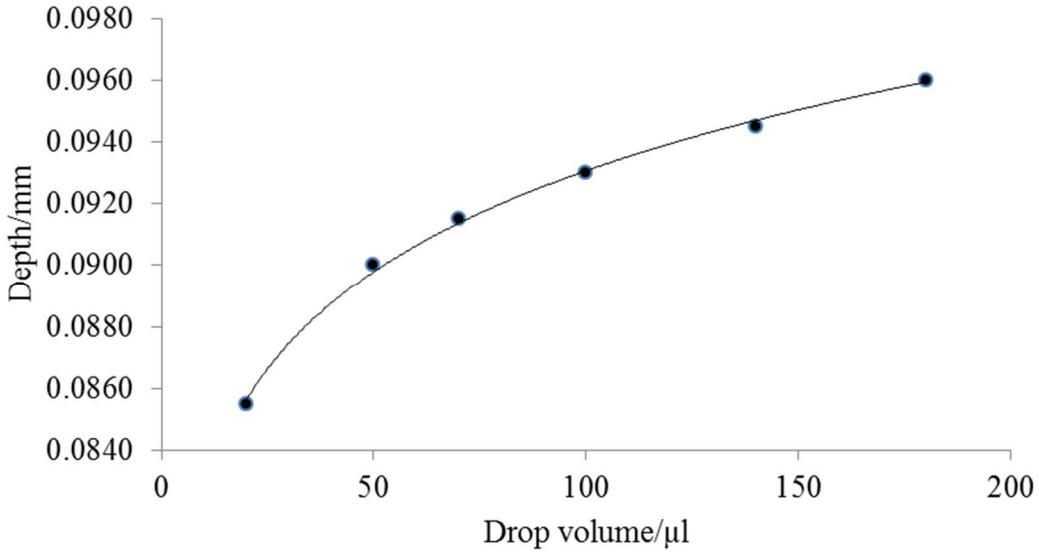

Figure 6.24 Depth of penetration against droplet volume for theta of 111° (equivalent to paraffin wax on a flat surface). Penetration depth and therefore critical contact angle ($\theta_{critical}$) is dependent on drop volume, the larger the volume, the lower the critical contact angle.

Based on the calculation assumptions underlying Figure 6.23 for spherical, homogenous, close-packed, spheres under this set-up a contact angle of $\leq 51^{o}$ (this critical angle will be identified as $\theta_{critical}$) would be necessary for the water to make contact with the second layer of spheres. However, soil is not made up of particles which are uniform in size and shape nor are they close-packed. In a loose-packed arrangement with a distribution of particle sizes the distance between the first and second layer surface will be less than in a close-packed array, and therefore contact through the first layer of adhesionally wetted particles at the base of the drop into the bulk soil probably occurs for soils whereby θ is significantly larger than 51^{o}. In order to achieve a contact angle of $\theta_{critical}$ in a water repellent soil, molecular restructuring will be required to reduce the initial contact angle from a high value to $\theta_{critical}$.

The rate of any restructuring process can be given by an activation energy term (Equations 6.18 and 6.19) for the restructuring, multiplied by the length of the solid-liquid contact line. Immediately after adhesional-immersional wetting the solid-liquid contact line is at a minimum but as branching capillary wetting occurs the solid-liquid contact increases rapidly.

The rate of infiltration at any time may then be given by:

$$rate = kL_{CL}{}^{t} \tag{6.18}$$

where $L_{CL}{}^{t}$ is the contact line at time *t* and *k* is rate constant of the usual form:

$$k = A_{\mathrm{e}}{}^{-\frac{E_A}{RT}} \tag{6.19}$$

where:

A = pre-exponential frequency factor for the reaction
$e^{-EA/RT}$ = exponential factor with activation energy E_A
R= universal gas constant (8.314 J k^{-1} mol^{-1})
T= absolute temperature k = reaction rate constant

As the contact line increases with branching capillary wetting, the rate of infiltration is expected to increase rapidly. As a working hypothesis the following is suggested with regards to $\theta_{critical}$.

The hatched surface in Figure 6.25 is the area which must undergo chemical change (molecular restructuring) by branching capillary wetting to allow a soil of contact angle θ to reach the second layer. Here, *d,* is the depth of penetration of the water drop on the soil surface and $d_{critical}$ is the depth required for water to contact the second layer of grains. This depth is only achieved when the contact angle reaches $\theta_{critical}$. In order to achieve $\theta_{critical}$ the soil surface must undergo molecular restructuring to permit water to flow to the critical depth whereby it can contact the next layer of soil grains.

Consider the scenario where $\theta \leq \theta_{critical,}$ here rapid infiltration through the first layer of soil grains around the drop would be expected, followed by branching capillary wetting through the pores of the soil. If $\theta > \theta_{critical}$ rapid infiltration cannot occur, therefore the transition from adhesional-immersional wetting to capillary wetting requires some change in the chemical nature of the solid-liquid interface i.e. molecular restructuring.

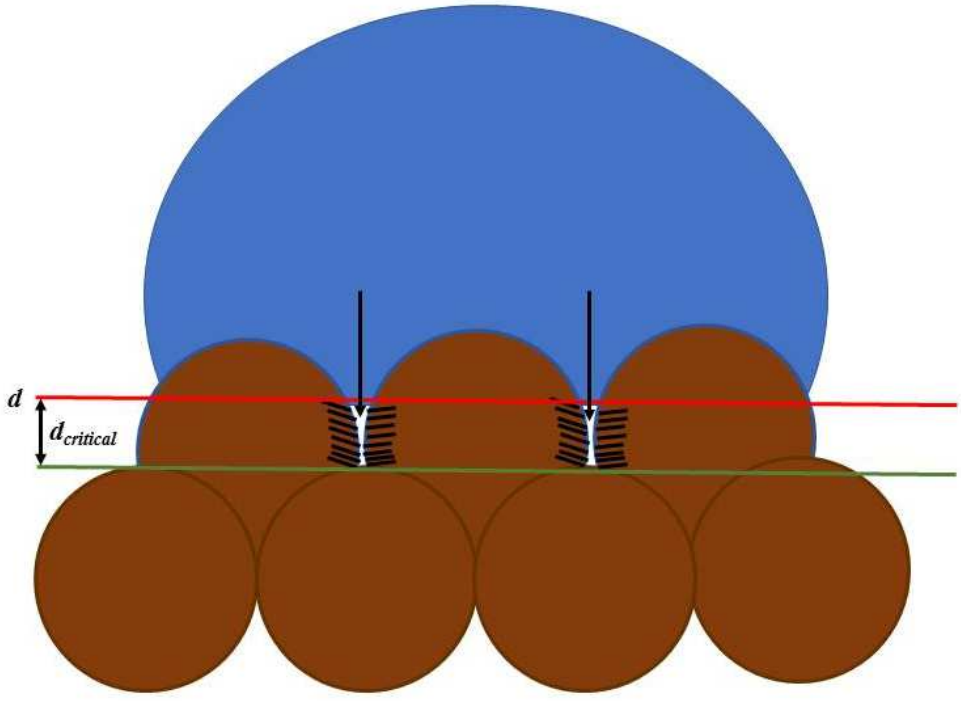

Figure 6.25 Schematic of water droplet sitting on soil grains. Branching capillary wetting and infiltration cannot occur until hatched area undergoes molecular restructuring to permit water flow. The depth from where the water drop is sitting on the grains to the critical depth where it reaches the second layer of grains is controlled by the restructuring process and $\theta_{critical}$.

If $\theta \leq \theta_{critical,}$ rapid adhesional-immersional wetting followed by rapid infiltration is expected. If $\theta_{critical} < \theta < 90^{o}$ rapid adhesional-immersional wetting followed by slower initial infiltration rate which will accelerate as the solid-liquid contact increases during the branching capillary wetting process can be expected. If $\theta_{critical} < 90^{o} < \theta$ no branching capillary wetting will occur and the water will not penetrate to the next layer of soil grains, without some chemical restructuring on the surface.

Overall, this model predicts a difference in behaviour for soil with $\theta \leq \theta_{critical}$ and those where $\theta > \theta_{critical}$. A schematic of the overall process is given in Figure 6.26 and a discussion of the significance of the model in section 6.3.4.

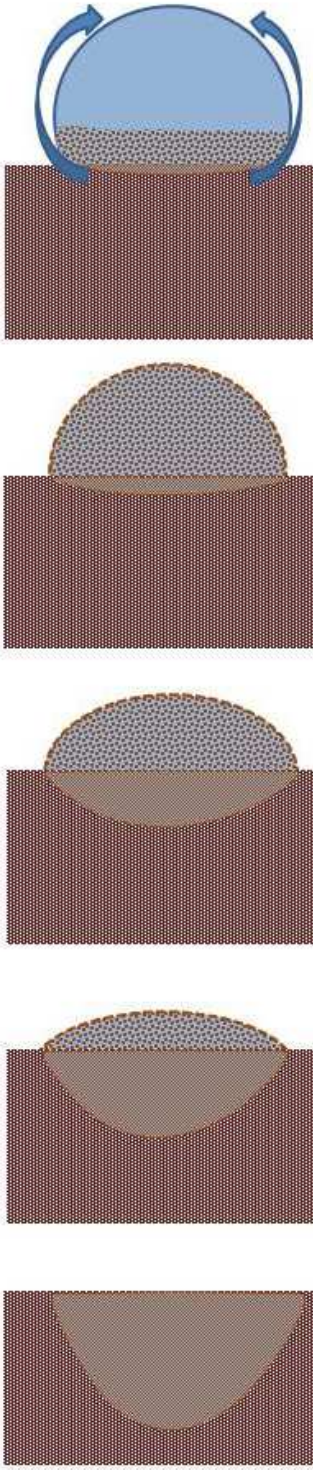

Adhesional-immersional wetting is the initial stage where water drop is dispensed onto soil surface and grains are forced up and around the water droplet. The liquid-vapour interface is reduced by adhesional-immersional wetting of soil grains, leading to a layer of packed grains around the droplet.

Adhesional-immersional wetting continues as the water droplet becomes fully (as shown) or partially covered by a loose-packed layer of soil grains. Due to removal of grains up around the drop a small crater is formed underneath the water drop.

Branching capillary wetting commences through the first layer of adhering grains in the bulk soil, where the packing of many soil grains create capillaries into which the water can spread.

Branching capillary wetting continues to extend the wetting front contact line.

Full penetration of water droplet into soil.

Figure 6.26 Schematic showing proposed model and wetting processes and stages for the penetration of water drop into a water repellent soil.

6.3.4. Discussion of significance of the model

The model proposed in this chapter and outlined in Figure 6.26 is to the best of the author's knowledge the first detailed model proposed for water drop penetration into a dry water repellent soil. The model provides physical insight into the processes involved in infiltration and gives an explanation for why a water droplet may stay on the soil surface for a prolonged period of time. The introduction of the different stages allows consideration of the various factors that influences these stages individually. The model also introduces some concepts which are experimentally verifiable e.g. the two stage process, and this will be the subject of experimental work described in the remaining sections of this chapter.

6.3.5. The initial state

Starting with a static water droplet on the soil surface in contact with some soil grains immediately beneath the droplet *in their original positions on the surface*, i.e. before there is any movement of soil grains. Note that this is not an equilibrium position because at this stage the surface forces acting on the soil grains are unbalanced and will pull soil grains upwards and onto the surface of the water droplet in the first, adhesional-immersional, stage of wetting. In energetic terms the major driving force is the reduction in the high energy water-air interface and its replacement by the lower energy soil-water interface, the energy of which depends upon the hydrophobicity of the soil. Water has a surface energy of 72.75 mJ m^{-2} in air at 20 ^{o}C (Lide, 1994).

6.3.5.1. Soil characterisation in initial state: particle size distributions, bulk density and surface roughness

The mean particle diameter range of soils used was 274.0 – 334.9 μm and total carbon content from 0.45 to 2.19 wt %. Fractional void space increases with lower bulk density and loose and close packed bulk density is given in Table 6.5.

Table 6.5 Soil bulk density, mean particle size, fractional void space and total carbon data.

Soil	Bulk density loose-packed/ g cm^{-3}	Bulk density close-packed/ g cm^{-3}	Mean particle diameter/ µm	Fractional void space	Average total carbon/ Wt %
NIC2	1.443	1.598	334.9	0.397	0.67 ± 0.07
LLAN1	1.208	1.459	274.0	0.450	2.19 ± 0.44
NIC1	1.418	1.603	322.7	0.395	0.45 ± 0.03
NL1	1.184	1.405	286.9	0.470	1.52 ± 0.33

6.3.5.2. Soil surface roughness: profilometer

Soil surface roughness is recognised as a factor that can influence water repellency measurements (McHale *et al.*, 2005; 2009). Profilometer measurements were made using a Dektak profilometer on UKC soil adhered to a glass microscope slide using double-sided tape. UKC soil has a mean particle diameter of 435 µm and whilst this is larger than the other sandy soils used, the results provide a representative insight into typical surface roughness for this textural class. Profile data was collected over 10,000 µm lengths and at 25 µm spaced intervals. Cross-sectional profiles show the variability in surface roughness that a water droplet will come in to contact with. A series of profiles taken from equal distances over a 10,000 µm sample are compiled in Figure. 6.27, with typical 20 and 50 µl droplet widths (taken from goniometer images) for NIC2 and NL1 provided to emphasise the difference in soil surface footprint coverage between these droplet volumes and the effect of water repellency levels on drop contact area.

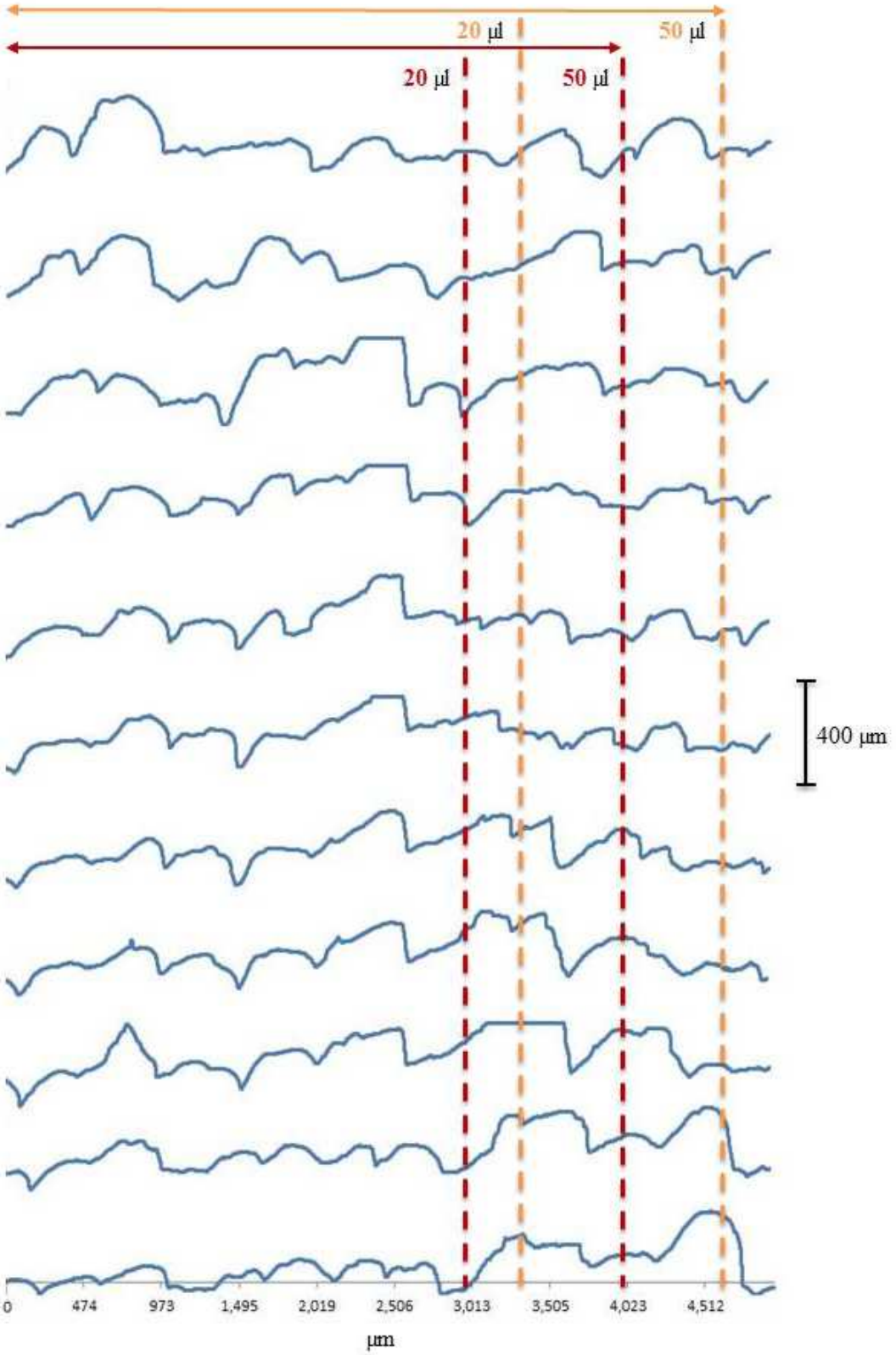

Figure 6.27 Cross-sectional profiles from profilometer measurements on UKC (wettable sandy dune soil) showing surface roughness. Approximate indications of diameters for 20 and 50 µl droplets on NIC2 (orange) and NL1 (red) soils based on goniometer test images are given to demonstrate typical contact areas for droplets on a soil surface and how they vary with repellency levels (NIC2 his classified as strongly repellent and NL1 as extremely repellent). Vertical scale marker included.

The heterogeneous nature of the soil underneath a water drop means that repellency measurements for smaller droplets are based on fewer particles compared with those of larger droplets. The data in Figure 6.27 highlights the impact a variation in footprint size from a 20 µl drop compared to a 50 µl drop can have. Hallin *et al.* (2013) found that, for the WDPT test, smaller drops give a more representative insight into the variability of the soil water repellency at the micro-scale due to fewer particles being covered by the droplet footprint. As a result, the WDPT measurements for small droplets are likely to be more variable. Whereas larger drops provide a better assessment of the bulk soil water repellency. Evidently both droplet volume and surface roughness are important variables to consider when measuring water repellency in soils, particularly when using the WDPT test.

6.3.6. The final state

6.3.6.1. Water drop penetration time test

Water drop penetration time (WDPT) tests as described in section 6.2.1, classified NIC1 as strongly-severely repellent, NIC2 and LLAN1 as strongly repellent, and NL1 as severely-extremely repellent depending on drop volume used (Table 6.6). Table 6.6 includes end mass of each pellet obtained from the WDPT test.

Table 6.6. Average water drop penetration time (WDPT) test data and standard error of the mean (SEM) for six droplets per volume size for each soil type and average end mass of pellet from WDPT tests.

Soil	Drops per test	Drop volume /µl	Average WDPT /s	WDPT classification (Bisdom *et al.*, 1993)	Weight dry pellet/g
NIC2	6	20	167 ±18.5	Strongly	0.1077
		30	136 ± 21.3		0.1714
		50	142 ±23.2		0.2832
		80	126 ±24.7		0.4300
		100	101 ±25.2		0.5896
LLAN1	6	20	221 ±32.7	Strongly	0.0800
		50	257 ±53.3		0.1936
		80	242 ±67.6		0.3271
		100	172 ±26.3		0.4089
NIC1	6	20	840 ±122.3	Strongly-Severely	0.0954
		50	730 ±42.8		0.2590
		80	544 ±58.6		0.4300
		100	523 ±162.3		0.5194
NL1	6	20	9558 ±366.3	Severely - Extremely	0.0127
		50	11117 ±1681.5		0.0622
		80	11693 ±1147.4		0.1339
		100	12301 ±310.0		0.2143

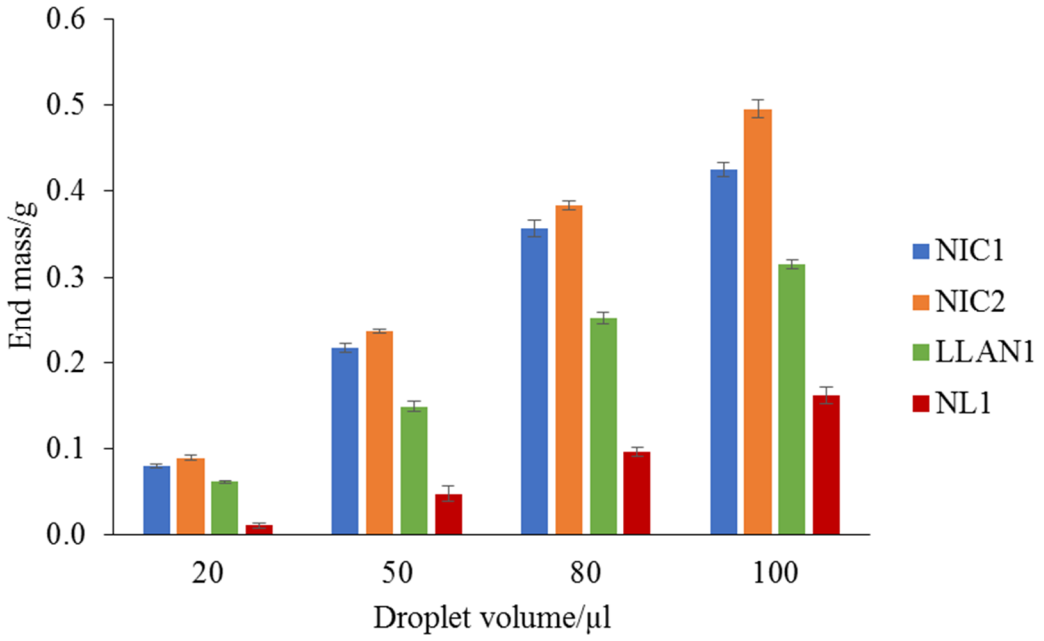

Figure 6.28 Water drop penetration time (WDPT) test end pellet dry masses (g) of NIC1, NIC2, LLAN1 and NL1 soils and one standard error of the mean error bars.

The general trend of end masses of WDPT pellets show (Figure 6.28), mass increasing with droplet volume. For NIC2, LLAN1 and NIC1 WDPTs decrease with increasing drop volume whereas for NL1, the most repellent soil, WDPTs remain constant within experimental error with increasing drop volume.

6.3.6.2. Dimensions of wetted soil pellet over penetration time: liquid nitrogen measurements

Experiments using liquid nitrogen on AUC soil (chosen for its long WDPT) to freeze droplets at different stages of the penetration process found that, over time, the droplet/soil pellet increased in diameter to *ca*. twice that of the original droplet, (Figure 6.29) while penetrating the soil to a depth of ~7 mm. Thus showing the water spreading laterally as well as vertically in the infiltration process.

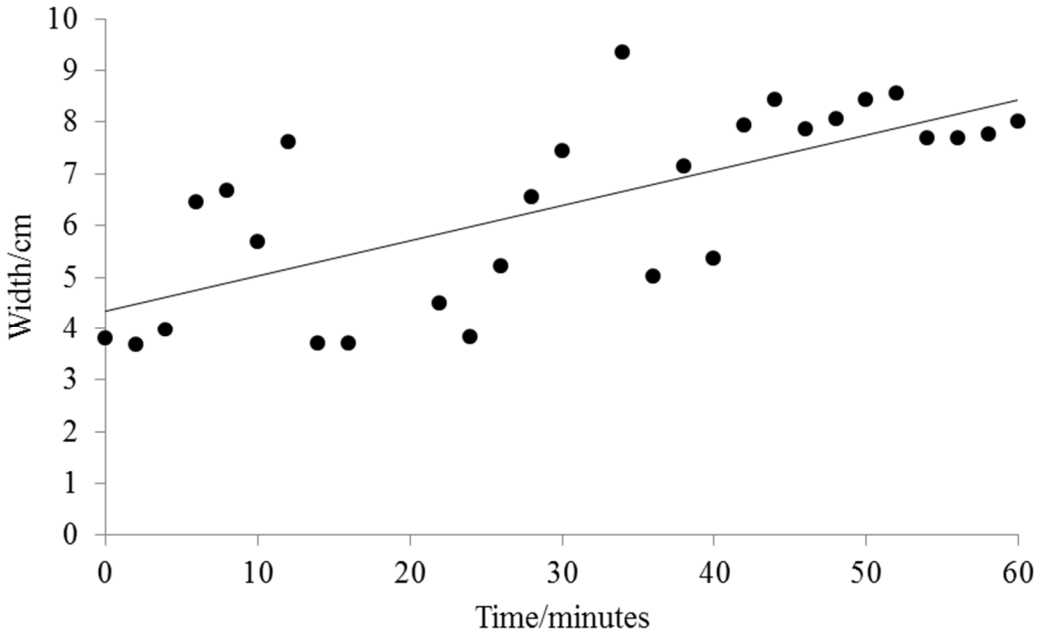

Figure 6.29 Width dimension measurements of frozen, wetted soil pellet against penetration time using liquid nitrogen.

6.3.7. Kinetics: considering the transition from initial to final state of wetting

6.3.7.1. Activation energy

Preliminary tests looking at how WDPT is affected by temperature used UK2 soil which has an average WDPT at room temperature of ~16 s. This soil was chosen due to adequate supply and as it has a relatively short WDPT time subtle changes with temperature could be easily observed. The average WDPT results over a range of temperatures are given in Figure 6.30. The average WDPT for this soil changed from 16 s at around 20 ^{o}C to 10 s at 32 ^{o}C and 39 s at 5 ^{o}C. The activation energy was calculated as 33.6 ±1.7 kJ mol^{-1} which is somewhat lower than the 42 kJ mol^{-1} measured by Diehl and Schaumann (2007) on the water repellent soils used in their study. Diehl and Schaumann (2007) suggest chemical reactions require an activation of > 60 kJ mol^{-1}, whilst physically controlled processes require an activation energy of < 42 kJ mol^{-1}. In this work, this suggests that the activation energy is a result of a physical restructuring rather than a chemical transformation.

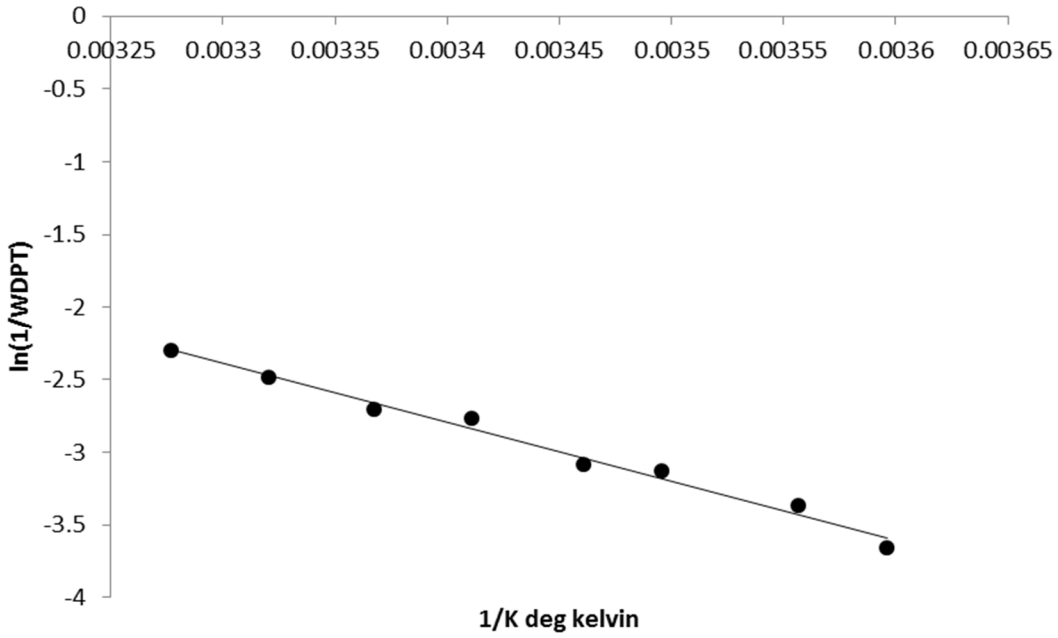

Figure 6.30 Arrhenius plot for water drop penetration time on UK2 soil, showing relationship between temperature and penetration time.

6.3.8. Adhesional-immersional wetting

During the adhesional-immersional wetting stage, soil grains are observed jostling underneath the water drop, which results in grains being forced up and around the drop.

For the wetting of water repellent soils by a water drop, mechanical energy is required to lift soil grains up and around the droplet during the adhesional-immersional stage of the wetting process. As soil grains become adhered to the droplet surface it causes a loss in water-air interface which is replaced by the creation of a soil-water interface. Calculations of the energetics of this process indicate that the energy released through the destruction and formation of interfaces is enough to lift soil particles (of the sizes found in soils used here) to the top of a 100 µl droplet, although this does not include any consideration of inter-particulate or particle-water friction inhibiting movement.

In water repellent soils the water droplet will become covered by a single layer of soil grains over time, how quickly this happens is dependent on the severity of the repellency present. During this process it appears that the drop begins to penetrate into the soil, however the drop is actually sitting lower than the initial soil surface, in the small crater that has formed from the grains that have been displaced from underneath the drop. The grains adhered to the water drop surface are not wetted fully, but, as previously described, penetrate into the drop with a depth determined by (γ^{SL}-γ^{SV}) for the soil surface.

6.3.8.1. Adhesional-immersional wetting: optical microscopy and time-lapse images

The optical microscopy and goniometer time-lapse images of NIC1 (Figures 6.31 and 6.32) provide visual confirmation of the initial adhesional-immersional wetting stage in water repellent soils. Loosely packed soil grains can be seen adhered to the outside of the water droplet and partly immersed in both instances. Observations made during the WDPT tests suggested that this initial process occurred at different rates depending on the severity of the repellency of the soil. For example, a layer of soil grains covered the droplet on NIC2 and LLAN1 soils much more rapidly than for NIC1 and NL1. It is worth noting that for NL1, (extremely repellent soil), a full

coverage of soil grains often did not occur before the drop began to infiltrate into the soil.

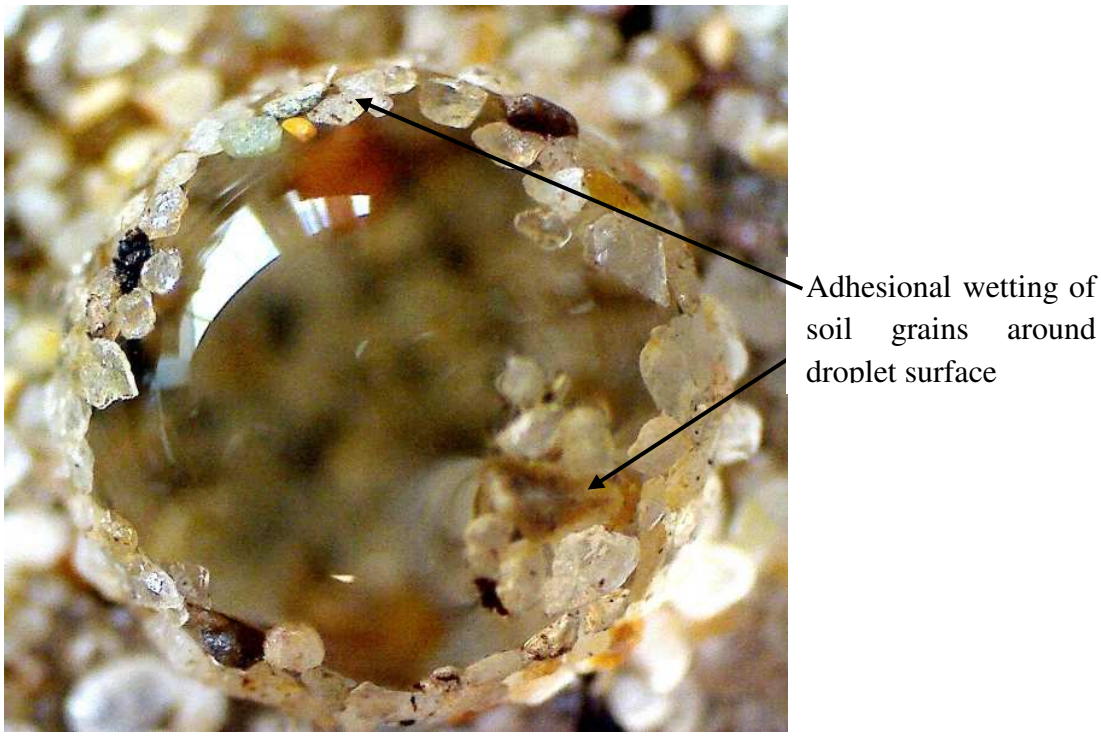

Figure 6.31 Optical microscopy image of water droplet (20 µl) on NIC1 soil showing adhesional stage of wetting process with grains adhered to the droplet surface.

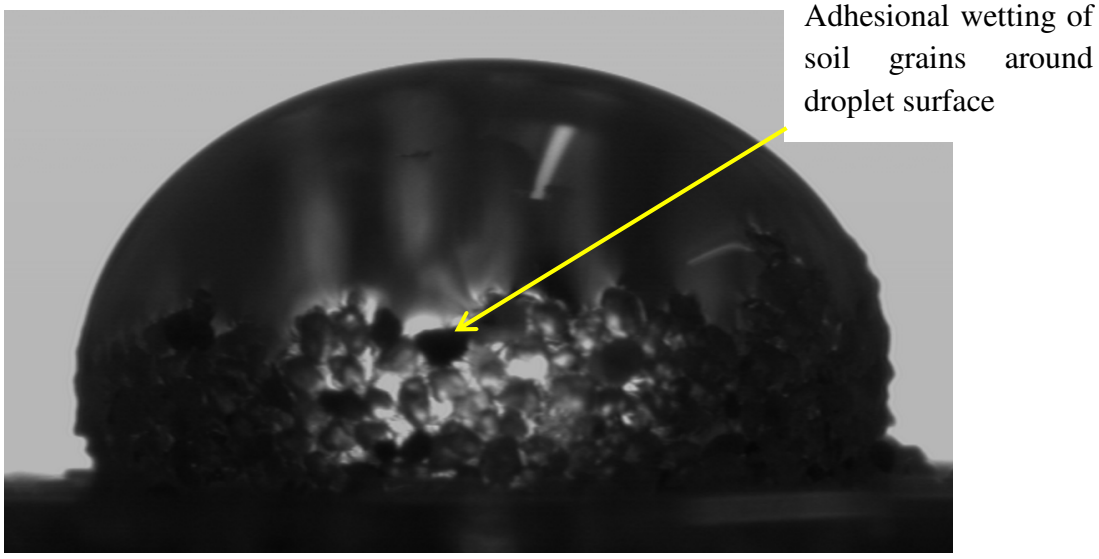

Figure 6.32 Goniometer time-lapse image of NIC1 soil with 50 µl droplet during penetration time showing adhesional stage of wetting process with single layer of grains adhered to the droplet surface.

6.3.8.2. Initial mass pick up (mass removal experiments)

The mass removal experiments aimed to measure the mass of soil grains wetted at different time intervals over the full period of water drop penetration time. Using the method described in section 6.2.5, the average initial soil grain masses (removed after ~ 8 seconds), which reflects the mass of grains adhered to the outside of the drop within that time period, are given in Table 6.7.

Table 6.7 Initial mass of soil removed (within 8 s) per soil type and droplet volume.

Drop volume / µl	NIC2	LLAN1	NIC1	NL1
	Mass/g			
20	0.0175	0.0152	0.0155	0.0052
50	0.0516	0.0176	0.0242	0.0078
80	0.0450	0.0225	0.0276	0.0118
100	0.0729	0.0354	0.0374	0.0158

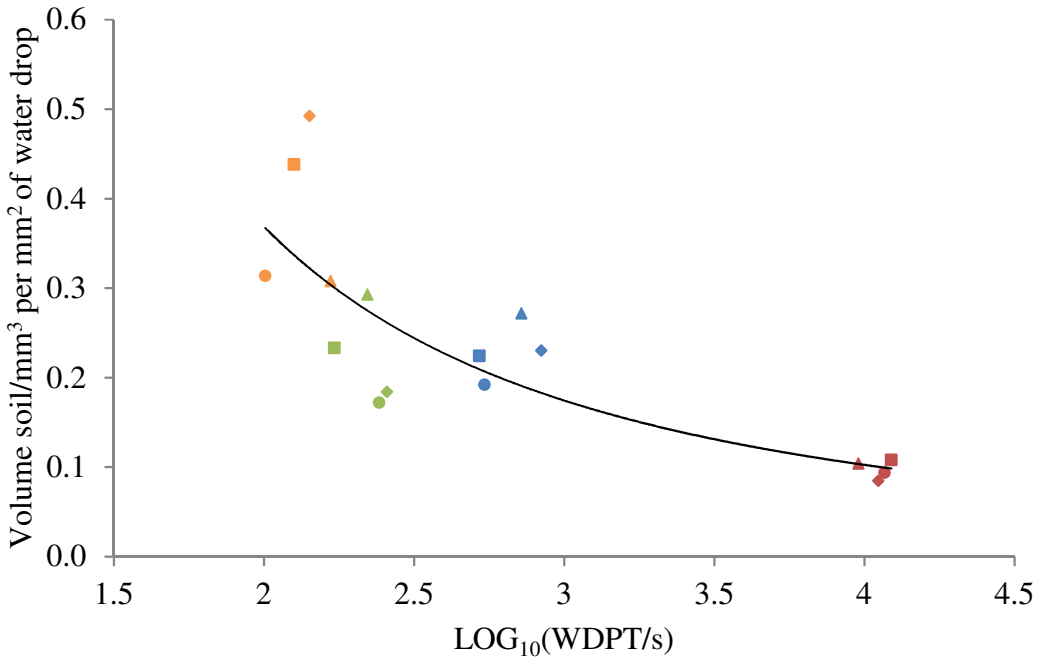

Figure 6.33 Initial volume of soil (mm^3) per mm^2 of water drop against water drop penetration time for NIC2 (orange) and LLAN1 (green) NIC1 (blue), and NL1 (red). Triangle (20 µl), diamond (50 µl), circle (80 µl) square (100 µl) soils at different droplet volumes. The curve has been included just as a guide for the eye. Bulk density of the soils has been taken into consideration.

Considering the initial mass removed against the WDPT, it suggests that for NIC2 which is the least repellent soil, that there is a 3-4 times increase in volume (mm^3) of soil per mm^2 surface area of the water drop, compared to NL1 which is the most repellent (Figure 6.33). The data here reflects observations made during the WDPT tests whereby soil grains are picked up and cover a water drop more rapidly for a less repellent soil compared to a more repellent one. This process can be explained by the polarity of the soil surface and the relevant surface energies involved.

A less repellent soil will have a more polar surface compared to a more repellent soil, and therefore less energy is required to form the solid-liquid interface. The rate at which this process occurs is dependent upon the hydrophobicity of the soil, for example in the case of NIC2, upon contact with water the droplet becomes rapidly covered with soil grains as there is a greater release of energy to allow this process to happen compared to the most repellent NL1. Due to the higher organic content of NL1, it is possible that the initial grain coverage of the surface will be dominated by the lighter organic fractions being preferentially picked up compared to the soil grains as a result of lower energy requirements.

6.3.8.3. Theoretical and experimental initial mass removal

Theoretical initial masses ($initial_{theo}$) were calculated for each soil type and drop volume, based on the assumption that a hemispherical drop was instantly covered by a complete single layer of spherical soil grains. In Figure 6.34a-d the experimental initial masses ($initial_{exp}$) are presented along with the calculated theoretical masses). For LLAN1, NIC1 and NL1 soils the $initial_{exp}$ mass is lower than $initial_{theo}$ mass. $Initial_{theo}$ mass assumes that a complete layer of soil grains is covering the droplet however, at the < 8 s extraction point for the $initial_{exp}$ masses for the soils mentioned a full soil grain layer has not yet been achieved, due to the repellency levels of the individual soils respectively which influence how quickly this process occurs. This initial stage of adhesional-immersional wetting clearly occurs over time and is not instantaneous. Due to the rapid adhesional-immersional process for NIC2, the least repellent soil it is much closer or even exceeds the $initial_{theo}$ mass, an explanation may be that due to the rapidly nature of the first stage of wetting the at the secondary stage of branching capillary wetting has already commenced here and therefore picks up a larger mass of grains that expected.

The least repellent soil, NIC2, highlights the difference in repellency level as it exceeds the $initial_{theo}$ mass for two of the four droplet volumes, and it is suggests that the next stage of the wetting process has already commenced by the point of measurement here.

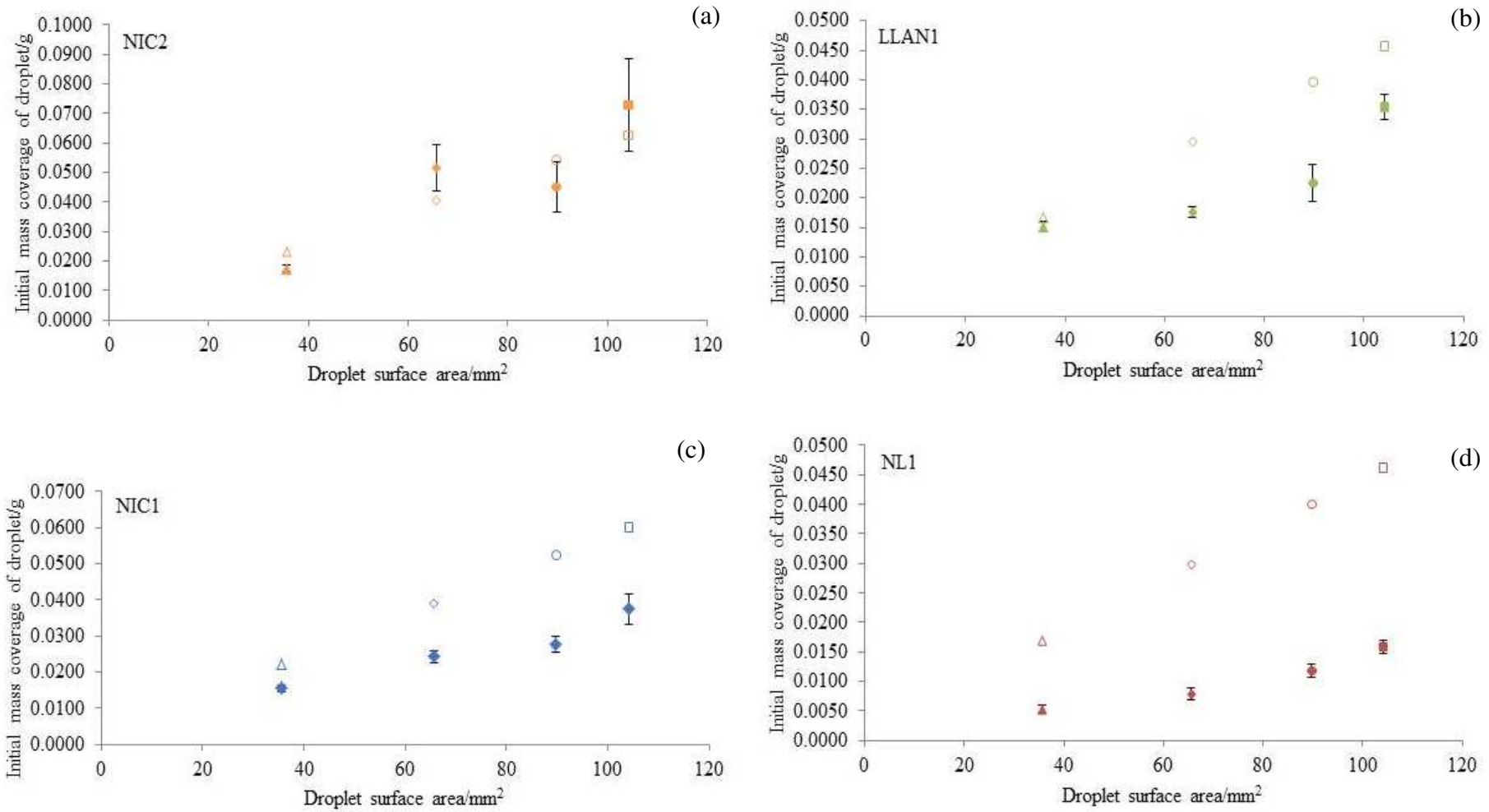

Figure 6.34a-d Average initial mass (closed data point) and theoretical initial mass based on spherical particles covering a hemisphere (open data point) (a) NIC2 (b) LLAN1 (c) NIC1 (d) NL1 and SEM (error bars are one SEM) for experimental mass data points.

6.3.9. Branching capillary wetting

Previous research (Douglas *et al.*, 2007) has suggested for spreading wetting to occur in water repellent soils, the non-polar organics present on the surface of the soil grains will have to undergo chemical changes or reorientation of molecules to permit the penetration of the polar water wetting front through into the soil profile.

6.3.9.1. Mass removal of grains over water drop penetration time

Data from the mass removal over time experiments is presented in Figures 6.35-6.38. Mass removed as a function of time varies with both droplet volume and soil water repellency. The general shape of the curves suggests two initial kinetic interpretations: 1) A 'two stage process' with an initial period where the mass removed increases slowly steadily with time until a point is reached where there is a rapid increase in mass removed. 2) A single process represented by a single uniform curve with a higher than one order dependence upon time. Unfortunately, the quality of the data does not allow a clear distinction between these two possibilities. For NL1, the most water repellent soil tested, there is the added complication of evaporation over the long penetration time which might go some way to explain the rather scattered data at long times for this soil.

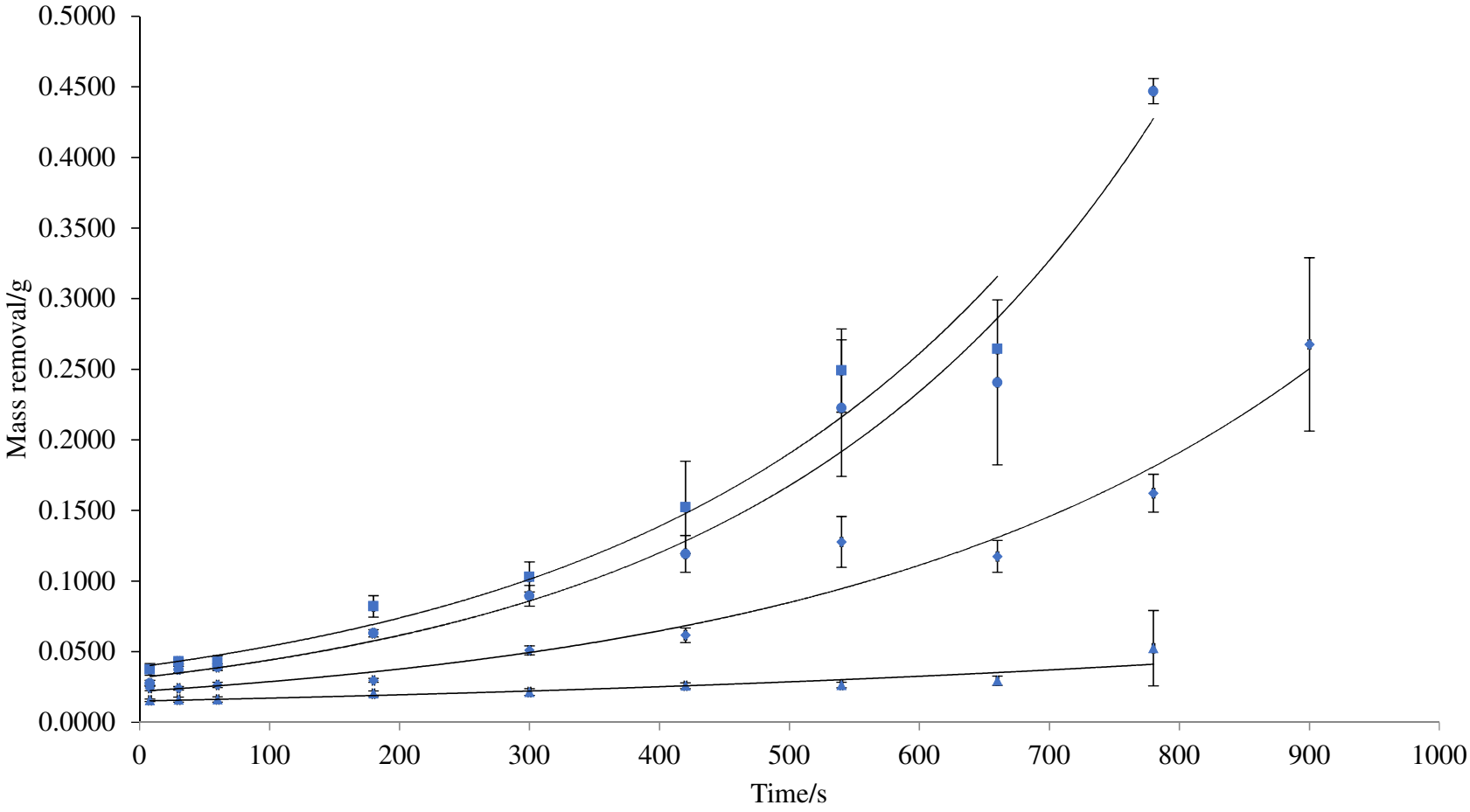

Figure 6.35 NIC1 mass removal of soil grains over time, 100 µl (square), 80 µl (circle), 50 µl (diamond), 20 µl (triangle) and one standard error of the mean error bars. The curves here have no interpretive value and are added as an aid for the eye to follow the data points.

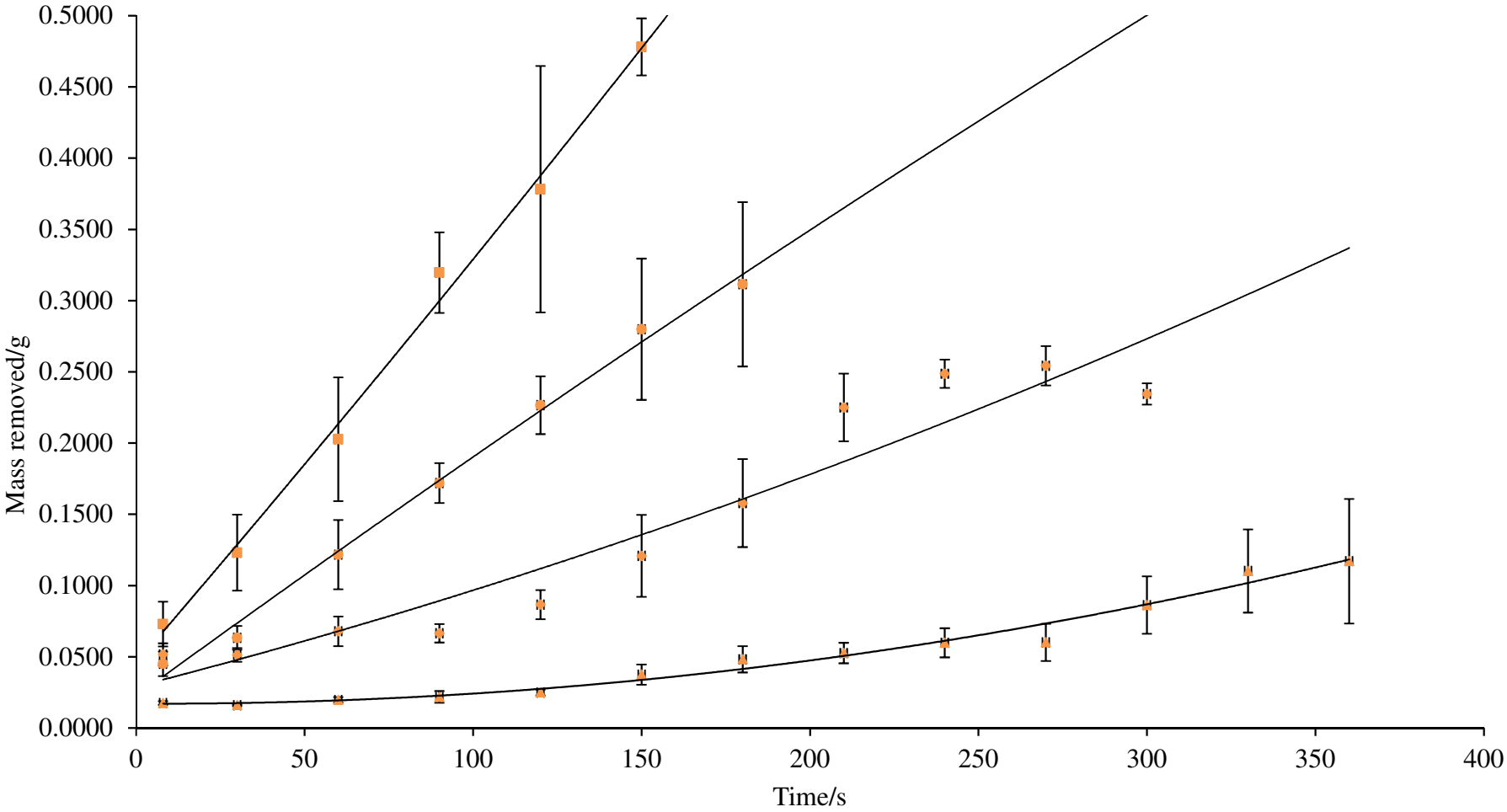

Figure 6.36 NIC2 mass removal of soil grains over time, 100 µl (square), 80 µl (circle), 50 µl (diamond), 20 µl (triangle) and one standard error of the mean error bars. The curves here have no interpretive value and are added as an aid for the eye to follow the data points.

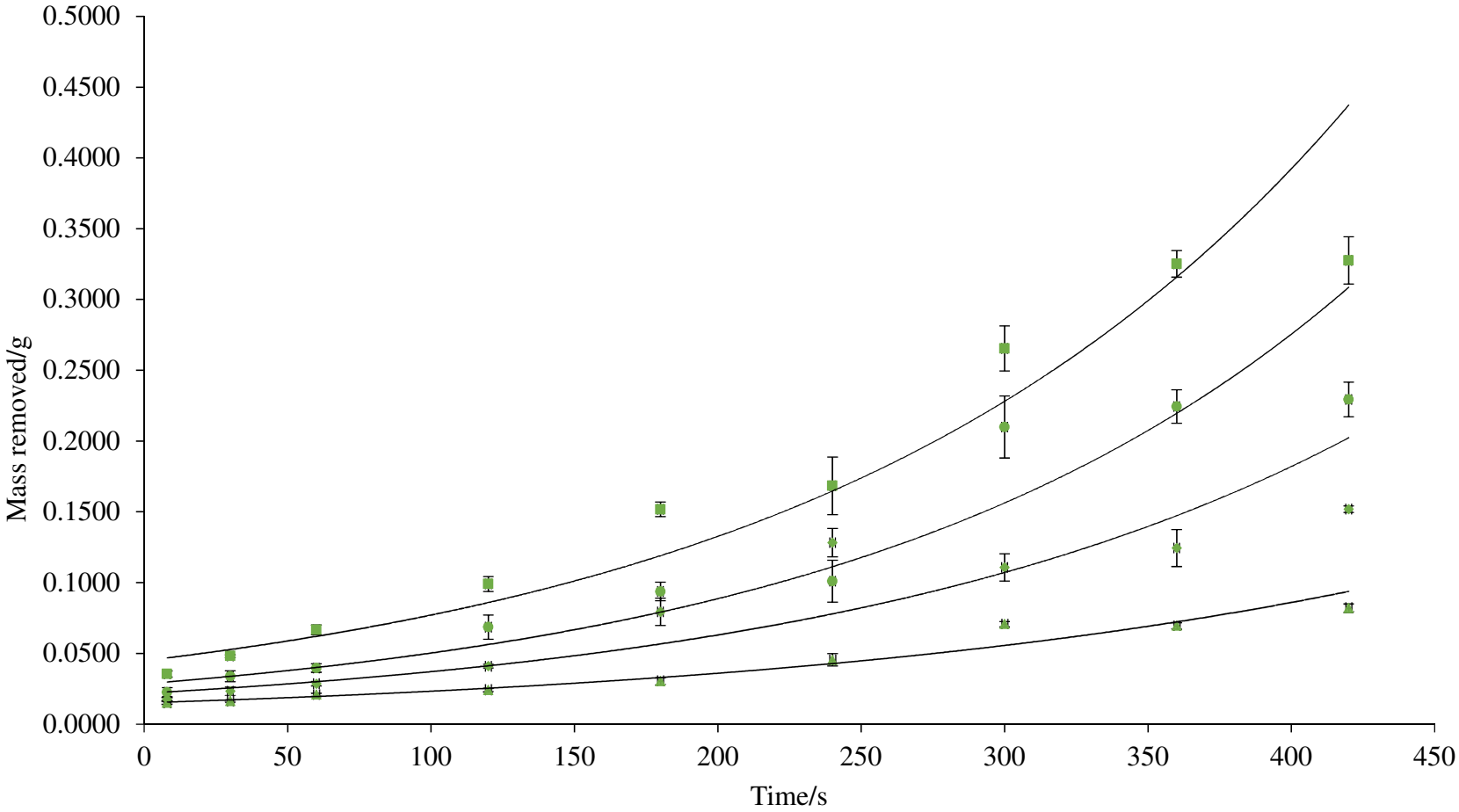

Figure 6.37 LLAN1 mass removal of soil grains over time, 100 µl (square), 80 µl (circle), 50 µl (diamond), 20 µl (triangle) and one standard error of the mean error bars. The curves here have no interpretive value and are added as an aid for the eye to follow the data points.

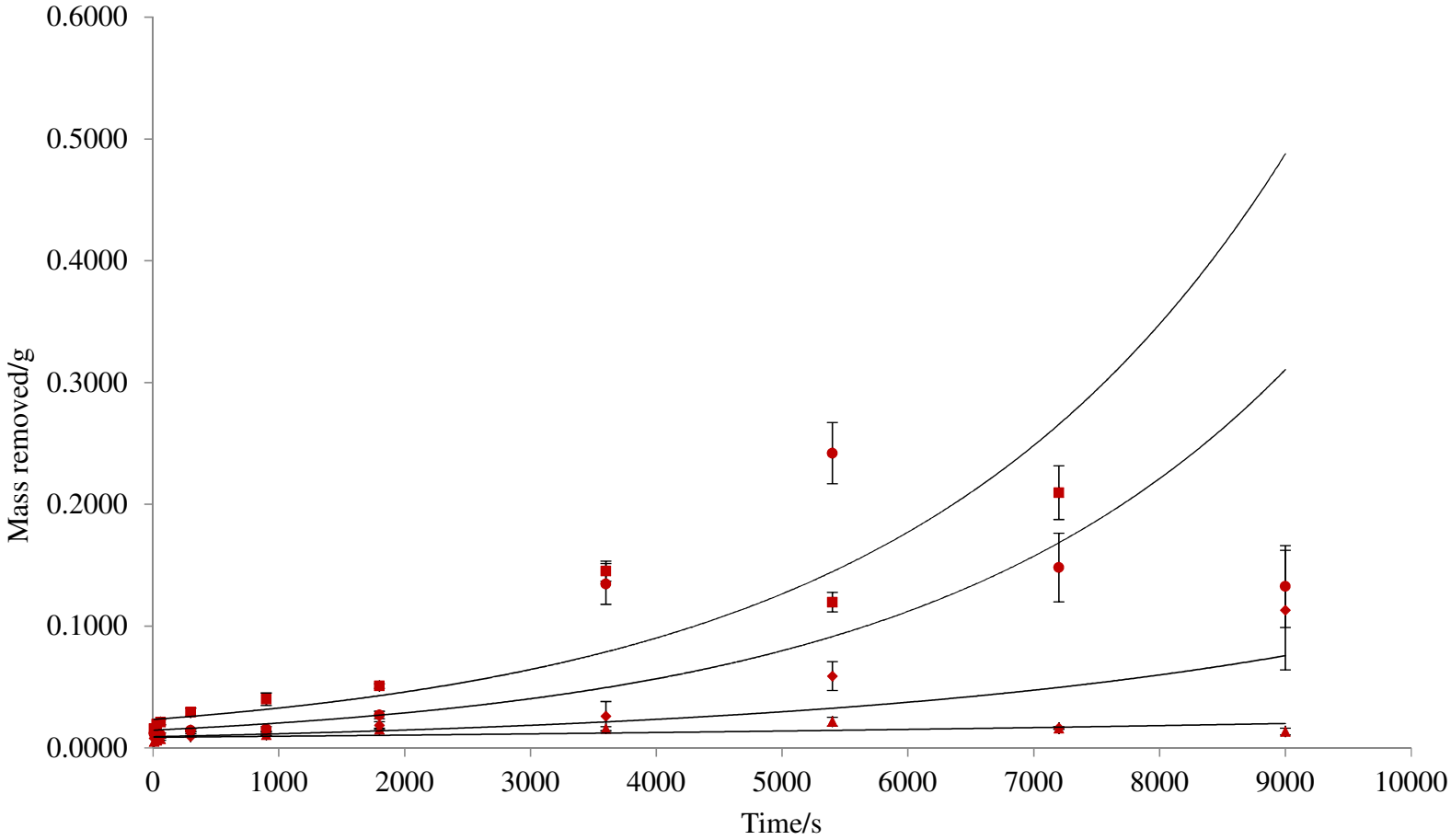

Figure 6.38 NL1 mass removal of soil grains over time, 100 µl (square), 80 µl (circle), 50 µl (diamond), 20 µl (triangle) and one standard error of the mean error bars. The curves here have no interpretive value and are added as an aid for the eye to follow the data points.

6.3.9.2. Time-lapse infiltration images: goniometer

WDPT time-lapse images taken using a goniometer, as described in section 6.2.8, can be used to provide a measurement of the volume of the water droplet which has not penetrated the soil over time. As soil grains cover the surface of the water drop, the drop will sit slightly lower than the initial soil surface in the small crater created from the movement of grains up and around the drop. Therefore, part of the droplet volume is hidden from view and the measured volume is less than the applied volume. Because of this, the percentage drop not yet infiltrated is given by the measured volume, plus this small hidden volume (the hidden volume is never more than 15 % and this is only in NIC2 soil which is the least repellent and therefore water will penetrated into the soil much more rapidly; for the remaining soils the correction is < 10 %). Therefore, a small correction for hidden volume in each instance was applied to the date in Figures 6.39-6.42.

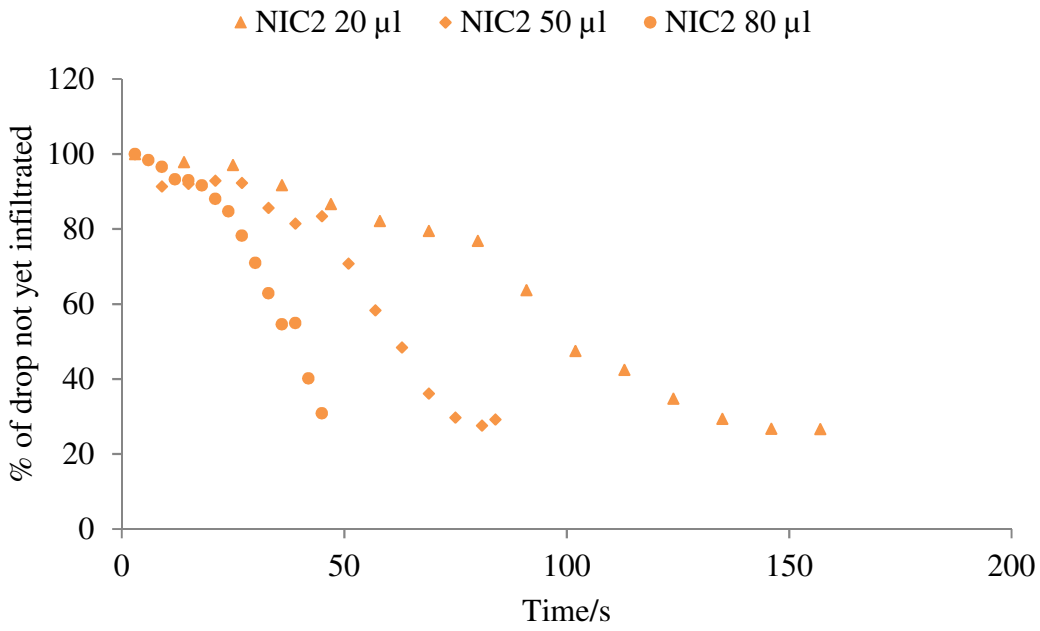

Figure 6.39 NIC2: volume of droplet not yet penetrated into soil over time as a percentage against time (adjusted for volume seen as discussed in section 6.3.9.2).

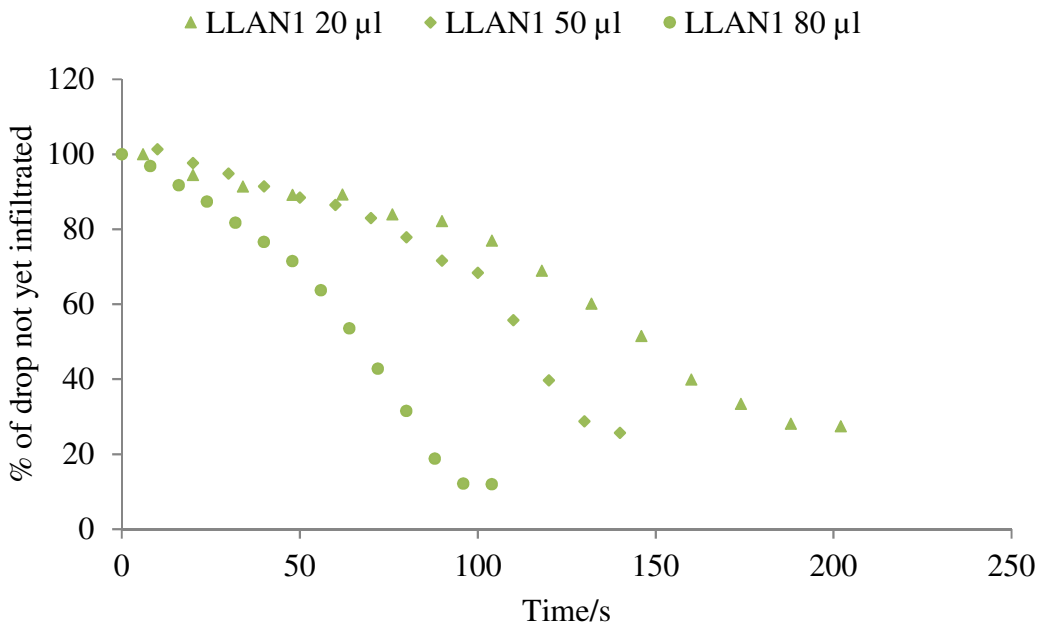

Figure 6.40. LLAN1: volume of droplet penetrated into soil over time as a percentage against time (adjusted for volume seen as discussed in section 6.3.9.2).

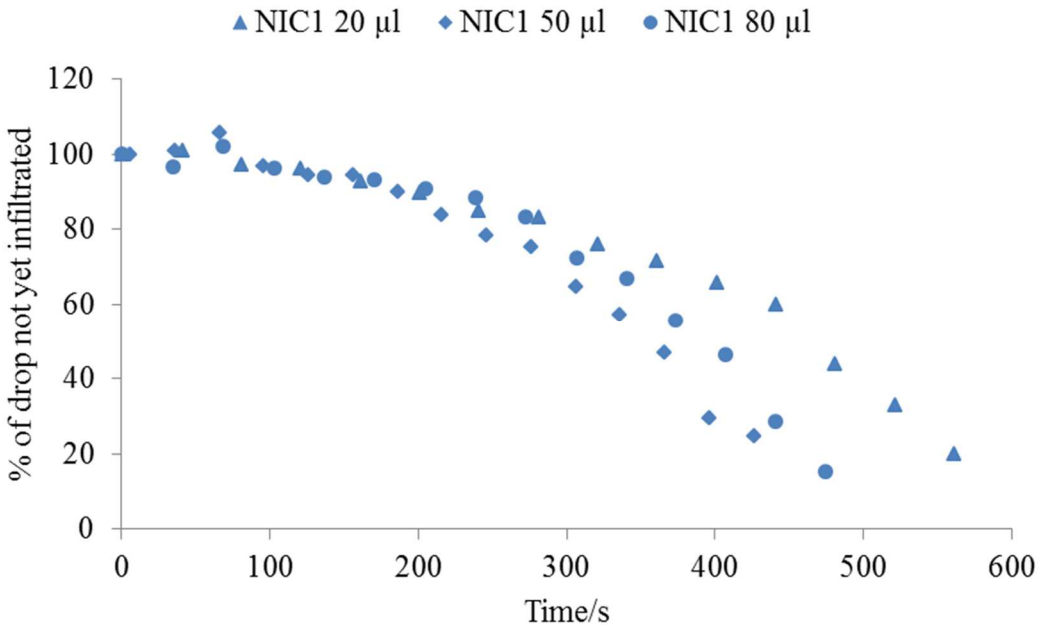

Figure 6.41 NIC1: volume of droplet penetrated into soil over time as a percentage against time (adjusted for volume seen as discussed in section 6.3.9.2).

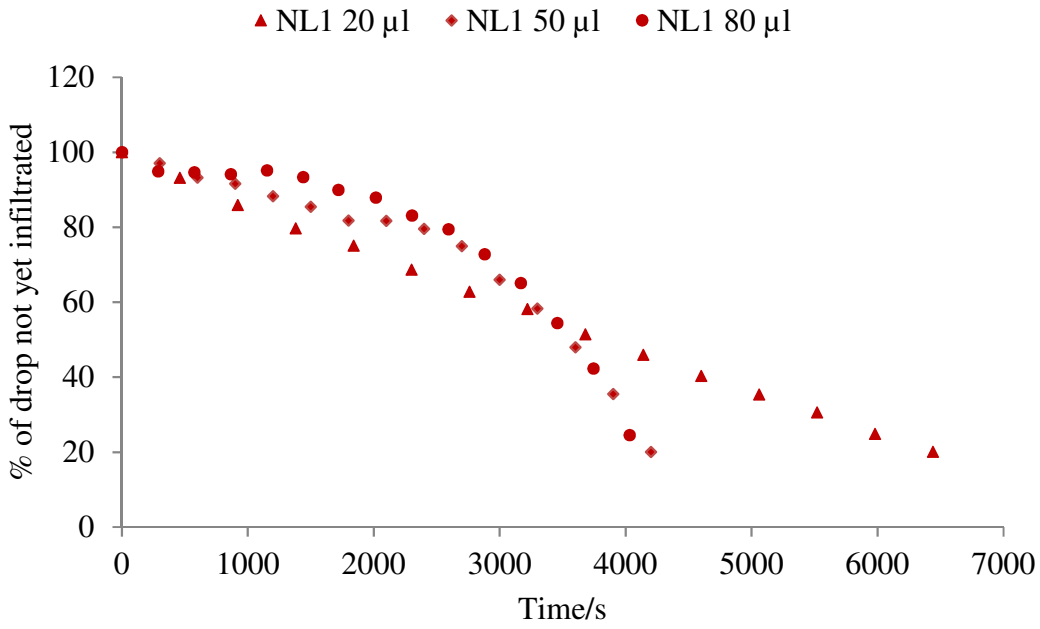

Figure 6.42 NL1**: v**olume of droplet penetrated into soil over time as a percentage against time (adjusted for volume seen as discussed in section 6.3.9.2).

The data in Figures 6.39-6.42 shows that in general small droplets (20 µl) take longer to infiltrate than large droplets. This behaviour matches that for mass removal but it is easier to see the different stages, and the data suggests a 'two stage process' with an initial period where the water penetration proceeds linearly and relatively slowly until a point is reached where there is a rapid increase in water penetration rate.

6.3.9.3. Contact angle transition zone (80-100º)

Contact angle measurements were calculated from the WDPT time lapse-images to explore any correlation between contact angle and the transition from a linear penetration rate to a rapidly increasing penetration rate. To begin, Figures 6.43-6.45 present the average contact angle θ (average of left and right θ per drop image), against the penetration time for a 20, 50 and 80 µl drop for NIC1 soil. In each instance a grey transition zone is suggested highlighting a region where water penetration proceeds from a relatively linear, slow rate, to one that is much more rapid. The WDPT static image either side of the suggested transition zone is provided to show the difference in contact angle between these points. Finally, the mass removal data is plotted against the goniometer penetration data to confirm any

trends in the data. It is expected that the mass removed would be a reflection of the percentage of water that had penetrated the soil at that point. The datasets are not directly comparable as the tests were carried out under different conditions, i.e. the mass removal experiments were conducted in a constant temperature/relative humidity room whereas the goniometer was restricted to the laboratory conditions where it was set up. As a result, to give the best fit between the data, the data has been adjusted by contracting the WDPT values for the mass removal experiments to compensate for the difference in WDPT times.

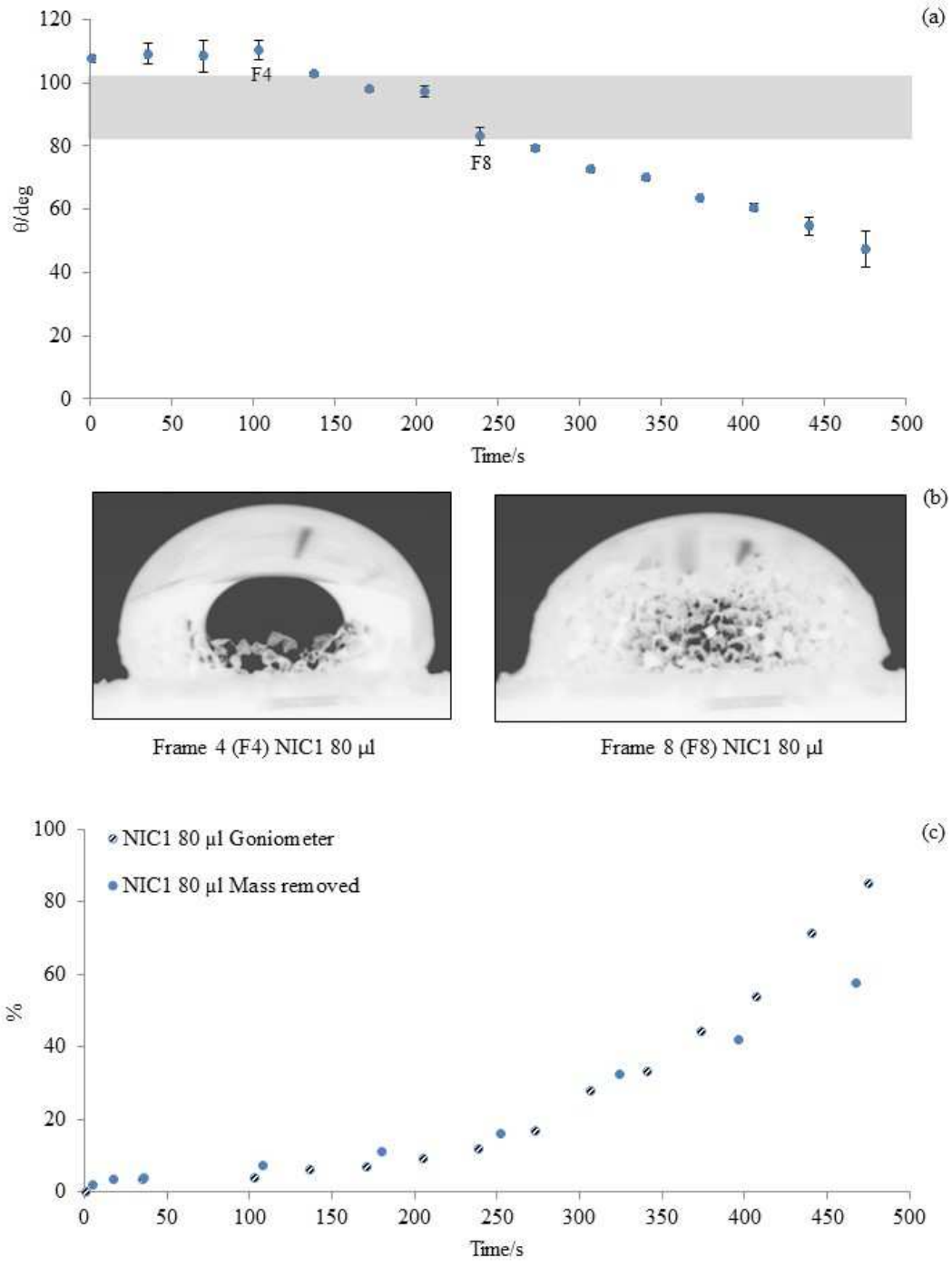

Figure 6.43 NIC1 80 µl a) Average contact angle (θ) from time-lapse goniometer images against time. Transition zone (grey) identified. b) Corresponding time-lapse images for either side of transition zone c) Goniometer and mass removal data plotted against time (data adjusted to allow for same WDPT timescales).

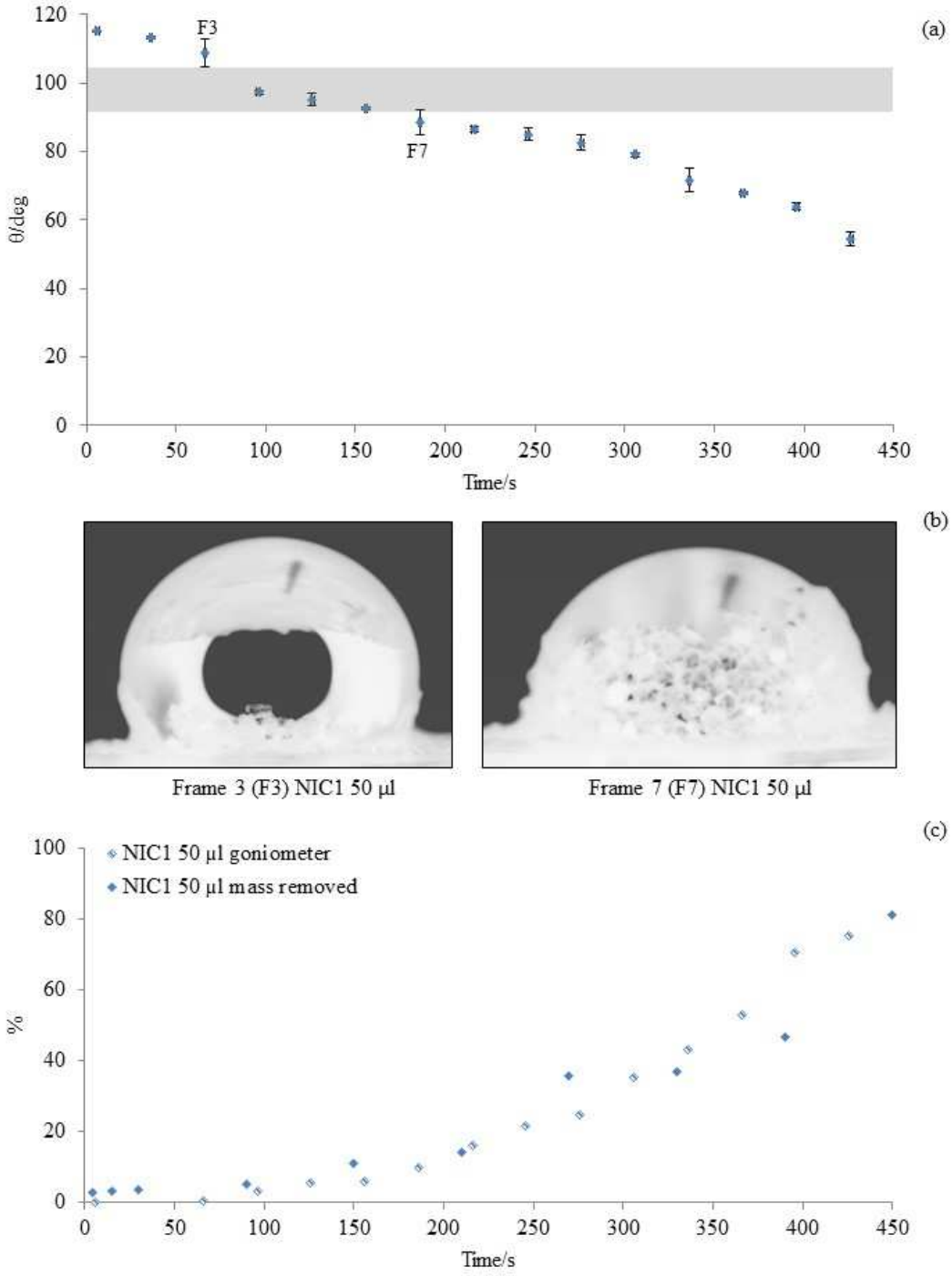

Figure 6.44 NIC1 50 µl a) Average contact angle (θ) from time-lapse goniometer images against time. Transition zone (grey) identified. b) Corresponding time-lapse images for either side of transition zone c) Goniometer and mass removal data plotted against time (data adjusted to allow for same WDPT timescales).

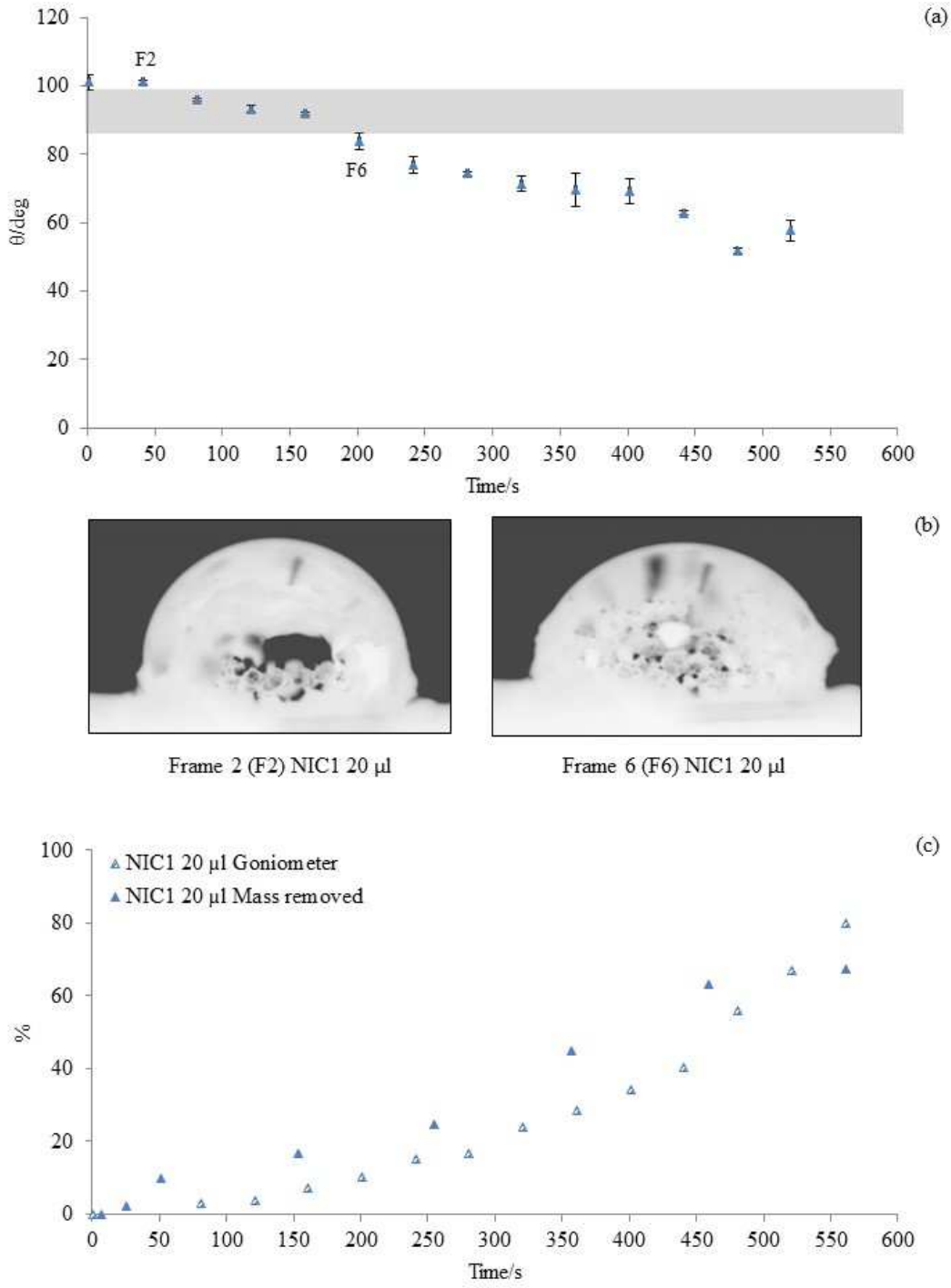

Figure 6.45 NIC1 20 µl a) Average contact angle (θ) from time-lapse goniometer images against time. Transition zone (grey) identified. b) Corresponding time-lapse images for either side of transition zone c) Goniometer and mass removal data plotted against time (data adjusted to allow for same WDPT timescales).

Where the contact angle appears to be ≥100^{o} the infiltration rate appears to be relatively steady, however once the contact angle drops to ~ between 80-100^{o}, the droplet begins to infiltrate more rapidly. The point at which the transition zone is reached is identified in Figures 6.43-6.45 and the corresponding droplet images for either side of the transition zone are presented for reference in each case.

6.3.9.3.1. Less water repellent soils

For soils NIC2 and LLAN1 which are less water repellent than NIC1, the results from the goniometer time-lapse images and mass removal over time comparison (Figures 6.46. and 6.47 for a 80 µl drop) identify that the contact angle of both of these soils reach the transition zone much more rapidly than for NIC1 (Figure 6.43). For both soils this means that the soil surface environment is already more polar and therefore more readily wettable, or the organics present (particularly perhaps in the case of LLAN1) can be chemically altered more rapidly than those present in NIC1. Due to the significant increase in speed for the wetting process in NIC2 it makes it more difficult to define separate wetting stages, i.e. where adhesional-immersional and branching capillary wetting starts and ends and it may be possible that both processes occur at the same time in more hydrophilic soils and the branching capillary wetting process becomes the dominant driving force. The overall patterns from the data obtained however support the model presented by the NIC1 data for the wetting process.

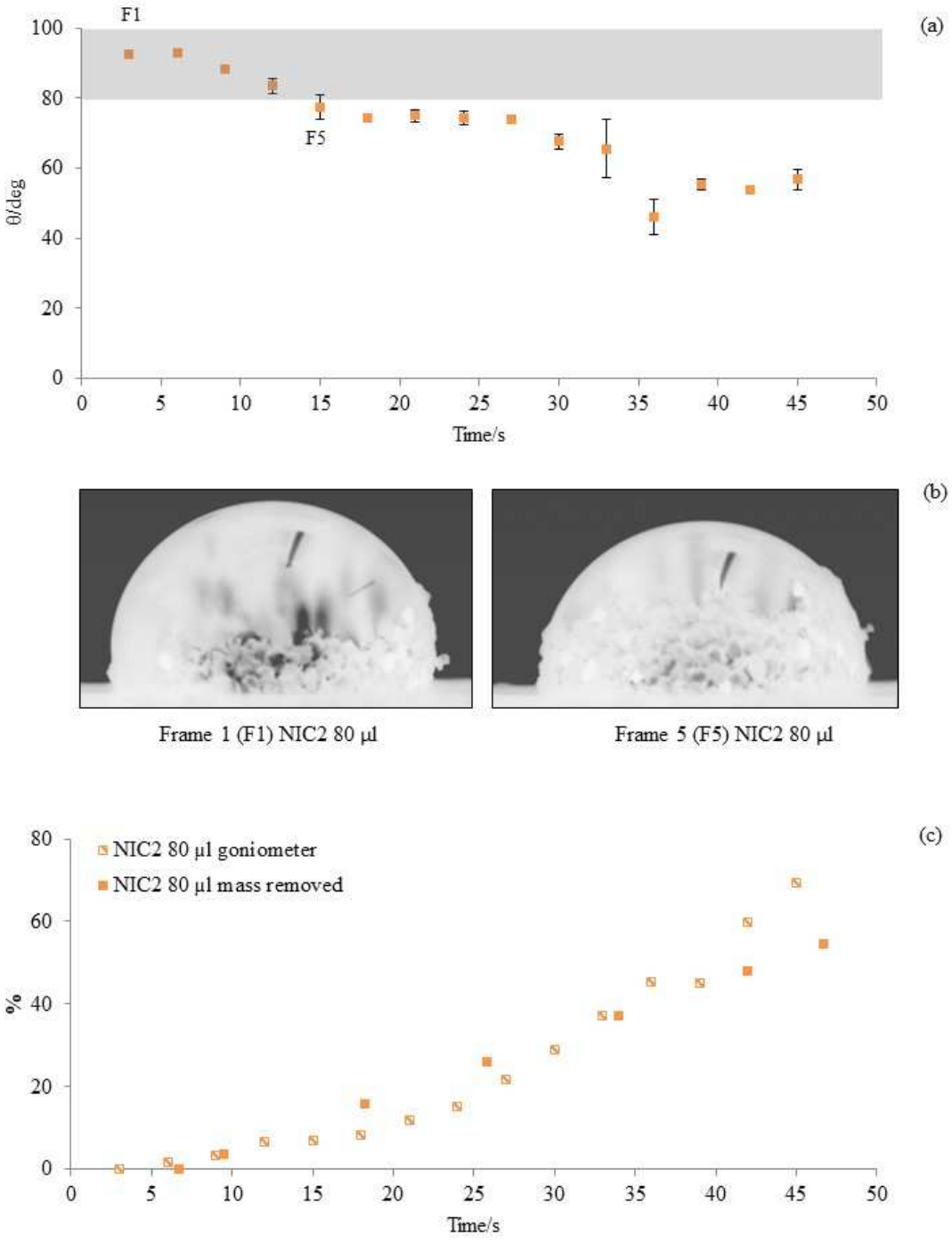

Figure 6.46 NIC2 80 µl a) Average contact angle (θ) from time-lapse goniometer images against time. Transition zone (grey) identified. b) Corresponding time-lapse images for either side of transition zone c) Goniometer and mass removal data plotted against time (data adjusted to allow for same WDPT timescales).

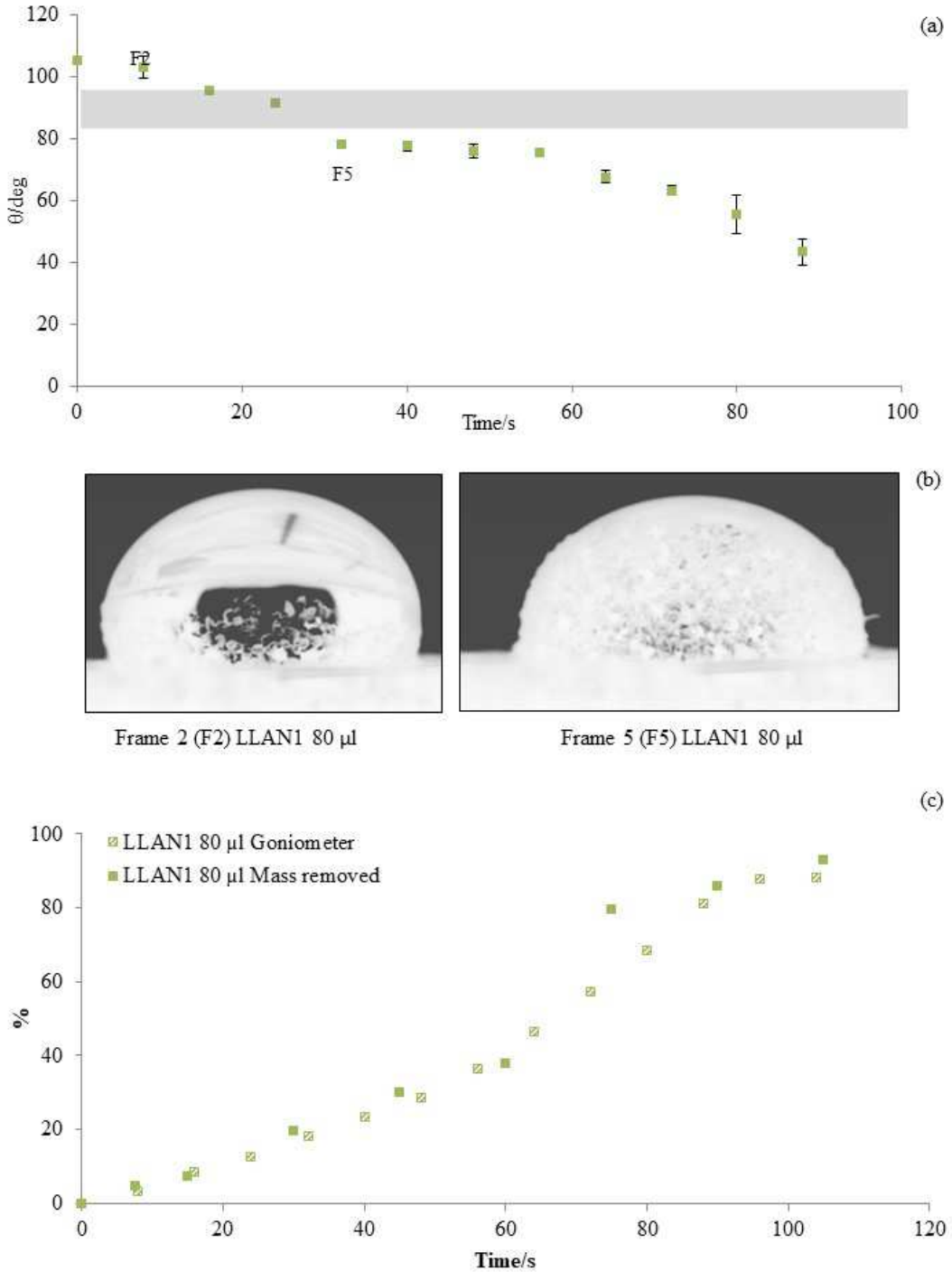

Figure 6.47 LLAN1 80 µl a) Average contact angle (θ) from time-lapse goniometer images against time. Transition zone (grey) identified. b) Corresponding time-lapse images for either side of transition zone c) Goniometer and mass removal data plotted against time (data adjusted to allow for same WDPT timescales).

6.3.9.3.2. More water repellent soils

For NL1 (Figure 6.48) which is significantly more repellent than NIC1, there are other variables to consider that will influence the results. The WDPT for NL1 is several hours, which means that evaporation will play a key role in the wetting process. Whilst overall for larger drops the general trends remain the same, the time taken to reach < 100^{o} contact angles is significantly longer. If evaporation causes a loss in droplet volume this will affect the amount of mass picked up over time as there will be less surface area for the grains to adhere to during the adhesional wetting process, and as this process takes a long time in severely water repellent soil, it is unlikely a full coverage of soil grains around the droplet will be achieved before evaporation becomes an issue. As a result of evaporation, a reduced volume of water droplet will be available to infiltrate into the soil and therefore result in mass removed at each stage being affected. Therefore, whilst the overall model may be applicable it is less reliable in severely repellent soils and as a result the mass removal technique may not be best suited for measurements on soils with severe repellency. However, the goniometer measurements give data consistent with a two stage process.

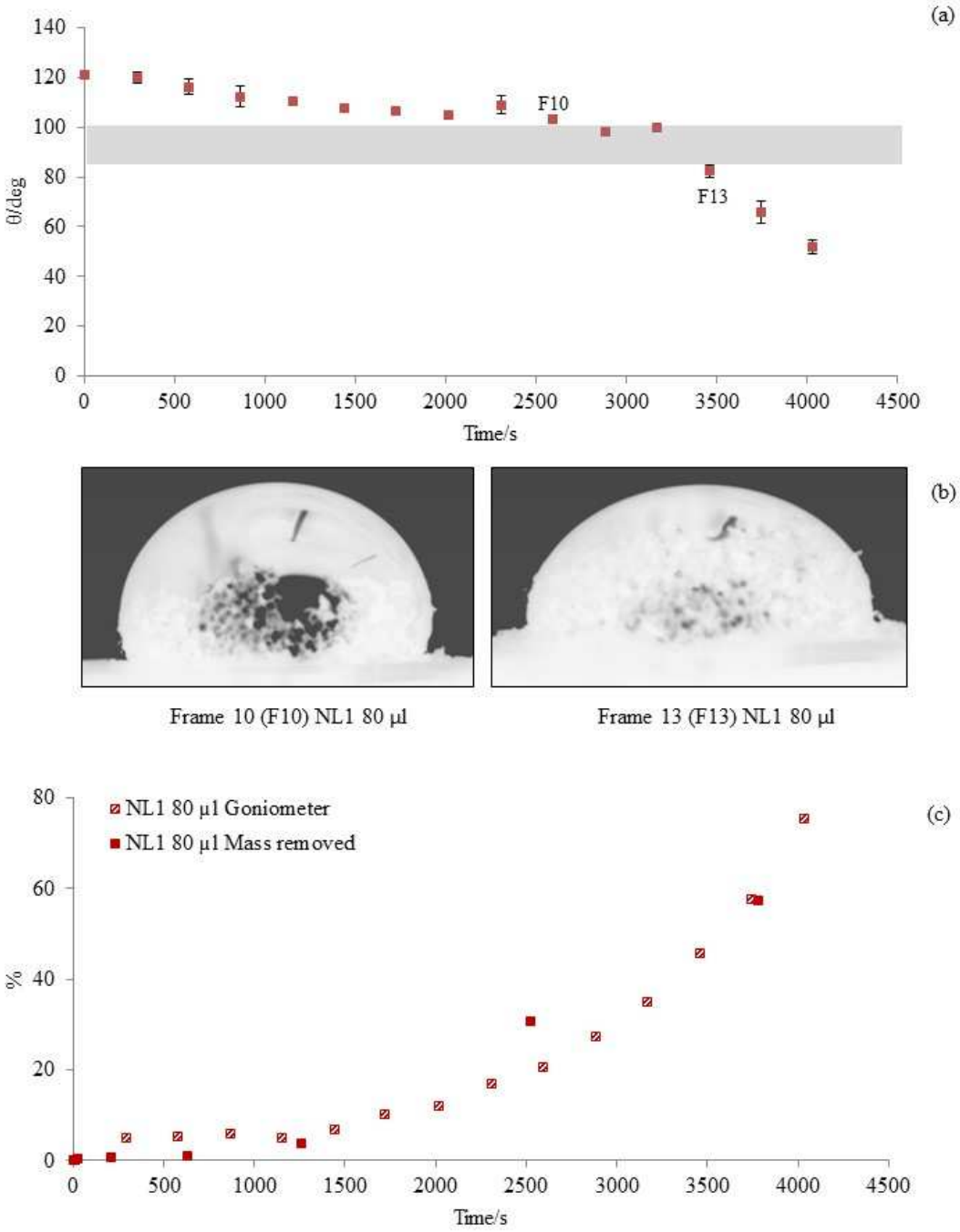

Figure 6.48 NL1 80 µl a) Average contact angle (θ) from time-lapse goniometer images against time. Transition zone (grey) identified. b) Corresponding time-lapse images for either side of transition zone c) Goniometer and mass removal data plotted against time (data adjusted to allow for same WDPT timescales).

6.3.10. Water drop penetration time through variable soil thicknesses (sinter data)

The details for the experiment are described in section 6.2.6; in short, layers of soil of different thickness were placed on top of hydrophilic glass sinters, which allow rapid water infiltration, and the time for the drop to penetrate though the soils measured.

The data presented so far suggested a two stage process in water drop penetration, the first during which the droplet does not penetrate the soil surface but rather picks-up particles by adhesional-immersional wetting, and the second during which the water droplet does penetrate into the soil surface (branching capillary wetting). This trend suggested a set of experiments in which the time taken for a droplet to penetrate through different thickness of soil were measured; if the idea of a two stage process is correct then, in its simplest form, a plot of time taken to penetrate against thickness should result in a positive intercept corresponding to the time required for the first process to be completed, i.e. the data should show an induction period. The data might be expected to show a linear relationship between penetration time, t_{pen}, and thickness, Δ_{soil}, of the form:

$$t_{pen} = t_{inf} + t_t \Delta_{soil} \tag{6.20}$$

where t_{inf} is the time taken for infiltration to start i.e. the induction period, and t_t is the time taken to penetrate a fixed thickness of soil. There is an additional complication in that the movement of soil grains from underneath the droplet also causes the droplet to move through the soil layer, although this is by displacement not penetration, for the moment we put this to one side but will return to it later.

The global plot sinter data for each soil type presented in Figures 6.49-6.52. For NIC2 a 30 µl droplet was added to see if it fitted the overall trend. The data are quite scattered and a number of equations of varying complexity give comparable correlation coefficients, but a linear fit is simple, has some possible theoretical basis in Equation 6.20, and gives as good a fit as almost any other equation. As Figures 6.49-6.52 show there is different behaviour for LLAN1 and NL1 soils compared to NIC1 and NIC2.

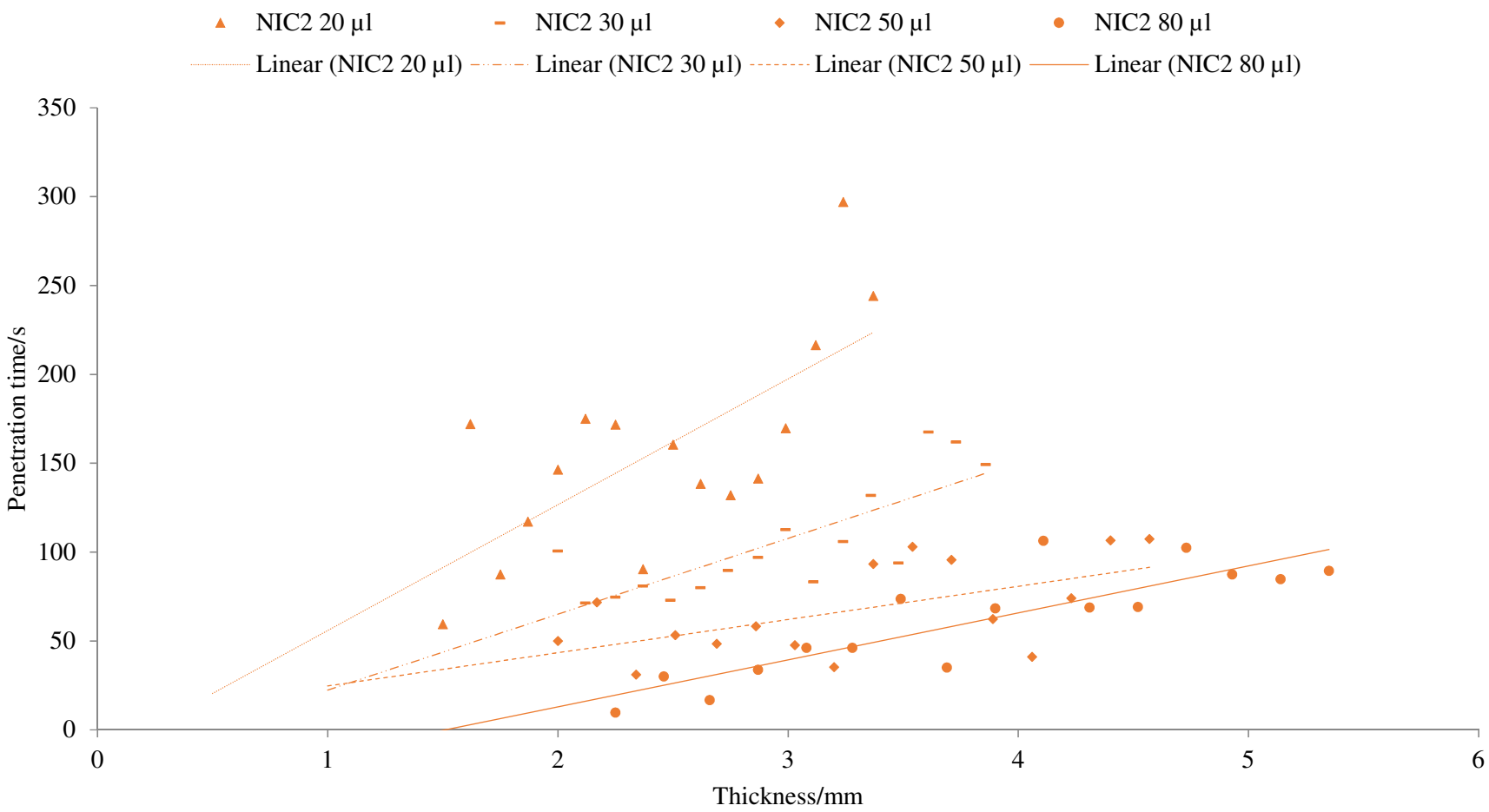

Figure 6.49 Global plot of sinter water drop penetration time data, based on an average measurement from three droplets per data point for NIC2 soil and drop volumes 20, 30, 50 and 80 µl.

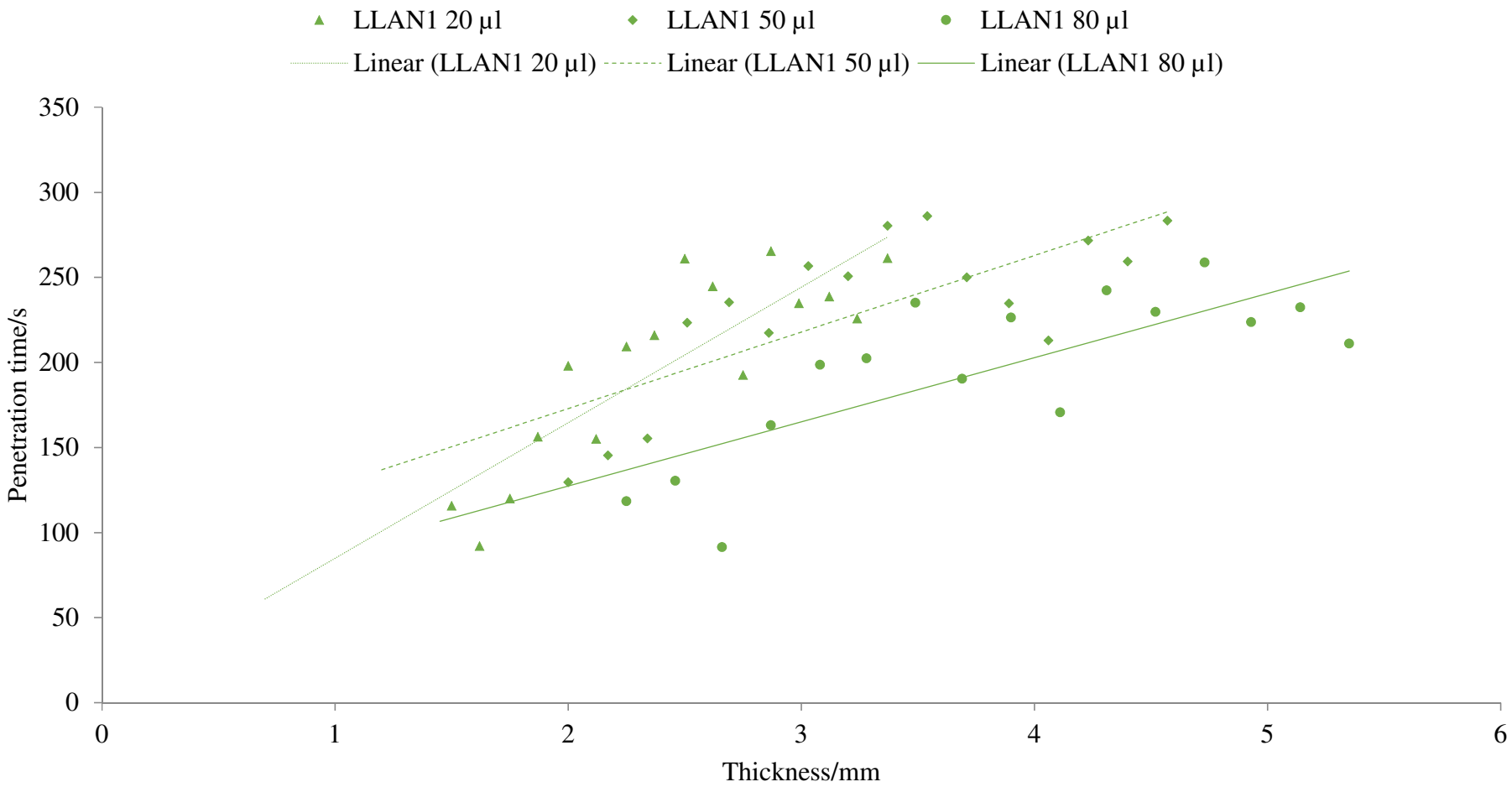

Figure 6.50 Global plot of sinter water drop penetration time data, based on an average measurement from three droplets per data point for LLAN1 soil and drop volumes 20, 50 and 80 µl.

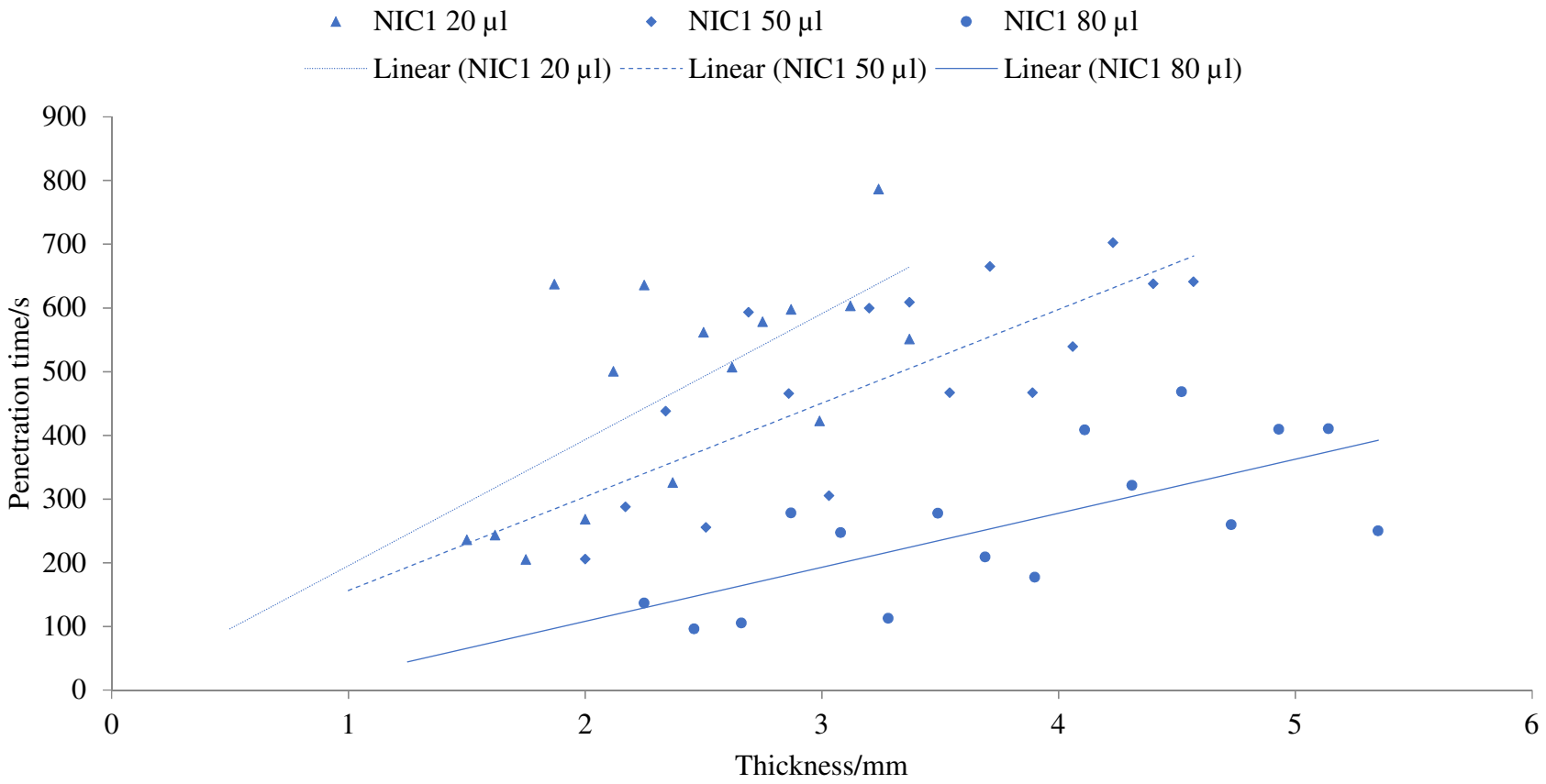

Figure 6.51 Global plot of sinter water drop penetration time data, based on an average measurement from three droplets per data point for NIC1 soil and drop volumes 20, 50 and 80 µl.

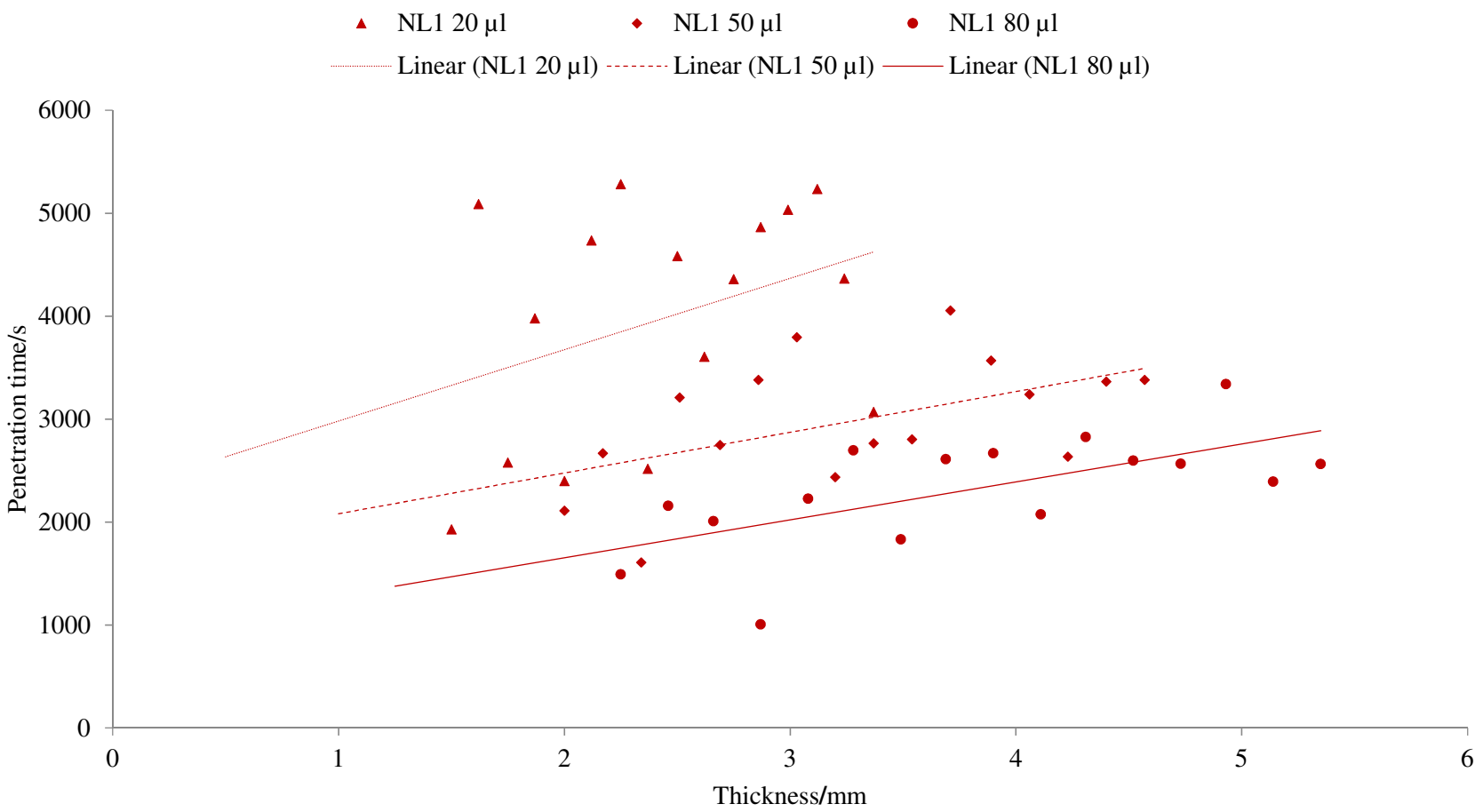

Figure 6.52 Global plot of sinter water drop penetration time data, based on an average measurement from three droplets per data point for NL1 soil and drop volumes 20, 50 and 80 µl.

LLAN1 and NL1 (Figures 6.50 and 6.52) have a positive intercept suggesting the occurrence of an induction stage that takes time, whereas NIC1 and NIC2 (Figures 6.49 and 6.51) have a 0 or negative intercept suggesting there is no initial holding process and that soil grains cover the water drop more rapidly. The intercepts and slopes are included in Table 6.8.

Table 6.8 Intercepts and slope – sinter data.

Soil	Drop volume	Intercept/s*	Slope/s mm^{-1}*
NIC2	20	-17 ±35	72 ±14
	50	2 ±15	19 ±4
	80	-34 ±13	25 ±3
LLAN1	20	38 ±28	62 ±11
	50	99 ±36	42 ±11
	80	14 ±27	45 ±7
NIC1	20	-25 ±110	210 ±42
	50	-12 ±89	151 ±27
	80	-111 ±65	94 ±17
NL1	20	2442 ±667	610 ±256
	50	1679 ±442	397 ±134
	80	656 ±295	421 ±79

*Error estimate is one standard deviation

The negative intercept (possibly 0 intercept when accounting for experimental error) may arise from the removal of soil from beneath the droplet by adhesional-immersional wetting 'thinning' the soil layers by some fixed value.

LLAN1 and NL1 have a notably higher total carbon content compared to NIC1 and NIC2 the longer induction stage before droplet penetration could be a reflection of this. However, this does not correlate with WDPT as LLAN1 is less repellent than NIC1. Overall this might suggest that the induction stage observed for LLAN1 may be as a result of the type of organics present within the soil causing this initial stage and yet molecular restructuring is faster in this instance compared to NIC1.

6.3.11. Droplet density experiments

The severity and persistence of soil water repellency can be assessed by considering the time taken for a water droplet to fully infiltrate into the soil. A parameter to consider in this process is the role of gravity. Previous energy calculations (Figures

6.53-6.54) have indicated that the influence of gravity, via drop mass, is not a major energy term, however drop size does influence WDPT, and also, calculations show, the depth to which a drop sits on the grains. The influence of gravity which might be assessed by examining if the density of the droplet applied is an influential factor in the wetting process.

An experiment was designed to assess how solutions with similar surface tensions, but varying densities, behaved when applied to water repellent soils. Four halide solutions, namely, caesium chloride (1.34 g/cm^3), potassium chloride (1.14 g/cm^3), sodium chloride (1.11 g/cm^3) and lithium chloride (1.07 g/cm^3) were made up to give solutions (~4 M) of varying density but very similar surface tensions (78.1 m N m^{-1}) using data obtained from Slavchov *et al.,* 2012; Ozdemir *et al.,* 2009 and Jarvis and Scheiman, 1967. Assessments were made using 80 µl droplets on two water repellent soils, NIC1 and NIC2. Initial tests were carried out on NIC2 (Figure 6.53) which has an average WDPT time of 126 s (80 µl), and NIC1 (Figure 6.54) with an average WDPT time of 544 s (80 µl) for pure water.

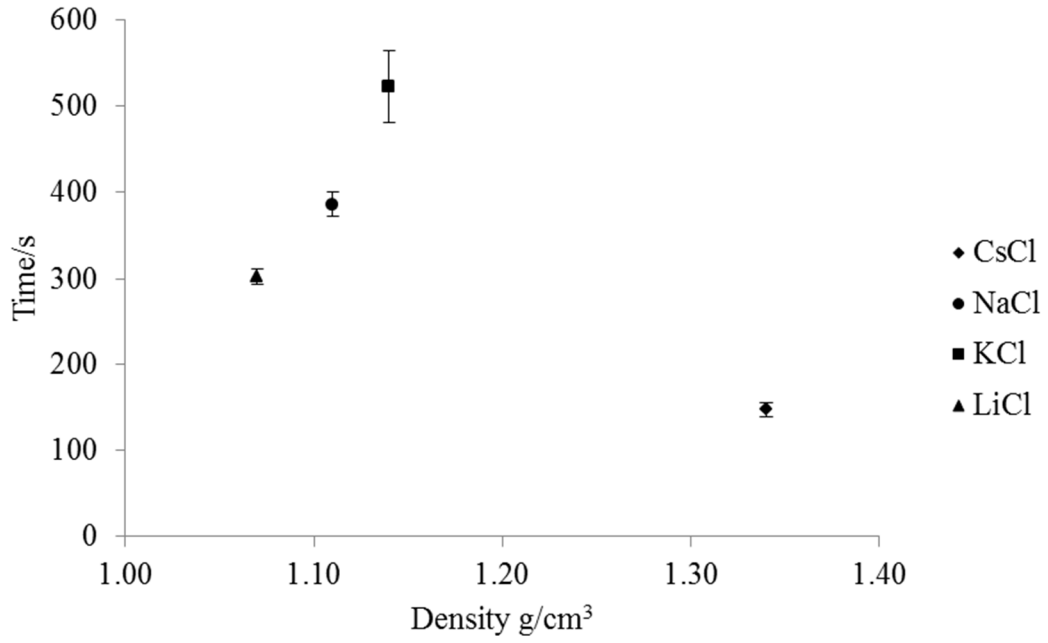

Figure 6.53 Average total infiltration time (based on 30 drops) for caesium chloride, potassium chloride, sodium chloride and lithium chloride solutions on NIC2 soil with one standard error of the mean error bars.

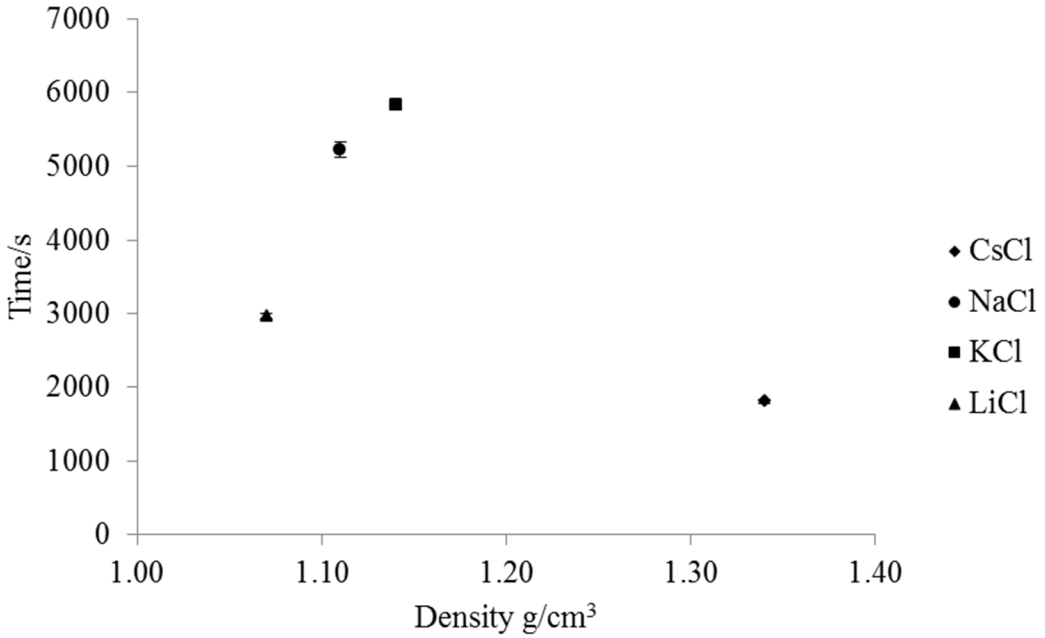

Figure 6.54 Average total infiltration time (based on 10 drops) for caesium chloride, potassium chloride, sodium chloride and lithium chloride solutions on NIC1 soil with one standard error of the mean error bars.

Caesium chloride, with the highest density, had the most rapid infiltration time for both soils (Figures 6.53 and 6.54), however, the WDPTs of the remaining three halides did not give a pattern to suggest that density was a dominant role in the infiltration process. Both potassium chloride and sodium chloride took notably longer to infiltrate compared to the lowest density halide, lithium chloride. As a result of these preliminary tests it was not possible to confirm or deny whether the density of solution plays a role in the infiltration process, other features such as viscosity may be a factor in what is a complex process, but the results do confirm changes in gravitational energy of the water/solution as it infiltrates is not a dominant energy factor. After analysing the data from NIC1 and NIC2 it was established that the same pattern emerged and therefore further tests were not considered worth pursuing.

6.3.12. Assessment of techniques used

The mass removal technique is suitable for soils with strong-severe repellency. The wetting process may be too fast to capture accurately for less repellent soils that wet within a couple of minutes, equally over long lengths of time, factors such as

evaporation can be an issue for severely repellent soils. In terms of droplet size used, the technique is appropriate for smaller droplets in the range of ~20 – 80 µl but droplets bigger than that were difficult to extract effectively due to the volume of soil and water droplet compared to the size of a standard cotton bud. For droplets smaller than 20 µl it was difficult to accurately dispense the droplet onto the surface without influencing the grain coverage, as the droplet remained adhered to the pipette and failed to detach effectively.

The time-lapse images produced from the goniometer provided a measurement of the volume of the droplet that had infiltrated over time. The measurement could be refined further by using smaller sections on the image volume calculations and graph paper < 1 mm. Direct comparisons between mass removal and goniometer time-lapse image data could not be made due to different experimental conditions, the mass removal experiments were all conducted in a controlled temperature / relative humidity room however this was not possible for the goniometer measurements due to its location in another laboratory and therefore the overall WDPT times could be expected to be different between the two datasets. Probably the most important experimental feature is the variability of a soil surface, which give results with high standard deviation, thus requiring averaging of many data to obtain data precise enough for useful comparison. WDPT and mass removal are easy to repeat many times whereas the goniometer measurements are much more time consuming – although it is possible they could be automated.

6.4. Conclusions and implications of findings

The research described in this chapter has identified two discrete stages in the wetting process of water repellent soils, adhesional-immersional wetting and branching capillary wetting. The two stages can occur independently of one another and are both influenced by water drop size and the inherent repellency level of the soil. For soils that are more hydrophilic, both processes occur rapidly, and it is hard to define each stage. For more hydrophobic soils it becomes easier to identify the initial wetting stage where the water droplet becomes covered in soil grains, followed by the infiltration of the water droplet into the soil through capillary wetting over time. For soils that are extremely repellent the processes are complicated by issues such as evaporation.

The implications of this research on the WDPT test should be considered when using the test on water repellent soils. The sinter data shows that it is crucial to have a suitable depth of soil for tests with respect to droplet volume being used. It also supports previous research that showed droplet volume influences the outcome of repellency tests (Hallin *et al.*, 2013). Small droplets (~20 µl) generally take longer to infiltrate, and so assessment of repellency class for a soil may depend on size of droplet used. Equally for drop sizes of any volume on severely repellent soils the influence of evaporation will lead to a decrease in overall droplet volume and therefore will inevitably impact upon the final WDPT result obtained. Furthermore, the profilometer results indicating variation in surface roughness of a soil surface shows how variable measurements on soils can be depending on the droplet size and placement.

Amelioration techniques such as clay or biochar additions will alter the overall particle size distribution of a soil. Both will increase the surface area of the soil and therefore the active wetting front at the point of infiltration has increased area to spread over which are more polar in nature. It is possible that these techniques permit a flowpath for water through the soil profile and whilst the soil appears to wet it may actually be the wettable component that is wetting readily and the areas of repellent soils will continue to take time to wet over time due to the need for chemical changes of the soil grain surfaces.

Chapter 7 A study of the cause of the anomalously high contact angles observed on soils

In this chapter, the current experimental and theoretical approaches to soil contact angle measurements on soils using dynamic sessile drop measurements obtained using a goniometer are evaluated. Research described in this chapter challenges the current approach to understanding the anomalously high contact angles measured on soils. An alternative interpretation of the anomalously high contact angles measured on soils is proposed using a geometric correction factor for a water drop sitting on hydrophobic particles. To assess the applicability of the proposed correction, measurements were made using regularly arranged ballpoint needles and metal spheres, and acid-washed sand and natural soil coated in paraffin wax. An assessment of how this applies to natural soils is also considered. Overall, results suggest that current theoretical approaches are not appropriate, while the approach presented here shows promising results for correcting anomalously high measured contact angles.

7.1. Background

Soil water repellency can be assessed by considering the balance of interfacial tensions at the three-phase (solid, liquid and vapour) contact line (Jaycock and Parfitt, 1981). To achieve this, a direct measurement of the soil-water contact angle (θ) can be made.

At equilibrium, the liquid at the intersection between the three interfaces is stationary and the contact angle adopted is determined by the need for a resultant zero force acting along the three-phase contact line, and the balance of forces is given by Young's equation (1805) in Equation 7.1.

$$\cos\theta = \left(\frac{\gamma^{SV} - \gamma^{SL}}{\gamma^{LV}}\right) \tag{7.1}$$

To make the distinction between 'wetting' and 'non-wetting' of the surface, it is often considered that if $\theta > 90^o$ the liquid does not wet the solid and if $\theta \leq 90^o$ the liquid does wet the solid, although complete spreading wetting only occurs if $\theta = 0^o$ (Jaycock and Parfitt, 1981). For all angles where $\theta > 0^o$ the water drop remains as a drop but one with an increasing solid-liquid interfacial area as θ is reduced; at $\theta = 90^o$, ignoring the effect of gravity, the drop adopts a hemispherical shape, while at $\theta = 0^o$ the water spreads completely across the surface (Jaycock and Parfitt, 1981).

Currently contact angles are widely used by soil scientists as an empirical measurement for water repellent soils as they are relatively straight forward to carry out.

7.1.1. Theoretical models: contact angle measurements

In general, contact angles of irregular non-planar surfaces measured using a goniometer are higher than those of a flat surface of the same material. Understanding this amplification of contact angle by surface structure has for many years been based on the theoretical models of Wenzel (1936) for complete wetting of a jagged surface, and Cassie and Baxter (1944) for bridge-like wetting over the top of protrusions. Both models are based on the thermodynamics of surface energies, i.e. the contact angle is calculated from the energy required to expand the surface via the destruction and creation of interfacial areas respectively. An outline of both models is given in the following sections.

7.1.2. Wenzel (1936)

As water wets a solid surface the solid-vapour (air) interface is replaced by a solid-liquid interface leading to a net increase or decrease of total surface energy respectively. The rate and extent of the wetting that occurs will be dependent upon the magnitude of the free energy change (Wenzel, 1936). On rough surfaces Wenzel (1936) recognised that a greater surface area will be wetted underneath a droplet compared to a smooth planar surface (Figure 7.1).

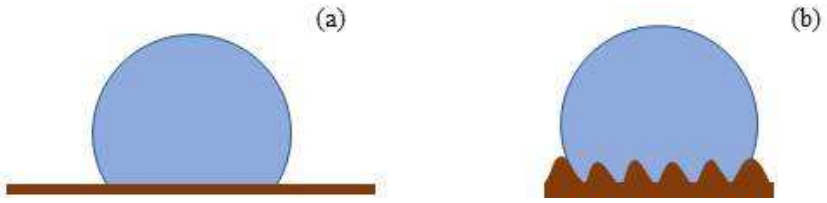

Figure 7.1 Wetting of a smooth surface (a) wetting of a rough surface as suggested by Wenzel (1936 (b).

Wenzel (1936) suggested the following equations to accommodate for the roughness of a solid surface (Equation 7.2):

$$R = roughness\ factor = \frac{actual\ surface}{geometric\ surface} \tag{7.2}$$

where the roughness factor, *R,* is calculated from the ratio between the actual surface and the geometric surface area, and therefore Young's equation was adapted to give Equation 7.3 (given by Gao and McCarthy, 2009).

$$\cos\theta^{w} = \frac{R(\gamma^{SV} - \gamma^{SL})}{\gamma^{LV}} \tag{7.3}$$

Wenzel (1936) argued that a rough surface will essentially magnify the wetting properties of a solid and this needed to be taken into consideration.

7.1.3. Cassie and Baxter (1944)

Cassie and Baxter (1944) proposed a further extension to Wenzel's work on contact angles by considering the influence of porous surfaces (specifically, textile fabrics).

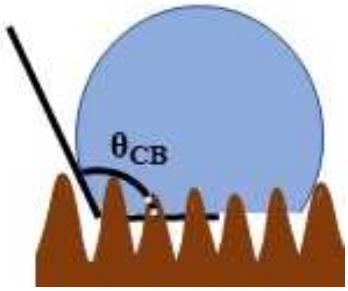

Figure 7.2 Wetting of a rough surface as suggested by Cassie and Baxter (1944) with the water drop bridging over the top of protrusions.

The Cassie and Baxter model suggests that for a rough solid surface, the water drop bridges over the protrusions (Figure 7.2) and therefore spreading of the surface would need to account for both an expansion of the water-air and water-solid interfaces. The spreading of water over a solid surface leads to the destruction of solid-vapour (air) interface resulting in energy gained, and creation of the solid-liquid interface and therefore, energy consumption. Cassie and Baxter (1944) explained the overall net energy, E_D, for this occurrence via Equation 7.4.

$$E_D = f_1(\gamma^{SL} - \gamma^{SV}) + f_2\gamma^{LV} \tag{7.4}$$

where f_1 refers to the total area of the solid-liquid interface and f_2 to the total area of the liquid-air interface. An advancing contact angle (θ_A) for the solid-liquid interface may be defined from Young's equation as (Equation 7.5):

$$\cos\theta_A = \left(\frac{\gamma^{SV} - \gamma^{SL}}{\gamma^{LV}}\right) \tag{7.5}$$

Therefore Equation 7.4 now becomes (Equation 7.6):

$$E_D = \gamma^{LV}(f_2 - f_1\cos\theta_A) \tag{7.6}$$

And therefore Equation 7.5 may be written as Equation 7.7:

$$\cos\theta_A = \frac{-E}{\gamma^{LV}} \tag{7.7}$$

since $\gamma^{SL} - \gamma^{SV}$ is the energy, E, required to form unit area of the solid-liquid interface, an apparent contact angle $\theta_{measured}$ may be defined for the porous surface.

$$\cos\theta_{measured} = \frac{-E_D}{\gamma^{LV}} = f_1\cos\theta_A - f_2 \tag{7.8}$$

Equation 7.8 gives the apparent contact angle for water advancing on to a dry surface and f_1 and f_2 can be derived from θ_A using Equations 7.9 and 7.10 to give the final Equation 7.11.

$$f_1 = \left\{\left(\frac{\pi r}{r+d}\right)\right\}\left(\frac{1-\theta_A}{180}\right) \tag{7.9}$$

$$f_2 = 1 - \frac{r \sin \theta_A}{(r+d)} \tag{7.10}$$

$$\cos \theta_{measured} = f_1 \cos \theta_A - f_2 \tag{7.11}$$

The Cassie and Baxter model has been applied to soils to measure contact angles, such as McHale *et al.* (2005) who developed a geometric model of the soil surface where soil particles were represented as smooth spheres in a hexagonally packed arrangement. The Cassie and Baxter model allows the calculation of the inter-particulate distance and so was considered useful for assessing effect of imperfect packing of particles (McHale *et al.*, 2005). For close-packed arrays, the inter-particulate distance is zero, however as this increases so too will the contact angle using the Cassie and Baxter equation.

7.1.4. Validity of Cassie and Baxter model for measuring soil contact angles

Even though still widely used, there has been much debate in the literature about the validity of the thermodynamic models of Wenzel and Cassie-Baxter for the measurement of contact angles on rough and heterogeneous surfaces.

Both the Cassie and Baxter (1944) and Wenzel (1936) equations have adjustable parameters which can be used to fit data, and as a result these models can almost always give a fit for contact angle measurements. However, the required fitting parameter values are sometimes found to be physically unreasonable (Ahn, 2014). For example, in the case of Cassie and Baxter the inter-particle distance (i.e. the length of the air gap between particles) is an adjustable parameter which, for the best fit to the experimental data, is often required to be bigger than physically sensible (Ahn, 2014). A better approach to examining the suitability of the Cassie and Baxter equation for irregular surfaces would be to replace this adjustable parameter with a measured parameter. However, for soils there is the difficulty of inhomogeneous particle sizes, variable particle surface roughness, and essentially unknown particle packing arrangements. The literature to date has used soil and semi-homogenous

glass spheres or semi-homogenous roughly close-packed spheres (McHale *et al.*, 2005; Ahn, 2014), so modelling of the data is complicated by particle inhomogeneity and variable packing efficiency.

Ahn (2014) found for hydrophobized glass beads and sands of particle diameters between 350-400 µm that measured contact angles were 119 ±5.1^{o} and 137.0 ±2.0^{o} respectively, which were both considerably higher than the 85 ±2.0^{o} on a hydrophobized flat surface.

In 2007 Gao and McCarthy challenged the validity of the use of Wenzel or Cassie and Baxter theories for contact angle measurements on rough, heterogeneous surfaces. They argue that the contact angle measured from interactions between the liquid and solid interfaces are solely reliant on the three-phase contact line and not the interfacial areas within the contact perimeter of the wetted area.

Gao and McCarthy (2007; 2009) argue that Wenzel wrongly substituted Young's equation, that considers the *interfacial forces* along a contact line, with that of *interfacial surface energies*. Therefore, Cassie and Baxter's further adaptation of Wenzel's interpretation was also fundamentally flawed. Gao and McCarthy (2007; 2009) suggest that both Wenzel and Cassie and Baxter equations may inadvertently produce results which are consistent with the theories, however this arises coincidently and is not scientifically sound.

7.1.5. Alternative geometric approach

Here a simple geometric correction, taking into consideration how a water drop sit on the surface, along with measurements from precisely controlled model substrates, is described, which shows why contact angles measured using a goniometer designed for flat surfaces, are always higher than expected for soil grains compared to flat surface contact angle values, without the need to invoke Cassie and Baxter effects.

7.1.6. Research objective

1. To propose and test an alternative geometric correction factor to explain anomalously high measured contact angles using the sessile drop method on a goniometer on model soils and natural soils.

7.2. Materials and Methods

1 mm diameter metal spheres and 0.53 mm diameter ballpoint needles, along with model (AWS) and natural (UKC, 125-250 µm homogenous sieved fraction) soils were coated with paraffin wax using a rotary evaporator.

In each instance, a selected volume of a solution of 1.66 g paraffin wax in 100 ml heptane stock solution was added to 4 g of 1 mm metal spheres, 200 ballpoint needles, or 4 g of model or natural soils, along with 20 ml of heptane in a round bottomed flask. The materials and laydown coverages of wax are given in Table 7.1, with substrate surface areas calculated from the calculated (metal spheres, needles) or measured surface areas. The laydowns were chosen to ensure a full coverage of the substrate surface, the laydowns for the ballpoint needles and metal spheres give an approximate wax thickness of around 7.8 µm and 3.3 µm respectively. The laydowns given all assume full deposition of wax applied on to the substrate surface during the preparation process. For organics on AWS and soil, previous work (Hallin, 2013) shows laydowns efficiencies of ~90 % and so for these cases this is a reasonable assumption, but the laydown efficiency for wax onto steel is not known.

Table 7.1 Materials and wax laydowns.

Material	Diameter/mm	Weight/ g	Wax concentration	Application/ µl	Laydown/ g/cm^{2*}
Metal sphere	1.00	4	1.66g/100 ml	1320	7.21×10^{-4}
Ballpoint needle	0.53	200 needles		2000	3.05×10^{-4}
AWS	0.33	4		200	2.84×10^{-6}
				400	5.68×10^{-6}
				1000	14.21×10^{-6}
				2000	28.42×10^{-6}
				4000	56.85×10^{-6}
UKC	0.39	4		200	2.84×10^{-6}
				1000	14.21×10^{-6}
				2000	28.42×10^{-6}
				4000	56.85×10^{-6}

*Laydown coverages for AWS and UKC soil are calculated using the specific surface area of AWS (292 ±3 $cm^2\ g^{-1}$) from Hallin (2013)

The rotory evaporator was initially set to run at 40 ºC, which allowed the wax solution to stay in liquid form during the coating process, and the sample spun at a rotory speed of ~120 rpm until no visible liquid remained. After this, the sample was run for a further 15 minutes at 50 ºC, before being poured onto filter paper and stored in a desiccator prior to use.

A triangular stencil was used to create closed-packed arrays of the 1 mm metal spheres held in place using a magnetic square stuck to a glass microscope slide. Ballpoint needles were closely packed length-ways across the magnetic surface. These regular arrangements were essential to allow a clear view of the water substrate contact. Model and natural soil samples were prepared as described in Bachmann *et al.* (2000a, 2000b), where soil was sprinkled onto double-sided adhesive tape attached to a microscope slide, creating a single layer of soil grains. Example sample set-ups are shown in Figure 7.3. At least three replicates of each sample were produced per measurement type.

For the metal spheres experiment, measurements were repeated over three consecutive days, with samples dried in a desiccator overnight post-sampling in each instance, this was to assess the reproducibility of the measurements on the wax surface.

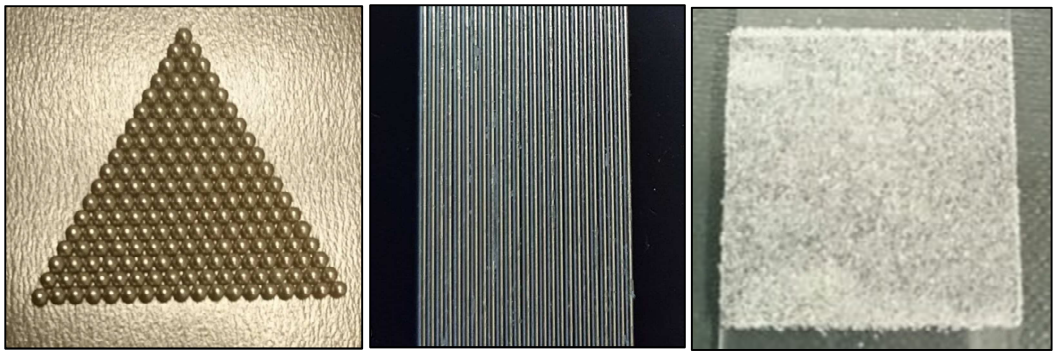

Figure 7.3 Example sample set-up: (left) metal spheres, (middle) ballpoint needles (right) model soil.

To re-use the metal spheres for subsequent sample runs, it was necessary to strip them of the wax that had been deposited before re-coating to make new samples. To do this they were placed in 10 ml of acetone, followed by two rinses with 10 ml of

petroleum ether and sonicated for 5-10 minutes at each stage and then poured onto a filter paper to dry and subsequently stored in a desiccator until required.

7.2.1. Goniometer and drop shape analysis software

A KRUSS Easy Drop FM40 goniometer (Figure 7.4) with Drop Shape Analysis (DSA) software was used to measure dynamic, advancing contact angles on model and natural soils, using sessile drops. Dynamic drop measurements are measured whilst the droplet volume is altered, either by being increased (advancing) or reduced (receding) and therefore the boundary surface is constantly changing. Dynamic contact angle measurements are different to static contact angle measurements which use droplets of fixed volume with the droplet produced prior to measurement. An advantage of static contact angle measurements is that they are not prone to distortion from the needle still being inserted in the droplet, thus permitting the whole droplet shape to be analysed rather than just the contact area. A disadvantage of static contact angle measurements relates to any localised irregularities such as contamination or a non-homogenous surface which is picked up in the measurement and always present in multiple measurements. Dynamic contact angle measurements were considered the most appropriate for use in this work.

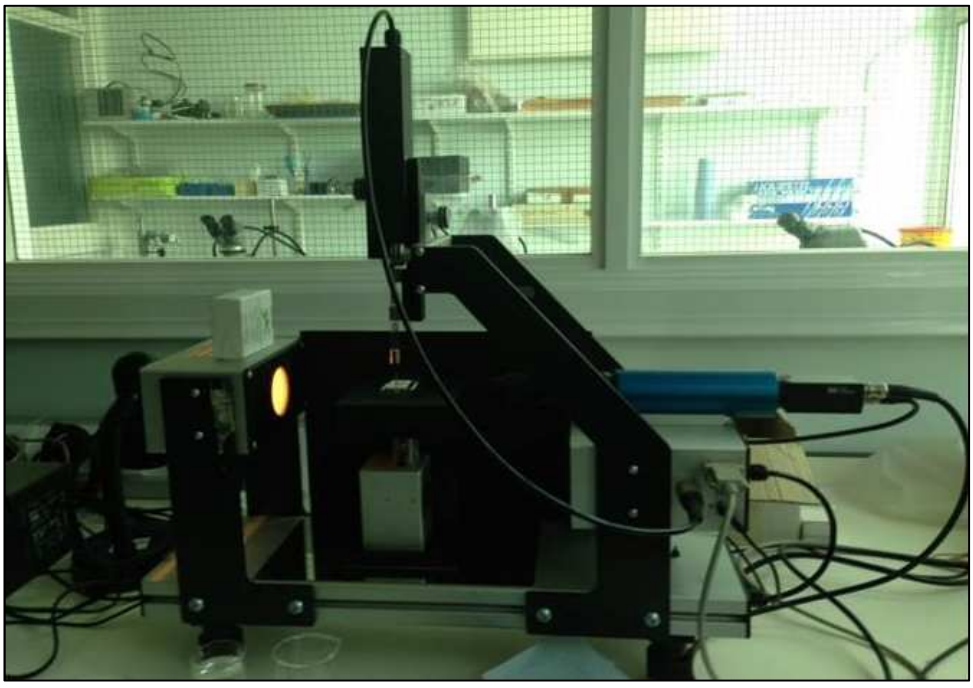

Figure 7.4 KRUSS Easy Drop FM40 goniometer set up used to measure dynamic, advancing contact angles on model and natural soils, using sessile drops.

The Drop Shape Analysis (DSA) software provides four different fitting methods for contact angle measurements (conic section method, polynomial method, circle method and Young-Laplace method), all of which are described in more detail in Technical Note TN314e (www.kruss-scientific.com). The polynomial method (Tangent 2 method) was selected as the most appropriate as it can adapt to a range of contour shapes as the contact area being assessed is made directly at the three-phase contact point.

Distilled water was dispensed onto sample surfaces using a 1000 µl syringe with a 1.065 mm blunt tip needle. A small hanging drop of approximately 5 µl was expelled before being brought into contact with the substrate surface and water was thereafter dispensed at a rate of 100 µl min^{-1}, allowing the droplet to advance across the surface until a final drop volume of 90 µl was obtained. Contact angles were measured using videos recorded at 6.25 fps. Where possible the left and right contact angles for the droplet were averaged for each point using the DSA software; if it was not possible to measure an angle for both sides the angle successfully extracted was taken as representative for that measurement point. Advancing angles were measured at intervals through the video footage and averaged to give an overall contact angle for each sample. Contact angle measurements were carried out at temperatures of between 20-24 ºC and relative humidity of 45-56 %.

7.3. Results and discussion

7.3.1. Smooth planar surfaces

Measuring contact angles on smooth planar solid surfaces with a goniometer is relatively straightforward as the plane of the solid-liquid interface is easily recognizable. The placement of the horizontal baseline (green line Figure 7.5) is key to obtaining an accurate contact angle (θ) for the surface. Once the baseline has been positioned in the appropriate place the droplet contour can be extracted using the DSA software and an average contact angle measurement (from the left and right-side angles where possible) can be obtained. For paraffin wax deposited on a glass microscope slide (Figure 7.5) a solid-liquid (water) contact angle of 111.7° ± 0.6° was obtained which is in close agreement with the literature value of 110/111º given by Pashley and Karaman (2004) and Jaycock and Parfitt (1981).

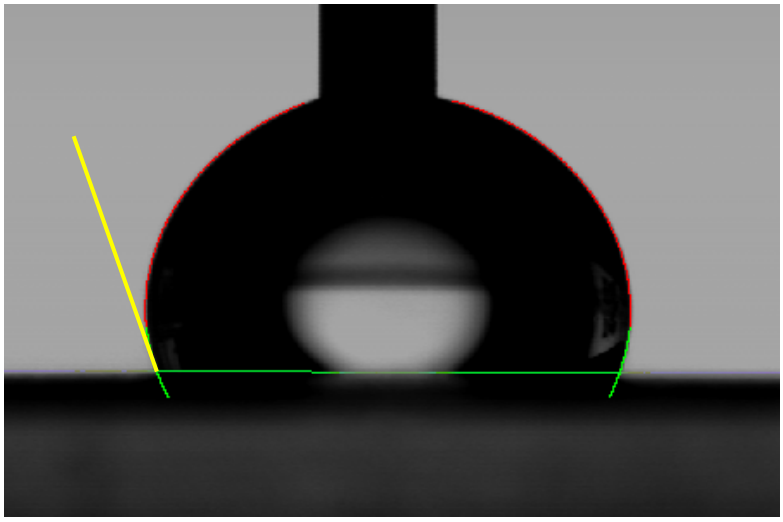

Figure 7.5 Video still of pendant water droplet on a paraffin wax coated planar surface with droplet contact angles extracted using DSA software (red line). Baseline is shown in green and yellow line gives measurement point of contact angle.

Typically for advancing angle measurements on pendant droplets, the baseline is manually positioned across the top of the particle surface (example positioning in Figure 7.6) and contact measurements are produced using this reference point.

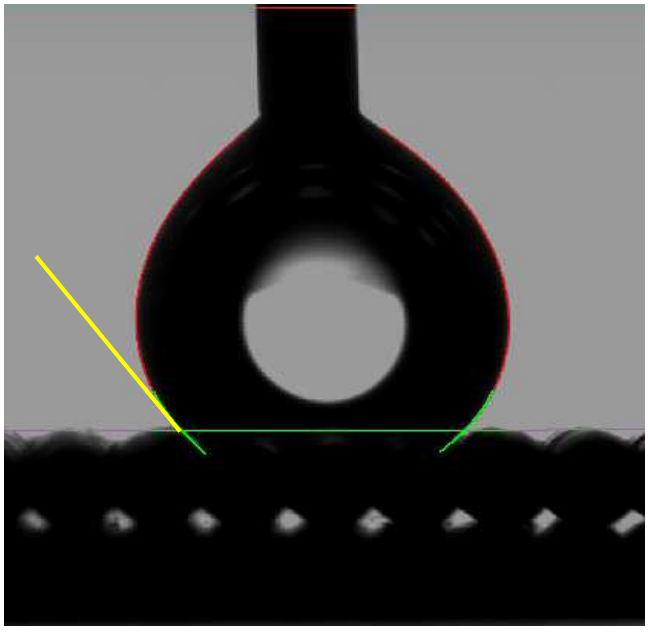

Figure 7.6 Video still of water droplet on a precisely controlled model surface of metal spheres coated in paraffin wax with droplet contact angles extracted using DSA software (red line). Baseline is shown in green and yellow line gives measurement point of contact angle.

An irregular surface covered in paraffin wax would be expected to have a contact angle of ~110/111° relative to the tangent of the surface when measured at any point on the surface. However, for geometric reasons, when using a goniometer the measured contact angle ($\theta_{measured}$) will always be higher than the real contact angle at the vapour-solid-liquid three-phase contact point, because the experimental base line used is not the tangent to the surface at the point of contact because of the way the droplet sits on the surface.

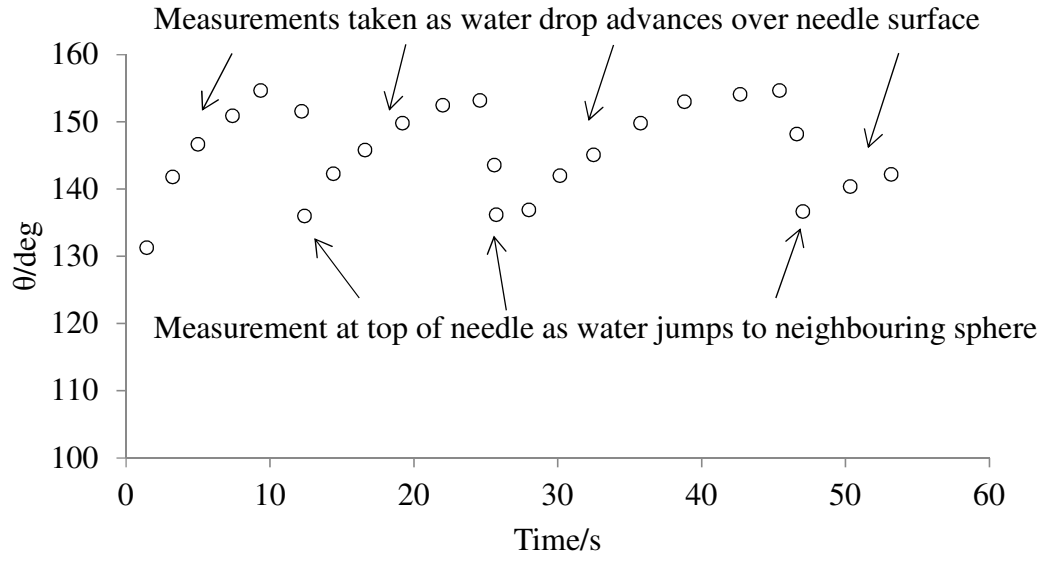

Figure 7.7 Advancing angle measurements on a closely packed irregular surface (wax coated ballpoint needles) shows the sawtooth pattern of contact angles as $\theta_{measured}$ increases as a water drop advances over the surface, followed by a dip as it jumps to the next needle.

Neither the Cassie and Baxter nor Wenzel theories indicate why $\theta_{measured}$ shows the saw-tooth pattern as the drop moves over the substrate (Figure 7.7). The measured contact angles depend on where on the particle surface the three-phase contact line sits. With this in mind, the following section discusses an alternative approach to understanding the enhance contact angles measured on non-planar surfaces.

7.3.2. Geometric correction

The way a water droplet sits on a smooth planar surface is different to how it sits on a non-planar surface, such as soil. Figure 7.8 shows the positioning of a water drop

on a flat surface compared to one on a circular curved surface e.g. on a cylinder, or sphere.

To compensate for the change in angle of the tangent at the point of contact the angle κ (Figure 7.8) is required, with ($\theta_{measured}$-κ) giving the contact angle which would be seen on a flat surface (θ_{flat}). κ can be obtained from the radius of the particle and the depth the droplet sits from the top of the particle as given in Equations 7.12 and 7.13.

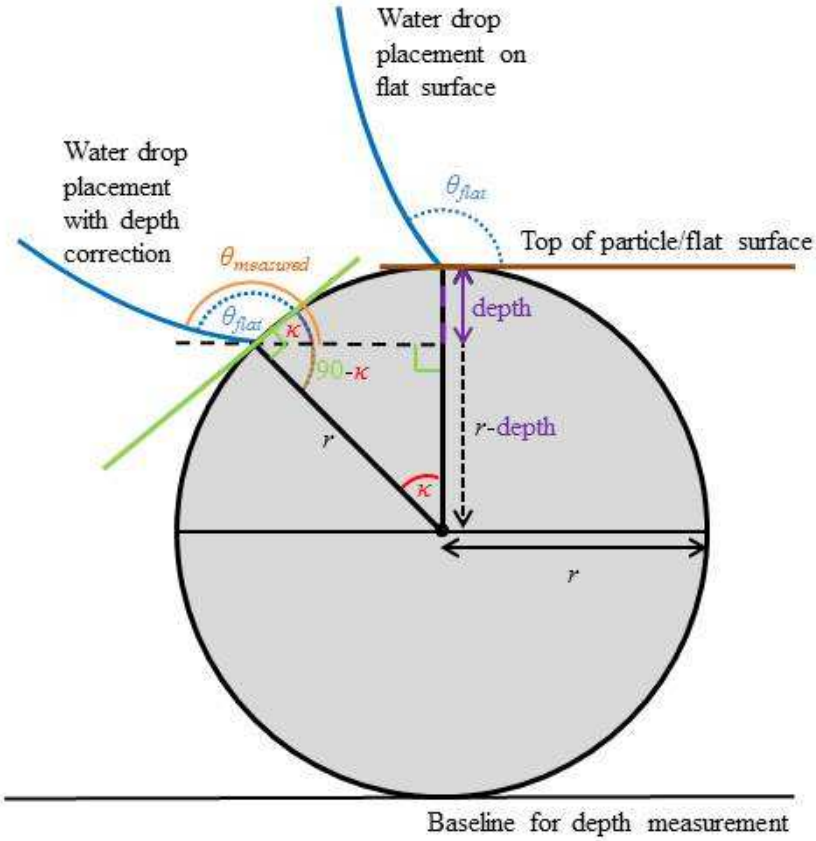

Figure 7.8 Correction factor schematic.

$$\kappa = \cos^{-1}\left(\frac{r-depth}{r}\right) \times \left(\frac{180}{\pi}\right) \tag{7.12}$$

$$\theta_{corrected} = \theta_{measured} - \kappa \tag{7.13}$$

where, θ_{flat} is the theta contact angle measured on flat surface, $\theta_{measured}$ is theta measured prior to correction, $\theta_{corrected}$ is theta measured minus correction factor, κ is the calculated correction factor (degrees), r is radius (mm) and depth is the distance from point of contact to top of particle (mm).

The calculated difference in baseline position is subtle, an example is provided in Figure 7.9. Despite the minimal difference in baseline position, it is enough to compensate for the difference between in the measured contact angle on particles and on a flat surface. Zimmermann *et al.* (2009) suggested the positioning of the baseline was critical in soil contact angle measurements and their study highlighted an adjustment in height by one pixel in their measurements could account for a notable change in contact angle.

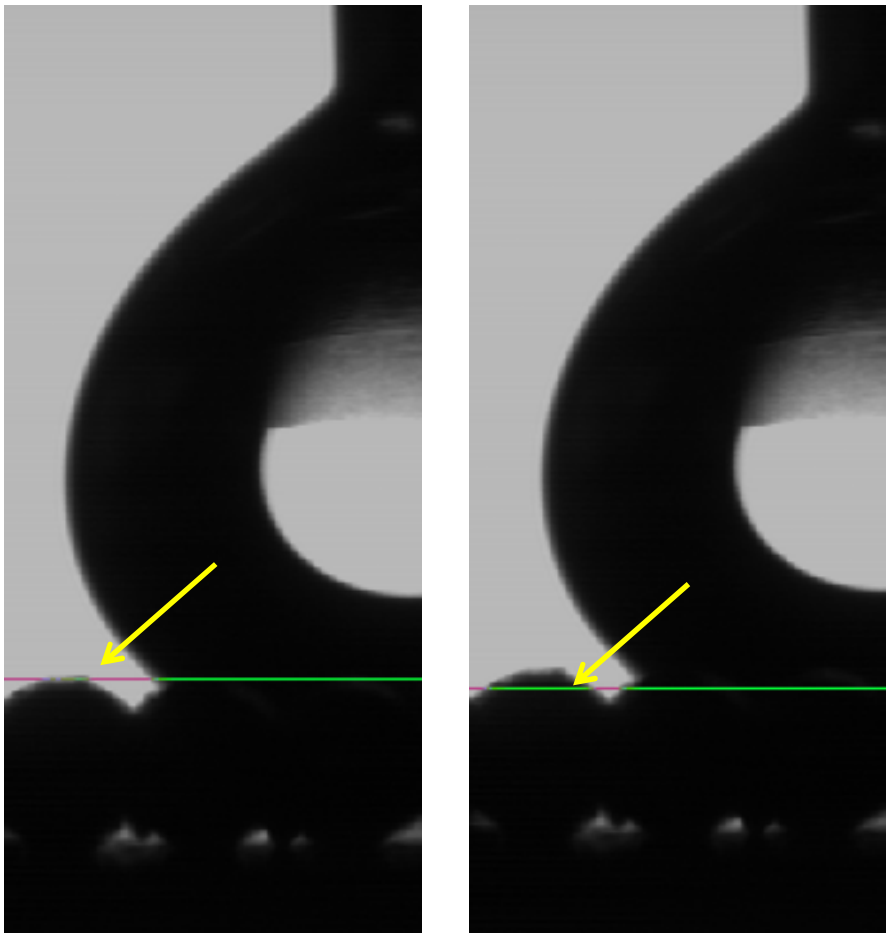

Figure 7.9 Pendant water drop on 1 mm diameter metal spheres with baseline positioned according to top particle surface and $\theta_{measured}$ at 139.1° ±1.05 (left) and at depth where water drop actually contacts the ball bearing and $\theta_{measured}$ at 146.8° ± 2.23 (right).

7.3.3. Ballpoint needles

The first substrate studied was closely-packed ballpoint needles covered in paraffin wax; this substrate was chosen as it was similar to the wax coated wires used by Cassie and Baxter in their 1944 study. Analysis using the geometric correction

factor described in section 7.3.2 was applied to a series of advancing angle measurements on closely-packed ballpoint needles covered in paraffin wax, the results are presented in Figures 7.10 and Table 7.2. The $\theta_{measured}$ using the DSA software using a baseline of either the top of the spheres (as is standard practice) or at the three phase contact point at the particle surface was considerably higher than the contact angle of paraffin wax on a flat surface of ~111°. It can be noted that there is generally up to ~4° difference between these two measurements, with the top of the particle surface measurements giving slightly lower $\theta_{measured}$ than the adjusted baseline measurement (Figure 7.9). The overall average of $\theta_{measured}$ = 147.34° (± 0.7) and after correction factor applied $\theta_{corrected}$ = 108.0° (± 1.3). Once the correction factor had been applied, accounting for the depth of the water placement on the particle surface, contact angles ($\theta_{corrected}$) fell within 6° of the contact angle of paraffin wax on a planar surface (Table 7.2).

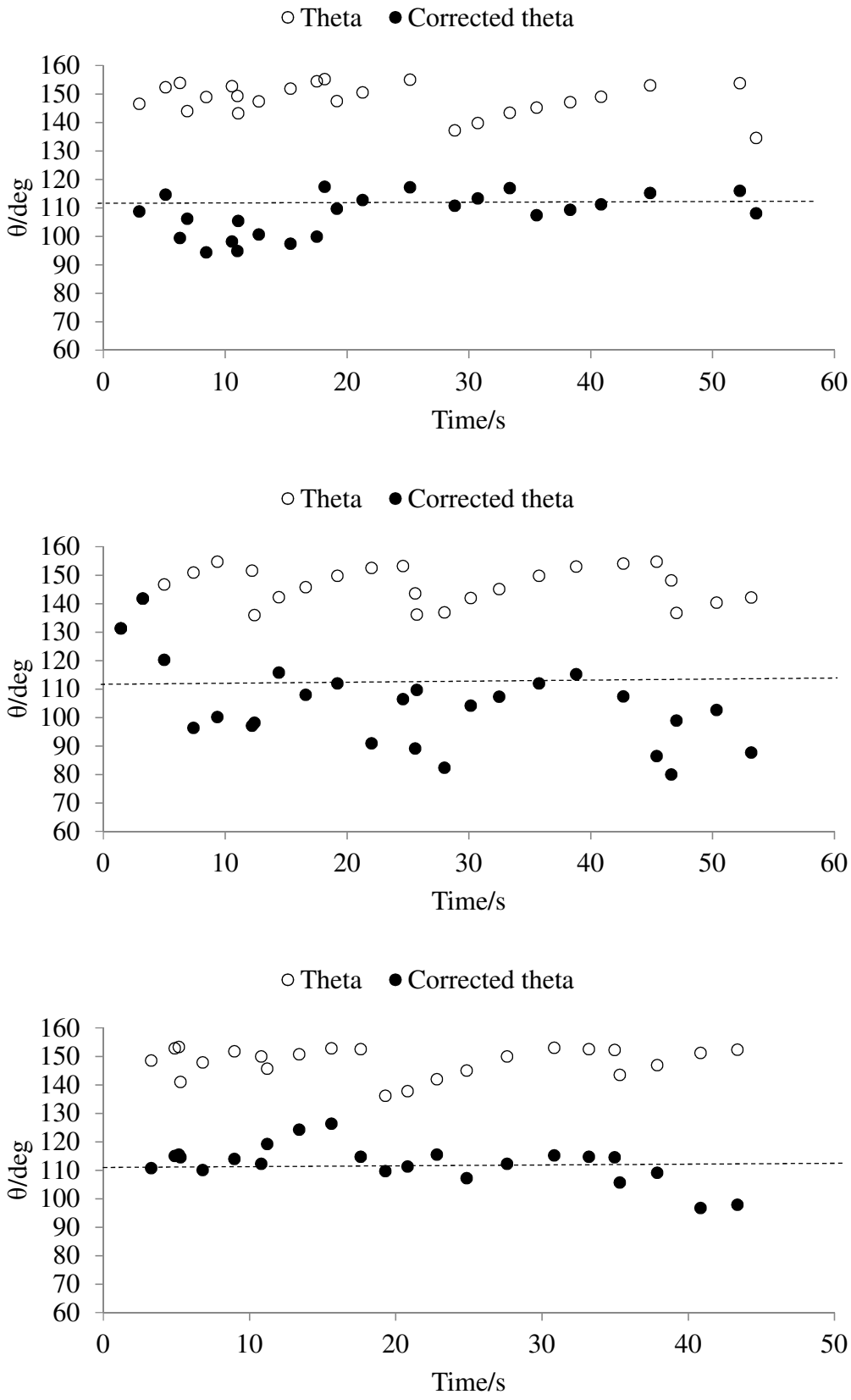

Figure 7.10 S1BN (top), S2BN (middle), S3BN (bottom) ballpoint needles. Open circles, measured contact angle; closed circles corrected contact angle; the dashed line gives the contact angle for paraffin wax on a flat surface.

Table 7.2 Measured theta ($\theta_{measured}$) and corrected theta ($\theta_{corrected}$) results for paraffin wax coated (laydown 3.05 $\times 10^{-4}$ g/cm^2) ballpoint needles (0.53 mm diameter).

Sample	$\theta_{measured}$ degrees	$\theta_{corrected}$ degrees	Average $\theta_{corrected}$ degrees	Top of particle surface θ / degrees	Top of particle surface corrected θ /degrees	Top of particle average corrected / θ degrees
S1BN	148.2 ±1.2	107.7 ±1.5	108.0 ±1.3	145.8 ±0.8	105.4 ±1.5	106.2 ±1.3
S2BN	145.6 ±1.4	104.1 ±2.9		145.2 ± 1.2	103.7 ±3.0	
S3BN	148.3 ±1.1	112.5 ±1.9		145.6 ±1.0	109.8 ± 1.8	

7.3.4. Metal spheres

The next stage of the experiment was designed to consider 1 mm diameter homogenous, closely-packed metal spheres coated with paraffin wax (Figure 7.11).

Figure 7.11 Precisely controlled homogenous close packed 1 mm metal spheres with 90 µl water drop for scale.

Table 7.3 presents the laydown and corresponding measured ($\theta_{measured}$) and corrected ($\theta_{corrected}$) contact angles for a series of measurements using wax-coated metal spheres. Measurements were repeated over three consecutive days, with samples dried in a desiccator overnight post-sampling in each instance, this was to assess the reproducibility of the measurements on the wax surface. The figures presented in 7.12-7.15 show the $\theta_{measured}$ and $\theta_{corrected}$ measurements for the replicate samples over the three-day period, with the dashed line showing the measured contact angle for paraffin wax on a flat surface (θ_{flat}).

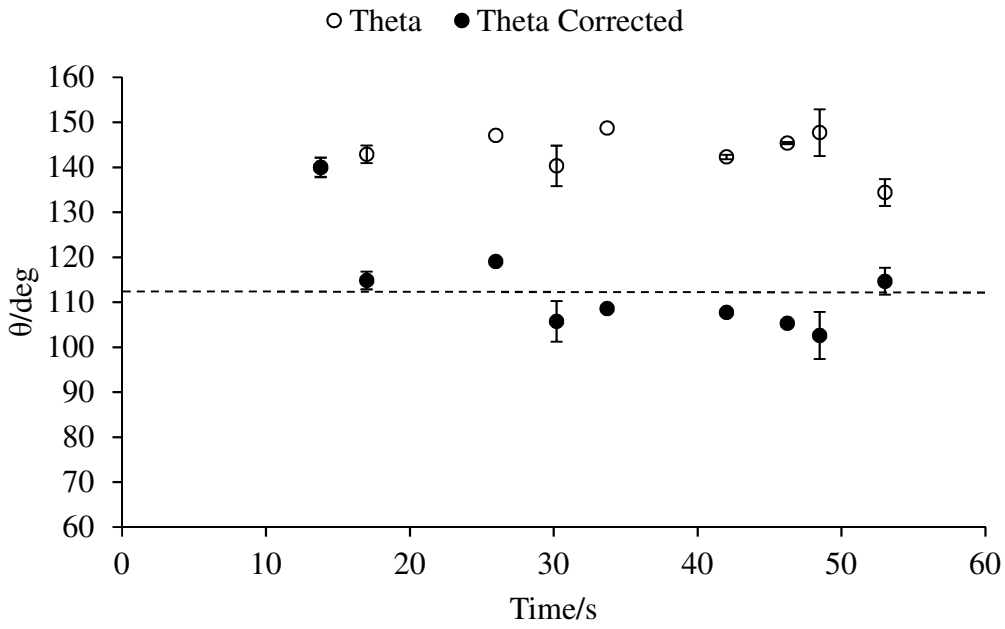

Figure 7.12 S1MST2 metal spheres. Open circles, measured contact angle; closed circles, corrected contact angle; the dashed line gives the contact angle for paraffin wax on a flat surface. Error bars shows variation between left and right contact angle (θ) measurements for each data point.

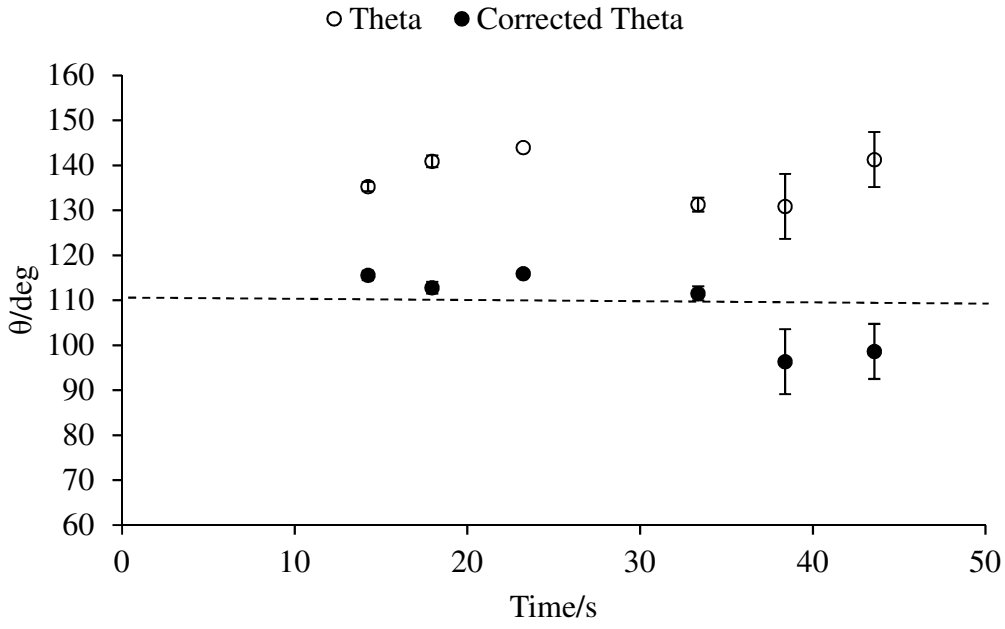

Figure 7.13 S2MST1 metal spheres. Open circles, measured contact angle; closed circles, corrected contact angle; the dashed line gives the contact angle for paraffin wax on a flat surface. Error bars shows variation between left and right contact angle (θ) measurements for each data point.

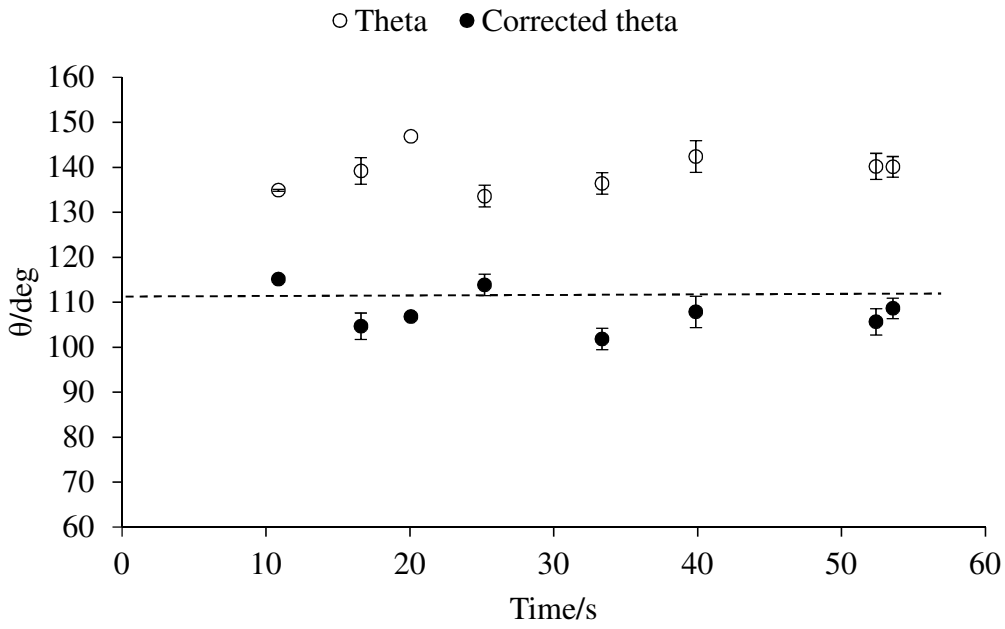

Figure 7.14 S3MST3 metal spheres. Open circles, measured contact angle; closed circles, corrected contact angle; the dashed line gives the contact angle for paraffin wax on a flat surface. Error bars shows variation between left and right contact angle (θ) measurements for each data point.

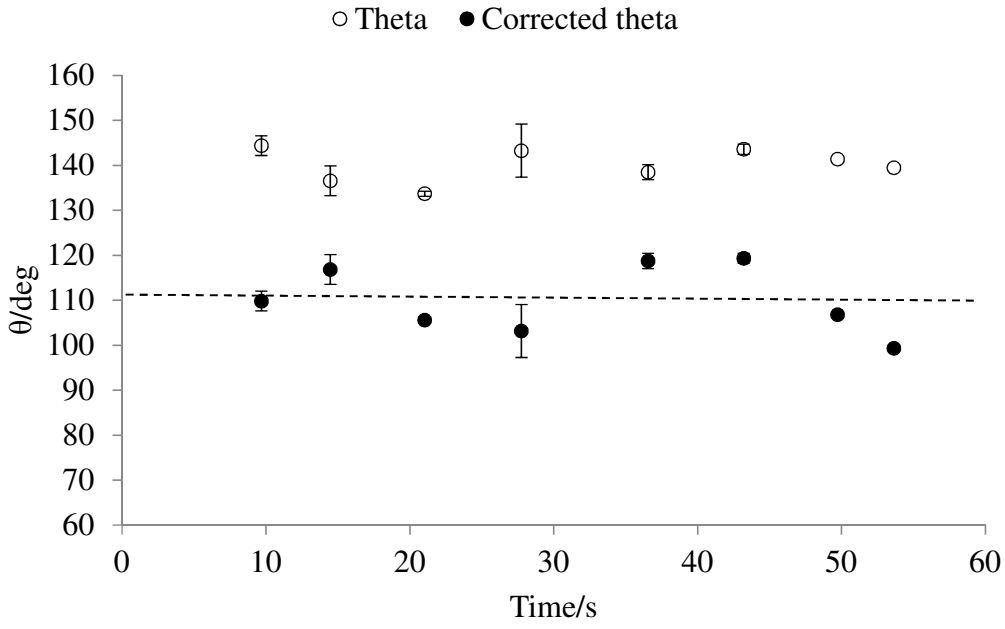

Figure 7.15 S4MST3 metal spheres. Open circles, measured contact angle; closed circles, corrected contact angle; the dashed line gives the contact angle for paraffin wax on a flat surface. Error bars shows variation between left and right contact angle (θ) measurements for each data point.

Table 7.3 Average $\theta_{measured}$ and $\theta_{corrected}$ contact angles for 1 mm metal spheres with application wax laydown of 7.21 $\times 10^{-4}$ g/cm^2 assuming all wax has been deposited.

Sample	Test	Measured θ / degrees	Corrected θ / degrees	Average corrected θ / degrees	Top of particle measured θ / degrees	Top of particle corrected θ / degrees	Top of particle average corrected θ / degrees
S1MS	1	142.1 ±1.8	101.2 ±2.0	108.6 ±2.2	136.8 ±0.9	96.0 ±2.7	103.9 ±2.6
	2	143.2 ± 1.5	113.2 ±3.8		137.7 ±0.7	107.6 ±4.7	
	3	143.1 ±1.4	111.3 ±4.3		139.0 ±1.0	107.2 ±4.9	
S2MS	1	137.3 ±2.3	108.5 ±3.6	105.0 ±1.6	137.4 ±1.4	108.6 ±3.1	102.0 ±2.1
	2	140.2 ±2.1	104.0 ±2.6		137.1 ±1.2	100.9 ±3.6	
	3	141.7 ±0.8	102.4 ±2.1		136.8 ±0.8	97.5 ±3.1	
S3MS	1	137.7 ±1.4	111.6 ±5.5	110.1 ±2.0	136.6±1.4	110.5 ±5.8	107.9 ±2.1
	2	139.9±3.3	110.6 ±3.9		137.5±1.2	108.2±2.8	
	3	139.2±1.5	108.0± 1.6		136.2±0.6	105.1±2.3	
S4MS	1	137.9 ±1.6	108.1±3.4	109.2 ±1.8	136.0±0.7	106.2±4.1	105.9 ±1.9
	2	140.5±3.7	109.4±3.4		136.5±2.4	105.4 ±3.1	
	3	140.2±1.3	110.0 ± 2.7		136.1±0.8	106.0±3.0	

The results from experiments on metal spheres indicate that the geometric correction factor can produce contact angles that are in closer agreement with the contact angle of paraffin wax on a flat surface for 1 mm particle sizes. Samples S1MS-S4MS in Table 7.3 and corresponding Figures 7.12-7.15 show that corrected contact angles generally fall within 6° of the expected contact angle for wax of 110-111°. The overall average of $\theta_{measured}$ =140.4° (±0.6) on 1 mm metal spheres, which after the correction factor was applied reduced to $\theta_{corrected}$ = 108.2° (±1.0). This geometric approach successfully provides a correction term, and gives a theoretical basis for understanding, the high apparent contact angles measured on non-planar surfaces.

7.3.5. Model and natural soils

The key to evaluating this method experimentally was the use of regular arrays of particles of a reasonable size, unfortunately soils are not homogeneous and preparing a regular array is not easy, furthermore the particle size is rather small for measurements of the precision required. However, the principle remains the same, and we would expect the measured contact angle on soil to be around the same as that on metal spheres, perhaps somewhere between that measured using the surface of the sphere, and the point of contact as the baseline. To explore this, wax coated acid-washed sand and natural soil (UKC, a sieved fraction size of 125-250 µm was used to keep particle sizes relatively homogeneous) were both coated with variable laydowns of paraffin wax to see if their $\theta_{measured}$ advancing angles were in a similar range to those obtained on the homogenous controlled surfaces. (To make depth correction measurements on these samples would have required a different experimental set up as the particle sizes were significantly smaller than the metal spheres and baseline positioning could not be made with sufficient accuracy to obtain meaningful results).

The average $\theta_{measured}$ contact angle is presented in Figure 7.16 against wax application for AWS and the natural soil (UKC) used in this set of experiments. The data shows that above *ca.* 2.84×10^{-6} g/cm^2 laydown contact angles are independent of laydown, but at laydowns lower than this the contact angle is reduced.

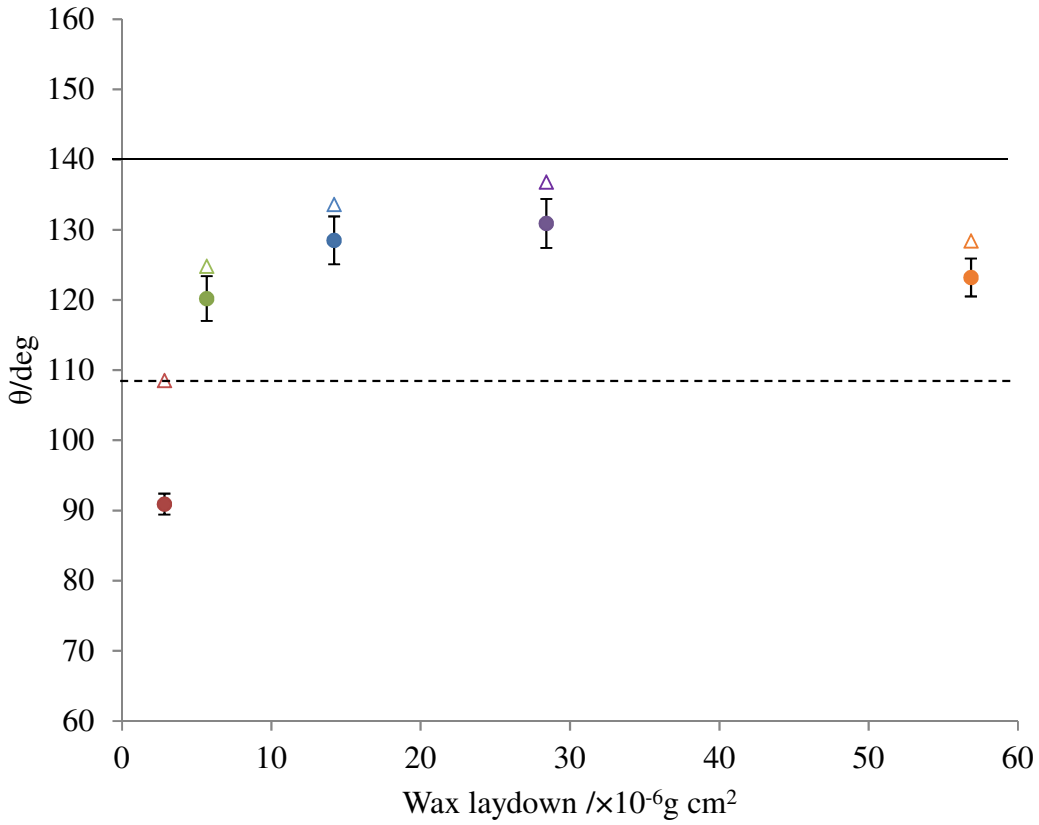

Figure 7.16 UKC (125-250 µm sieved fraction) (closed circles) and AWS wax (open triangles) against average $\theta_{measured}$. Solid line shows average $\theta_{measured}$ (140.4° ±0.6) on metal spheres and dashed line shows $\theta_{corrected}$ (108.2° ±1.0). Laydowns are as follows: 2.84×10^{-6} g/cm^2 (red), 5.86×10^{-6} g/cm^2 (green), 14.20×10^{-6} g/cm^2 (blue), 28.42×10^{-6} g/cm^2 (purple) and 56.85×10^{-6} g/cm^2 (orange).

With the limitations in mind the results of advancing angles made on model and natural soil with variable paraffin wax laydowns are given in Table 7.4.

Table 7.4 Average advancing contact angles (based on six droplets) on model (AWS) and natural sandy soil (UKC) coated in paraffin wax. *Laydown coverages are calculated using the specific surface area of AWS from Hallin (2013).

Sample ID	Application/ µl	Laydown g/cm^{2*}	Average advancing angle (θ)/ Degrees
AWS 1	200	2.84×10^{-6}	108.3 ±1.3
AWS 2	400	5.68×10^{-6}	125.4 ±1.3
AWS 3	1000	14.20×10^{-6}	133.6 ±0.8
AWS 5	2000	28.42×10^{-6}	136.9 ±0.8
AWS 4	4000	56.85×10^{-6}	128.9 ±1.0
UKC 1	200	2.84×10^{-6}	90.5 ±1.8
UKC 2	400	5.68×10^{-6}	121.1± 1.0
UKC 3	1000	14.21×10^{-6}	128.4 ±1.1
UKC 4	2000	24.42×10^{-6}	130.4 ±1.1
UKC 5	4000	56.85×10^{-6}	122.9 ±1.7

A laydown of 2.84×10^{-6} g/cm^2 of wax produced lower contact angles compared to higher laydowns; this may indicate that this laydown level does not provide a full consistent wax coverage over all particles. It is also possible to visually observe the difference in contact angles from still frames of a water drops on AWS. All three images in Figure 7.17 are taken from similar points in the advancing angle process (around 12 s), it is evident the contact angle for Figure 7.17 (left) is lower than that for (middle) and (right) which have higher laydowns of wax.

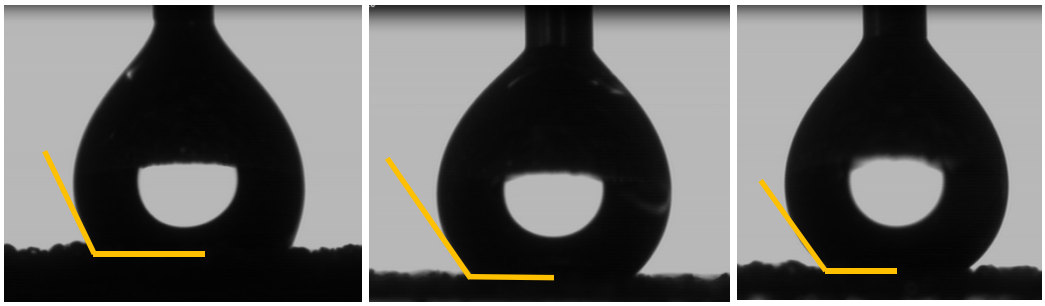

Figure 7.17 Goniometer droplet profiles of (left) AWS 1 application 200 µl with average $\theta_{measured}$ 108.3° ±1.3, (middle) AWS A1 1000 µl with average $\theta_{measured}$ 133.6° ±0.8, (right) AWS C1 2000 µl with average $\theta_{measured}$ 136.9° ±0.8.

The average advancing angle ($\theta_{measured}$) on model and natural sandy soil (UKC sieved 125-250 µm fraction) in Table 7.4 are intermediate between the average measured values and corrected values on close packed metal spheres. A reasonable explanation of this lies in the maximum depth the water droplet can reach on close

pack spheres and the loose packed particles of a soil. If, in a soil, as a consequence of the loose packed heterogeneous particle size and shape, the water drop transfers the droplet front from particle to particle at a lower relative depth than would be possible for homogeneous spheres then the maximum advancing contact angle measured will be smaller on the soil than on close packed heterogeneous spheres. The average measured contact angles will also be smaller on the soil. Further experimental work, or modelling, will be necessary to evaluate this idea, but it is an interesting working hypothesis.

7.3.6. Implications of correction factor and contact angle measurements for water repellent soils

The research described in this chapter shows that the proposed geometric correction factor applied to model surfaces (metal spheres and ballpoint needles) that have been coated with paraffin wax successfully adjusts the high $\theta_{measured}$ to give a $\theta_{corrected}$ which lies, within experimental error, in the range of paraffin wax on a flat surface. The method provides a simple theoretical basis for understanding the increased contact angle measured on rough surfaces when using a goniometer, without recourse to Wenzel or Cassie and Baxter theories.

Goniometer measured contact angles on both model and natural soils coated in wax are ~20-30^o higher than that for a flat surface of wax. Although for these samples it is not possible, with the equipment available for this work, to make the measurements to correct the measured values, the explanation for high measured values remains scientifically sound. Irregular surfaces coated in hydrophobic material are likely to return a higher contact angle than a flat surface of the hydrophobic material. It is this latter value which is important from a point of view of assessing the polarity/hydrophobicity of the hydrophobic coating, along with any conclusions which might be drawn from such an assessment. Overestimates of contact angle of the order of 20-30^o for soils are to be expected, and have, indeed, been found by other workers in the group (Ahn, 2014). Further consideration of a wider range of particle sizes and increased accuracy of baseline placement for model and natural soil samples would be beneficial for testing the application of this correction factor further.

7.4. Conclusions

The proposed geometric correction factor gives a simple theoretical basis for understanding the increase in measured contact angles on soil surfaces compared to planar surfaces. These experiments support the idea that it is the three-phase contact line where the water drop sits on a particle surface that is critical for the assessment of advancing angles on soils and indicate that the Cassie and Baxter (1944) and Wenzel models are inappropriate for the interpretation of measured of contact angles on irregular surfaces such as soils. Even for samples where correction cannot be made because the required measurements cannot be made the theoretical basis for the increased measured contact angle over that expected for a plane surface remains sound. Overestimates of flat-plane contact angles of the order of 20-30^{o} for soils are to be expected. Further application of this correction method to a wider range of particle sizes and organic applications would be the next step in assessing its effectiveness as suitable tool in the measurement of contact angles using a goniometer and the sessile drop method on water repellent soils.

Chapter 8 Conclusions and future work

This chapter summarises the key findings and suggests future opportunities for the development of techniques, and experimental work, that could be carried out linked to this research.

8.1. Conclusions and future work

This work aimed to explore new approaches to the study of hydrophobicity and wetting of model and natural sandy soils by considering existing measurement methods and theories and where applicable applying new techniques and theories. This was achieved by addressing three main research objectives.

8.1.1. To evaluate the use of fluorescence probes, namely nile red and pyrene, as tools to assess the polarity and viscosity of the soil surface environment

Given the important role of surface polarity in determining soil water repellency, the opportunity to explore and apply cross-disciplinary techniques to study polarity of organics adsorbed to soils was taken. Fluorescent probes have been successfully used for decades to study biological and chemical environments (Evans *et al.*, 2013). The research described in chapters 4 and 5 explored the use of fluorescent probes as a method for both the direct *in-situ* determination of the polarity of organics on soil surfaces, and the molecular mobility within the organic layer.

8.1.1.1. Auto-luminescence and nile red

The application of nile red fluorescent probe to model and natural soils show that it is possible to image emission of nile red after adsorption to soils using fluorescence microscopy. However, nile red gave results contrary to expectation in that areas of organics which could be seen to be dyed red by nile red under room light did not give intense emission. Instead, nile red adsorbed onto uncoated acid-washed sand gave a more intense emission image than nile red adsorbed onto natural soils. Similarly, nile red on natural soil surfaces stripped of organics and made acidic gave a more intense emission than observed on basic surface, or natural unstripped soils.

A further complication identified was the interference with imaging of intense soil auto-luminescence from grains or part grains; auto-luminescence will likely be problematic for any luminescence imaging probe work.

Overall fluorescence imaging probe work with nile red is not promising for soil studies, however the general methodology and ability to succesfully image samples in this way suggests further research using alternative probes is worthy of investigation.

8.1.1.2. Pyrene

Pyrene gives measurable steady-state and time-resolved emission spectra when adsorbed onto grain surfaces or absorbed into the organic layer around natural soils. On model soils, pyrene fluorescence response varies with polarity and viscosity of organics used. For natural soils there are small but measurable differences in polarity of the pyrene environment. Co-deposition with typical hydrophobic compounds found on soils, gives pyrene emission spectra and excimer formation kinetics which indicates environments of varying polarity and fluidity depending on the organic compounds present. When natural soils are used there are differences in both the efficiency of pyrene adsorption and polarity of the pyrene environment.

With model soils, high quality spectra could be obtained, and for these spectra vibration band ratios correlated well with the polarity of the organic under examination. Furthermore, lifetime studies show clearly different behaviour as the organic layer was changed from a liquid (hexadecane), through a relatively soft wax (octadecane) to a harder wax (stearic acid). This immediately suggests the possibility of using pyrene to examine the fluidity of the organic layer as say a hexadecane coated acid-washed sand taken across its melting point (5-25 °C), to see if this correlates with changes in soil water drop penetration time.

For natural soils, adsorption of pyrene from water gives samples which also give useable spectra, although these are much weaker than those found for pyrene co-deposited directly with organics, and soil auto-luminescence gives rise to large background signals for these spectra.

Overall, this work shows that it is possible to obtain both steady-state and time resolved spectra *in-situ* from pyrene co-deposited onto acid-washed sand or adsorbed directly onto soil. Work with acid-washed sand and other model soils may allow studies of correlation of organic polarity and soil hydrophobicity for model soils made using different organics and combinations of organics (Mainwaring *et al.*, 2013), and may also allow time dependent studies of polarity as a soil is wetted. For natural soils, further work, with a wider range of soils and soil hydrophobicities, will be necessary to determine how well any of the spectral features correlate with the hydrophobicity of soils.

8.1.2. Using the WDPT method to assess if water infiltration is a single step process and if not, what steps are involved in the wetting process of water repellent soils

The process of wetting is well researched and the different types of wetting that can occur with a water drop on a flat surface, or particles with an infinite volume of water can be found in many sources, e.g. Jaycock and Parfitt (1981), but the wetting process of a water droplet on a water repellent soil is more complex. In chapter 6 experimental work involving a variety of measurements used to develop a model of the kinetic processes involved in the wetting of water repellent soils from initial dispensation to complete infiltration were presented.

Two discrete stages were theoretically and experimentally identified in the wetting process of water repellent soils, (1) adhesional-immersional wetting and (2) branching capillary wetting. Both stages can occur independently of one another and are influenced by water drop size and the inherent repellency level of the soil. For soils that are more hydrophilic, both processes occur rapidly and it is hard to define each stage as a result. For more hydrophobic soils it becomes easier to identify the initial adhesional-immersional wetting stage where the water droplet becomes covered in soil grains, followed by the infiltration of the water droplet into the soil through branching capillary wetting over time. For extremely repellent soil the processes are complicated by issues such as evaporation.

A study of the energetics involved in wetting reveals that both particle size and roughness will play an important role. Larger particle sizes will require more energy to move them up and around the water droplet during the adhesional-immersional wetting stage and this is dependent on the energy balance between the solid-vapour interface being destroyed and formation of new solid-water interface. For more hydrophilic soils there is a greater tangential force pulling grains towards the droplet and then forcing them up and around compared to more hydrophobic soils.

The implications of this research on the commonly used WDPT test should be considered. For example, the sinter based experiments identify the importance of carrying out measurements on sufficient depths of soil with regards to the droplet volume used. The data also supports research that droplet volume will influence the outcome of repellency tests. Small droplets (~20 µl) will take longer to infiltrate, which may increase the repellency class for a soil. Equally for drop sizes of any

volume on severely repellent soils the influence of evaporation will lead to a decrease in overall droplet volume and therefore will inevitably impact upon the final WDPT result obtained.

Future research may consider the impact amelioration techniques such as clay or biochar additions may have on the overall particle size distribution of a soil. Both will increase the surface area of the soil and therefore the active wetting front at the point of infiltration has an increased, and more polar, area to spread. It is possible that this permits a flowpath for water through the soil profile and whilst the soil appears to wets it may actually be the wettable component that is wetting readily and the areas of repellent soils will continue to take time to wet over time due to the need for chemical changes within the organics coating the soil grain surfaces.

8.1.3. To assess the validity of current contact angle measurements and theories used for measuring water repellent soils to see if they are suitable and to suggest an alternative geometric approach

In general, the contact angles of irregular surfaces measured using the sessile drop method on a goniometer are higher than those of a flat surface of the same material using the same technique. Understanding the amplification of contact angle by surface structure has for many years been based on the thermodynamic theoretical models of Cassie and Baxter (1944), for bridge-like wetting over the top of protrusions, and Wenzel (1936) for complete wetting of an irregular surface. Even though still widely used, ongoing debate in the literature continues to query the validity of these models for application to soil science and soil water repellency (Gao and McCarthy, 2007; 2009; Marmur and Bittoun, 2009; Kwon *et al.*, 2010; Cheng and McCarthy, 2011; Li and Shan, 2012; Milne and Amirfazli, 2012). The research described in chapter 7 examined this problem via the study of precisely controlled model soil surfaces.

The proposed geometric correction factor in chapter 7 offers a simple theoretical basis for understanding the increase in measured contact angles on soil surfaces compared to planar surfaces. These experiments support the idea that it is the three-phase contact line where the water drop sits on a particle surface that is critical for the assessment of advancing angles on soils and indicate that the Cassie and Baxter (1944) and Wenzel (1936) models are inappropriate for the interpretation of

measured contact angles on irregular surfaces such as soils. Even for samples where correction cannot be made because the required measurements cannot be obtained the theoretical basis for the increased measured contact angle over that expected for a plane surface remains sound. Overestimates of flat-plane contact angles of the order of 20-30^{o} for soils are to be expected.

Further application of this correction method to a wider range of particle sizes and organic applications would be the next step in assessing its effectiveness as a suitable tool in the measurement of contact angles using a goniometer and the sessile drop method on water repellent soils.

8.1.4. Implications for the study of water repellent soils

Due to the heterogeneity of natural soils it is often difficult to assess new methodologies and techniques because of the degree of variability present. Model soils in this work, in the form of acid-washed sand (AWS) co-deposited with organics naturally found in water repellent soils; and man-made materials such as metal spheres and ballpoint needles coated in paraffin wax, offer an homogenous, controlled substrate which permits the application and assessment of novel techniques in a controlled environment.

For researchers studying soil water repellency the key implications of this research lie with the way current measurement techniques are used and executed, particularly the popularly used WDPT test and equally common contact angle measurement using a goniometer to study dynamic sessile drops. The research described clearly demonstrates the significance of droplet volume choice on the resultant WDPT measurement. Frequently researchers fail to report drop volume and number of drops used (Hallin *et al.*, 2013), however as evidenced here drop volume can lead to differences in repellency classifications and for contact angle measurements the larger the volume drop the further down it will sit on particle surfaces, which may influencing the overall measurement.

The importance of cross-disciplinary techniques such as the use of fluorescent probes to study soils offers an exciting novel approach and further research in these areas may help to increase understanding of the behaviour of the organic layer known to induce repellency in soil but which is still not fully understood.

References

Adamson, A.W. 1990. Physical Chemistry of Surfaces. John Wiley and Sons. New York.

AGCS, 2018 Burning Issues California Wildfire Review.

Ahn, S. 2014. Physical parameters for the manifestation of soil water repellency and their effects on rainsplash erosion of model soil particles. PhD Thesis. Swansea University, Swansea.

Alanis, N., Hernández-Madrigal, V.M., Cerdà, A., Muñoz-Rojas, M., Zavala. L.M. and Jordán, A. 2017. Spatial gradients of intensity and persistence of soil water repellency under different forest types in central Mexico. *Land Degradation and Development.* 28, 317–327.

Albani, J.R. 2007. Fluorescence Spectroscopy Principles (Chapter 7). Principles and applications of fluorescence spectroscopy. Chichester. John Wiley and Sons.

Altemüller, H.J. and Van Vliet-Lanoe, B. 1990. Soil thin section fluorescence micrsopy. *Developments in Soil Science*. 19, 565-579.

Atanassova, I. and Doerr, S.H. 2010. Organic compounds of different extractability in total solvent extracts from soils of contrasting water repellency. *European Journal of Soil Science*. 61, 298-313.

Bachmann, J., Ellies, A. and Hartge, K.H. 2000a. Development and application of a new sessile drop contact angle method to assess soil water repellency. *Journal of Hydrology*. 231-232, 66-75.

Bachmann, J., Horton, R., van der Ploeg, R.R. and Woche, S. 2000b. Modified sessile drop method for assessing initial soil-water contact angle of sandy soil. *Soil Science Society of America Journal.* 64, 564-567.

Bachmann J., Woche, S.K., Goebel M.-O., Kirkham, M.B. and Horton R. 2003. Extended methodology for determining wetting properties of porous media. *Water Resources Research*. 39, (12), 1353-1366.

Bayer, J. 2009. Soil water repellency: Comparison between individual particles and bulk properties. PhD Thesis. Swansea University, Swansea.

Birks, J.B., Dyson, D.J. and Munro, I.H. 1963. 'Excimer' fluorescence II. Lifetime studies of pyrene solutions. *Proceedings of the Royal Society A*. 575-588.

Birks, J.B., Lumb, M.D. and Munro, I.H. 1964. 'Excimer' fluorescence V. Influence of solvent viscosity and temperature. *Proceedings of the Royal Society A*. 289-297.

Bisdom, E.B.A., Dekker, L.W. and Schoute, J.F.T. 1993. Water repellency of sieve fractions from sandy soils and relationships with organic material and soil structure. *Geoderma.* 56, 105-118.

Blackwell, P.S. 1993. Improving sustainable production from water repellent sands. *Western Australia Journal of Agriculture.* 34, 160-167.

Blackwell, P.S. 2000. Management of water repellency in Australia, and risks associated with preferential flow, pesticide concentration and leaching. *Journal of Hydrology*. 231-232, 384-395.

Blanco-Canqui, H. 2017. Biochar and soil physical properties. *Soil Science Society of America Journal*. 81, 687-711.

Borisover, M., Laor, Y., Bukhanovsky, N., Saadi, I. 2006. Fluorescence-based evidence for adsorptive binding of pyrene to effluent dissolved organic matter, *Chemosphere*. 65, 1925-1934.

Brini, E, Fennell, C.J., Fernandez-Serra, M., Hribar-Lee, B., Luksic, M. and Dill, K.A. 2017. How water's properties are encoded in its molecular structure and energies. *Chemical Reviews* 117, 12385-12414.

Burch, G.J., Moore, I D. and Burns J. 1989. Soil hydrophobic effects on infiltration and catchment runoff. *Hydrological Processes*. 3, 211-222.

Butzen, V., Seeger, M., Marruedo A., de Jonge, L., Wengel, R., Ries, J.B. and Casper, M.C. 2015. Water repellency under coniferous and deciduous forest — Experimental assessment and impact on overland flow. *Catena*. 133, 255-265.

Carter, D.J. 1990. Water repellence in soils and its effect on wind erodibility. *Proceedings of the National Workshop on Water Repellency in Soils.* Adelaide, South Australia. 56-59.

Cassie, A. and Baxter, S. 1944. Wettability of porous surfaces. *Transactions of the Faraday Society.* 44, 11–16.

Cesarano, G., Incerti, G. and Bonanomi, G. 2016. The influence of plant litter on soil water repellency: insight from 13C NMR spectroscopy. *PLoS ONE*. 11(3).

Chan, K.Y. 1992. Development of seasonal water-repellence under direct drilling. *Soil Science Society of America Journal.* 56, 326-329.

Chang, H. and Wang, L. 2010. A Simple Proof of Thue's Theorem on Circle Packing. https://arxiv.org/abs/1009.4322v1 - accessed February 2019.

Chatfield, C. 1983. Statistics for technology. Third edition. Chapman and Hall Ltd. pp 381.

Chen, S.H. and Frank, C.W. 1989. Infrared and fluorescence spectroscopic studies of self-assembled n-alkanoic acid monolayers. *Langmuir*. 5, 978-987.

Cheng, D.F and McCarthy. T.J. 2011. Using the fact that wetting is contact line dependent. *Langmuir*. 27, 3693-3697.

Chmyrov, A. 2010. Photo-induced dark studies in fluorescence spectroscopy – investigations and applications. PhD Thesis. KTH Engineering Sciences, Stockholm.

Clothier, B.E., Vogeler, I. and Magesan, G.N. 2000. The breakdown of water repellency and solute transport through a hydrophobic soil. *Journal of Hydrology*. 231-232, 255-264.

Contreras, S., Canton, Y. and Sole-Benet. A. 2008. Sieving crusts and macrogaunal activity control soil water repellency in semiarid environments: Evidences from SE Spain. *Geoderma*. 145, 252-258.

Costa T., Seixas de Melo, J.S. and Burrows, H.D. 2009. Fluorescence behaviour of a pyrene-end-capped poly(ethylene oxide) in organic solvents and in dioxane-water mixtures. *Journal of Physical Chemistry B*. 113, 618-626.

Costa, A.L., Gomes, A.C., Pillinger., M, Goncalves, I.S., Seixas de Melo, J.S. 2015. Controlling the fluorescence behaviour of 1-Pyrenesulfonate by cointercalation with a surfactant in a layered double hydroxide. *Langmuir*. 31, 4769-4778.

Crockford, S., Topalidis, S. and Richardson, D.P. 1991. Water repellency in a dry sclerophyll forest - measurements and processes. *Hydrological Processes*. 5, 405-420.

DeBano, L.F. 1991. The effects of fire on soil properties. *United States Department of Agriculture Forestry Service General Technical Report INT-280.*

DeBano,L.F. 2000a. The role of fire and soil heating on water repellency in wildland environments: a review. *Journal of Hydrology.* 231-232, (Special issue: "Water Repellency in soils"), 195–206.

DeBano, L.F. 2000b. Water repellency in soils: a historical overview. *Journal of Hydrology*. 231-232, 4-32.

DeBano, L.F., Mann, L.D. and Hamilton, D.A. 1970. Translocation of hydrophobic substances into soil by burning organic litter. *Soil Science Society of America Proceedings*. 34, 130-133.

DeBano, L.F., Savage, S.M. and Hamilton, A.D., 1976. The transfer of heat and hydrophobic substances during burning. *Soil Science Society of America Proceedings*. 40, 779-782.

de Blas., E., Rodriguez-Alleres, M. and Almendros, G. 2010. Speciation of lipid and humic fractions in soils under pine and eucalyptus forest in northwest Spain and its effect on water repellency. *Geoderma.* 155, 242-248.

de Blas, E., Almendros, G. and Sanz, J. 2013. Molecular characterisation of lipid fractions from extremely water-repellent pine and eucalyptus forest soils. *Geoderma.* 206, 75-84.

de Jonge, L.W., Jacobsen, O.H. and Moldrup, P. 1999. Soil water repellency: effects of water content, temperature, and particle size. *Soil Science Society of America Journal* 63, 437-442.

de Jonge, L.W., Moldrup, P. and Schjonning, P. 2009. Soil infrastructure, interfaces and translocation processes in inner space ('soil-it-is'): towards a road map for the constraints and crossroads of soil architecture and biophysical processes. *Hydrology and Earth Systems Sciences*. 13 (8), 1485–1502.

Dekker, L.W. and Ritsema, C.J., 1994. How water moves in a water repellent sandy soil. 1. Potential and actual water repellency. *Water Resources Research.* 30, 2507-2517.

Dekker, L.W. and Ritsema, C.J. 1995. Fingerlike wetting patterns in two water-repellent loam soils. *Journal of Environmental Quality*. 24, 324-333.

Dekker, L.W. and Ritsema, C.J. 1996. Variation in water content and wetting patterns in Dutch water repellent peaty clay and clayey peat soils. *Catena.* 28, 89-105.

Dekker, L.W., Ritsema, C.J. and Oostindie, K. 2000. Extent and significance of water repellency in dunes along the Dutch coast. *Journal of Hydrology*. 231-232, 112-125.

Dekker, L.W., Ritsema, C.J., Oostindie, K., Moore, D. and Wesseling J.G. 2009. Methods for determining soil water repellency on field-moist samples. *Water Resources Research*. 45 (4).

Dekker, L.W., Ritsema, C.J., Oostindie, K., Wesseling, J. and Geissen, V. 2019. Effects of a soil surfactant on grass performance and soil wetting of a fairway. *Geoderma*. 338, 481-492.

Deng, Y. and Dixon, J.B. 2002. "Soil organic matter and organic–mineral interactions". In Soil Mineralogy with Environmental Applications, Edited by: Dixon, J.B. and Schulze, D.G. 69–107. Madison: Soil Science Society of America. SSSA Book Series No.

Deye, J.F., Berger, T.A. and Anderson, A.G. 1990. Nile red as a solvatochromic dye for measuring solvent strength in normal liquids and mixtures of normal liquids with supercritical and near critical fluids. *Analytical Chemistry*. 62, (6), 615-622.

Diamantis, V., Pagorogon, L., Gazani, E, Gkiougkis, I., Pechtelidis, A., Pliakas, F., van den Elsen, E., Doerr, S.H., and Ritsema, C.J. 2017. Use of clay dispersed in water for decreasing soil water repellency. *Land Degradation and Development*. 28, 328–334.

Diehl, D. and Schaumann, G.E. 2007. The nature of wetting on urban soil samples: wetting kinetics and evaporation assessed from sessile drop shape. *Hydrological Processes*. 21, 2255–2265.

Doerr, S.H. 1998. On Standardizing the 'water drop penetration time' and the 'molarity of an ethanol droplet' techniques to classify soil hydrophobicity: a case study using medium textured soil. *Earth Surface Processes and Landforms* 23, 663-668.

Doerr, S., Shakesby, R. and Walsh, R. 1996. Soil hydrophobicity variations with depth and particle size fraction in burned and unburned Eucalyptus globulus and Pinus pinaster forest terrain in the Águeda basin, Portugal. *Catena*. 27, (1), 25–47.

Doerr, S.H., Shakesby, R.A. and Walsh, R.P.D. 1998. Spatial variability of soil hydrophobicity in fire-prone eucalyptus and pine forests, Portugal. *Soil Science*. 163, 313-324.

Doerr, S.H., Shakesby, R.A. and Walsh, R.P.D. 2000. Soil water repellency: its causes, characteristics and hydro-geomorphological significance. *Earth Science Reviews*. 51, 33-65.

Doerr, S.H., Dekker, L.W., Ritsema, C.J., Shakesby, R.A. and Bryant. R. 2002. Water repellency of soils: the influence of ambient relative humidity. *Soil Science Society of America Journal*. 66, 401-405.

Doerr, S.H., Llewellyn, C.T., Douglas, P., Morley, C.P., Mainwaring, K.A., Haskins, C., Johnsey, L., Ritsema, C.J., Stagnitti, F. and Allinson, G. 2005. Extraction of compounds associated with water repellency in sandy soils of different origin. *Australian Journal of Soil Research*. 43 (3), 225-237.

Doerr, S.H., Woods, S.W., Martin, D.A. and Casimiro, M. 2009 Natural background soil water repellency in conifer forests in north-western USA: its prediction and relationship to wildfire occurrence. *Journal of Hydrology*. 371, 12-21.

Doerr, S. H. and Thomas, A. D. 2000. The role of soil moisture in controlling water repellency: new evidence from forest soils in Portugal. *Journal of Hydrology.* Special issue: "Water Repellency in soils", 134–147.

Douglas, P., Mainwaring, K.A., Morley, C.P., Doerr, S.H. 2007. The kinetics and energetics of transitions between water repellent and wettable soil conditions: a linear free energy analysis of the relationship between WDPT and MED/CST. *Hydrological Processes*. 21, 2248-2254.

Evans, R.C., Douglas, P. and Burrows, H.D. 2013. Applied Photochemistry. Springer, Netherlands.

Fishkis, O., Müller, K., Hable, R. and Huwe, B. 2016. Effects of throughfall exclusion, soil texture and spatial continuity on soil water repellency in Fichtel Mountains, Germany. *Soil Science Society of America Journal*. 80, 554-562.

Fitzpatrick E A 1993. Soil microscopy and micromorphology. Chichester. John Wiley and Sons. pp304.

Franco, C.M.M., Clarke, P.J., Tate, M.E. and Oades, J.M. 2000. Hydrophobic properties and chemical characterisation of natural water repellent materials in Australian sands. *Journal of Hydrology*. 231-232, 47-58.

Gago, S., Telma, C., Sexias de Melo, J, Goncalves, I.S. and Pillinger, M. 2008. Preparation and photophysical characterization of Zn-Al layered double hydroxides intercalated by anionic pyrene derivatives. *Journal of Materials Chemistry.*18, 894-904.

Ganaye, V.A., Keiding, K., Vogel., T.M., Viriot, M. and Block, J. 1997. Evaluation of soil organic matter polarity by pyrene fluorescence spectrum variations. *Environmental Science and Technology*. 31, (10), 2701-2706.

Gao, L. and McCarthy, T.J. 2007. How Wenzel and Cassie were wrong. *Langmuir.* 23, (7), 3762–3765.

Gao, L. and McCarthy, T J. 2009. Wetting 101 °. *Langmuir*. 25, (4), 14105-14115.

Glushko, V., Thaler, M.S.R. and Karp, C.D. 1981. Pyrene fluorescence fine structure as a polarity probe of hydrophobic regions: Behavior in model solvents. *Archives of Biochemistry and Biophysics*. 210, (1), 33-42.

Goebel, M-O., Bachmann, J., Reichstein M., Janssens, I., Guggenberger, G. 2011. Soil water repellency and its implications for organic matter decompositions: is there a link to extreme climatic events? *Global Change Biology.* 17, (8), 2640-2656.

Greenspan, P., Mayer, E.P. and Fowler, S.D. 1985. Nile red: A selective fluorescent stain for intracellular lipid droplets. *The Journal of Cell Biology.* 100, 965-973.

Hallett, P.D., Douglas, J.T., Ritz, K., Wheatley, R.E. and Young, I.M. 2001. Plant root and microbial derived soil water repellency. In: *Scottish Crop Research Institute Annual Report* 2000/2001 (Macfarlane-Smith, W.H. and Heilbronn,T. editors), 148-151.

Hallin, I.L., Douglas, P., Doerr, S.H. and Bryant, R. 2015. The effect of addition of a wettable biochar on soil water repellency. *European Journal of Soil Science*. 66 1063-1073.

Hallin, I.L. 2013. Impact of heterogeneity and biochar on soil water repellency: measurements and mechanisms. PhD Thesis. Swansea University, Swansea.

Hallin, I. L, Douglas, P., Doerr, S.H. and Bryant, R. 2013. The role of drop volume and number on soil water repellency determination. *Soil Science Society of America Journal.* 77, 1732-1743.

Hallin, I.L., Douglas, P., Doerr, S.H., Matthews, I., Bryant, R. and Charbonneau, C. 2017. The potential of biochar to remove hydrophobic compounds from model sandy soils. *Geoderma*. 285, 132-140.

Hansel, F.A., Aoki, C.T., Maia, C.M.B.F., Cunha, A. J. and Dedecek, R.A. 2008. Comparison of two alkaline treatments in the extraction of organic compounds associated with water repellency in soil under Pinus taeda. *Geoderma*. 148, 167–172.

Harper, R.J. and Gilkes, R.J. 1994. Soil attributes related to water repellency and the utility of soil survey for predicting its occurrence. *Australian Journal of Soil Research.* 32, 1109-1124.

Haynes, W.M. (ed.). 2015. CRC Handbook of Chemistry and Physics. 95th Edition. CRC Press LLC. p3-294.

Hermansen, C., Moldrup, P., Müller K., Weber Jensen, P., van den Dijssel, C., Jeyakumar, P. and de Jonge L.W. 2019. Organic carbon content controls the severity of water repellency and the critical moisture level across New Zealand pasture soils. *Geoderma.* 338, 281-290.

Hillel. D. 1998. Environmental soil physics. San Diego, CA. Academic Press.

Horne, D.J. and McIntosh, J.C. 2000. Hydrophobic compounds in sands in New Zealand - extraction, characterisation and proposed mechanisms for repellency expression. *Journal of Hydrology*. 231-232, 35-46.

Intergovernmental Panel on Climate Change (IPCC), 2018. Global warming of 1.5 ^{o}C. An IPCC special report on the impacts of global warming of 1.5 ^{o}C above pre-industrial levels and related global greenhouse gas emission pathways, in the context of strengthening the global response to the threat of climate change, sustainable development, and efforts to eradicate poverty. World Meteorological Organization, Geneva, Switzerland. 32pp.

Jackson, M.L. 1958. Soil Chemical Analysis. Prentice-Hall, New Jersey.

Jaramillo, D.F., Dekker, L.W., Ritsema, C.J. and Hendrickx, J.M.H. 2000. Occurrence of soil water repellency in arid and humid climates. *Journal of Hydrology*. 231-232, 105-111.

Jarvis, N.L. and Scheiman M.A. 1967. Surface potentials of aqueous electrolyte solutions. *NRL Report 6583*. Naval Research Laboratory, Washington.

Jaycock, J. and Parfitt, G. 1981. Chemistry of interfaces. Ellis Horwood series in chemical science. Chichester, England. pp279.

Jee, A-Y., Park, S., Kwon, H. and Lee, M. 2009. Excited state dynamics of nile red in polymers. *Chemical Physical Letters.* 477. 112-115.

Jex, G.W., Bleakley, B.H., Hubbell, D.H. and Munro, L.L. 1985. High humidity-induced increase in water repellency in some sandy soils. *Soil Science Society of America Journal*. 49, 1177-1182.

Jiménez-Morillo1, N.T., González-Pérez, J.A., Jordán, A., Zavala, L.M., de la Rosa, J.M., Jiménez-González, M.A. and González-Vila, F.J. 2016. Organic matter

fractions controlling soil water repellency in sandy soils from the Donana National Park (southwestern Spain). *Land Degradation and Development*. 27, 1413–1423.

Johnson, I. and Spence, M. (2010). The Molecular Probes Handbook: A Guide to Fluorescent Probes and Labeling Technologies. Carlsbad, CA: Life Technologies Corporation.

Jordan, C.S., Daniels, J.L. and Langley, W. 2017. The effects of temperature and wet-dry cycling on water-repellent soils. *Environmental Geotechnics*. 4, (4), 299-307.

Kalayanasundaram, K. and Thomas, J.K. 1977. Environmental effects on vibronic band intensities in pyrene monomer fluorescence and their application in studies of micellar systems. *Journal of American Chemical Society*. 99, (7), 2039-2044.

King, P.M. 1981. Comparison of methods for measuring severity of water repellence of sandy soils and assessment of some factors that affect its measurement. *Australian Journal of Soil Research.* 19, 275-285.

Krishna, P. and Pandey, D. 1981. Close-packed structures. International Union of Crystallography. University College Cardiff Press. Cardiff, Wales.

Kruss Scientific, 2018. Technical note TN314e. www.kruss-scientific.com – accessed June 2018.

Kwon, Y., Choi, S., Anantharaju N, Lee, J., Panchagnula, M.V. and Patankar, N.A. 2010. Is the Cassie-Baxter formula relevant? *Langmuir*. 26, (22) 17528-17531.

Lakowicz, J.R. 2006. Principles of fluorescence spectroscopy. Plenum. New York.

Leelamanie, D.A. and Karube, J. 2007. Effects of organic compounds, water content and clay on the water repellency of a model sandy soil. *Soil Science and Plant Nutrition*. 53, 711-719.

Leelamanie, D.A. and Karube, J. 2009. Effects of hydrophobic and hydrophilic organic matter on the water repellency of model sandy soils. *Soil Science and Plant Nutrition.* 55, 462-467.

Leelamanie, D.A., Karube, J. and Yoshida, A. 2008. Relative humidity effects on contact angle and water drop penetration time of hydrophobized fine sand. *Soil Science and Plant Nutrition.* 54, 695-700.

Leelamanie, D.A., Karube, J. and Yoshida, A. 2010. Clay effects on contact angle and water drop penetration time of model soils. *Soil Science and Plant Nutrition.* 56, 371–375.

Leelamanie, D, A. and Karube, J. 2012. Drop size dependence of soil-water contact angle in relation to the droplet geometry and line tension. *Soil Science and Plant Nutrition.* 58, 675-683.

Lehmann, J. and Joseph, S. 2009. Biochar for environmental management - an introduction. Chapter 1 in Biochar for Environmental Management Science and Technology. Lehmann, J. and Joseph, S. (Eds). Earthscan Publications Ltd., London, England. 448.

Leighton-Boyce G., Doerr, S.H., Shakesby, R.A. and Walsh, R.P.D. 2007. Quantifying the impact of soil water repellency on overland flow generation and erosion: a new approach using rainfall simulation and wetting agent on in situ soil. *Hydrological Processes*. 21, 2337-2345.

Lemmnitz, C., Kühnert, M., Bens, O., Gunter, A., Merz, B. and Hüttl R.F. 2008. Spatial and temporal variations of soil water repellency and the influence on surface runoff. *Hydrological Processes.* 22 (12).

Letey, J. 1969. Measurement of contact angle, water drop penetration time, and critical surface tension. In: DeBano, L.F., Letey, J. (Eds.), *Proceedings of a Symposium on Water Repellent Soils*, May 6-10. 1968, Riverside, CA, pp. 43-47, 354p.

Letey, J., Osborn, J. and Pelishek, R.P. 1962. Measurement of liquid-solid contact angles in soil and sand. *Soil Science*. 93, 149-153.

Letey, J., Carrillo, M.L.K. and Pang, X.P. 2000. Approaches to characterize the degree of water repellency. *Journal of Hydrology*, 231-232, 61-65.

Lide, D.R. 2005. CRC Handbook of Chemistry and Physics 86th Edition 2005-2006. CRC Press, Taylor & Francis, Boca Raton, FL. pp3-462.

Li, R., and Shan, Y. 2012. Contact angle and local wetting at contact line. *Langmuir.* 28, 15624-15628.

Llewellyn, C.T. (2005). Studies of the molecular basis of soil water repellency. PhD Thesis. Swansea University, Swansea.

Lozano E., Garcia-Orenes, F., Bárcenas-Moreno, G., Jiménez-Pinilla, P, Mataix-Solera, J., Arceneguil, V., Morugán-Coronado, A. and Mataix-Beneyto, J. 2014. Relationships between soil water repellency and microbial community composition under different plant species in a Mediterranean semiarid forest. *Journal of Hydrology and Hydromechanics.* 62, (2), 101–107.

Liu, J., He., X. and Zhang, J. Z. 2017. Structure of liquid water – a dynamical mixture of tetrahedral and 'ring-and-chain' like structures. *Phys Chem Chem Phys.* 19. 11931-11936.

Mainwaring, K.A. (2004). Chemical characterization and repellency-inducing effects of organic compounds isolated from sandy soils. PhD Thesis. Swansea University, Swansea.

Mainwaring, K.A., Morley, C.P., Doerr, S.H., Douglas, P., Llewellyn, C.T., Llewellyn, G., Matthews, I. and Stein, B.K. 2004. Role of heavy polar organic

compounds for water repellency of sandy soils. *Environmental Chemistry Letters.* 2, (1), 35-39.

Mainwaring, K., Hallin, I.L., Douglas, P., Doerr, S.H. and Morley, C.P. 2013. The role of naturally occurring organic compounds in causing soil water repellency. *European Journal of Soil Science*. 64, 667-680.

Mallik, A.U. and Rahman, A.A. 1985. Soil water repellency in regularly burned *Calluna* heathlands: comparison of three measuring techniques. *Environmental Management*. 20, 207-218.

Mao, J., Nierop, K.G.J., Sinninghe Damsté, J.S. and Dekker, S.C. 2014 Roots induce stronger soil water repellency than leaf waxes. *Geoderma.* 232-234, 328-340.

Mao, J., Nierop, K.G.J., Rietkerk, N., Sinninghe Damsté, J.S., Dekker, S.C. 2016. The influence of vegetation on soil water repellency-markers and soil hydrophobicity. *Science of the Total Environment*. 566-567, 608-620.

Mao, J., Nierop K.G.J, Dekker, S.C., Dekker, L.W. and Chen, B. 2019. Understanding the mechanisms of soil water repellency from nanoscale to ecosystem scale: a review. *Journal of Soils and Sediments.* 19, 171–185.

Marmur, A. and Bittoun E. 2009. When Wenzel and Cassie are right: Reconciling local and global considerations. *Langmuir*. 25, 1277-1281.

Ma'Shum, M., Tate, M.E., Jones, G.P., and Oades, J.M. 1988. Extraction and characterization of water-repellent materials from Australian soils. *Journal Soil Science*. 39, 99-110.

Ma'Shum, M., Oades, J.M and Tate M E. 1989. The use of dispersible clays to reduce water repellency of sandy soils. *Australian Journal of Soil Research*. 23, 623-626.

Mataix-Solera, J. and Doerr, S.H. 2004. Hydrophobicity and aggregate stability in calcareous topsoils from fire-affected pine forests in southeastern Spain. *Geoderma.* 118, 77–88.

Mazur, M. and Blanchard, G. J. 2005. Probing Intermolecular Communication with Surface-Attached Pyrene. *Journal of Physical Chemistry B*. 109, 4076-4083.

McGhie, D.A. and Posner, A.M. 1980. Water repellence of a heavy-textured western Australian surface soil. *Australian Journal of Soil Research.* 18, 309-323.

McGhie, D.A. and Posner, A.M. 1981. The effect of plant top material on the water repellence of fired sands and water-repellent soils. *Australian Journal of Agricultural Research*. 32, 609-620.

McHale, G., Newton, M.I. and Shirtcliffe, N.J. 2005. Water-repellent soil and its relationship to granularity, surface roughness and hydrophobicity: a materials science view. *European Journal of Soil Science*. 56, (4), 445–452.

McIntosh, J.C. and Horne, D.J. 1994. Causes of repellency: I. The nature of the hydrophobic compounds found in a New Zealand development sequence of yellow-brown sands. In: *Proceedings of the 2nd National Water Repellency Workshop*, August 1994, Perth, Western Australia, pp. 8-12.

McKissock, I., Gilkes, R.J. and Walker, E.L. 2002. The reduction of water repellency by added clay is influenced by clay and soil properties. *Applied Clay Science*. 20, 225-241.

McKissock, I., Walker, E.L., Gilkes, R.J. and Carter, D.J. 2000. The influence of clay type on reduction of water repellency by applied clays: a review of some West Australian work. *Journal of Hydrology.* 231-232, 323-332.

Michel, J.C., Rivière, L.M. and Bellon-Fontaine, M.N. 2001. Measurement of the wettability of organic materials in relation to water content by the capillary rise method. *European Journal of Soil Science.* 52, 459-468.

Miller, J.C. and Miller, J.N. 1993. Statistics for analytical chemistry. Third edition. Ellis Horwood PTR Prentice Hall. pp 233.

Milne, A.J.B. and Amirfazli A. 2012. The Cassie equation: How it is meant to be used. *Advances in Colloid and Interface Science*. 170, 48-55.

Montalti, M., Credi, A., Prodi, L. and Gandolfi, M.T. 2006. Handbook of Photochemistry. 3rd Edition. CRC Press. Taylor & Francis Group. USA.

Moore, W.J. 1972. Physical Chemistry. Longman Group Ltd., London, England (844p).

Moore, P.A., Lukenbach, M.C., Kettridge, N., Petrone, R.M., Devito, K.J. and Waddington, J.M. 2017. Peatland water repellency: importance of soil water content, moss species and burn severity. *Journal of Hydrology*. 554, 656-665.

Morley, C.P., Mainwaring, K.A., Doerr, S.H., Douglas, P., Llewellyn, C.T. and Dekker, L.W. 2005. Organic compounds at different depths in a sandy soil and their role in water repellency. *Australian Journal of Soil Research*. 43, (3), 239-249.

Müller, K. and Deurer, M. 2011. Review of the remediation strategies for soil water repellency. *Agriculture, Ecosystems and Environment*. 144, 208-221.

Müller, K., Deurer, M., Kawamoto, K., Kuroda. T., Subedi, S., Hiradate, S., Komatsu, T. and Clothier B.E. 2014. A new method to quantify how water repellency compromises soils' filtering function. *European Journal of Soil Science.* 65, 348-359.

Nakajima, A. 1971. Solvent effect on the vibrational structures of the fluorescence and absorption spectra of pyrene. *Bulletin of the Chemical Society of Japan*. 44, 3272.

Nakajima, A. 1974. Solvent enhancement in the first singlet-singlet transition of pyrene-d_{10}. *Spectrochimica Acta Part A: Molecular Spectroscopy.* 30, (3), 860-862.

Nakajima, A. 1976. Effects of isomeric solvents on vibronic band intensities in fluorescence spectrum of pyrene. *Journal of Molecular Spectroscopy.* 61, (3), 467-469.

Olympus-lifescience, 2019. https://www.olympus-lifescience.com/en/microscope-resource/primer/techniques/fluorescence/filters/ -accessed - January, 2019

Ozdemir, O., Karakashev, S.I., Nguyen, A.V. and Miller, J.D. 2009. Adsorption and surface tension analysis of concentrated alkali halide brine solutions. *Minerals Engineering*. 22, 263–271.

Papierowska, E., Matysiak, W., Szatylowicz, J.M., Debaene, G., Urbanek, E., Kalisz B. and Łachacz, A. 2018. Compatibility of methods used for soil water repellency determination for organic and organo-mineral soils. *Geoderma.* 314, 221–231.

Pashley, R.M. and Karamen, M.E. 2004. Applied Colloid and Surface Chemistry. John Wiley & Sons, Ltd. United Kingdom.

Petrucci, R.H. 1989. General Chemistry Principles and modern applications. 5th Edition. Macmillan Publishing Company. USA.

Poulenard, J., Michel, J.C., Bartoli, F., Portal, J.M. and Podwojewski, P. 2004. Water repellency of volcanic ash soils from Eucadorian Paramo: effect of water content and characteristics of hydrophobic organic matter. *European Journal of Soil Science*. 55, 487-496.

PubChem, 2019. https://pubchem.ncbi.nlm.nih.gov – accessed September 2018.

Ratcliff, B., Johnson, D., Eccles, H., Nicholson., J. and Raffan., J. 2000. Chemistry 1.Cambridge Advanced Sciences. Cambridge University Press. 224pp.

Reichardt, C. 1988. Solvents and Solvent Effects in Organic Chemistry. Second, revised and enlarged edition. Weinheim. Pp 534.

Reichardt, C, 1994. Solvatochromic dyes as solvent polarity indicators. *Chemical Reviews*, 94, 2319-2358.

Rigby, M., Smith, E. B., Wakeham W.A. and Maitland, G.C. 1986. The Forces Between Molecules. Oxford Science Publications. Clarendon Press, Oxford. Oxford University Press.

Ritsema, C.J. and Dekker, L.W. 1994. Soil moisture and dry bulk density patterns in bare dune sands. *Journal of Hydrology*. 154, 107-131.

Ritsema, C.J. and Dekker, L.W. 1995. Distribution flow: a general process in the top layer of water repellent soils. *Water Resources Research*. 30, 2519-2531.

Ritsema, C.J. and Dekker, L.W. 1996. Water repellency and its role in forming preferred flow paths in soils. *Australian Journal of Soil Research*. 34, 475-487.

Ritsema, C.J., Dekker, L.W., van den Elsen, E.G.M., Oostindie, K. and Nieber, J.L. 1997a. Recurring fingered flow pathways in a water repellent sandy field soil. *Hydrology and Earth System Sciences.* 44, 777-786.

Ritsema, C.J., Dekker, L.W. and Heijs, A.W.J. 1997b. Three-dimensional fingered flow patterns in a water repellent sandy field soil. *Soil Science*. 162, 79-90.

Roberts, F.J. and Carbon, B.A. 1971. Water repellence in sandy soils of south-western Australia. 1. Some studies related to field occurrence. *Field Station Record of the CSIRO Division of Plant Industry*. 10, 13-20.

Roberts, F.J. and Carbon, B.A. 1972. Water repellence in sandy soils of south-western Australia. 2. Some chemical characteristics of the hydrophobic skins. *Australian Journal of Soil Research*. 10, 35-42.

Rodriguez-Alleres, M., de Blas, E. and Benito, E. 2007. Estimation of soil water repellency of different particle size fractions in relation with carbon content by different methods. *Science of the Total Environment.* 378, (1-2), 147–150.

Roy, J.L. and McGill, W.B. 2000. Flexible conformation in organic matter coatings: an hypothesis about soil water repellency. *Canadian Journal of Soil Science*. 80, 143-152.

Roy, J.L. and McGill, W.B. 2002. Assessing soil water repellency using the molarity of ethanol droplet (MED) test. *Soil Science*. 167, 83-97.

Rye, C.F. and Smettem, K.R.J. 2017. The effect of water repellent soil surface layers on preferential flow and bare soil evaporation. *Geoderma.* 289, 142-149.

Sackett, D.L. and Wolff, J. 1987. Nile red as a polarity-sensitive fluorescent probe of hydrophobic protein surfaces. *Analytical Biochemistry*. 167, (2), 228-34.

Savage, S.M., Martin, J.P. and Letey, J. 1969. Contribution of some soil fungi to natural and heat-induced water repellency in sand. *Proceedings of the Soil Science Society of America*. 33, 405-409.

Savage, S.M., Osborn, J, Letey, J. and Heaton, C. 1972. Substances contributing to fire-induced water repellency in soils. *Proceedings of the Soil Science Society of America Journal.* 36, 674-678.

Scott, D.F. 1991. The influence of eucalypts on soil wettability. In: A.P.G. Schönau (Editor), The Role of Eucalypts. *Proceedings of the IUFRO Symposium on Intensive Forestry, Durban, South African Institute of Fores*try. Pretoria, South Africa.

Scott, D.F. 2000. Soil wettability in forested catchments in South Africa; as measured by different methods and as affected by vegetation cover and soil characteristics. *Journal of Hydrology.* 231-232, 87-104.

Siebold, A., Walliser, A., Nardin, M., Oppliger, M. and Schultz, J. 1997. Capillary rise for thermodynamic characterization of solid particle surface. *Journal of Colloid and Interfacial Sci*ence. 186, 60–70.

Shimoaka T., Itoh, Y. and Hasegawa, T. 2012. Dynamic rearrangement of stearic acid molecules adsorbed on a gold surface induced by ambient water molecules studied by infrared spectroscopy. *Journal Physical Chemistry. C. 116* (32), 17142–17148.

Skoog, D.A., Holler, F.J. and Nieman, T.A. 1998. Principles of Instrumental Analysis (5th Edition). Thomson Learning, Inc, Ohio, USA. 850p.

Slavchov, R.I. and Novev, J.K. 2012. Surface tension of concentrated electrolyte solutions. *Journal of Colloid and Interface Science*. 387, 234-243.

Smith, E.B. 1990. Basic chemical thermodynamics. Fourth Edition. Oxford Science Publications. Clarendon.

Spohn, M. and Rillig, M.C. 2012. Temperature- and moisture-dependent soil water repellency induced by the basidiomycete Agaricus bisporus. *Pedobiologia.* 55, 59–61

Striker, G., Subramaniam, V, Siedel, C.A.M. and Volkmer, A. 1999. Photochromicity and fluorescence lifetimes of green fluorescent protein. *Journal of Physical Chemistry B*. 103, 8612.

Sumner, M.E. and Wilding, L.P. 1999. Chapter 1 Introduction In: Handbook of soil science. Sumner, M.E. 1999. 2148 p CRC Press. New York.

Swift, R.S. 1989. Molecular weight, size, shape, and charge characteristics of humic substances: some basic considerations. In: Hayes, M.H.B., MacCarthy, P., Malcolm, R.L. and Swift, R.S. (Eds.) Humic Substances II. In Search of Structure, Wiley, New York, pp. 449–465.

Tilley, R. 2000. Colour and the optical properties of materials. An exploration of the relationship between light, the optical properties of materials and colour. John Wiley and Sons, Ltd. Chicester. Pp 335.

Tillman, R.W., Scotter, D.R., Wallis, M.G. and Clothier, B.E. 1989. Water repellency and its measurement by using intrinsic sorptivity. *Australian Journal of Soil Research*. 27, 637-644.

Tippkotter, R. 1990. Staining of soil microorganisms and related materials with fluochromes. In Douglas, L.A. *ed*. *Soil Micromorphology*: a basic and applied cience. Amsterdam. Elsevier. pp 605-611.

Urbanek, E., Hallett, P., Feeney, D. and Horn, R. 2007. Water repellency and distribution of hydrophilic and hydrophobic compounds in soil aggregates from different tillage systems. *Geoderma.* 140, 147–155.

Van't Woudt, B.D. 1959. Particle coatings affecting the wettability of soils. *Journal of Geophysical Research.* 64, 263-267.

Vogelmann, D.S., Reichert, J.M., Prevedello, J., Awe, G.O. and Reinert, D.J. 2015. Soil hydrophobicity: comparative study of usual determination methods. *Ciência Rural*. 45, (2), 260-266.

Wallis, M.G. and Horne, D.J. 1992. Soil water repellency. In: *Advances in Soil Science* (Stewart, B.A., editor), Springer-Verlag. New York, Vol 20, 91-146.

Wallis, M.G., Horne, D.J. and McAuliffe, K.W. 1990a. A study of water repellency and its amelioration in a yellow brown sand. 1. Severity of water repellency and the effects of wetting and abrasion. *New Zealand Journal of Agricultural Research*. 33, 139-144.

Wallis, M.G., Horne, D.J. and McAuliffe, K.W. 1990b. A study of water repellency and its amelioration in a yellow brown sand. 2. The use of wetting agents and their interaction with some aspects of irrigation. *New Zealand Journal of Agricultural Research.* 33, 145-150.

Ward, P.R. and Oades, J.M. 1993. Effect of clay mineralogy and exchangeable cations on water-repellency in clay-amended sandy soils. *Australian Journal of Soil Research.* 31, 351-364.

Watson, C.L. and Letey, J. 1970. Indices for characterizing soil-water repellency based upon contact angle-surface tension relationship. *Soil Science Society of America Proceedings*. 34, 841-844.

Wenzel, R.N. 1936. Resistance of solid surfaces to wetting by water. *Industrial Engineering Chemistry*. 28, 988-994.

Whelan, A., Kechavarzi, C., Coulon, F. and Doerr, S.H. 2015. Experimental characterization of the impact of temperature and humidity on breakdown of soil water repellency in sandy soils and composts. *Hydrological Processes*. 29, 2065-2073.

Wijewardana, N.S., Kawamoto, K., Moldrup, P., Komatsu., T., Kurukulasuriya, L.C. and Priyankara, N.H. 2015. Characterization of water repellency for hydrophobized grains with different geometries and sizes. *Environmental Earth Sciences*. 74, 5525–5539.

Woche, S.K, Goebel, M.–O., Kirkham, M.B., Horton, R., Van der ploeg, R.R. and Bachmann, J. 2005. Contact angle of soils as affected by depth, texture and land management. *European Journal of Soil Science.* 56, 239-251.

Wolfram Mathworld, 2019. http://mathworld.wolfram.com/SphericalCap.html - accessed February 2019.

Yiannos, P.N. 1962. Molecular reorientation of some fatty acids when in contact with water. *Journal of Colloid Science.* 17, 334–347.

York, C.A. and Canaway, P.M. 2000. Water repellent soils as they occur on UK golf greens. *Journal of Hydrology*. 231-232, 126-133.

Young, T. 1805. On the cohesion of fluids. *Philosophical Transactions of the Royal. Society London, Series A*. 95, 65, 82.

Zhang, L., C, X. and Cai, W. 2011. Observations of the effect of confined space on fluorescence and diffusion properties of molecules in single conical nanopore channels. *Journal of Fluorescence.* 21, 1865-1870.

Zimmermann, J, Seeger, S. and Reifler, F.A. 2009. Superhydrophobic surfaces water shedding angle: a new technique to evaluate the water-repellent properties of hydrophobic surfaces. *Textile Research Jorunal.* 79, (17), 1565–1570.